UNIVERSITY OF CALIFORNIA

Los Angeles

Cyclic and Post-Cyclic Behavior of Sherman Island Peat

A dissertation submitted in partial satisfaction of the

requirements for the degree Doctor of Philosophy

in Civil Engineering

by

Ali Shafiee

2016

ABSTRACT OF THE DISSERTATION

Cyclic and Post-Cyclic Behavior of Sherman Island Peat

by

Ali Shafiee

Doctor of Philosophy in Civil Engineering

University of California, Los Angeles, 2016

Professor Scott Joseph Brandenberg, Co-Chair

Professor Jonathan Paul Stewart, Co-Chair

The Sacramento-San Joaquin Delta is a 700,000 acre estuary at the confluence of the Sacramento and San Joaquin rivers, which consists of below sea-level islands surrounded by levees. Many of theses levees are not engineered structures, consisting of uncompacted sands, silts, clays, and organics often founded upon natural levees and in some cases on peaty organic soil. Many hazards threaten the Delta, but the seismic hazard is exceptional because of the potential for multiple simultaneous breaches inundating many islands within the Delta. The objectives of this research are to improve fundamental understanding of cyclic and post-cyclic behavior of peat that could affect levee performance, and develop analysis tools to predict this behavior.

Laboratory testing is performed on 22 undisturbed Shelby tube samples gathered from Sherman Island at depths ranging from approximately 1 to 6 m. The shear testing in this research is carried out using the UCLA bi-directional broadband simple shear device, which is a digitally-

controlled device with capabilities for chamber pressure control and multidirectional excitation. The apparatus was improved as part of this research program to add capabilities for testing under constant-height and stress-controlled conditions.

Oedometer tests are carried out on Sherman Island peat to evaluate its compressibility properties. To facilitate accurate determination of the end of primary consolidation, a new consolidometer was fabricated that provides single drainage through the top of the specimen, while pore pressure is measured at the bottom. For specimens with high organic content (OC > 28%), values of coefficient of consolidation ($\boldsymbol{c_v}$) for normally-consolidated load stages are observed to decrease as vertical effective stress increases, often by more than two orders of magnitude over the stress range tested in the consolidometer. For the Sherman Island peat $\boldsymbol{c_v}$ is as high as 400×10^{-4} cm^2/s at σ_p'. The trend of compression index (C_c), and recompression index (C_r) confirms that they are positively correlated with in situ water content (w_0) and OC. The values of C_α/C_c (where C_α is secondary compression index) for the Sherman Island peat ranges from 0.05 to as high as 0.12 with an average of 0.08. Hydraulic conductivity k depends on void ratio, and decreases with the decrease in void ratio. The slope of e versus $logk$ (i.e., C_k) increases with initial void ratio (e_0), and the best fit for the data is $C_k = 0.20e_0$.

Monotonic test results show that lightly overconsolidated peat with OCR < 2 shows contractive behavior, while higher OCR's result in dilative behavior. The Normal Consolidation Line (NCL) and Failure State Line (FSL) are approximately parallel for OC ≤ 35%. Normalized shear strength (the normalization is with respect to pre-shear vertical effective stress) has been evaluated as a function of OCR. The soil behavior generally supports the concept of normalization, with the strength ratio being higher for high OC (80-85%) than for low OC (≤35%).

Cyclic strain-controlled tests show that for low shear strain amplitude, γ_c (< 0.7%), although hysteretic loops form, cyclic degradation of stiffness does not occur and pore pressures do not accumulate. Accordingly, stress paths are similar to those for a drained test. For higher γ_c, r_{ur} increases from cycle-to-cycle and reaches to around 0.1 after 15 cycles at 4% shear strain. The soil stiffness degrades slightly to achieve the uniform strain amplitude.

One of the principle contributions in this dissertation is to demonstrate that evaluation of the rate of secondary compression following primary consolidation is related to the vertical distance in void ratio – effective stress space between soil state and a secondary compression reference line (SCRL). The traditional approach takes this rate as logarithmically decaying with time following load application, but is shown to not be generally applicable. For example, it fails for the case of a small load increment applied to a soil element. I develop a conceptual and analytical framework to compute the rate of void ratio change as a function of soil state given this framework, which predicts slower secondary compression as OCR (overconsolidation ratio) increases. The proposed framework provides a much improved match to observations for conditions differing from those in traditional consolidation tests in which the ratio of load increase to initial stress is approximately unity.

When peaty organic soils are cyclically loaded, they can experience an increase of secondary compression rate relative what would have been present without dynamic loading. This increased rate of volume change occurs even for shear strain amplitudes that do not induce a pore pressure response. For a given soil, the rate change increases with strain amplitude and number of cycles, which can be viewed as a partial resetting the secondary compression clock without change in total stress. However, rather than modeling this in a time-based framework, I demonstrate that this reset behavior can be captured by a vertical shift of the SCRL, which can be quantified by a

reset index (I_R). The value of I_R varies between 0 (no reset) to 1 (fully reset). An empirical model is developed for I_R as a function of cyclic shear strain amplitude, number of uniform loading cycles, organic content, over-consolidation ratio, initial overburden pressure, and amount of static shear stress.

A simplified procedure is developed to estimate post-earthquake settlement of organic soils in consideration of post-earthquake pore pressure dissipation and accelerated rates of secondary compression. The procedure uses 1-D site response analysis to find representative profiles of peak shear strain and its phasing in time. The irregular shear strain time series is then converted to uniform shear strain cycles at some specified amplitude as a fraction of the peak. Reset index and pore pressure ratio at the conclusion of shaking are then calculated using predictions equations conditioned on strain amplitude, number of cycles, over-consolidation ratio, organic content, and pre-earthquake stress conditions. The resulting values of reset index and pore pressure can be used in a non-linear consolidation code to calculate post-earthquake settlement versus time.

The dissertation of Ali Shafiee is approved.

Mladen Vucetic

Lingsen Meng

Scott Joseph Brandenberg, Co-Chair

Jonathan Paul Stewart, Co-Chair

University of California, Los Angeles

2016

To my wife, Gelareh and sons, Nick & Ryan.

TABLE OF CONTENTS

LIST OF FIGURES

LIST OF TABLES

ACKNOWLEDGEMENTS

As I approach the end of my long career as a Ph.D. student at UCLA, I would like to acknowledge the help, support, and guidance I received from a number of people over the last five years. The research and this dissertation would not have been possible without them, and I am simultaneously humbled and grateful for all of the assistance they have provided.

I would like to express my deepest gratitude to my advisors, Professors Scott J. Brandenberg, and Jonathan P. Stewart, for their excellent guidance, caring, patience, and providing me with an excellent atmosphere for doing research.

Besides my advisors, I would like to thank the rest of my thesis committee: Professor Mladen Vucetic and Professor Lingsen Meng, for their insightful comments and encouragement, but also for the hard question which incented me to widen my research from various perspectives.

Financial support for the work described here was provided by the Department of Water Resources (DWR), the U.S. Geological Survey (USGS), and generous donations to the UCLA soil dynamics laboratory by Mr. Thierry Sanglerat. This support is gratefully acknowledged.

I would also like to thank my parents. They were always supporting me and encouraging me with their best wishes.

Finally, I would like to thank my wife, Gelareh, for her constant moral support and encouragement during my entire time at UCLA.

1 Introduction

1.1 HISTORICAL BACKGROUND

The Sacramento-San Joaquin Delta is a 700,000 acre estuary at the confluence of the Sacramento and San Joaquin rivers, which drain California's central valley west into the San Francisco Bay (Fig. 1.1). Prior to the mid-19th century, natural levees were formed by repeated historical flooding, but nearly 60 percent of the Delta was submerged daily by tides, and large areas were often inundated by seasonal river flooding. Water within the interior of the tidal wetland was primarily fresh, though water salinity within the Delta fluctuated significantly, which supported a diverse ecosystem (Lund et al. 2007).

The numerous plant species that thrived in the Delta combined with sediments delivered by historical flooding to form thick layers of peaty organic soil that is rich in nutrients and extremely compressible. These rich peaty soils led gold rush settlers to begin farming the natural levees in the mid-19th century. Limited availability of natural highlands in the Delta resulted in efforts to reclaim the low-lying areas by placing fill atop the natural levees. Many levees are not engineered structures, consisting of uncompacted sands, silts, clays, and organics often founded upon natural levees and in some cases on peaty organic soil.

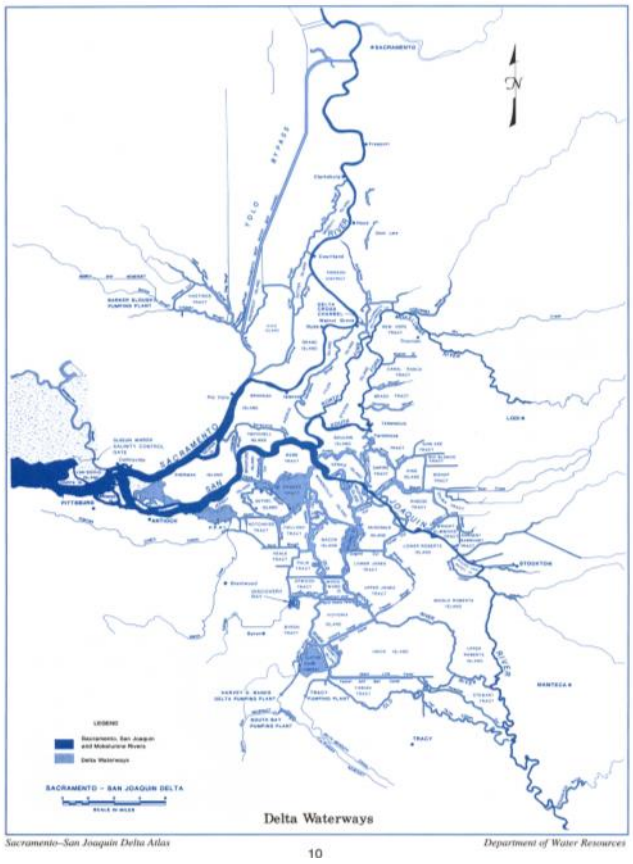

Figure 1.1 Waterways in the Sacramento-San Joaquin Delta (CDWR 1992)

To enhance reclamation efforts the State of California began selling Delta lands in 1858, and local reclamation districts were formed from collections of smaller parcel owners. Large "islands" were enclosed by levees as technology permitted more rapid levee construction by mechanized dredging, fill placement, and pumping of low-lying areas. Between 1860 and 1930, 441,000 acres were reclaimed (Thompson 1957). Approximately 400 miles of project levees within the Delta are now maintained by the State, while the remaining 700 miles of private levees are maintained by local reclamation districts with limited State cost sharing.

1.1.1 Subsidence and Consequences of Flooding

Historical flooding that had delivered sediments to the Delta prior to reclamation has been largely controlled in the past century as the Delta has been maintained as a fresh water conveyance system. Drying and tilling of farmland has caused oxidation and wind erosion of the peaty organic soils in the interior of the islands (Fig. 1.2), and subsidence of some islands has exceeded rates of $10 cm/year$. Many islands now lie as much as 3 to $5m$ below sea level, and often provide only $1m$ of freeboard at high tide. A levee breach therefore draws a significant volume of water into the island and large-scale inundation during periods of low fresh water outflow can locally reverse the flow direction, drawing saline water from the west into the Delta. This is a potentially catastrophic scenario that would compromise water intakes for the State Water Project and Central Valley Project, removing the sole water source for many communities and inundating farm land, wildlife habitat, and many utilities that run through Delta islands (Torres et al. 2000). Such large-scale inundation is unlikely in the event of an individual levee breach caused by burrowing animals and other local hazards because the existing emergency response system can respond to a single breach within a matter of hours and effect repair within

a matter of weeks. For example, a single levee breach caused inundation of upper and lower Jones Tracts in 2004 and the breach was quickly repaired, albeit at a cost of more than $100 million.

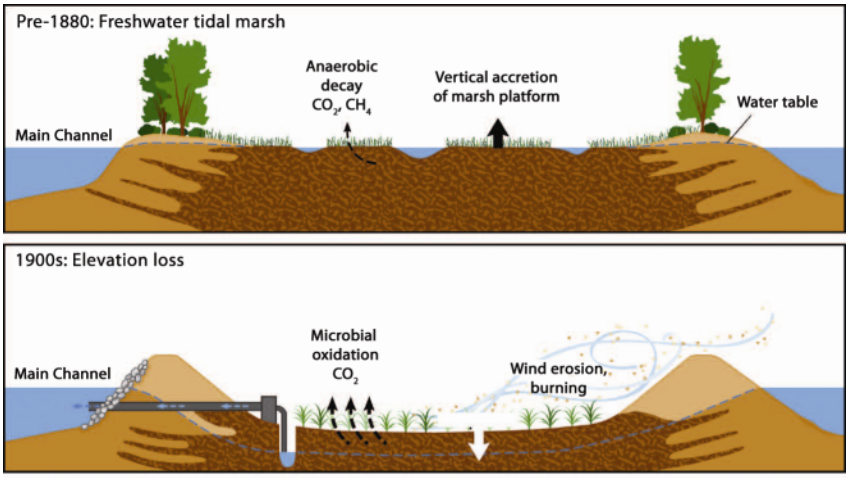

Figure 1.2 Mechanism of Delta peat subsidence (Mount and Twiss 2005)

1.1.2 Seismic Hazard

Many hazards threaten the Delta, but the seismic hazard is exceptional because of the potential for multiple simultaneous breaches inundating many islands within the Delta. Seismic risk in the Delta arises principally from faults on the western side of the central valley, which are NW trending features sub-parallel to the San Andreas plate boundary. The State of California via bond measures recently sponsored the Delta Risk Management Strategy (DRMS) to quantify seismic risk and flood risk in the Delta using the best information currently available. Peak horizontal ground accelerations with a return period of 500 years approach 0.4g for soil conditions consistent with Pleistocene soils that underlie the peat (DRMS 2009). Based on approximate levee risk assessment procedures that preceded the present research and other recent

relevant work (Kwak et al. 2015), this shaking level would be expected to cause 10 to 70 failures of the existing levees in a single earthquake, which would flood multiple islands, draw in saline water from San Francisco Bay, and compromise water intakes at pumping stations. Such widespread system failure has been forecast to interrupt fresh water deliveries from the Delta for 20 to 30 months (DRMS 2009). Some in fact question whether such a sequence of breaches might permanently change the regional morphology such that either alternative water sources would need to be identified or major sectors of the California economy/population would need to be reconfigured or relocated.

1.2 MOTIVATION

A significant shortcoming of seismic levee risk assessments in the Delta is our poor understanding of the engineering properties of the peat soils that comprise the foundation materials for many levees. In this study, I seek to gain improved understanding of the behavior of peaty organic soils when subject to dynamic earthquake loading. I suspect that there are modes of potential failure for levees founded on such soils that are not considered in current levee hazard assessment studies, such as the aforementioned DRMS study (2009). The applicable research questions are: (1) Are there potentially significant failure mechanisms that are not considered in current procedures used to evaluate seismic risk to levees? (2) Can analysis tools be developed to predict seismic risk to levees from such mechanisms? (3) Can the reliability of those analysis tools be verified against applicable case history and model test data?

To provide context for understanding the value of the study, it must be recognized that current practice requires categorizing levee sites as being either potentially liquefiable or non-liquefiable, as done in the DRMS study. Liquefiable soils are known from extensive prior

research to potentially exhibit significant strength loss that can lead to levee instability during earthquakes, and control 90% of the levee hazards identified in the DRMS study. Non-liquefiable soils do not exhibit significant strength loss during undrained shearing and current analyses show that such materials will relatively rarely cause levee failures. Peats fall under the 'non-liquefiable' category and hence do not significantly contribute to current assessments of seismic risk in the Delta. Therein lies the problem – peats are highly unusual soils that may threaten levee functionality in unique ways that are not present for traditional non-liquefiable soils such as clays and plastic silts. I contend that a better understanding of peat is needed to advance our scientific understanding of how these materials may or may not threaten levee functionality in a seismic or post-seismic environment.

Peat is more pervasive than liquefiable sand in the Delta, but much less is known about its seismic behavior. Deformations of levees on non-liquefiable soils (including peat) were estimated in the DRMS study using Newmark sliding block analysis. The Newmark approach assumes sliding along a distinct failure surface of a rigid mass of soil, but its applicability to problems involving levees on highly deformable peaty organic soils is unknown. Typically, yield acceleration (an important input for the Newmark approach) is estimated using limit equilibrium analysis methods that assume soil behavior is rigid until the point of failure (i.e., rigid-plastic), and then forms a distinct failure surface along which shear strength is fully-mobilized. However, the peat soils in the Delta are among the softest in the world, and are therefore far from being rigid prior to failure. To clarify just how soft these materials are, shear wave velocities less than $30 m/s$ have been measured in the unconsolidated free-field peat on Sherman Island (GeoVision 2000). For comparison, soft young bay mud, which is widely recognized as a soft problematic soil in the region, typically exhibits $V_s > 100 m/s$. The extremely

soft peat materials would be very unlikely to exhibit distinct rupture surfaces, and therefore limit equilibrium analysis methods are clearly inappropriate. Using limit equilibrium methods, the DRMS study predicted < 10% of the levee failures would be associated with non-liquefiable soils, including peat.

We cannot look to observations from the Delta levees themselves to evaluate seismic risk of levees on peat because they have not been strongly shaken in their current configuration. Levees on peat soils have been shaken elsewhere, often with poor performance, but the lessons from these case studies are often difficult to discern. For example, a number of failures involving levees on soft peaty soils shaken by the 1993 Hokkaido earthquake in Japan also included lenses of liquefiable materials either in the levee itself or in the foundation, complicating the interpretation of the importance of the peats in the levee response.

Based on the above, it is clear that we do not adequately understand the mechanisms by which levees founded on soft peaty soils might fail due to earthquake shaking nor the relative risk levels such mechanisms might present relative to better-understood phenomena such as soil liquefaction. A possible failure mechanism for levees on peat soils that could cause a critical loss of freeboard and overtopping is shown in Fig. 1.3. The viability of this mechanism has been verified as part of the present research (preliminary results of which are provided in Shafiee et al. 2013, 2015) and developed here into a procedure suitable for practical application. The post-cyclic settlement mechanism cannot be captured by Newmark analysis, and better information is needed to develop reliable evaluation procedures for seismic deformations of levees on peat.

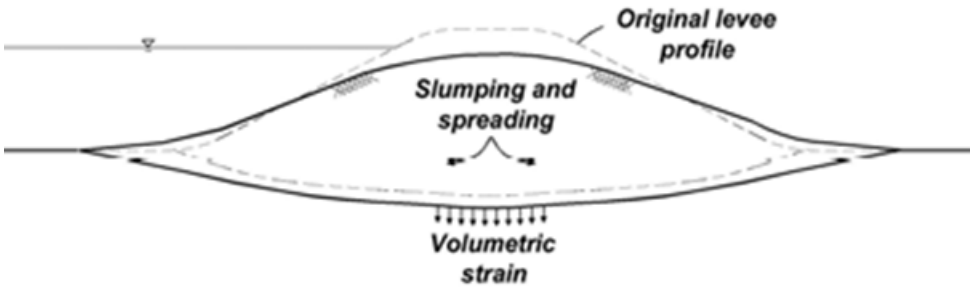

Figure 1.3 Mechanism of levee deformation by deviatoric slumping and spreading and volumetric strain

1.3 SCOPE OF RESEARCH

The objectives of this research are to improve fundamental understanding of cyclic and post-cyclic behavior of peat that could affect levee performance, and develop analysis tools to predict this behavior. More specifically, the objectives related to peat behavior characterization are to perform a series of monotonic and cyclic tests on consolidated specimens of peaty organic soil to evaluate factors affecting post-cyclic re-consolidation. I then seek to derive from those data simple relationships for evaluation of post-cyclic volume change that are amenable to application in engineering design practice, and could eventually be implemented in constitutive models for more advanced numerical simulation.

Laboratory testing is performed on 22 undisturbed Shelby tube samples gathered from Sherman Island at depths ranging from approximately 1 to 6 m. Peat gathered from this site was also used in for centrifuge testing project at UC Davis. The shear testing in this research is carried out by UCLA bi-directional broadband simple shear device, which is a digitally-controlled device with capabilities for chamber pressure control and multidirectional excitation

(Duku et al. 2007). The apparatus was improved as part of this research program to add the abilities for testing under constant-height and stress-controlled conditions.

1.4 ORGANIZATION OF DISSERTATION

This dissertation focuses on the cyclic and post-cyclic behavior of Sherman Island peat in the Sacramento-San Joaquin Delta. It consists of the following seven chapters and one Appendix including all the results of cyclic strain/stress shearing experiments with post-cyclic volume change measurements.

Chapter 1: Introduction

The historical background of the Sacramento-San Joaquin Delta is introduced. The importance of post-cyclic volume change of the peaty layer on the stability of the levees is described. The objectives are introduced, and the organization of the dissertation is presented.

Chapter 2: Adaptation of Bi-Directional Broadband Simple Shear Device for Constant Volume and stress-controlled testing

An existing digitally controlled simple shear device, originally designed for drained testing with strain-control is adopted to perform constant height testing under strain- or stress-controlled conditions. The performance of the device following upgrade to the constant volume and stress-controlled testing features is evaluated by tracking errors when, for example, loading amplitude or frequency are changed. To demonstrate the current capabilities of the device, dry pluviated specimens of Silica No. 2 sand are subjected to a range of tests including monotonic, cyclic strain- and stress-controlled tests, and bi-directional stress-controlled tests.

Chapter 3: Background on Monotonic, Cyclic and Post-Cyclic Behavior of Peat

Geotechnical literature on the static compressibility, monotonic shear behavior (i.e., frictional resistance and undrained shear strength), and dynamic shear behavior including modulus reduction and damping ratio curves of the peat is reviewed. It is also shown that post-cyclic volume change behavior of peat has not been studied.

Chapter 4: Tested Material and Site Characterization

The characteristics of the site used for drilling boreholes and retrieving undisturbed samples is introduced in terms of cone penetration testing and shear-wave velocity measurements. The details of manual drilling and Shelby tube sampling is described, and the values of index properties and in situ water contents of the peat at different depths are presented.

Chapter 5: Static Compressibility of Sherman Island Peat

The characteristics of a new consolidometer that permits pore water pressure measurements during consolidation is described. The results of oedometer tests with Load Increment Ratios (*LIR*=load increment/current vertical load on the soil) of 1 is presented, and the static compressibility properties of peat including compression and recompression indices, coefficient of permeability variation, coefficient of consolidation, and secondary compression index are presented. An approach is introduced to formulate the secondary compression strain rate as a function of distance to a reference secondary compression line (RSCL) in e-logσ_v' space with the aid of the tests with LIR<1.

Chapter 6: Monotonic, Cyclic and Post-Cyclic Shearing Behavior of Sherman Island Peat

Monotonic behavior of peat at different organic contents is investigated through constant volume direct simple shear (DSS) tests. Test results are presented, and an evaluation of the normalized shear strength of Sherman Island peat is introduced. The results of strain-controlled constant volume cyclic DSS tests with post-cyclic volume change measurements are presented. The cyclic behavior of peat is described by stress-strain loops, stress paths, and strain-dependent excess pore water pressure. It is shown how cyclic straining could reset the secondary compression clock by increasing the time rate of secondary compression, a phenomenon that increases in significance with increasing shear strain amplitude. The amount of reset is then quantified by introducing a dimensionless parameter called the reset index, which quantifies the extent to which cyclic loading resets secondary compression. The framework introduced in chapter 5 is extended to describe the relationship between reset index and various parameters, including the amplitude of applied cyclic shear strains. The effects of static shear stress and number of loading cycles on the reset of secondary compression clock is also investigated.

Cyclic pore pressure generation and post-cyclic shear strength of the peat is also investigated through cyclic strain-controlled tests followed by monotonic test under constant volume conditions. Finally, mathematical models are introduced to describe reset index and residual pore water pressure in terms of influencing parameters including shear strain amplitude, number of loading cycles, static shear stress, overconsolidation ratio and organic content. A simplified procedure is developed to estimate post-earthquake settlement in Sherman Island peat. The procedure is explained with a simple example of a 4m levee atop 11m of peat utilizing the mathematical models for reset index and pore water pressure, computer program DeepSoil, and non-linear consolidation code.

Chapter 7: Summary, Conclusions and Future Work

Conclusions from the study are summarized and several recommendations for future work are presented.

2 Adaptation of Bi-Directional Broadband Simple Shear Device for Constant Volume Testing

2.1 INTRODUCTION

Simple shear test apparatuses are often preferred for cyclic testing of soils because the deformations imposed on test specimens mimic the effects of vertical one-dimensional shear wave propagation under in situ conditions. The University of California Los Angeles (UCLA) Bi-Directional Broadband Simple Shear (BB-SS) device is a digitally-controlled NGI-type simple shear device with capabilities for broadband multidirectional excitation. A device schematic is shown in Fig. 2.1. Duku et al. (2007) describe the device and its unique attributes relative to other research-level devices in the literature. Those unique attributes include the following: (1) it operates with servo-hydraulic actuators that can reproduce broadband (earthquake-like) excitation with relatively precise control as a result of device-specific true digital control algorithms; (2) it can shear soil specimens simultaneously in two horizontal directions with minimal cross coupling between the horizontal motions to more realistically simulate field stress paths; and (3) it has a stiff tri-post frame and high performance track bearing (Fig. 2.1) that minimizes (but does not eliminate) system compliance associated with top cap rocking.

The bottom cap is free to displace horizontally in two perpendicular directions but cannot displace vertically. Horizontal shear loading is applied at the specimen base through two independently controlled tables, each mounted on linear track bearings. The top cap is fixed against horizontal movement but can displace vertically while maintaining a constant vertical load. Vertical loads are applied by the actuator visible in Fig. 2.1 atop the frame; the loads are applied to the top cap.

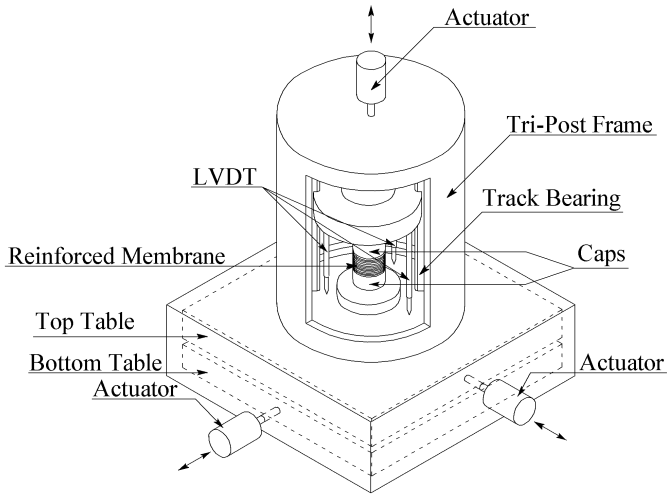

Figure 2.1. UCLA bi-directional broadband simple shear apparatus

The UCLA BB-SS device was designed to test cylindrical soil specimens with a diameter of 10.2 cm or less. The specimen is located between relatively rigid bottom and top caps and is typically confined by a wire reinforced membrane (Fig. 2.1). Once the specimen is secured between the two caps, three LVDTs equally spaced around the specimen are mounted on the top adaptor plate and fixed to the plate by set screws (Fig. 2.1). The specimen is then consolidated by a vertical stress and is ready for shearing. At the 10.2 cm diameter and a typical height of 2.5 cm, the specimen aspect ratio is approximately 4:1, which Shen et al. (1978) have shown to produce

nearly true simple shear conditions over most of the specimen cross-section despite the lack of complimentary shear stresses on vertical faces (i.e., at the membrane-soil interface). The UCLA BB-SS device was originally developed for relatively large-strain applications including seismic compression and shear strength (e.g., Duku et al., 2008; Yee et al., 2013), with testing conducted under strain-controlled conditions. The original operational strain range was approximately cyclic shear strains (γ_c) of 0.1% and larger. Yee et al. (2011) extended its low strain capabilities by characterizing noisy signals and utilizing several statistical methods to extract meaningful responses for shear strains as low as approximately 0.03%.

In this chapter, I describe modifications of the UCLA BB-SS device to maintain constant height during shear and to enable shearing under stress-controlled conditions. The original constant vertical load configuration, which allows the top cap to displace vertically, is capable of simulating drained or partially drained conditions. This capability is maintained, while adding the option for constant-height control, which mimics constant volume (undrained) test conditions. Likewise, the original strain-controlled capabilities are maintained while adding the option for stress-controlled testing, which is important for many applications in soil liquefaction and cyclic softening (e.g., Idriss and Boulanger, 2008).

2.2 DEVICE MODIFICATIONS

2.2.1 Constant Volume Testing

True undrained shear testing is commonly conducted in triaxial devices by applying specified external loads on saturated specimens while measuring pore pressures using transducers hydraulically connected to the specimen pore fluid via a porous stone in the specimen end cap. A critical detail in this testing is ensuring saturation through back-pressure saturation (Lowe and

Johnson, 1960), so that contractive or dilatant soil behavior is reflected through pore pressure change and not volume change.

This testing approach is typically not practical for simple shear because most devices are not configured to apply external cell pressures needed for back-pressure saturation. For this reason, alternative approaches have been developed in which unsaturated specimens are used and the device is configured to maintain constant specimen volume by varying external vertical loads during shear. The underlying assumption is that the change in vertical stress as the specimen volume is maintained constant during shear is equal to the excess pore pressure that would have been measured in a truly undrained test (Bjerrum and Landva, 1966). This principal has previously been implemented in a Roscoe-type apparatus with constant total vertical stress by maintaining the boundary conditions of constant height and zero lateral strain (Vaid and Finn, 1979).

For NGI-type devices, application of the same principles is referred to as "constant height" testing because lateral boundary conditions are not controlled as part of the test aside from the use of wire-reinforced membranes. Such testing has been performed to investigate cyclic undrained behavior of sands with regard to liquefaction and cyclic degradation (e.g., Ishihara and Yamazaki 1980, Tatsuoka and Silver 1981) and undrained shear strength of clays (e.g., Hanzawa et al. 2007, Bro et al. 2013).

The veracity of the constant volume (or constant height) approach is well established from an experimental basis. This was demonstrated by Dyvik et al. (1987) by performing both true undrained simple shear testing, with constant load and pore pressure measurements, and by constant volume simple shear testing on similar specimens of normally consolidated clay. The stress–strain and stress path plots obtained by the two test types were nearly identical, thus

indicating that the changes in vertical stress required to maintain constant volume are equivalent to the measured pore pressures in an undrained test.

Some prior simple shear devices configured for constant volume testing have maintained height control mechanically, typically by clamping top and bottom caps against vertical displacement (e.g., Finn and Vaid 1977, Ishihara and Yamazaki 1980, Wijewickreme 2010). Others have used a control algorithm to adjust the vertical force using a servo-pneumatic actuator (e.g., Degroot et al. 1991) or electro-mechanical step motor (e.g., Porcino et al. 2006). We adopt the second approach but with a servo-hydraulic vertical actuator. This was accomplished by equipping the vertical axis with a servo electric valve, an actuator, and a load cell. A closed-loop control system (Fig. 2.2) was designed so that the feedback from vertical LVDTs are read and if the displacement during shear is not zero, the vertical load is adjusted to return the vertical displacement to zero. The advantage of servo-hydraulic control systems is that they are more responsive than pneumatic systems when loading involves high-frequencies of up to 20 *Hz*. Prior control-based systems are reliable only for frequencies less than 1 *Hz* (e.g., Porcio et al. 2006).

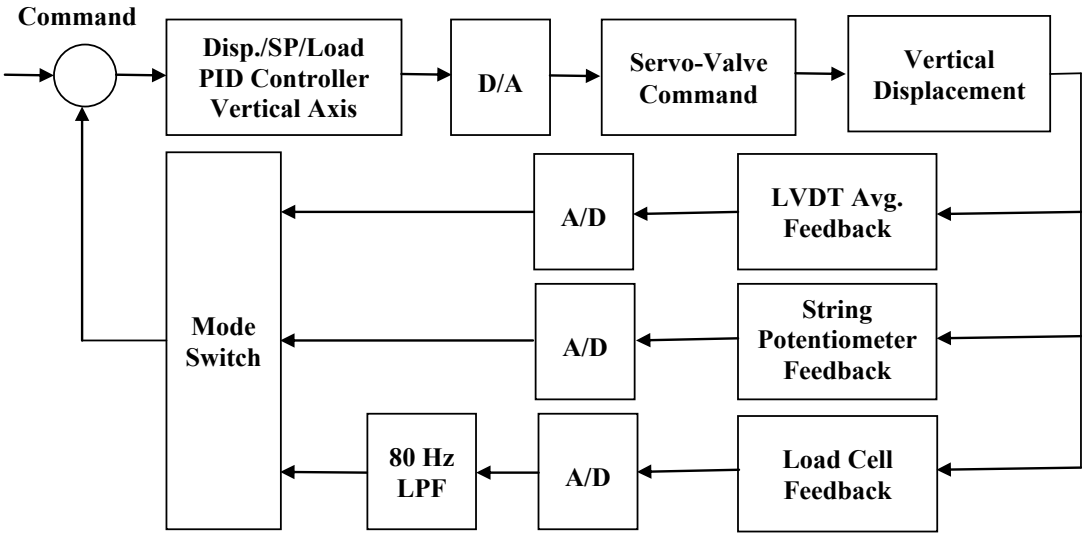

Figure 2.2. Schematic configuration of the elements of the UCLA BB-SS constant height control system

The device control system was upgraded by replacing two dSPACE DS1104 control boards with an OPAL-RT OP5600-based control system. The new system provides 16 16-bit analog-to-digital (A/D) channels and 16 16-bit digital-to-analog (D/A) channels in a single chassis, as opposed to 8 16-bit and 8 12-bit A/D channels along with 16 16-bit D/A channels split over two unsynchronized boards in the older configuration. The new OP5600-based system is able to read three load-cells in each of the three axes and five LVDTs (two on horizontal axes and three on the vertical axis), in addition to a string-potentiometer (SP) to enable coarse displacement-based control of the vertical axis during test set up (Fig. 2.2). These sensors utilize nine A/D channels leaving seven A/D channels free for additional sensors (such as pore-pressure sensors) that may be added at a later date. Three D/A channels are utilized to drive the servo-valves associated with the hydraulic actuators for the three axes, leaving 13 D/A channels for additional actuation functions. All channels are synchronized using the clock of a field-programmable gate array (FPGA).

The computational power of the system has also been enhanced with a 2.4 *GHz* 4-core CPU replacing the 250 *MHz* PowerPC 603e processors on the DS1104 boards. The OP5600 also has 2 *GB* of RAM instead of a total of 40 *MB* of on-board memory in the DS1104, allowing longer-data records or more channels to be captured at high sampling rates.

Displacement control of the vertical axis has been added as part of the device upgrade. Feedback control of the vertical axis allows consolidation to be performed using user-specified strain rates (within given tolerable error thresholds).

The hydraulic power supply for the device has been changed to an MTS Model 506.02 pump. This hydraulic pump provides a continuous operation pressure of 207 *bars* (20,700 *kPa*) and a flow rate of 22.8 *l/m*.

For the horizontal axes, a multiple-input multiple-output (MIMO) control algorithm (Duku et al. 2007) was replaced with decoupled PID (Proportional-Integral-Derivative) control of each axis. The MIMO controller had been implemented to improve multi-axial tracking control by compensating for motion induced in one axis due to the motion in the other. For the present application, we returned to simpler PID-based control of the horizontal axes because the changes in the control system for the vertical axis significantly complicate application of the MIMO control algorithm in the horizontal direction to the point that it was deemed impractical.

2.2.2 Stress-Controlled Testing

The capability for stress-controlled testing has been added to the UCLA BB-SS device for both horizontal axes. Stress-controlled testing is based on load cell feedback. The load cell is located at the interface between the actuator and the table and measures both soil resistance and

frictional resistance in bearings. As reported by Duku et al. (2007), frictional resistance is small (approximately 2.2 N) due to the use of high-quality linear track bearings. The small mean resistance from these bearings is subtracted from the measured loads within the control system, but small departures in sliding resistance from the mean (i.e., as the horizontal velocity and vertical bearing stress on the bearings change with time) can cause time-variable actuator loads that effectively manifests as noise on top of the relatively smoothly varying soil resistance.

Load control is provided with a PID controller operating at a sampling rate of 1 *kHz* (this rate was selected through carefully tuning of the controller for a range of vertical loads). The system operates on the change in force during shear (by subtracting the initial load from the signal) to ensure symmetric loading and minimize drift.

When the device is operated in load-control, the displacement associated with a given load command may exceed limits and damage LVDTs. To avoid exceeding displacement limits, a safety mechanism was implemented in which the system reverts to displacement control when limiting displacements are exceeded.

With these modifications, the device is now capable of operating under either strain- or stress-control in all three axes. The block diagram for stress-controlled feature on the horizontal axes is similar to the one for the vertical axis (Fig. 2.2) except that there is no string pot and there is only one LVDT per horizontal axis (hence no averaging of multiple signals is provided).

2.3 SYSTEM PERFORMANCE

Duku et al. (2007) evaluated BB-SS device performance operating under the previous MIMO control system. Performance was quantified by the misfit between command and feedback

horizontal signals for a variety of conditions, including sinusoidal and broadband loading applied along one or both of the horizontal axes. Some of the key results of that performance testing were: (1) there is a baseline level of noise in horizontal feedback signals that is controlled by the A/D converter. The noise had a nearly flat Fourier amplitude spectrum suggesting white noise characteristics; in the time domain the noise has zero mean and a standard deviation of approximately 0.0003 *mm*; (2) errors in command signal tracking were generally quite low, but increased as the amplitude of the command signal decreased and the frequency increased; (3) errors in command signal tracking for a reference (baseline) horizontal direction increase by approximately a factor of four when shaking is applied in the perpendicular horizontal direction.

Stewart et al. (2013) re-evaluated these horizontal displacement control attributes for conditions of constant vertical actuator force, which matches the conditions considered by Duku et al. (2007). The newly configured control system has similar features as the earlier system. In the following subsections, we evaluate control attributes for the case of constant specimen height (including vertical axis displacement and rocking) and stress-controlled testing. These are new features for which device performance has not previously been documented.

2.3.1 Vertical Axis Performance

The BB-SS device has been provided with functionality to maintain constant height conditions while varying the vertical stress through the control algorithm. Fig. 2.3 presents the results of a strain-controlled test on Silica No. 2 dry sand at 52% relative density (D_r) under constant height conditions. Silica No. 2 is a uniform sand with D_{50}=1.60 *mm* and maximum and minimum dry densities of 1.610 and 1.349 gr/cm^3, respectively. The strain history is seen to be maintained at a consistent amplitude, but the shear and normal stresses decrease with the number of cycles. The

decrease of normal stress with number of cycles is interpreted as an equivalent pore pressure change, as described in Section 2.2.1. Fig. 2.3(d) shows the variation with time of vertical strain, which reaches values as high as 0.027% but should ideally be zero if the control algorithm were working perfectly. In this subsection, we formally quantify the error in vertical top cap displacement from the feedback system (Z_i^f) relative to the command level of $Z_i^c = 0$ for i=1:N (where N is the number of time steps).

We quantify error using a normalized root mean square differential between feedback and command (applied previously for horizontal control by Duku et al. 2007 and Stewart et al. 2013). While it is customary to normalize error by the sum of the square of the command signal, this is undefined for the vertical axis. Instead, we normalize by the product of number of data points N and initial height h_0, which makes the error term akin to a standard deviation of vertical strain. The normalized root mean square error on the vertical axis (ε_{VRMS}) is defined as:

$$\varepsilon_{VRMS} = \frac{1}{h_0}\sqrt{\frac{\sum_{i=1}^{N}(Z_i^f - Z_i^c)^2}{N}} \tag{2.1}$$

An ASTM standard (ASTM D6528-00) allows a maximum vertical strain error of $\varepsilon_{VRMS} \leq 0.05\%$ for constant volume direct simple shear testing.

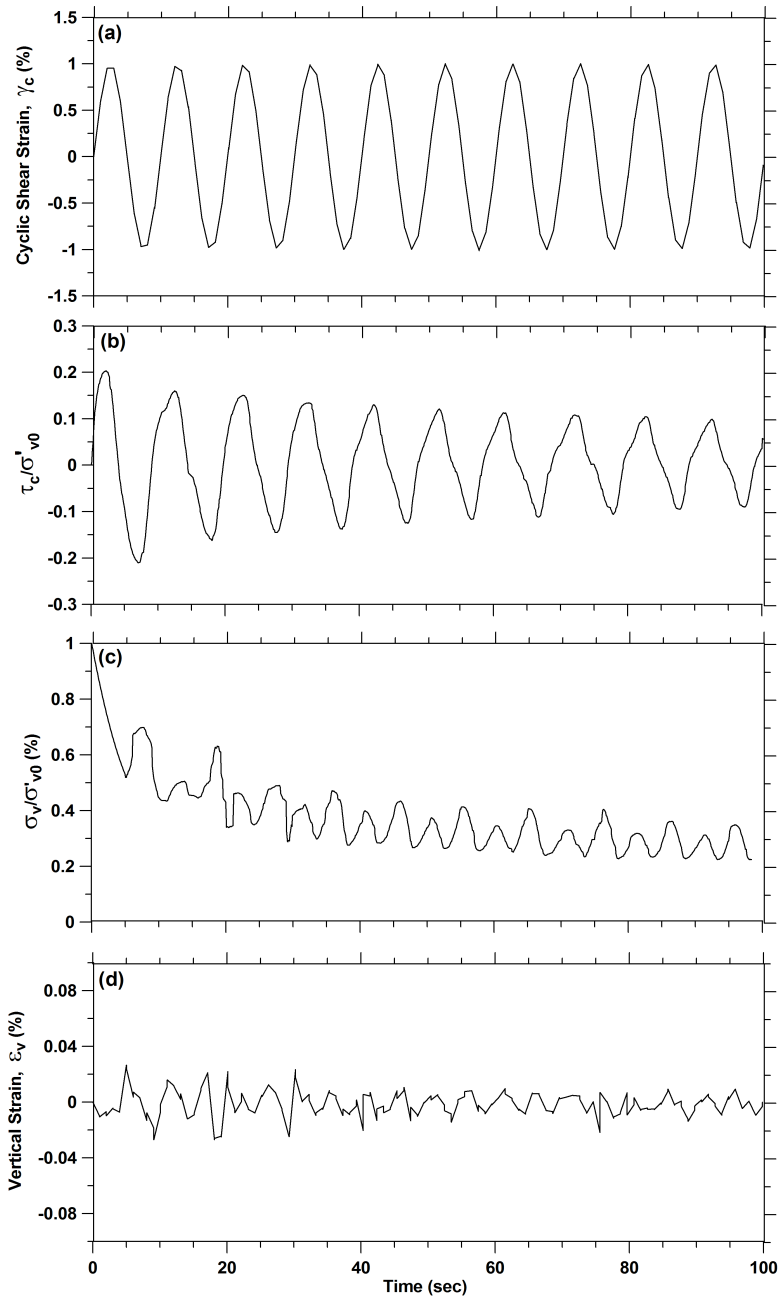

Figure 2.3. Constant height strain-controlled test on Silica No. 2 dry sand under an initial vertical stress σ_{v0}=100 *kPa*, loading frequency of 0.1 *Hz*.

Fig. 2.4 illustrates device performance when operated to maintain constant height in terms of ε_{VRMS} plotted against horizontal displacement amplitude. Results are shown for 15 displacement-

controlled cycles at 1.0 *Hz* in a single horizontal direction (uni-directional) and simultaneously in two horizontal directions (bi-directional). Ten tests were conducted for each displacement amplitude. We find ε_{VRMS} to be normally distributed and hence plot the mean and arithmetic standard deviation in Fig. 2.4. We find the mean of ε_{VRMS} to increase with horizontal displacement amplitude and to be higher when two axes are excited simultaneously. Even at the largest uni-directional displacement amplitude considered of 2.54 *mm* (corresponding to 10% shear strain), the vertical strain error is less than 0.03% which is much less than errors for horizontal axes (Stewart et al. 2013). Bi-directional errors for a given displacement amplitude are approximately 3 × those for uni-directional demands. If the ASTM threshold error of $\varepsilon_{VRMS} \leq$ 0.05% is selected, the limiting displacement amplitudes are 2.5 *mm* (10% shear strain) for uni-directional shearing and 0.76 *mm* (3% shear strain) for bi-directional shearing.

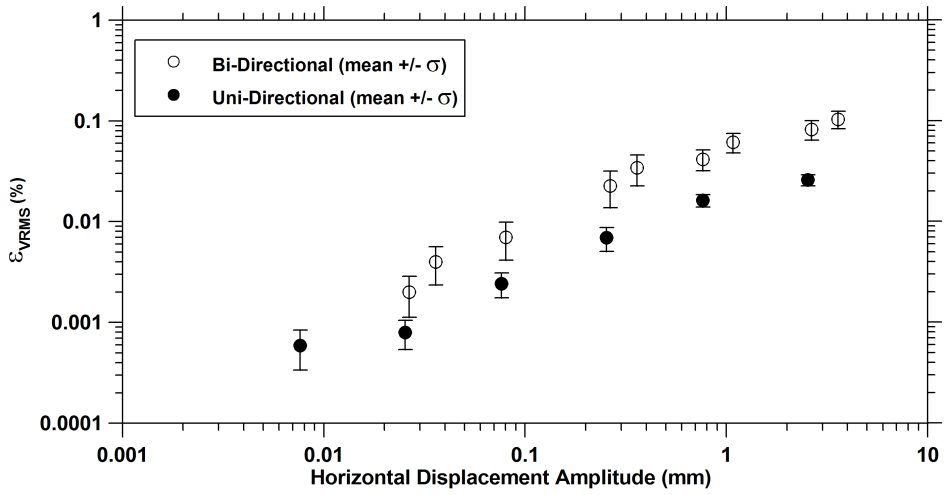

Figure 2.4. Performance of vertical axis in maintaining constant height condition, based on mean ± standard deviation (σ) of ε_{VRMS} from ten tests at each displacement amplitude. Tests performed on Silica No. 2. sand at a frequency of 1.0 *Hz* on 25 *mm* tall specimens.

The use of a single LVDT on the top cap is potentially problematic if there is top cap rotation, which is difficult to eliminate. In the presence of such rotation, the LVDT is likely to capture the sum of the average vertical displacement and the vertical displacement from top cap rotation at the LVDT location. Accordingly, our analysis of ε_{VRMS} (Eq. 2.1) from an individual test is based on the average vertical displacement, computed using three equally spaced vertical LVDTs. This averaging effectively removes rotation effects, thus providing a better basis for control than a point measurement from a single LVDT.

Prior investigations of vertical control error have been undertaken by Degroot et al. (1991) and Porcino et al. (2006). Degroot et al. (1991) tested a normally consolidated clay under monotonic loading and enforced constant height conditions using a control system interfacing with a servo-pneumatic actuator. Using a single LVDT on the top cap, they observed a maximum vertical strain of 0.003%. Porcino et al. (2006) similarly sheared dry sands monotonically,

enforcing constant height conditions using a control algorithm with an electro-mechanical actuator. They reported a maximum vertical strain of 0.015%, again from a single LVDT.

While we cannot know the extent to which rocking affected the vertical control achieved in earlier constant-height devices by Degroot et al. (1991) and Porcino et al. (2006), it is nonetheless encouraging that the levels of control achieved in our tests compare favorably, especially given the relatively rapid loading rates and cyclic conditions imposed in the present test program.

2.3.2 Top-Cap Rocking

A common problem in simple shear testing is rocking of one end cap relative to another during shear, which leads to undesirable stress concentrations around the specimen perimeter. A review of the literature reveals that the amount of rocking in terms of rotation/vertical deformation has not been well documented in past studies of simple shear device performance. Rutherford (2012) recently measured torques resulted from rocking in a direct simple shear device by using a multi-axis load cell. Hence, that study adopted a 'force-based' representation of the rocking effects, which does not measure actual rocking. We directly measure rocking of the specimen top cap using measurements from three vertical LVDTs.

As described by Duku et al. (2007), the BB-SS device was designed with a tri-post frame and high performance track bearing to accommodate vertical displacement of the top cap and minimize cap rocking (Fig. 2.1). The recent device upgrades include a relatively stiff connector between the top cap and actuator to further restrain rocking.

Fig. 2.5(a) shows the top cap rocking for a cyclic strain-controlled, constant volume test on a dry sand under an initial vertical pressure (σ_{v0}) of 100 *kPa*. The cyclic loading was applied with a shear strain amplitude (γ_c) of 4% and a frequency of 1 *Hz*. Assuming excitation in the *x* direction, angular distortion θ_{yy} indicates rotation within the vertical plane parallel to the *x*-axis, whereas θ_{xx} indicates rotation in the vertical plane perpendicular to the direction of excitation. These rotations are defined from the three LVDTs mounted on the specimen top cap. Fig. 2.5(a) shows the expected result that $\theta_{yy} > \theta_{xx}$ for excitation in the *x*-direction. Note that the amount of rocking decreases with the amplitude of the shear and vertical loads. Vertical deformations from top cap rocking can be expressed in a normalized form as follows:

$$\varepsilon_{\theta RMS} = \frac{1}{h_0}\sqrt{\frac{\sum_{i=1}^{N}\left(R\theta_{yy,i}\right)^2}{N}} \tag{2.2}$$

where *R* is the specimen radius, *N* is the number of time steps, and h_0 is the initial specimen height. This metric of performance has the physical meaning of average vertical strain at the specimen perimeter from rocking. A similar error term can be defined using θ_{xx}.

Fig. 2.5(b) shows device performance with regard to top cap rocking in terms of $\varepsilon_{\theta RMS}$ plotted against *x*-direction horizontal displacement amplitude for excitation frequencies of 1.0 and 0.1 *Hz*. Excitation is uni-directional. We find $\varepsilon_{\theta RMS}$ to increase with horizontal displacement amplitude and to be essentially frequency-independent. Even at the largest displacement considered of 1 *mm* (corresponding approximately to 5% shear strain), the vertical strain error is less than 0.02%. The value of $\varepsilon_{\theta RMS}$ is approximately half of ε_{VRMS} (Fig. 2.4).

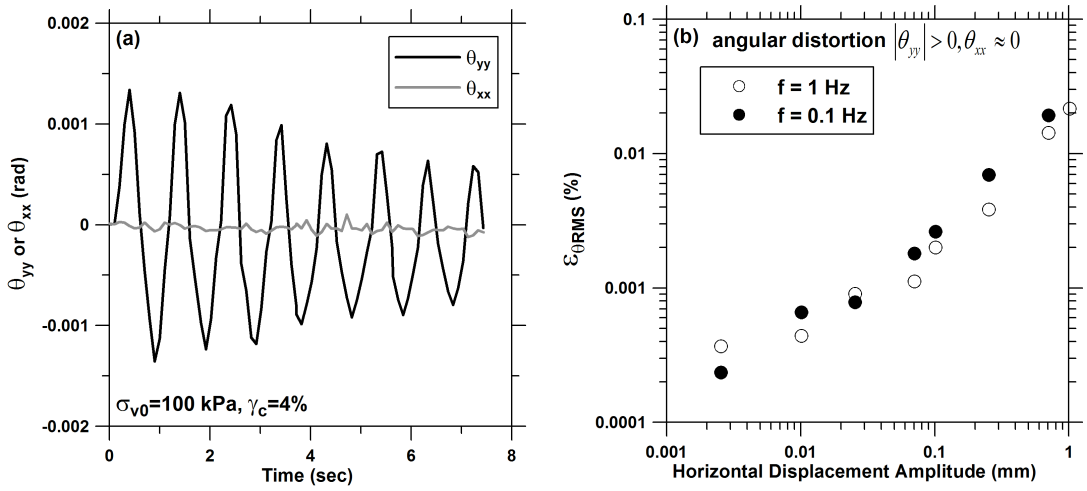

Figure 2.5. Performance of the UCLA BB-SS device in restraining rocking (a) angular distortions in a cyclic strain-controlled test (b) error term related to the vertical deformation caused by rocking

2.3.3 Precision of Stress-Control

(a) Tracking errors

Fig. 2.6 shows command and feedback horizontal force histories for a 1.0 *Hz* command signal having relatively low amplitude (Fig.2.6a) and at a high amplitude typical of what might be used for a liquefaction analysis (force amplitude of 111 N, which produces a CSR of 0.27 for a typical sample diameter of 72.6 *mm* under a vertical pressure of 100 *kPa*). The feedback signal has been adjusted for a phase shift of 0.03 *sec*, which is consistently observed regardless of loading amplitude and frequency. The load cell feedback signals were recorded using a sampling frequency of 1000 *Hz*. The mismatch seen between the command and feedback signals when the shear force is low (Fig.2.6a) is partly because of small departures in slide resistance from the

mean as explained in Section 2.2.2, and partly because of noise introduced to the control system by the A/D converter. The command and feedback signals are better matched when the amplitude of the shear force is increased to 111 N (Fig. 2.6b).

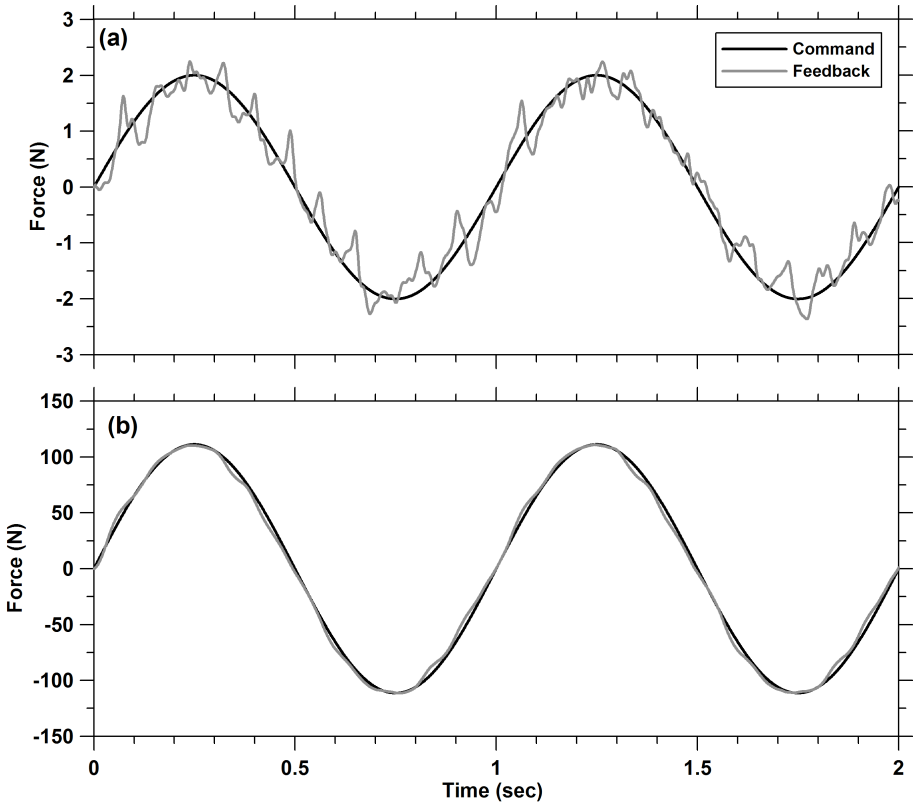

Figure 2.6. Sinusoid tracking of command signals (a) low amplitude force signal (b) large amplitude force signal

We evaluate performance of the UCLA BB-SS device when operated in stress-control mode by computing the normalized force root mean square error (ε_{FRMS}) as:

$$\varepsilon_{FRMS} = \sqrt{\frac{\sum_{i=1}^{N}(F_i^f - F_i^c)^2}{\sum_{i=1}^{N}(F_i^c)^2}} \tag{2.3}$$

where the summation occurs over N time steps and F^f and F^c represent the feedback and command force signals, respectively. We evaluated the variation of ε_{FRMS} with the strength of the command signal using stress-controlled tests performed at an initial vertical stress of $\sigma_{v0} = 100kPa$. We normalize the shear stress amplitude (τ_{hv}) by the initial vertical stress (σ_{v0}) to compute cyclic stress ratio $CSR = \tau_{hv} / \sigma_{v0}$. Note that CSR remains constant during testing.

Fig. 2.7(a) presents the variation of ε_{FRMS} with *CSR* for command frequencies of 0.1-25 *Hz* in uni-directional tests performed under conditions of constant vertical load (hence, volume change is allowed and the specimen response is drained). Error term ε_{FRMS} decreases with increasing *CSR* in a manner that mimics previously documented trends of normalized root-mean-square error from strain controlled testing when plotted against strain amplitude. Fig. 2.7(a) also shows that errors increase markedly with frequency. This increase results from the increased significance of small phasing errors that are not compensated for by the phase shift of 0.03 *sec* from feedback lag.

The effects of interaction between system responses in two horizontal directions were investigated by maintaining a consistent command signal along an arbitrarily chosen baseline axis (CSR=0.02 and 0.10; 1 *Hz* frequency) while commanding the perpendicular horizontal axis with signals of identical amplitude but variable frequency (0 to 25 *Hz*). Fig. 2.7(b) shows the resulting error terms per Eqn. (2.3) for the baseline axis feedback signals. The corresponding error terms for uniaxial loading are shown in Fig. 2.7(b) at zero frequency. Error on the baseline axis is increased by excitation on the perpendicular axis.

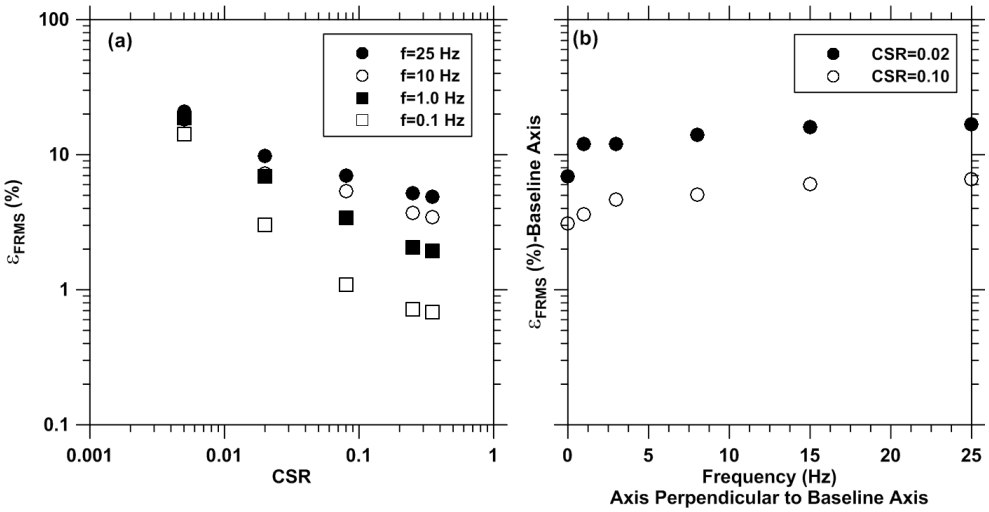

Figure 2.7. Performance of the stress-controlled feature of UCLA BB-SS device (a) effect of stress amplitude and frequency on tracking errors (b) tracking errors on baseline axis for varying frequencies of excitation on perpendicular axis (for reference, the result for uniaxial loading is shown at zero frequency).

(b) Relative tracking errors for strain-controlled vs stress-controlled testing

To compare the relative levels of error for the two test types (stress-control and strain-control), we consider a pair of tests under a constant vertical pressure (σ_{v0}) of 100 *kPa*. Fig. 2.8(c) shows the shear strain (γ) history of a constant vertical pressure stress-controlled test at *CSR* = 0.25 (Fig. 2.8a), in which the average strain amplitude (γ_c) following the first few cycles of hardening is about 0.4%. The value of ε_{FRMS} for this test is 2% from Fig. 2.7(a). On the other hand, for a constant vertical pressure strain-controlled test at $\gamma_c = 0.4\%$ (Fig. 2.8d) on a 25.4 *mm* tall specimen, the CSR after initial hardening is approximately 0.22 (Fig 2.8b). The value of ε_{RMS} (defined similarly to Eq 2.3 but based on strain misfit) is 5% in this case (Fig. 2.8b from Stewart et al 2013). Hence, it appears that ε_{FRMS} and ε_{RMS} are of comparable magnitude for these large-deformation conditions.

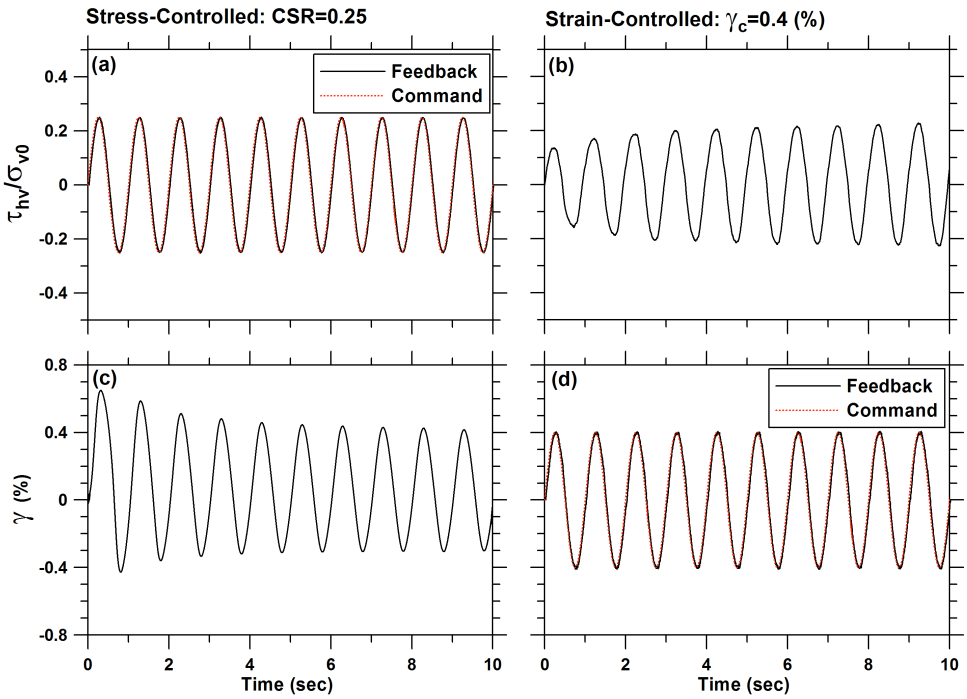

Figure 2.8. Comparison of tracking error in stress- and strain-controlled tests (a) feedback and command signals for a stress-controlled test with CSR=0.25 (b) normalized shear stress history for a strain- controlled test with $\gamma_c = 0.4\%$ (c) shear strain history of a stress- controlled test with CSR=0.25 (d) feedback and command signal for a strain-controlled test with $\gamma_c = 0.4\%$

(c) Control as demands approach material capacity

We next examine the capabilities of the control system to track the command when the horizontal shear stress becomes very close to the shear strength of the soil. Conditions approaching shear failure were produced in cyclic stress-controlled tests carried out under constant volume and constant vertical pressure conditions (to mimic undrained and drained loading conditions). The tested material is Silica No. 2 sand with $D_r = 40\%$, which was tested at CSR=0.15, $\sigma_{v0} = 100kPa$, and a range of loading frequencies.

Figs. 2.9 and 2.10 present test results for a relatively rapid loading frequency *f*=1 *Hz*. The tracking errors in these figures are time-dependent, being computed as:

$$\varepsilon_F(t) = \left| \frac{F_i^f - F_i^c}{F_i^c} \right| \tag{2.4}$$

where $t = i\Delta t$ (Δt is the time step). Because the error in Eq. (2.4) is computed at a single time step, the results are noisy. For this reason, we smooth the error using a weighted average within a Tukey window having a width of 21 data points (Ancheta and Stewart 2015). Figure 2.9a shows that the feedback signal tracks the command signal well until time t=6.5 *sec,* after which the feedback signal drops and cannot follow the command signal. Fig. 2.9b shows that the smoothed tracking error increases dramatically, becoming as large as 65%.

As shown in Fig. 2.10b, the large errors occur when pore pressure generation causes the stress path to approach the steady state line (SSL), achieving a condition known as *initial liquefaction* (Seed, 1979). Once this condition is reached, the shear strength falls below the command amplitude over the range of strains produced in the test and the stress path oscillates near the origin. In principle, the stress amplitude should be retained following initial liquefaction due to in-cycle dilation. However, the dilation effect is suppressed by the inability of the control system to accurately track the command signal during the rapid in-cycle changes in soil stiffness.

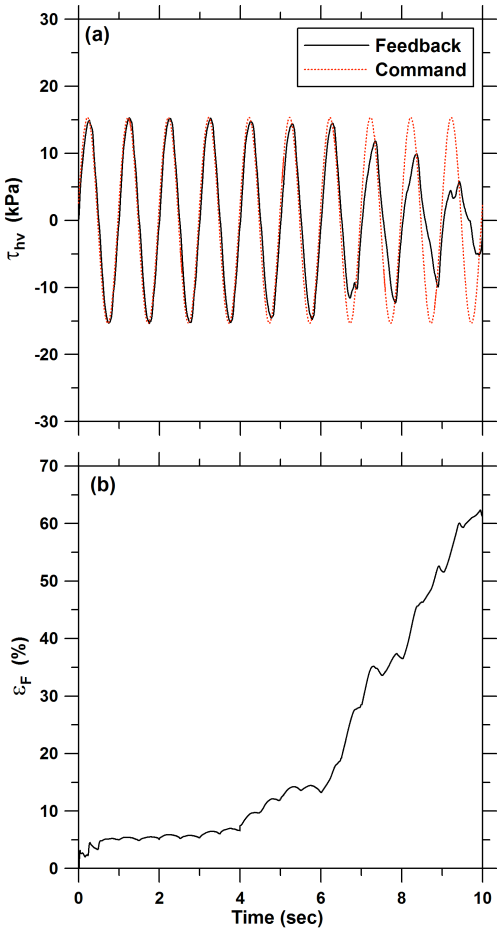

Figure 2.9. Constant volume stress-controlled test on Silica No. 2 at $D_r = 40\%$, $\sigma_{v0} = 100kPa$ and f=1 *Hz* (a) feedback and command signals for CSR=0.15 (b) smoothed tracking error

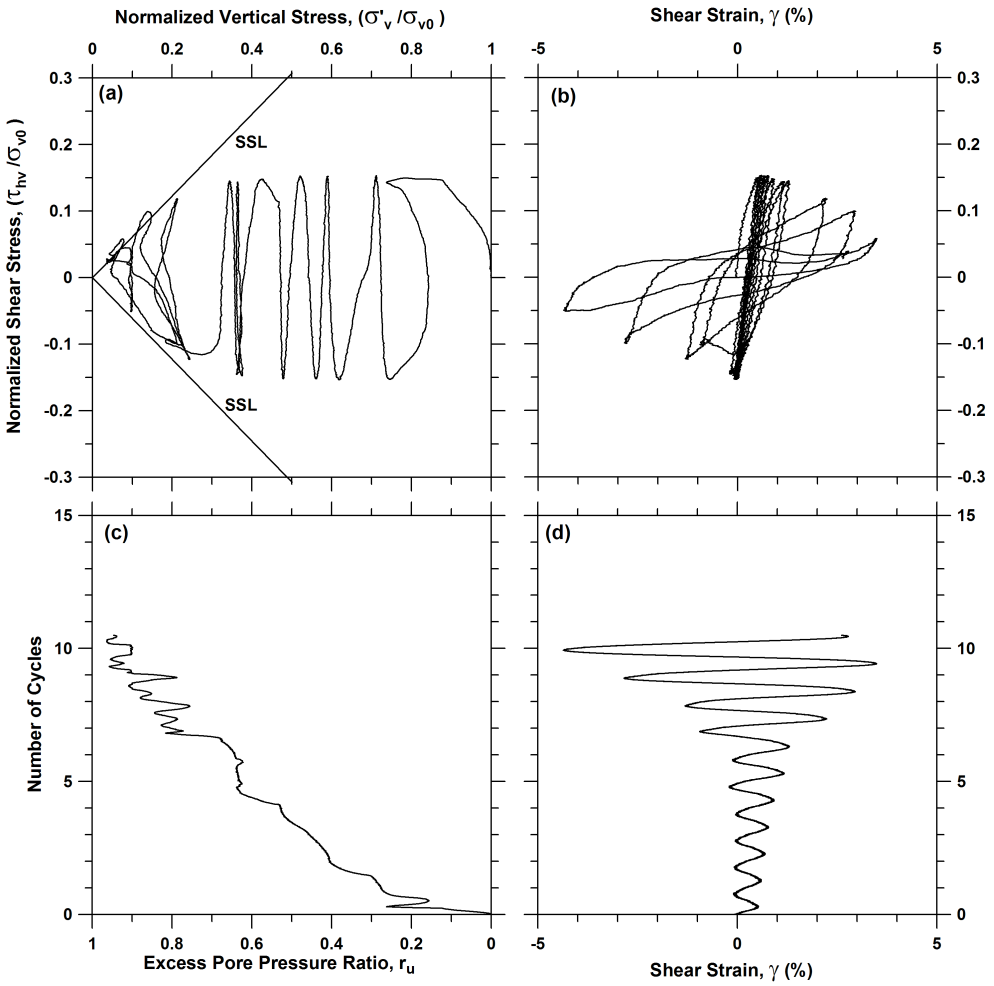

Figure 2.10. Constant volume stress-controlled test on Silica No. 2 at $D_r = 40\%$, $\sigma_{v0} = 100kPa$ and f=1 *Hz* (a) stress path (b) stress-strain loops (c) excess pore water pressure build-up (d) shear strain history

Fig. 2.11 shows the same test sequence as in Fig. 2.10 but now at a slower loading frequency of *f*=0.1 *Hz*. With this reduced loading rate, the in-cycle stiffness changes are slower, and the control system is able to capture in-cycle dilative behavior of the soil up to the command stress amplitude. Similar observations of undrained behavior of sand specimens sheared at 0.1 *Hz* were made by Kammerer et al. (2002) and Wu (2002) using a direct simple shear device and Boulanger and Truman (1996) using a cyclic triaxial device.

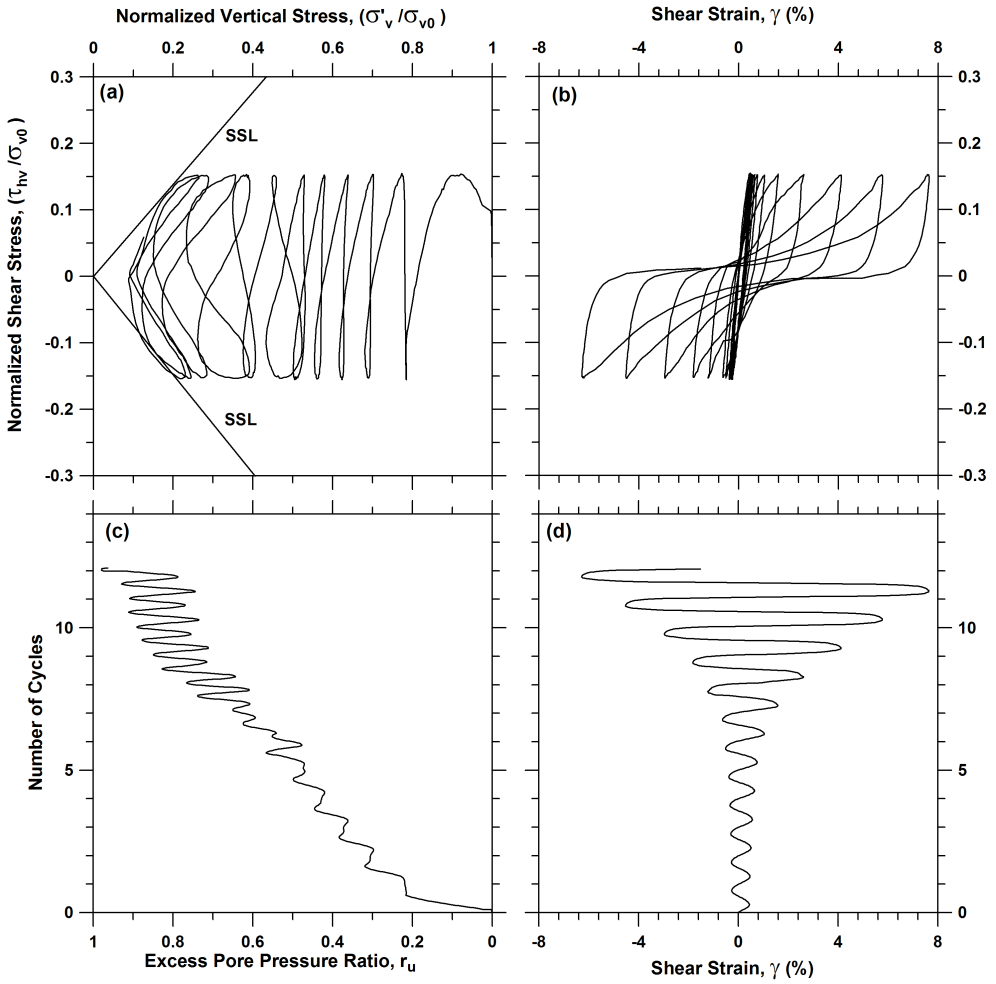

Figure 2.11. Constant volume stress-controlled test on Silica No. 2 at $D_r = 40\%$, $\sigma_{v0} = 100kPa$ and f=0.1 *Hz* (a) stress path (b) stress-strain loops (c) excess pore water pressure build-up (d) shear strain history

The results in Figs. 2.10 and 2.11 show that the control system can keep pace with in-cycle contraction/dilation for *f*=0.1 *Hz* but not for *f*=1.0 *Hz*. We investigate the variation of normalized force root mean square error with frequency by repeating constant-height tests on similar specimens for a range of frequencies between 0.1 and 1.0 *Hz*. Fig. 2.12 presents tracking errors computed for individual loading cycles (up to *N*=10) for six loading frequencies. Tracking errors consistently increase after the 4th cycle, after which initial liquefaction occurs. For frequencies ≤

0.5 *Hz*, errors do not continue to increase with *N* beyond the 6th cycle and ε_{FRMS} values are modest (e.g., 6% at *f*=0.5 *Hz*). On the other hand, for loading frequencies > 0.5 *Hz*, the control system experiences progressively increasing losses of control with each successive cycle beyond *N*=5.

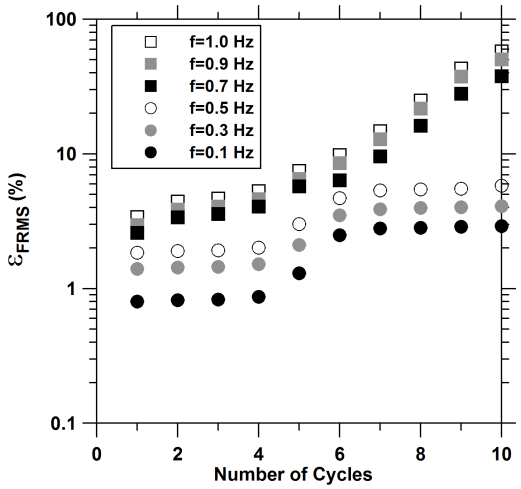

Figure 2.12. Performance of the UCLA BB-SS device control system for stress-controlled constant volume testing on sand with varying frequencies

Fig. 2.13 presents results for a constant vertical pressure (effectively drained) test in which three cycles of constant amplitude shear stress are applied, after which the stress amplitude is changed. The shear stress amplitudes are commanded to increase steadily from 13 to 45 *kPa*, after which they taper down. The test was carried out with *f*=1 *Hz* while maintaining vertical pressure σ_{v0}= 50 *kPa*. The feedback signal tracks the command well except at the largest stress amplitude. Misfit occurs beginning at time *t*=9 *sec* because the shear strength of the soil under $\sigma_v = 50kPa$, which is approximately 30 *kPa*, is less than the stress in the command signal. Accurate tracking resumes when the command τ_{hv} again falls below the steady state shear strength (*t*>18 *sec*). Because the test is stress-controlled, shear strains are allowed to deviate from

a mean-zero condition, and in this case the residual shear strain at the conclusion of testing is approximately 2%. Vertical strains from seismic compression of approximately 3% also develop over the duration of the testing.

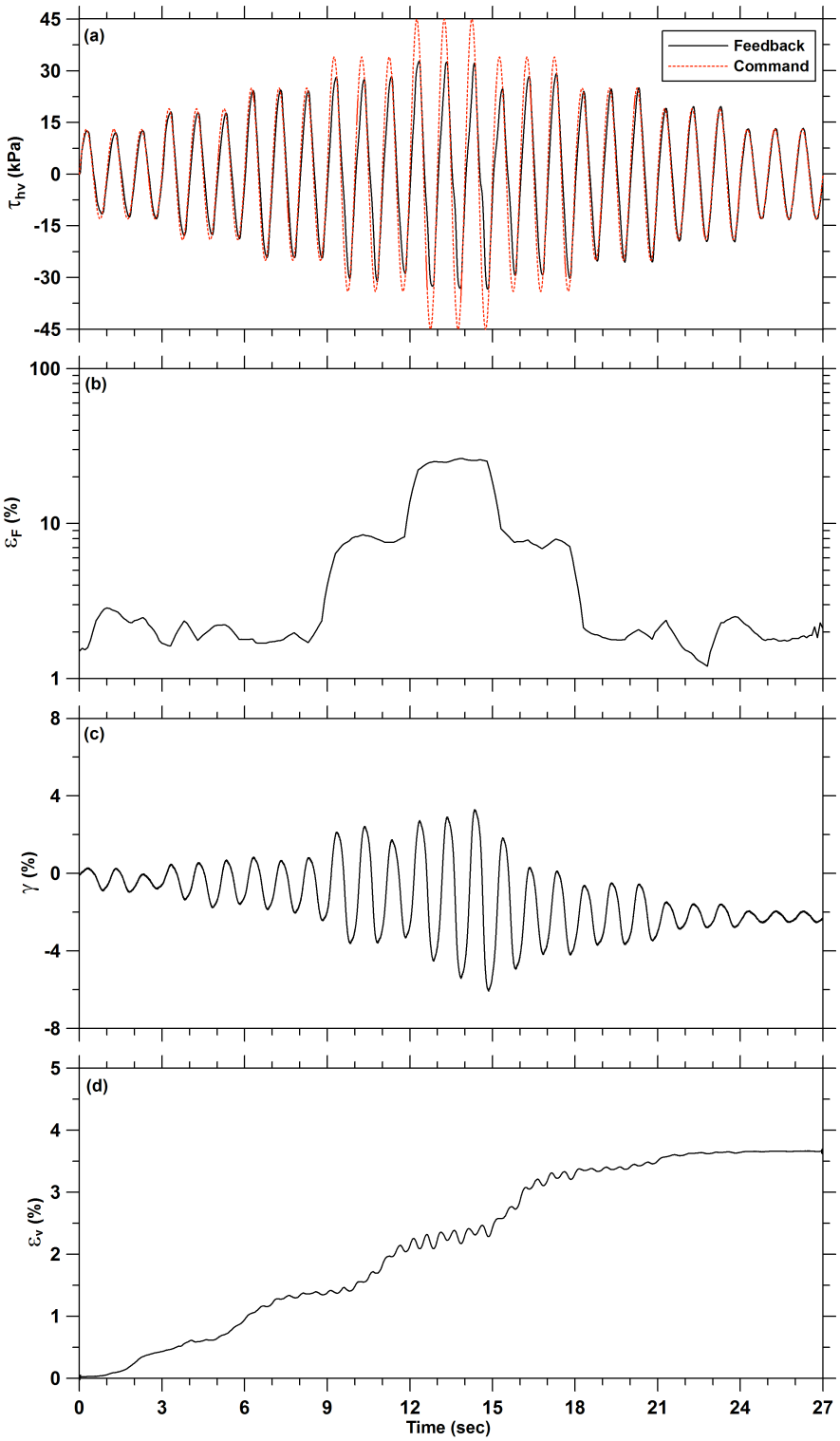

Figure 2.13. Constant vertical pressure stress-controlled test on Silica No. 2 at $D_r = 40\%$ and $\sigma_{v0} = 50kPa$ (a) feedback and command signals (b) tracking error (c) cyclic shear strain (d) volumetric strain

(d) Control under broadband excitation

Duku et al. (2007) investigated the ability of the device to command broadband strain demands. We extend that work to investigate the capability of the device to command broadband stress-controlled loading. The tested material is Silica No. 2 sand at $D_r = 45\%$. Testing was carried out under constant volume conditions with $\sigma_{v0} = 100kPa$. The phasing of stress demands were taken to match the EWl component of the accelerogram recorded at station TCU123 ($V_{S,30}$=273 m/s) from the **M** 7.6 Chi Chi, Taiwan earthquake. This acceleration history produces 15 equivalent uniform loading cycles at an amplitude that is 65% of the peak stress, based on Liu et al. (2001) procedure for counting stress cycles. We converted the acceleration history to a shear stress history by setting the amplitude of the irregular load ($\tau_{hv,\max} / \sigma_{v0}$) to 0.20. The equivalent CSR has an amplitude of 0.20×0.65=0.13, which produces initial liquefaction after 15 cycles of loading.

Fig. 2.14 shows that the feedback signal tracks the command well and ε_{FRMS} is relatively low as long as r_u is less than ≈0.85. This occurs for the time interval $t \le 19.2$ *sec*. During this time interval ε_{FRMS} ranges from approximately 2% to 20%, which is generally larger than errors of about 3% to 6% from 1 *Hz* sinusoidal commands at comparable stress amplitudes of CSR = 0.02 to 0.1 (Fig. 2.7a). The larger errors occur because of the additional complexity of broadband command that includes many frequencies and time intervals having motions with both weak and strong motions (Duku et al. 2007).

For the time interval t>19 *sec*, pore pressures are large and the shear strength of the soil is reduced. The stress path is located near the SSL for much of this time interval and the control system cannot keep pace with the rapid changes in soil stiffness within stress cycles, as described

previously in Section 2.3.3c. As a result, tracking errors are very large (up to 300%). If the time step of the broadband motion is increased by a factor of 10, the test results are as given in Fig. 2.15. For the same reasons given in Section 2.3.3c, the slower rate of shearing allows in-cycle contraction/dilation to occur and tracking errors are substantially reduced.

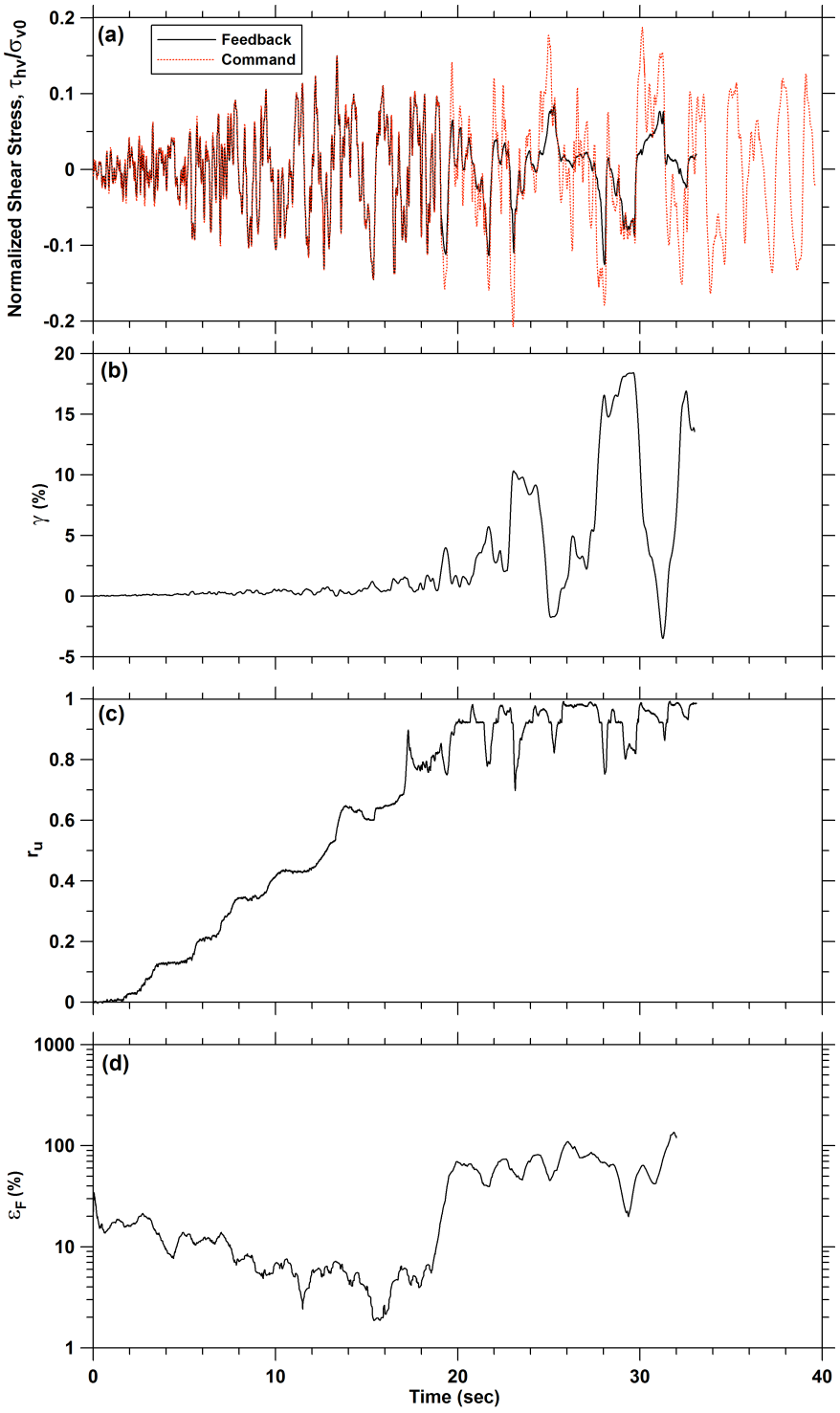

Figure 2.14. Uni-directional broadband constant volume testing of Silica No. 2 under an initial vertical stress (σ_{v0}) of 100 *kPa* and ($\tau_{hv,\max} / \sigma_{v0}$)=0.20 (a) feedback versus command signal (b) shear strain response (c) pore water pressure response (c) smoothed tracking error

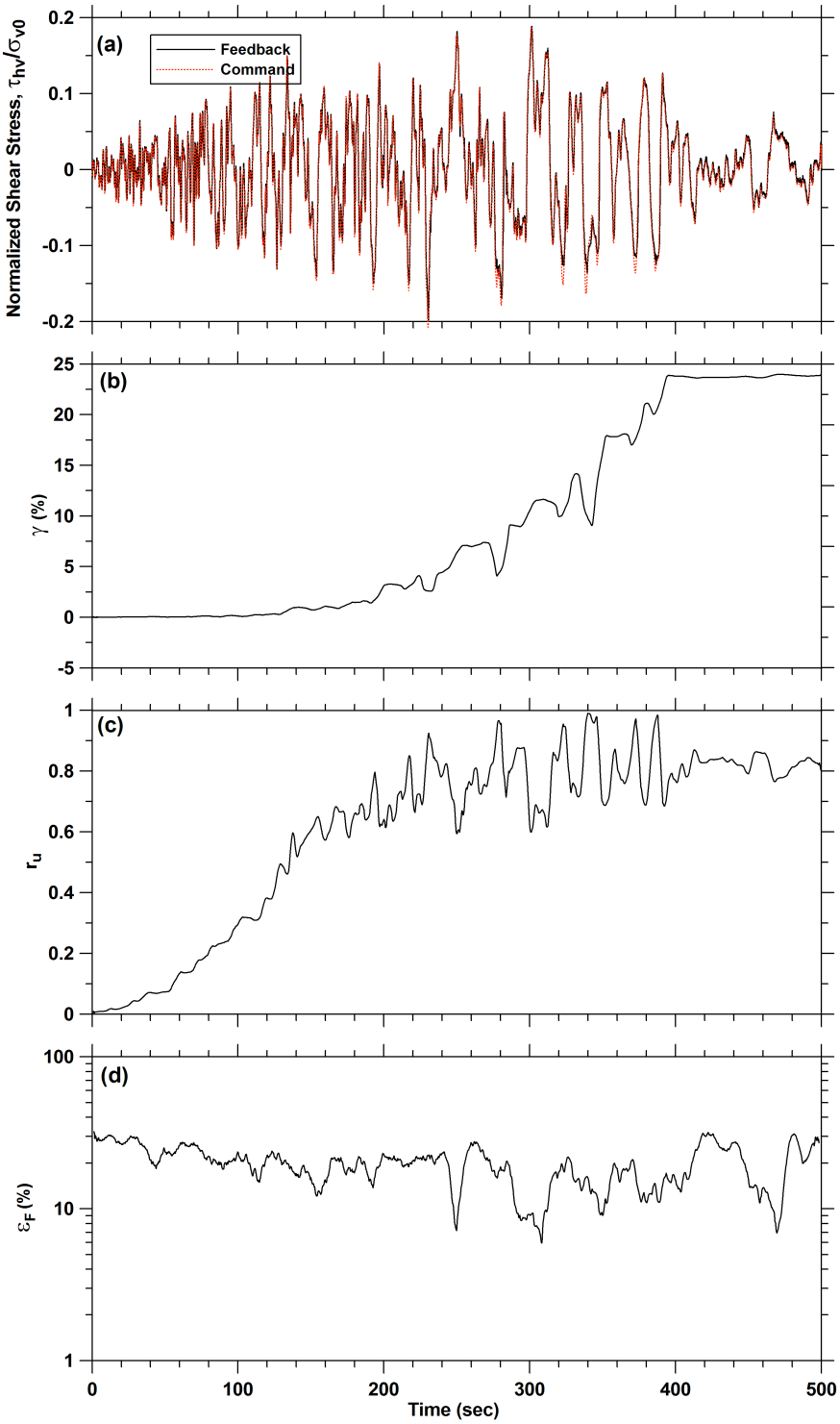

Figure 2.15. Uni-directional broadband constant volume testing of Silica No. 2 when time step is increased by a factor of 10 under an initial vertical stress (σ_{v0}) of 100 *kPa* and ($\tau_{hv,\max} / \sigma_{v0}$)=0.20 (a) feedback versus command signal (b) shear strain response (c) pore water pressure response (d) smoothed tracking error

Next, we decreased the amplitude of irregular load ($\tau_{hv,\max} / \sigma_{v0}$) to 0.15 to investigate the capability of the device to command broadband stress-controlled loading when liquefaction does not occur (Fig. 2.16). Fig. 2.16a shows that although r_u becomes as high as 0.5 (Fig. 2.16b), the feedback signal tracks the command signal well. The test shown in Figure 2.16 was performed at the native time step of the command signal (Δt = 0.005 sec).

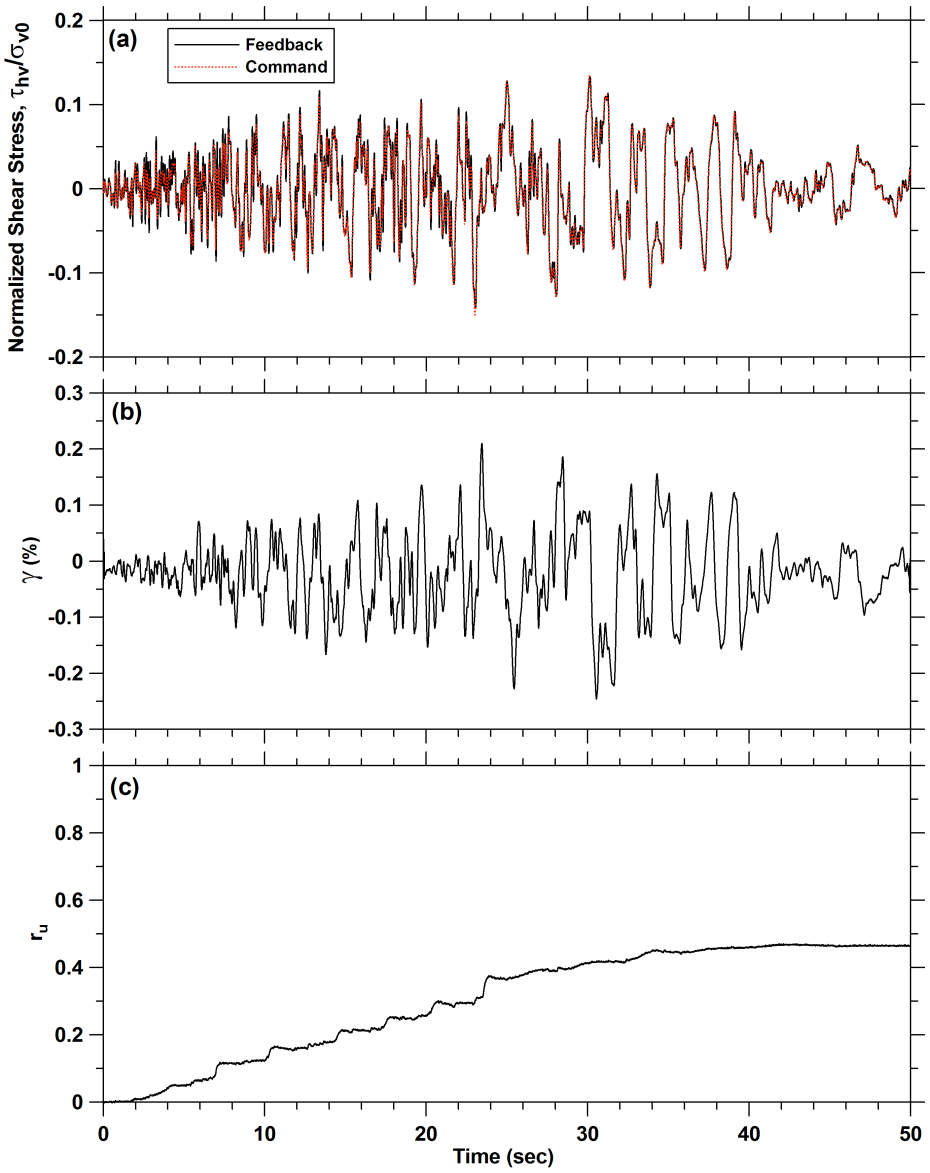

Figure 2.16. Uni-directional broadband constant volume testing of Silica No. 2 under an initial vertical stress (σ_{v0}) of 100 *kPa* and ($\tau_{hv,\max} / \sigma_{v0}$)=0.15 (a) feedback versus command signal (b) shear strain response (c) pore water pressure response

2.4 EXAMPLE TEST RESULTS

To demonstrate the current capabilities of the BB-SS device, dry pluviated specimens of Silica No. 2 sand prepared to various relative densities were subjected to a range of tests. These

specimens have a height and diameter of 25.4 and 72.6 *mm*, respectively. Initial tests were cyclic strain-controlled drained tests for specimens initially consolidated to a vertical stress of σ_{v0}=100 *kPa*, with the intent of verifying volume change results from the same device with the same material under the previous control system as reported in Duku et al. (2008). These results were confirmed, as described in Stewart et al. (2013).

The second phase of testing, reported here, demonstrates capabilities of the device when used for constant-height testing. The test suite includes monotonic strain-controlled, cyclic strain- and stress-controlled, and broadband stress-controlled loading. We do not have previous undrained test results against which to compare our findings for this specific material, but the general features of soil behavior are well understood, enabling the present results to be compared on a qualitative basis to those of other investigators (e.g., Ishihara, 1993; Matasovic and Vucetic, 1993; Boulanger and Truman, 1996; Kammerer et al., 2002).

2.4.1 Monotonic Shear Behavior

We investigated the monotonic shear behavior of Silica No. 2 sand at relative densities of 40 and 70%. In these tests we seek to examine phase transformation behavior of soils that are contractive at small strains and then become dilatant at large strains. The tests were performed at initial vertical pressures (σ_{v0}) of 30, 100 and 250 *kPa*.

Fig. 2.17 presents the stress path (i.e., shear stress versus vertical effective stress) response of the tested material. At the onset of loading, significant pore water pressure generates, irrespective of initial vertical pressure. Once stress paths reach the phase transformation line, negative pore water pressure generates indicating dilatant soil behavior as indicated by rapidly increasing shear

stress. All of the stress paths approach a common steady state line (SSL), as expected from previously similar tests by Ishihara (1993) on specimens of Toyoura sand.

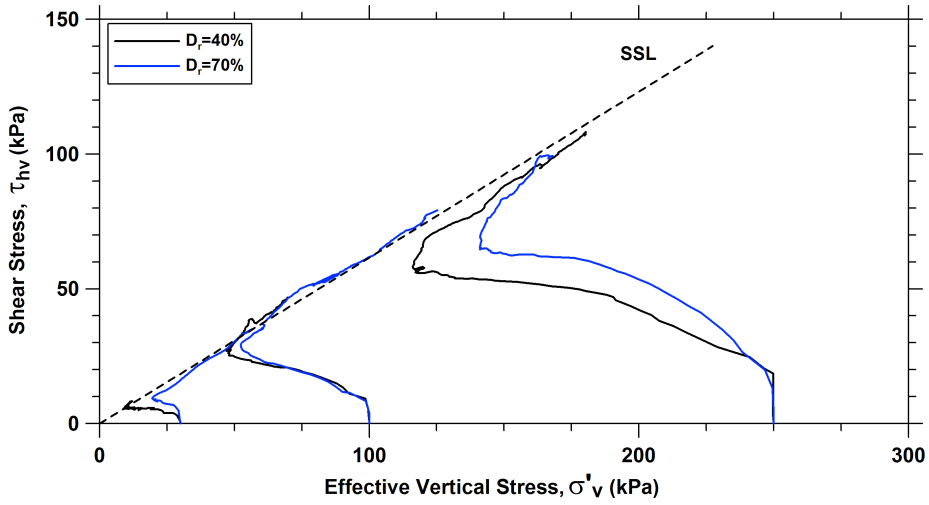

Figure 2.17. Stress paths under monotonic shear for Silica No. 2 sand under constant volume conditions

2.4.2 Cyclic Response under Strain- and Stress-Controlled Loading Conditions

We conducted cyclic strain- and stress-controlled tests on 40% relative density Silica No. 2 sand under an initial vertical pressure of σ_{v0}=100 *kPa* . A shear strain amplitude of 1% was applied at a frequency of 0.1 *Hz* in the strain-controlled test. The stress-controlled test was conducted with a *CSR* of 0.15 and the same frequency of 0.1 *Hz*. The change in vertical stress is taken as the change in pore water pressure (Δu), which is normalized by σ_{v0} to compute $r_u = \Delta u / \sigma_{v0}$. Figs. 2.18 and 2.19 present the stress-strain and pore water pressure response for the strain- and stress-controlled tests, respectively.

Although the sand reaches pore water pressure ratios (r_u) near unity in both tests (Figs. 2.18b and 2.19b), the material responses are very different. In the strain-controlled test the initial

secant shear modulus decreases continuously with progressive increases in r_u (Fig. 2.18b), approaching zero when initial liquefaction occurs (Fig. 2.18a). On the other hand, once the soil experiences softening in the stress-controlled test, the hysteresis loops take on an inverted s-shape as a result of hardening that occurs when applied shear strains exceed those applied in previous cycles. This is due to temporary (within-cycle) pore pressure decrease.

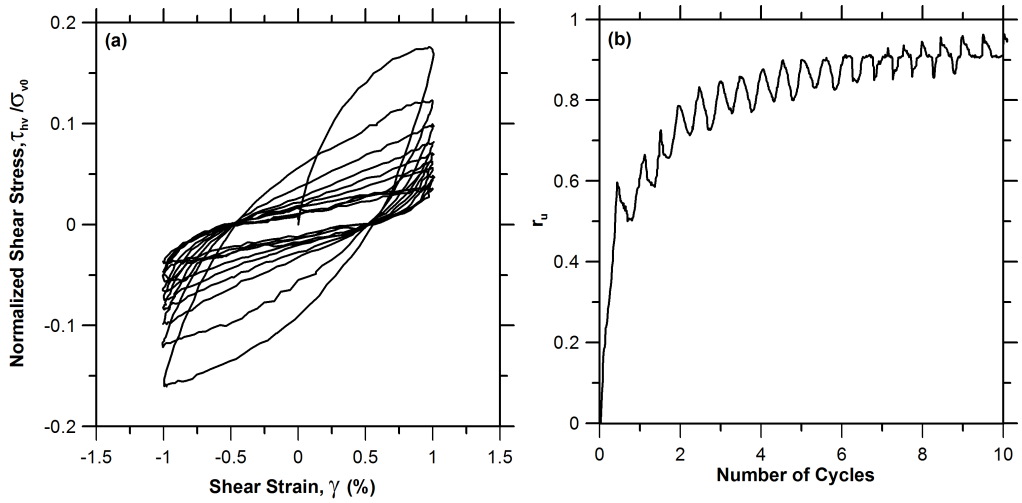

Figure 2.18. Cyclic strain-controlled test on Silica No.2 at $D_r = 40\%$ and $\sigma_{v0} = 100kPa$ under constant volume conditions (a) stress-strain (b) pore water pressure response

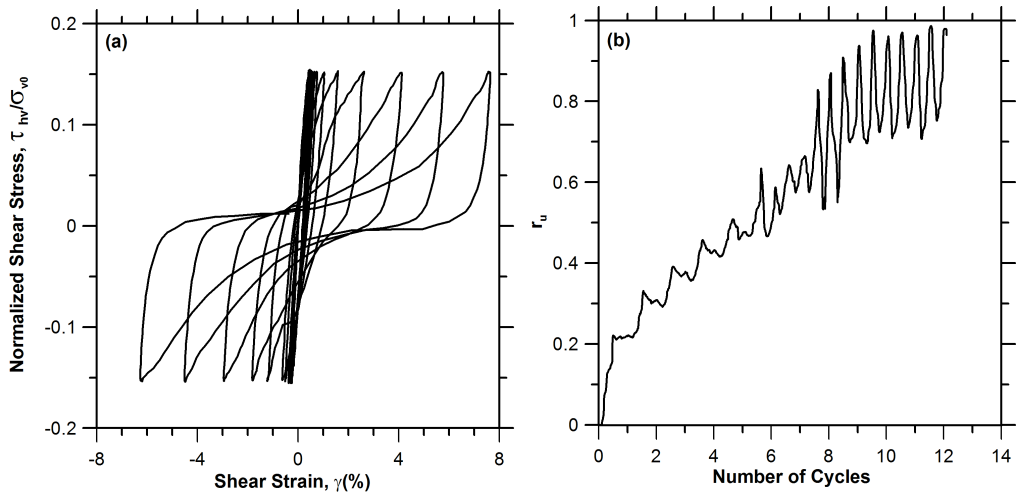

Figure 2.19. Cyclic stress-controlled test on Silica No.2 at $D_r = 40\%$ and $\sigma_{v0} = 100kPa$ under constant volume conditions (a) stress-strain (b) pore water pressure response

Features similar to those reported here have been found in earlier undrained strain-controlled cyclic tests on sand by Vucetic and Dobry (1988) and Matasovic and Vucetic (1993) and in stress-controlled tests by Boulanger and Truman (1996) and Kammerer et al. (2002).

2.4.3 Bi-Directional Broadband Stress-Controlled Testing

A unique capability of the UCLA BB-SS device is that the PID controller has the ability to command realistic earthquake waveforms in two horizontal directions. To demonstrate this feature, we conducted bi-directional, broadband, stress-controlled constant height testing on a specimen of Silica No. 2 sand prepared to a relative density of 45% and consolidated to an initial vertical pressure of σ_{v0}=100 *kPa*. Stress histories selected for testing were consistent with the EW and NS components of acceleration histories recorded at site TCU123 during the **M**7.6 Chi-Chi Taiwan earthquake, scaled to shear stresses using the procedure provided in Section 2.3.3. The response of the Silica No. 2 sand under uni-directional shaking, using only the EW component of the record, was shown in Figs. 2.14 to 2.16. For the bi-directional test, we increased the time step by a factor of ten relative to the native step of 0.005 sec to help the

control system keep pace with rapid changes in soil stiffness within stress cycles, as discussed previously in Section 2.3.3d.

Fig. 2.20(a) presents the stress histories (feedback signals) applied on axes 1 and 2. As depicted in Fig. 2.20(b), the rate of pore water pressure build-up is faster when two axes are excited simultaneously than during uni-directional shaking applied to either axis. Assuming that liquefaction occurs when shear strain (γ) reaches 5% (which corresponds in time approximately with the first occurrence of $r_u > 0.9$), the sand is liquefied after 363 seconds under bi-directional shaking, while it does not liquefy under uni-directional shaking. The bi-directional test stopped when shear strains reached the limit for the LVDT along axis 1 (Fig. 2.20c).

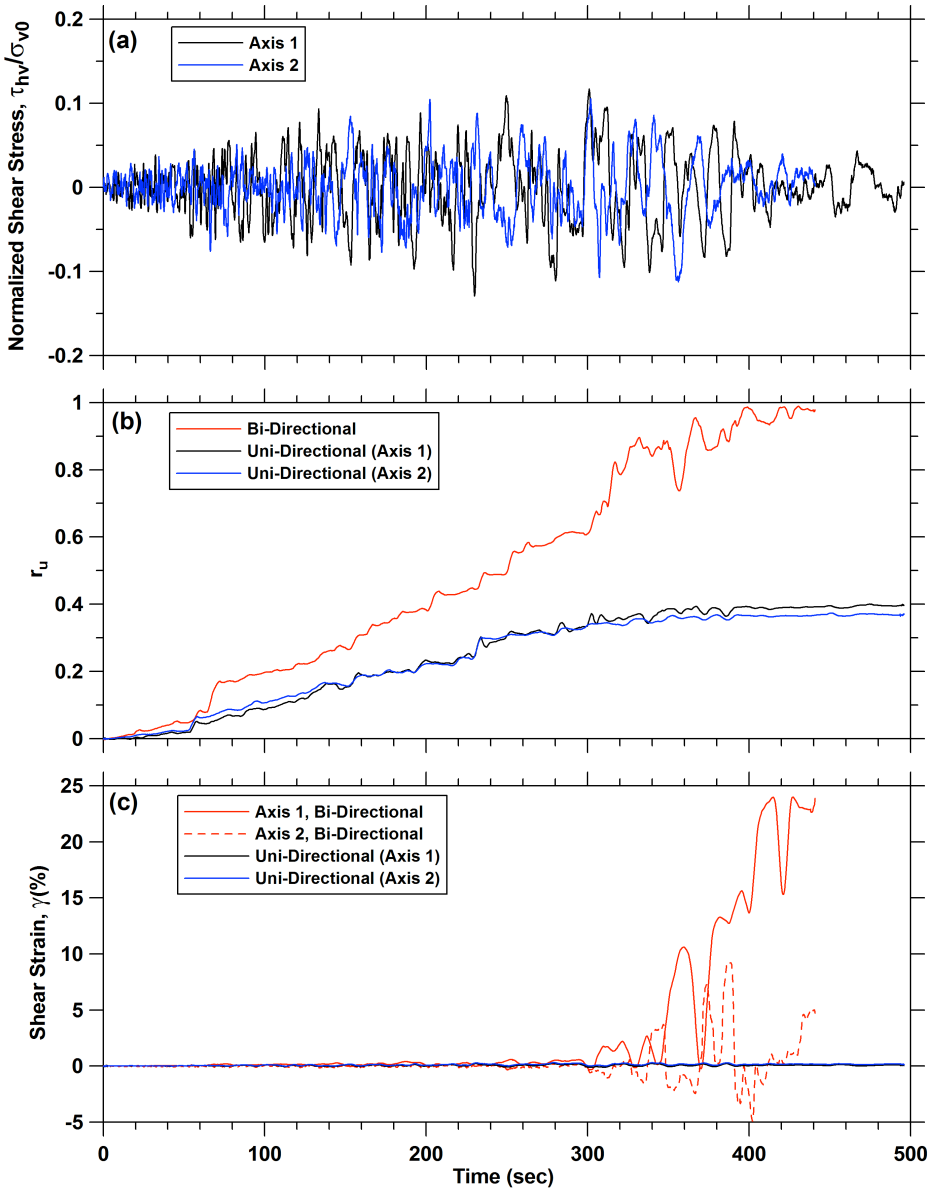

Figure 2.20. Bi-directional broadband constant volume testing of Silica No. 2 under an initial vertical stress (σ_{v0}) of 100 *kPa* (a) feedback signals (b) pore water pressure response (c) shear strains

3 Background on Monotonic, Cyclic, and Post-Cyclic Behavior of Peat

3.1 INTRODUCTION

Peat is a mixture of fragmented organic materials formed in wetlands under appropriate climatic and topographic conditions and it is derived from vegetation that has been chemically changed and fossilized (Edil and Dhowian, 1981). Peat-producing ecosystems are found throughout the world, and peat deposits constitute 5 to 8% of the land surface of the earth (Davis 1997). In the United States peat deposits are found in 42 states and are abundant in parts of Alaska, California, Florida, Maine, Michigan, Minnesota, New Jersey, New York, and Wisconsin.

Peat is often considered to be problematic due to its low shear strength and high compressibility, both of which derive in large part from its high water content (500% for organic content > 50%) and organic content (often more than 75%). Its color is usually dark brown or black (see Fig. 3.1) and it can be odoriferous (Craig, 1992). When peat becomes dried out, it can oxidize and be transported by wind or it can be combustible. These are sources of ground loss in peat soil deposits, along with volume change that accompanies decomposition processes known as humification.

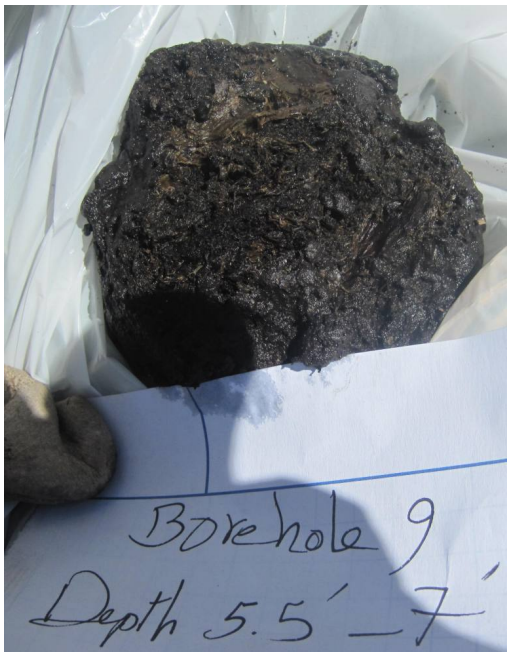

Figure 3.1. Sherman Island peat, California

Peats are accumulated if the rate of ground loss or decay is slower than the rate of addition (Bell, 2000). Furthermore, the content of peat may differ from location to location due to factors such as the types of locally growing plant fibers, temperature and degree of humification. Decomposition or humification involves the loss of organic matter either in gas or in solution, the disappearance of physical structure and the change in chemical state. The end products of humification are carbon dioxide and water, the process being essentially one of biochemical oxidation. Immersion in water reduces the oxygen supply enormously, which in turn, reduces aerobic microbial activity and encourages slower anaerobic decay. Table 3.1 shows the typical physical and chemical properties of peat. A key consideration in understanding the engineering properties of peat is the degree to which it contains fibers. Figures 3.2 and 3.3 show fibrous and non-fibrous peat specimens, respectively. While fibrous materials have higher void ratios and water contents, the fibers also provide a degree of reinforcement that increases shear strength.

Table 3.1. Physical and chemical properties of peat (Kazemian et al. 2011)

Peat type	Natural water content (w, %)	Bulk density (Mg/m^3)	Specific gravity (G_s)	Acidity (pH)	Ash content (%)	Reference
Fibrous-woody	484-909	-	-	-	17	Colley (1950)
Fibrous	850	0.95-1.03	1.1-1.8	-	-	Hanrahan (1954), Asadi et al., 2009, 2010
Peat	520	-	-	-	-	Lewis (1956)
	500-1500	0.88-1.22	1.5-1.6	-	-	Lea and Browner (1963)
Amorphous and fibrous	200-600	-	1.62	4.8-6.3	12.2-22.5	Adams (1965)
	355-425	-	1.73	6.7	15.9	
Amorphous to fibrous	850	-	1.5	-	14	Keene and Zawodniak (1968)
Fibrous	605-1290	0.87-1.04	1.41-1.7	-	4.6-15.8	Samson and LaRochell (1972), Moayedi et al.(2011a, b)
Coarse fibrous	613-886	1.04	1.5	4.1	9.4	Berry and Vickers (1975)
Fibrous sedge	350	-	-	4.3	4.8	Levesque et al. (1980)
Fibrous sphagnum	778	-	-	3.3	1	
Coarse fibrous	202-1159	1.05	1.5	4.17	14.3	Berry (1983)
Fine fibrous	660	1.05	1.58	6.9	23.9	NG and Eischen (1983)
Fine fibrous	418	1.05	1.73	6.9	9.4	
Amorphous granular	336	1.05	1.72	7.3	19.5	
Peat portage	600	0.96	1.72	7.3	19.5	Edil and Mochtar (1984)
Peat waupaca	460	0.96	1.68	6.2	15	
Fibrous peat (Middleton)	510	0.91	1.41	7	12	
Fibrous peat (Noblesville)	173-757	0.84	1.56	6.4	6.9-8.4	
Fibrous	660-1590	-	1.53-1.68	-	0.1-32.0	Lefebvre et al. (1984)
Fibrous peat	660-890	0.94-1.15	-	-	-	Olson and Mesri (1970)
Amorphous peat	200-875	1.04-1.23	-	-	-	
Peat	125-375	0	1.55-1.63	5-7	22-45	Yamaguchi et al. (1985)
Peat	419	1	1.61	-	22-45	Jones et al. (1986)
Peat	490-1250	-	1.45	-	20-33	Yamaguchi et al. (1987)
Peat	630-1200	-	1.58-1.71	-	22-35	Nakayama et al. (1990)
Peat	400-1100	0.99-1.1	1.47	4.2	5-15	Yamaguchi 1990
Fibrous	700-800	~1.00	-	-	-	Hansbo (1991)
Peat (Netherlands)	669	0.97	1.52	-	20.8	Termatt and Topolnicki (1994)
Fibrous (Middleton)	510-850	0.99-1.1	1.47-1.64	4.2	5-7	Ajlouni (2000)
Fibrous (James Bay)	1000-1340	0.85-1.02	1.37-1.55	5.3	4.1	

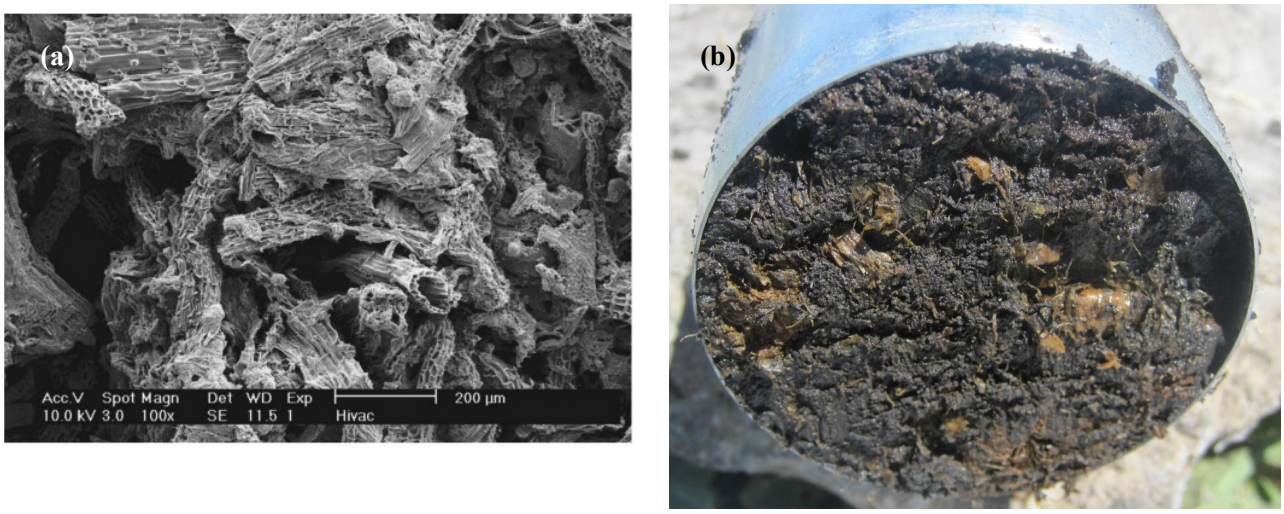

Figure 3.2. Fibrous peat: (a) scanning electron microphotograph of a vertical section of James Bay peat showing network of fibrous elements and perforated hollow particles (Mesri and Ajlouni, 2007), (b) Sherman Island, California

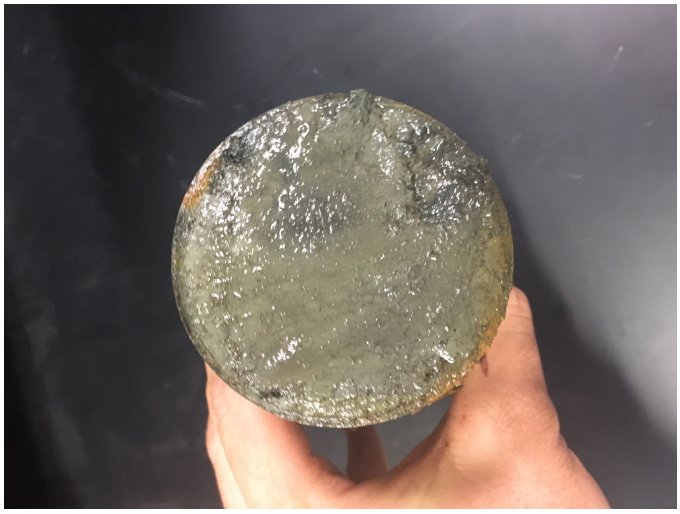

Figure 3.3. Non-fibrous peat, Sherman Island, California

3.2 STATIC COMPRESSIBILITY

The compressibility of soil generally consists of three stages - initial compression, primary consolidation, and secondary compression. Initial compression occurs immediately after the load is applied; whereas primary and secondary compressions depend on the length of time the load is applied.

The compression behavior of peat varies from the compression behavior of other types of soils in two ways: 1) the compression of peat is much larger than that of other soils, and 2) the creep portion of settlement plays a more significant role in determining the total settlement of peat than of other soil types. The primary consolidation of fibrous peat takes place very rapidly due to high hydraulic conductivity. Large volume change from secondary compression is also observed to take place (e.g., Fox and Edil 1992, Mesri et al. 1997, Mesri and Ajlouni 2007), and in some cases tertiary compression has been reported (Candler and Chartres, 1988; Fox and Edil, 1992). Tertiary compression is a creep-type deformation that is reported to follow secondary compression, with a slope in void ratio (e)-log (time) space that is steeper than that for secondary compression.

The dominant factors controlling the compressibility characteristics of peat include the fiber content, natural water content, void ratio, initial permeability, nature and arrangement of soil particles, and inter-particle chemical bonding in some of the soils (Mesri and Ajlouni, 2007). The in situ void ratio of fibrous peats is very high because of the fact that compressible and bendable hollow cellular fibers form an open network of particles with high water content. Surficial fibrous peat deposits can have in situ water contents of 500 to 2,000%, which correspond to in situ void ratios of 7.5 to 30, respectively (Hanrahan 1954; MacFarlane 1969; Hobbs 1986, 1987).

During both primary and secondary compression, water is expelled simultaneously from within and among the peat particles (Mesri and Ajlouni, 2007). Therefore, the $e - \log p'$ curves show a steep slope indicating a high value of compression index (C_c). Fibrous peats display especially large compressibility, with compression index values on portions of the virgin compression curve just beyond the preconsolidation pressure that are 5 to 20 times the corresponding compressibility of typical soft clays and silts (Mesri and Ajlouni, 2007). It is also

difficult to locate the beginning of secondary compression (t_p) from the settlement-time curve for a peat specimen because the primary consolidation occurs rapidly. Fox and Edil (1992) showed that the settlement-time (or compression) curves (Fig. 3.4) of peat have an unusual shape, and the end of primary consolidation is best determined by pore pressure measurement rather than graphical construction.

Although the time-rate of primary consolidation settlement in fibrous peat is very rapid, it decreases with the application of increasing consolidation pressure due to substantial reductions in hydraulic conductivity as the peat void ratio decreases. According to Lea and Brawner (1963), the coefficient of consolidation (C_v) can decreases by factors on the order of 5-100 as vertical effective stresses are increased from approximately 10 to 100 *kPa*.

The secondary compression of peat arises from bending and volumetric deformations of peat fibers along with decomposition, all of which lead to irreversible deformations of the peat soil fabric (Mesri et al., 1997; Mesri and Ajlouni, 2007). The secondary compression index (C_α) is the slope in e-log(time) space following primary consolidation, as depicted in Figure 3.4. This estimate is based on the assumptions that C_α is independent of time, thickness of compressible layer, and applied pressure. However, Fox and Edil (1992) showed the tertiary compression can follow secondary compression, which is evidenced by C_α not being constant but instead increasing in time under constant effective stress (Fig. 3.4).

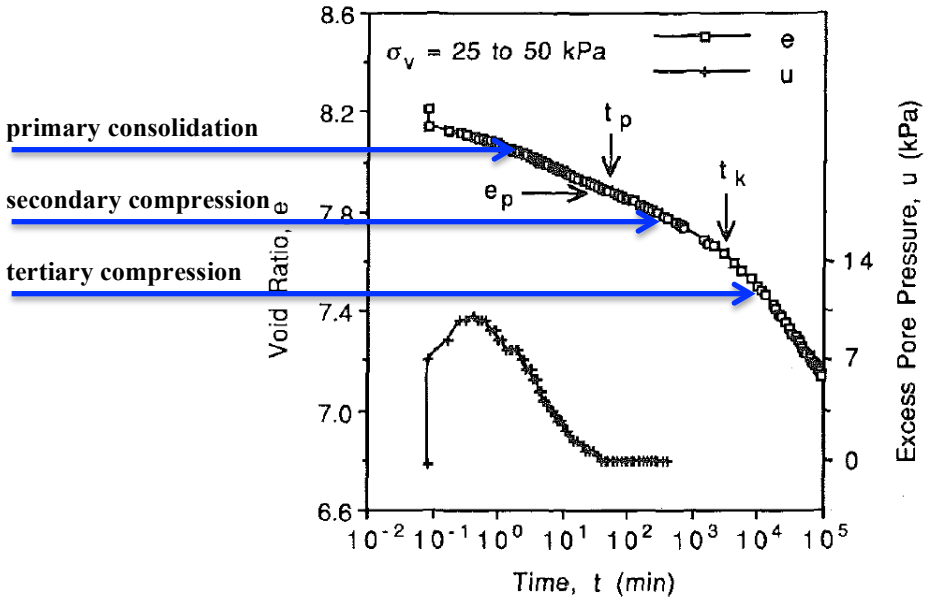

Figure 3.4. Primary consolidation followed by secondary and tertiary compression for peat (Fox and Edil 1992)

3.3 MONOTONIC SHEAR BEHAVIOR

This section includes a review of data for fibrous peats on their frictional resistance, and undrained shear strength.

3.3.1 Frictional Resistance

Frictional resistance of soils results from sliding resistance and geometrical interference and interlocking (Terzaghi et al. 1996). Geometrical interference and interlocking is determined by the strength, size, shape, and arrangement of soil particles.

Fibrous peats are frictional materials with high values of friction angle (MacFarlane 1969). Tensile strength of the fibers contributes to particle interlocking in fibrous peats (Adams 1961, 1965; Hardy 1968; Landva and La Rochelle 1983). Data on the friction angle of various fibrous peats tested in triaxial compression are summarized in Table 3.2. Triaxial compression data on relatively undisturbed specimens of Middleton peat consolidated under equal all-around pressure as well as under laterally constrained conditions are shown in Fig. 3.5. To perceive the very high values of φ' in Table 3.2 and Fig. 3.5, note the 200 μm thick relatively stiff peat mats (Landva and Pheeney 1980) that formed under 200 *kPa*, and are shown in Fig. 3.6. Shear deformations required to mobilize the maximum frictional resistance in fibrous peats are often 5 to 10 times those required for soft clay deposits (Tressider 1958; Hardy and Thomson 1956; MacFarlane 1969).

Table 3.2. Friction angle of fibrous peats from Triaxial compression tests on vertical specimens (Mesri and Ajlouni, 2007)

Source	Peat	w_o (%)	ϕ' (degrees)
Adams (1961)	Muskeg	375–430	50–60
Adams (1965)	Moose River	330–600	48
Ozden et al. (1970)	Muskeg	800	46
Tsushima et al. (1977)	Muck	—	52–60
Yasuhara and Takenaka (1977)	Omono	—	50–60
Tsushima et al. (1982)	Muck	—	51
Edil and Dhowian (1981) and Edil and Wang (2000)	Middleton	500–600	57
	Portage	600	54
Landva and LaRochelle (1983)	Escuminac	1,240–1,380	40–50
Marachi et al. (1983)	San Joaquin	200–500	44
Yamaguchi et al. (1985a,c,d)	Ohmiya	960–1,190	51–55
	Urawa	980–1,260	53
Ajlouni (2000)	Middleton	510–850	60

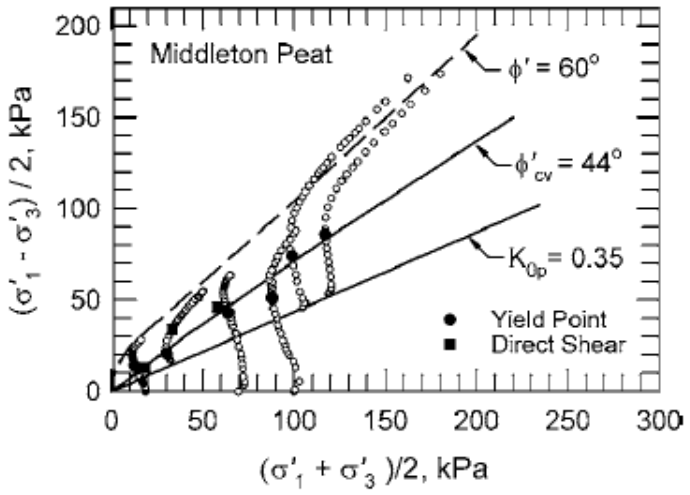

Fig. 3.5. Effective stress paths of Middleton peat specimens consolidated under equal all-around pressure or under laterally constrained condition and then subjected to undrained axial compression, and peak shear strength versus effective normal stress from three drained direct shear tests (Mesri and Ajlouni, 2007)

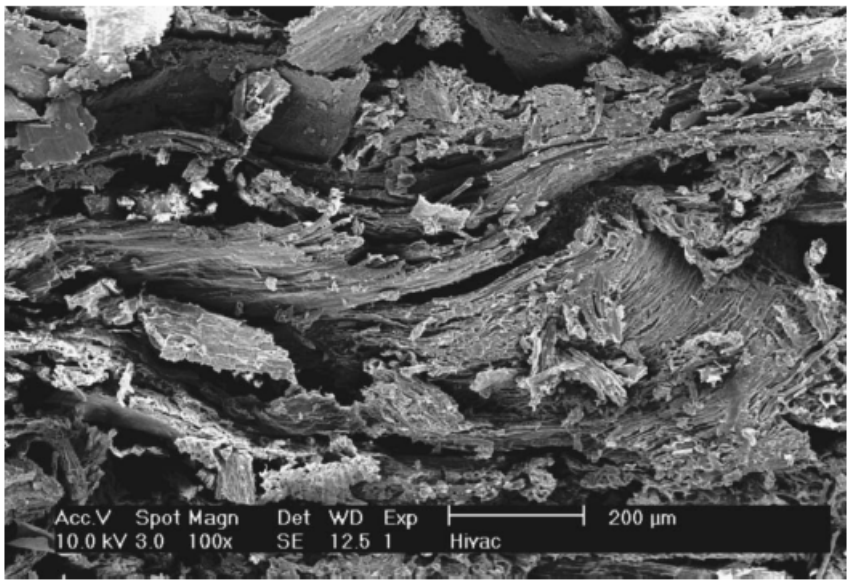

Figure 3.6. Scanning electron microphotograph of vertical section of James Bay peat showing thick relatively stiff peat mats formed after consolidation under 200 *kPa* (Mesri and Ajlouni, 2007)

Landva and La Rochelle (1983) suggested that shearing parallel to fiber orientation may lead to reduced particle interlocking and frictional resistance. Drained ring shear tests in an effective normal stress range of 10 to 50 *kPa*, reported by Landva and La Rochelle (1983), also suggest φ' values for a fibrous peat in the range of 32° to 40°. On the other hand, in the triaxial tests in which shear plane crosses the fibers, the range of φ' values was from 40° to 50°.

A comprehensive series of undrained triaxial tests with pore water pressure measurements was reported by Yamaguchi et al. (1985a,b) on undisturbed specimens of a fibrous peat cut with axes parallel to the vertical or horizontal direction in the ground. The friction angle from triaxial compression tests on horizontal specimens was 35° compared to 51 to 55° for vertical specimens.

It can be inferred that anisotropic fabric of peat leads to anisotropic shear behavior in such a manner that the lowest friction angle is obtained if the peat is sheared along the interfaces of fibers. The friction angle increases with the increase in the angle between shear plane and fibers'

plane. Theoretically, the maximum friction angle is obtained if the shear plane is perpendicular to fibers.

3.3.2 Undrained Shear Strength

Low initial undrained shear strength of peat deposits has led to spreading type failures of some embankments constructed sufficiently rapidly that shearing of foundation soil occurs under undrained conditions (e.g., Brawner 1958). Over the longer term, primary and secondary compression lead to appreciable increase in shear strength of fibrous peats (Lea and Brawner 1963; Weber 1969), so short-term undrained loading comprises the critical case for embankment stability. These principles are supported by experience in placing fills on peat, which suggests that a significant increase in the shear strength of peat occurs following the pore water pressure dissipation (MacFarlane, 1969). Void ratio decrease associated with secondary compression is also expected to lead to an increase in undrained shear strength (Mesri and Ajlouni, 1987).

Data from various researchers on the normalized undrained shear strength of fibrous peats for the compression mode of shear are shown in Table 3.3. Following classical procedures for clays, the normalization consists of dividing undrained shear strength (s_u) by the pre-shear major principle stress, which is typically in the vertical direction (σ'_{vc}). The ratio s_u/σ'_{vc} is known for clays to increase strongly with overconslidation ratio (OCR), with the minimum value for normally consolidated clays under direct simple shear conditions being about 0.2-0.25 (Ladd, 1991). As seen in Table 3.3, peats show very high values of s_u/σ'_{vc} as compared to typical values for clays. However, the undrained shear strength of surficial peats can be low because of their very low unit weight (see Table 3.1). As the fibrous structure is strongly responsible for

high frictional resistance and high values of s_u/σ'_{vc}, any humification (biochemical degradation) of the fiber structure is expected to lead to reduce both strength metrics (Mesri and Ajlouni, 2007).

Table 3.3. Normalized undrained shear strength of fibrous peats (Mesri and Ajlouni, 2007)

Source	Peat	w_o (%)	$s_u(\text{TC})/\sigma'_{vc}$
Moran et al. (1958)	Antioch, Algiers	230–1,000	0.48–0.60
Lea and Brawner (1959)	Burnaby	400–1,200	0.47–0.58
Adams (1965)	Moose River	330–600	0.68
Forrest and MacFarlane (1969)	Ottawa	900–1,200	0.50
Yasuhara and Takenaka (1977)	Omono	—	0.54
Tsushima et al. (1977)	—	—	0.52–0.54
Dhowian (1978) and Edil and Wang (2000)	Middleton	500–600	0.55–0.75
	Portage	600	0.70
Yamaguchi et al. (1985a,c,d)	Ohmiya	960–1,190	0.55
	Urawa	980–1,260	0.52
Den Haan (1997)	—	—	0.54–0.78
Ajlouni (2000)	Middleton	510–850	0.53[a]

[a]Defined at phase transformation yield point.

The undrained shear strength data in Table 3.3 correspond to the compression mode of shear on vertical specimens. Yamaguchi et al. (1985a,b) subjected vertical and horizontal peat specimens to undrained compression and extension shear. The values of $s_u(TC)/\sigma'_{vc}$ and $s_u(TE)/\sigma'_{vc}$ for vertical specimens were 0.55 and 0.57, respectively, whereas for the horizontal specimens they were 0.53 and 0.80 respectively. The $s_u(TC)/s_u(TE)$ for the fibrous peat tested by Yamaguchi et al. (1985a,b) was also 1.0 and 1.5 for vertical and horizontal specimens,

respectively. This clearly shows that some sort of anisotropy exists in undrained shear strength of peat.

3.4 CYCLIC SHEAR BEHAVIOR

Dynamic properties of peat, in terms of shear modulus and damping ratio, have received considerable attention in the geotechnical literature, although consensus on the critical factors controlling this behavior remains somewhat elusive.

Seed and Idriss (1970) showed that peat exhibited stronger nonlinearity and higher damping ratios than clays based on their analyses of the site response records for a free field unconsolidated peat deposit at Union Bay in Washington State. Relatively linear behavior up to cyclic shear strain amplitudes (γ_c) of about 1% was reported by Stokoe et al. (1996) based on resonant column and torsional shear tests on peat specimens from the Queensboro Bridge in New York with in situ vertical effective stresses (σ'_{v0}) of less than 150 *kPa*. Kramer (1996) carried out resonant column tests on peat from Mercer Slough in Washington state, and observed strong nonlinearity at low consolidation stresses (2–30 *kPa*). A significant finding from the Mercer Slough peat was that the degree of nonlinearity decreased significantly with increasing confining pressure. Boulanger et al. (1998) performed cyclic triaxial tests on samples of peaty organic soil from beneath the levee crest at Sherman Island in California with vertical stress of about 135 *kPa*. The samples exhibited relatively linear behavior (e.g., similar to that expected of very high plasticity clays) but not quite as linear as reported by Stokoe et al. (1996). Boulanger et al. (1998) also showed that overconsolidation had little effect on the normalized secant shear modulus ($G/G_{\max}$) and equivalent damping (D) relations for the peat samples experiencing σ'_{v0} of about 135 *kPa* and effective laboratory consolidation stresses (σ'_{vc}) of 66–200 *kPa*. Boulanger

et al. (1998) compared the median modulus reduction and damping relationships for the peat specimens with the curves recommended by Vucetic and Dobry (1991) (Fig. 3.7). As seen, the peat specimens showed a response that is comparable to that of high-plasticity clays with PIs of 100-200. In reviewing the above results, Kramer (2000) suggested there was a general trend of increasing linearity and decreasing damping with an increase in effective consolidation stress for different peats. Similar trends have been observed for sands (by, e.g., Iwasaki et al. 1978; Tatsuoka et al. 1978) and clays (by, e.g., Lanzo et al. 1997; Vucetic et al. 1998; Stokoe et al. 1999).

Wehling et al. (2003) also evaluated the nonlinear dynamic properties of a fibrous peaty organic soil underlying the south levee of Sherman Island. The normalized secant shear modulus ($G/G_{\max}$) and equivalent damping ratio (D) versus cyclic shear strain amplitude (γ_c) relations for the Sherman Island field samples were shown to be dependent on the consolidation stress (σ'_{vc}). As shown in Figure 3.8, the $G/G_{\max}$ behavior showed increasing linearity as σ'_{vc} increased from about 12 to about 40 *kPa*, after which further increases in σ'_{vc} had no significant effect. Similarly, the ξ values decreased as σ'_{vc} increased from about 12 to about 40 *kPa*, after which further increases in σ'_{vc} had no significant effect. Figure 3.8 shows that these results are consistent with the trends observed by Kramer (2000) for Mercer Slough peat under stresses of 2–30 *kPa* and with results from Queensboro Bridge (Stokoe et al. 1996) at higher overburden pressures.

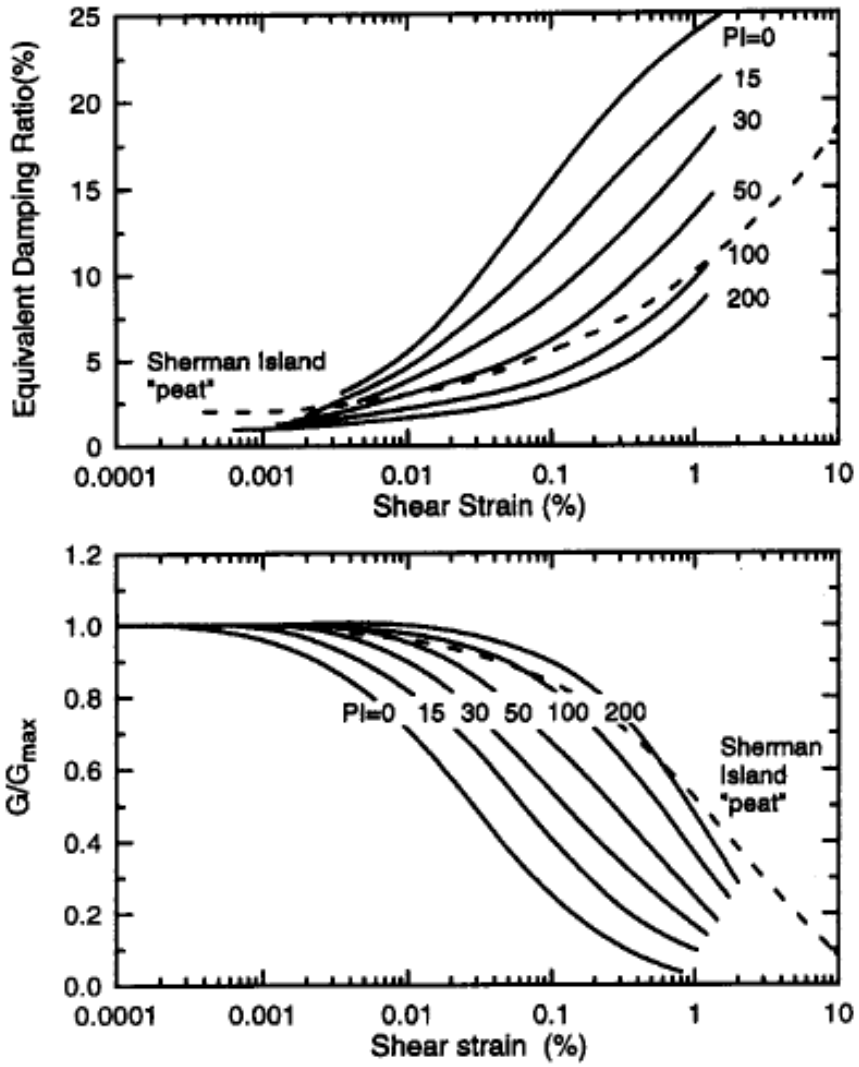

Figure 3.7. Median G/Gmax and damping ratio curves for Sherman Island peat versus curves recommended by Vucetic and Dobry (1991) (Boulanger et al. 1998)

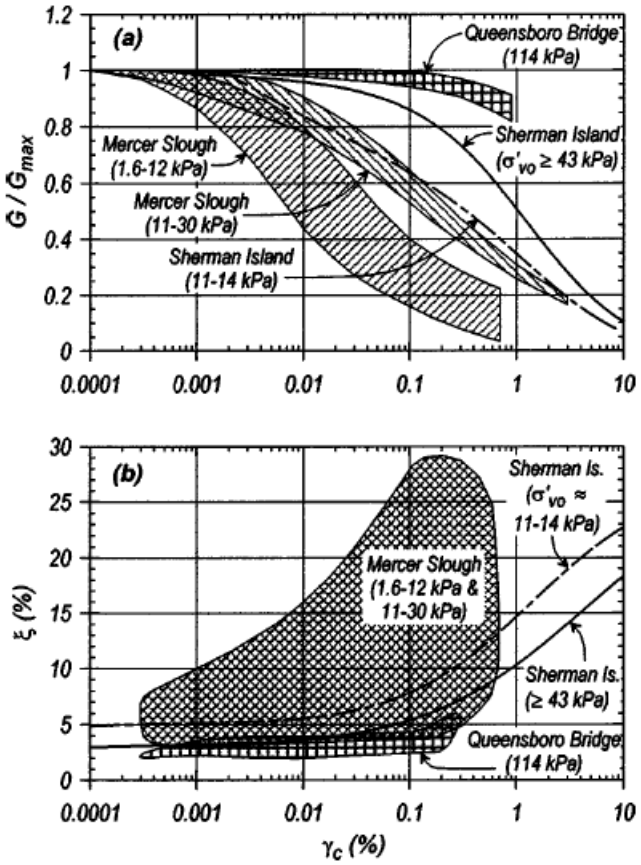

Figure 3.8. Wheling et al. (2003): Effect of vertical consolidation stress on modulus reduction and damping curves for peaty soils at Sherman Island, Mercer Slough (Kramer 2000), and Queensboro Bridge (Stokoe et al. 1996). Figure from Wehling et al. (2003)

Wehling et al. (2003) showed that the effect of sample disturbance on the $G/G_{\max}$ and D relations was likely be insignificant for practical purposes based on cyclic tests that involved prior undrained overstraining followed by reconsolidation. Prior undrained overstraining to $\gamma_c \approx$ 9% followed by reconsolidation resulted in $G/G_{\max}$ and D relations that were essentially unchanged from those for virgin loading of the field samples.

Loading frequency has been shown to affect the secant shear modulus (G) and ξ of organic soils (Stokoe et al. 1996; Kramer 1996; Boulanger et al. 1998; Kramer 2000). These studies were consistent in showing that G generally increased by about 10% over each log-cycle increase in

loading frequency (f). Damping ratios, however, were more complicated since they tended to decrease with an increase of f up to about 0.1 Hz and then increase with an increase of f above 0.1 Hz (Kramer 2000). These effects may be more fundamentally related to strain rate ($\dot{\gamma}$) (e.g., Isenhower and Stokoe 1981), which is a function of both γ_c and f, but the limited range of $\dot{\gamma}$ (and f) in the existing data for these soil types makes any such interpretations difficult.

Testing of reconstituted specimens also showed that $G_{\max}$ was more closely correlated to major principal consolidation stress than to other stress parameters (Wehling et al. 2003).

Kishida et al. (2009) synthesized the above results, supplemented by reinterpretation of some of the test results from Wehling et al. (2003). They produced predictive equations for $G/G_{\max}$ and D relationships conditional on shear strain amplitude, organic content, and initial effective overburden pressure. Figure 3.9 shows representative trends produced by those equations. Important features of this model are that it indicates a relatively small effect of effective consolidation stress (contradictory to previous findings from Wehling et al (2003) and Kramer 2000, as shown in Figure 3.8) and a large effect of organic content. The divergent views of the effects of effective consolidation stress, even among recent papers from the same group of researchers at UC Davis, represents a significant and unresolved source of epistemic uncertainty for this important set of soil properties.

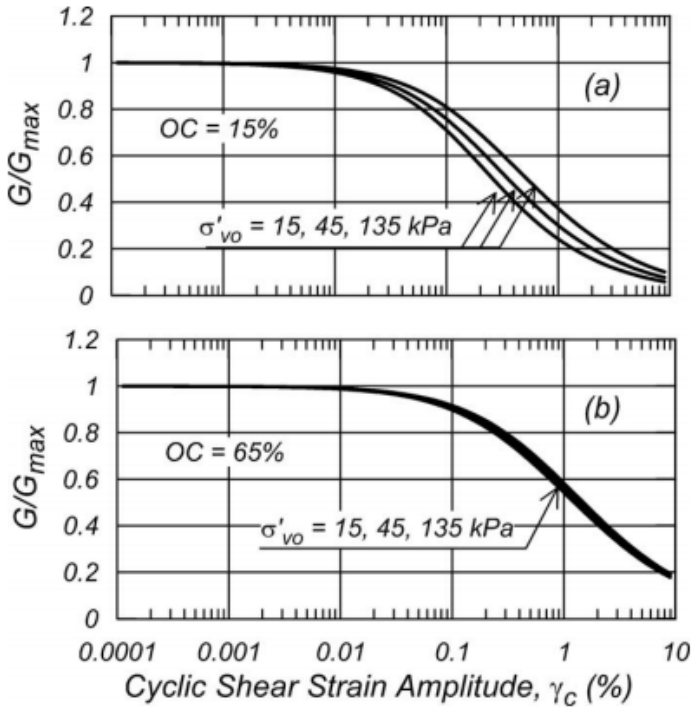

Figure 3.9. Modulus reduction curves for organics soils as a function of organic content and confining stress (Kishida et al. 2009)

3.5 POST-CYCLIC BEHAVIOR

Post-cyclic behavior of soil in a general sense refers to several phenomena, all related to the generation of excess pore pressure (Δu) during undrained cyclic loading of saturated materials. One phenomenon is post-cyclic volume change as the excess water pressures return to hydrostatic over time. Another phenomenon is strength loss associated with the reduced effective stress that accompanies pore pressure increase and, in some cases, cyclic degradation of the soil fabric. To our knowledge, despite the previous testing of dynamic properties described in the previous section, no previous research has specifically evaluated the post-cyclic volume change

behavior of peaty organic soils. Regarding post-cyclic shear strength, the only prior work that we have been able to identify was a study by Yasuhara (1994), who showed that post-cyclic undrained shear strength of Akita peat is a function of excess pore water pressure at the end of cyclic loading (Fig. 3.10). A major objective of this research is to begin to fill these knowledge gaps related to post-cyclic behavior. In the remainder of this section, we describe aspects of post-cyclic behavior observed for other materials such as clays and sands, to provide context for the peat results presented in subsequent chapters.

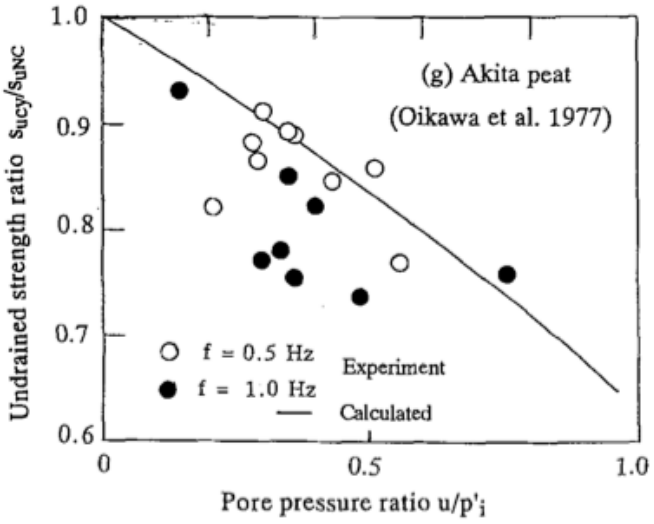

Figure 3.10. Decrease in post-cyclic shear strength with excess pore pressure (S_{ucy}: post-cyclic undrained shear strength; S_{uNC}: undrained shear strength of normally consolidated peat; u: excess pore pressure; p'_i: initial effective consolidation pressure) (Yasuhara 1991)

Pore pressures generated by cyclic loading are quantified by excess pore pressure ratios, $\Delta u/\sigma'_{vc}$. Dissipation of the generated pore pressure causes volume change and consolidation settlement of the soil following initial cyclic loading, and may also influence secondary compression. In loose sandy soils, post-liquefaction settlement has been studied well, since,

large post-liquefaction ground deformation has been known to occur and cause heavy damage to various structures, for example during the 1964 Niigata earthquake, the 1983 Nihonkai-Chuba earthquake and the 1995 Hyogoken Nambu earthquake. Classical procedures for prediction of volume change from post-cyclic reconsolidation of sands were presented by Tokimatsu and Seed (1987) and Ishihara and Yoshimine (1992). Both of these procedures are based on the fundamental premise that volume change is related to the amplitude of cyclic shear strains (or the peak strain in a broadband time series), the number of strain cycles or duration of shaking, and the soil's relative density. Tokimatsu and Seed (1987) developed their predictive model based on input parameters of magnitude-corrected cyclic stress ratio and SPT N-value of the sand. As shown in Figure 3.11, charts were presented for estimating settlements using these parameters, and the results were shown to compare favorably with settlements observed at six sites for which good data on settlements were observed. As shown in Figure 3.12, Ishihara and Yoshimine (1992) developed their model as a function of factor of safety against liquefaction and either relative density or overburden-normalized penetration resistance (CPT or SPT). More recent models extend prior results by considering fines contents up to 20% (Shamoto et al., 1998) or by considering testing of an additional clean sand material (Monterey No. 0/30; Wu and Seed, 2004).

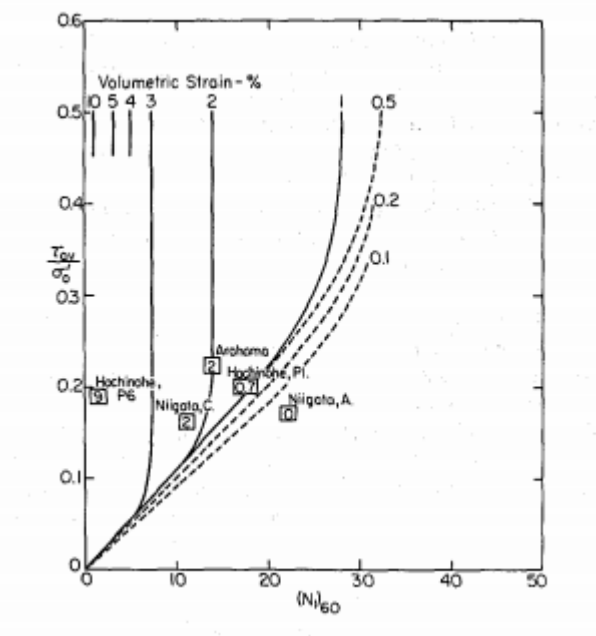

Figure 3.11. Post-cyclic volumetric strain in clean sands as a function of magnitude-corrected cyclic stress ratio, and SPT N-value (Tokimatsu and Seed 1987)

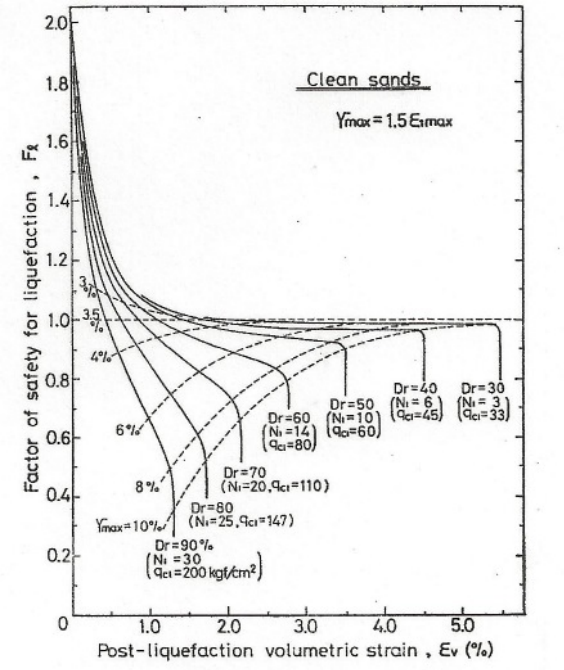

Figure 3.12. Chart for determining volumetric strain as a function of factor of safety (Ishihara and Yoshimine 1992)

Post-cyclic volume change behavior of saturated clays has received less attention. In the case of clays, the recompression settlements after cyclic loading continue over a long time. As shown in Fig. 3.13, initial confining pressure (p_c') (point A) will reduce to a value of p' (point B) because of the pore pressure (Δu) induced during undrained cyclic loading. Subsequent dissipation of pore pressure would lead to void ratio change (Δe_{vr}) and settlement. The value of effective pressure upon the completion of reconsolidation is p_c' (point C). Consolidation behavior of clays is better understood than for sands, and the isotropic consolidation line is known to be approximately a straight line in e-lnp' space. This framework provides a means for estimating post-cyclic reconsolidation strains following undrained loading. The key unknown parameter for the implementation of this procedure is the excess pore pressure ratio that can be expected in the clay as a result of undrained loading.

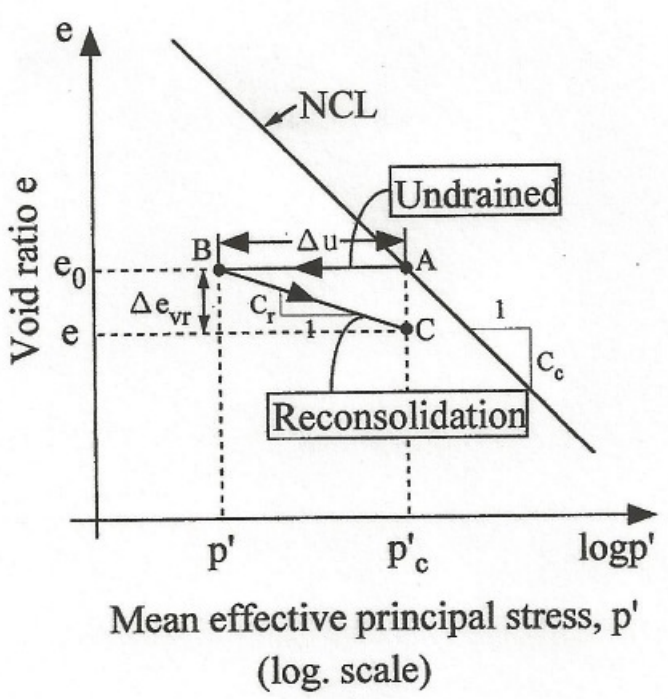

Figure 3.13. Reconsolidation settlement due to dissipation of cyclic-induced pore pressure (Yasuhara et al. 2001)

As expected by the framework describe above, Hyodo et al. (1988) and Yasuhara et al. (1992) showed that the volume changes are dependent on magnitude of generated excess pore pressure but are not dependent on other details of the undrained loading (sequencing, duration, etc.) (Fig. 3.14). Similarly, Matsuda et al. (2000) showed when a clay is subjected to the multi-directional shear strain, the larger the phase difference in the sinusoidal shear strains applied from two directions, the larger the excess water pressure, which in turn increases the settlement in the reconsolidation stage. Yasuhara et al. (2001) presented charts that related post-consolidation settlements to normalized pore pressure, plasticity index and factor of safety against bearing capacity failure.

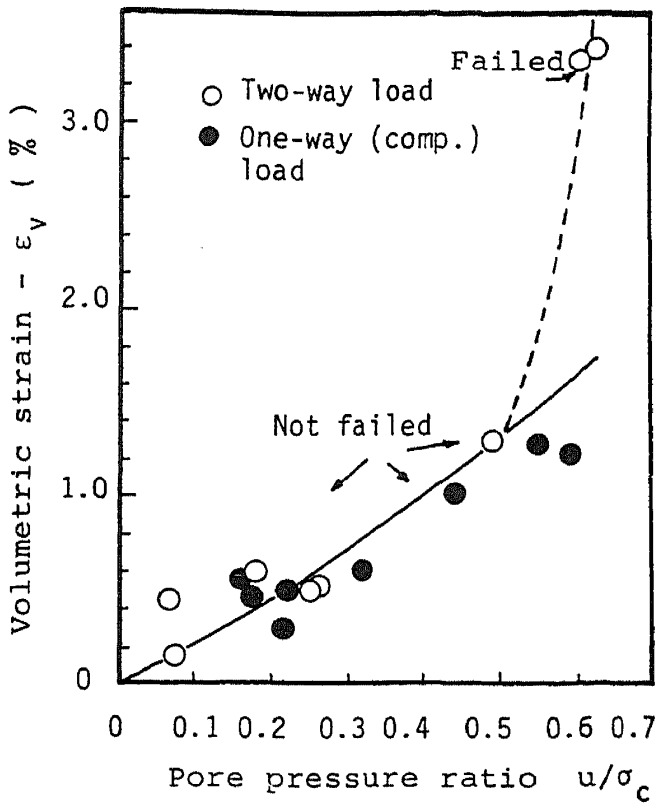

Figure 3.14. Relation between post-cyclic volumetric strain and induced pore pressure (Hyodo et al. 1988)

4 Tested Material and Site Characterization

The Sacramento / San Joaquin Delta consists predominantly of peaty organic soil overlying largely inorganic fluvial deposits. Although much of the Delta organic soil does not classify as "peat" based on its organic content, it is called "peat" herein for convenience, and to comply with local convention. Deposition of the peat began about 7000 years ago based on radio carbon dating performed by Drexler et al. (2007). During the depositional period, the Delta was a tidal marsh with variable salinity based on the flow rate of fresh water through the region. Much of the Delta was submerged daily by tides. During the mid 1800's to early 1900's, the Delta lands were reclaimed for agricultural purposes. Levees were constructed by dredging materials from an adjacent channel and placing the dredged material in an ad-hoc manner. The system of levees formed "islands" from which standing water was pumped to form arable land. Exposing the peat to air resulted in biodegradation and wind erosion, resulting is subsidence of the Delta islands. Many of the islands now lie below sea level, with a maximum amount of 8m.

Following reclamation of Delta lands, attention turned to exporting water for the purpose of irrigating farmland in the San Joaquin Valley, and for urban users in central and southern California via major conveyance systems including the California Water Project. The Delta is now maintained as a fresh-water conveyance system. A certain volume of water must flow into

the San Francisco Bay to prevent saline intrusion, and available water is pumped from the southern edge of the Delta, comprising the principle source for the California Water Project. The Delta ecosystem has significantly changed as a result of reclamation, with many native species such as the Delta Smelt becoming endangered, and other invasive species thriving in the Delta. Water resource management in the Delta is highly political, and is a significant issue for California. Central to political debates is the seismic threat to the Delta, which is the focus of this dissertation.

In 2011 and 2012, Reinert et al. (2012) performed a set of field experiments in which a model levee was constructed on the interior of Sherman Island, and shaken using a nees@UCLA eccentric mass shaker (nees.ucla.edu). Fig. 4.1 shows a map of the site where their testing was performed, and Fig. 4.2 is a photo of the model levee with the eccentric mass shaker mounted on top. Details of the field testing lie beyond the scope of this dissertation, but certain aspects related to site characterization are relevant. The site was characterized using the following techniques: (1) cone penetration testing was performed at three locations located just outside the access gate, (2) spectral analysis of surface waves measurements were performed between the model levee and the access gate, and (3) a total of 9 boreholes were hand-augered, and 24 Shelby tube samples were retrieved from depths ranging from approximately 1 to 6 *m* using a special piston sampler fabricated specifically for sampling peat. Details on the sampling procedures are provided subsequently in this chapter.

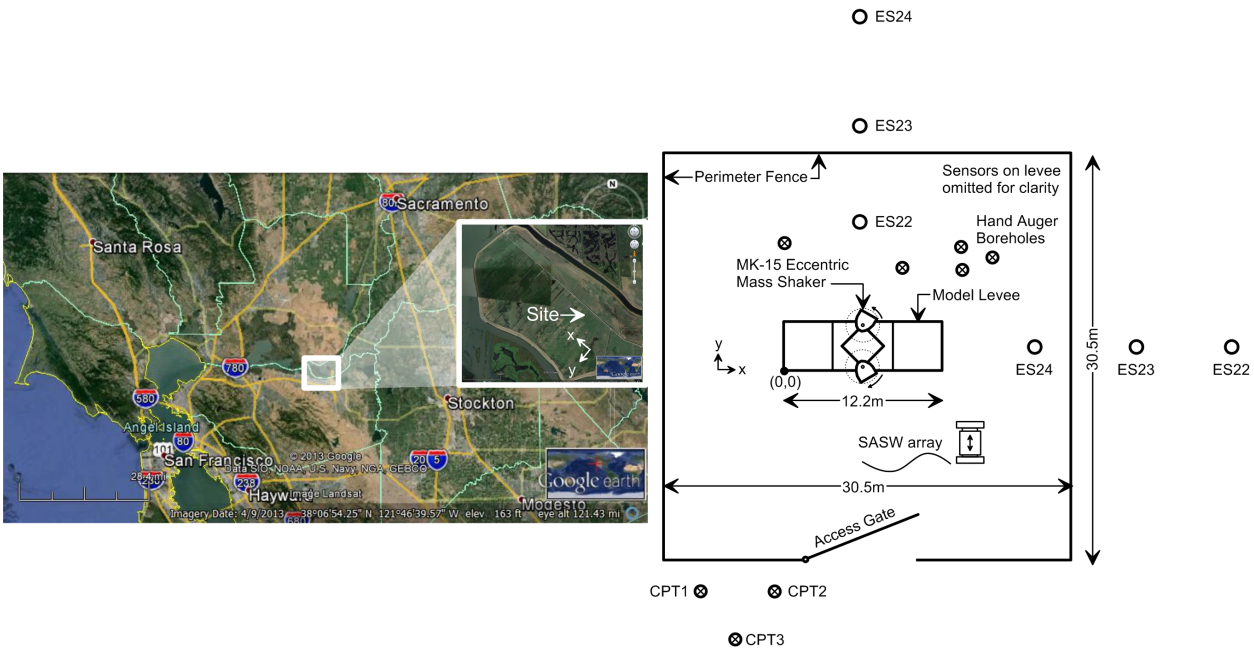

Figure 4.1. Map of Sherman Island test site (Reinert et al. 2012).

Figure 4.2. Eccentric mass shaker mounted atop model levee (Reinert et al. 2012).

4.1 CONE PENETRATION TEST MEASUREMENTS

Fig. 4.3 shows the results of the three CPT soundings performed just outside the access gate shown in Fig. 4.1. These tests were performed on September 12th and 13th, 2012. CPT soundings had previously been performed on August 2, 2011, but the recorded data were of poor quality

due to a grounding problem with the data acquisition system. These poor quality data are not presented here.

The CPT soundings identify three distinct strata within the depth of the investigation: (1) a 2*m*-thick upper crust layer, (2) an underlying 9*m* thick layer of very soft peat, and (3) sandy soils underlying the peat with gradually increasing penetration resistance with depth. The upper 2*m* of peat is desiccated due to groundwater pumping to maintain the phreatic surface below the ground surface for agricultural purposes. The 9*m* thick soft layer consists of very soft peat below the groundwater table. This layer has very low (near zero) CPT tip resistance (q_c), and in fact the CPT rod string had to be held up with pipe wrenches when the clamp on the hydraulic press was released to prevent the rod string from penetrating into the peat under its own weight. The soil beneath the peat has soil behavior type (SBT) primarily in the "Sand mixtures" category. The pore pressure measured in the peat is higher than hydrostatic, which could either be caused by the undrained response of the peat during CPT testing, or by artesian pressures. The presence of artesian pressures were verified by a dissipation test near the bottom of the peat deposit, which indicated excess pore pressures more than 50 *kPa* above hydrostatic. The artesian pressures are believed to be caused by hydraulic connection between the sand layer and the adjacent channel, which lies approximately 5*m* above the surface of the test site, and approximately 7*m* above the groundwater elevation at the test site.

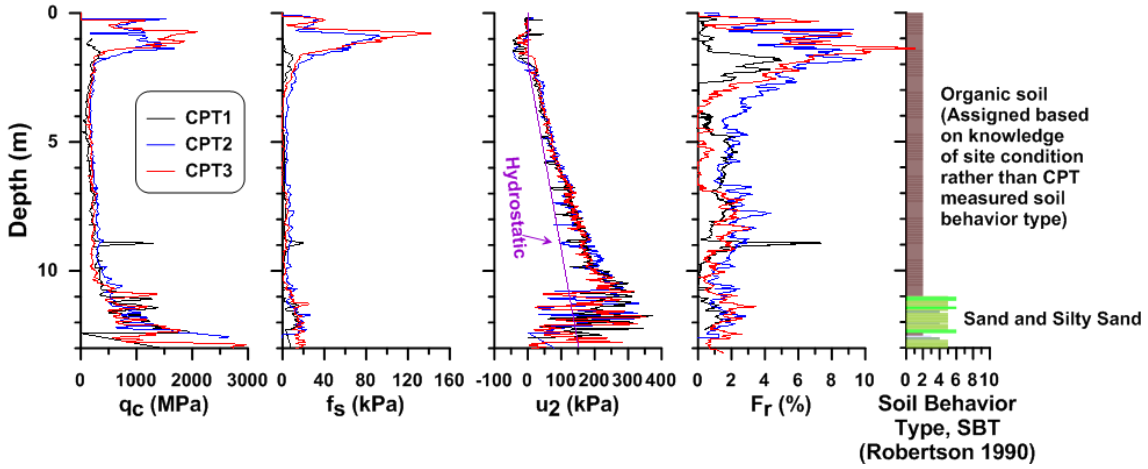

Figure 4.3. Cone penetration test results from three soundings performed in Sherman Island (Reinert et al. 2012)

4.2 RAYLEIGH WAVE DISPERSION CURVE

On August 24th 2011, the research team performed spectral analysis of surface waves (SASW) testing using a vertical shaker and triaxial Episensor accelerometers on the surface of the peat. Fig. 4.4 shows the experimental configuration and the resulting phase velocity dispersion curve. Dispersion curves were computed using two different input signals to the shaker: (i) a fast sweep that could easily be processed in the frequency domain, and (ii) a step sweep in which the frequency was increased in 1 *Hz* increments and maintained at each frequency for 10 *s* to reach a steady state response. The benefit of the fast sweep is that a fast Fourier transform can be computed for the entire signal, and phase lag can be computed in the frequency domain. The down side is that noise in the signals at low frequency translates to significant measurement noise in the computed phase velocity. The step sweep signals, on the other hand, was analyzed in the time domain by fitting harmonic functions in a least-squares sense to the measured data, and computing phase lag between the curve fit signals at adjacent frequencies. This approach attenuates

noise by averaging over the multiple cycles of loading, which produces a better dispersion curve at low frequencies.

As shown in Figure 4.4, the two dispersion curves agree very well at frequencies higher than 15 *Hz*, but the fast sweep dispersion curve exhibits more noise at lower frequencies. The phase velocity at low frequency is under 30 *m/s*. Furthermore, the phase velocity at higher frequency approaches 60 *m/s*, which likely corresponds to higher mode Rayleigh waves propagating inside the desiccated crust. We did not perform an inversion of the dispersion curve to obtain a shear wave velocity profile due to complexities associated with multi-mode response.

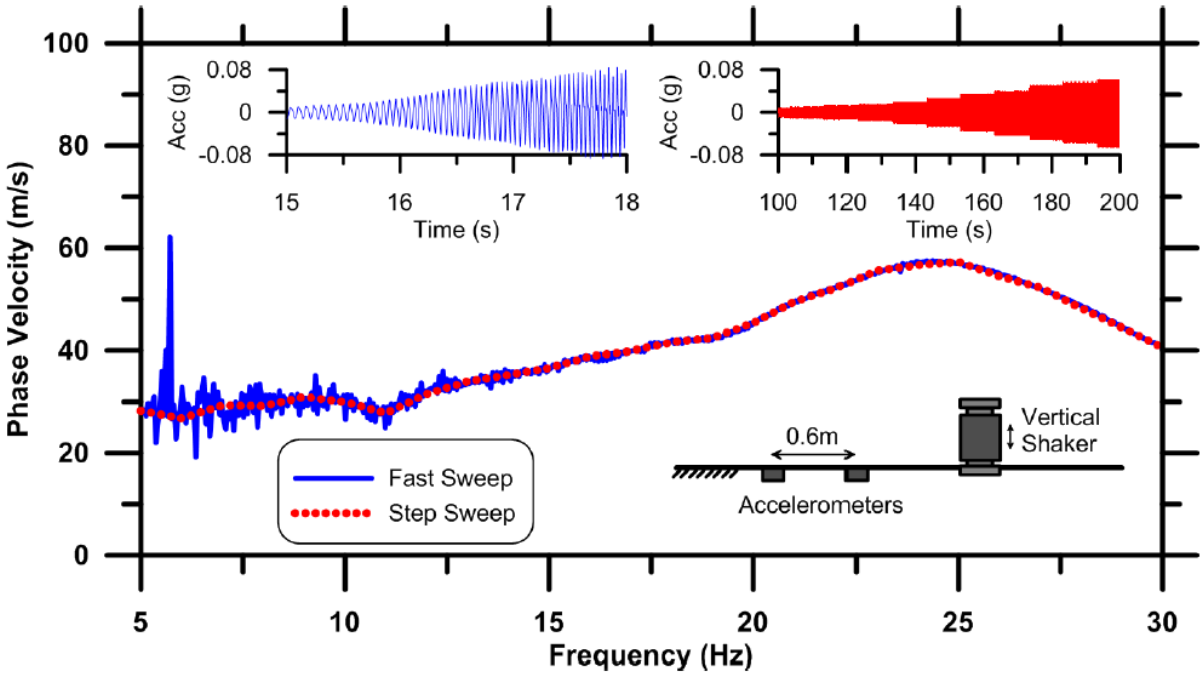

Figure 4.4. Spectral analysis of surface waves results (Reinert et al. 2012).

4.3 RETRIEVAL OF SHELBY TUBE PISTON SAMPLES

To retrieve samples of adequate quality for laboratory testing, a piston sampler was designed and constructed to be utilized with a hand auger operation. This technique does not require any machine power and works manually, and is only feasible for extremely soft ground. The main components of the system include a Shelby tube which is attached to external rods, a piston that is attached to all-thread rods and which fits into the Shelby tube, and all-thread rods that pass through external rods (see Fig. 4.5).

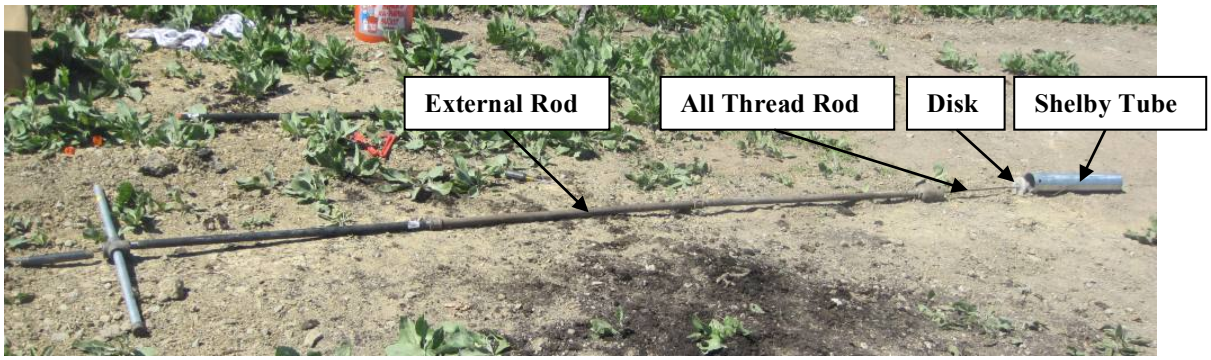

Figure 4.5. Components of undisturbed sampling system

A borehole is drilled utilizing a hand auger (Fig. 4.6) to the lesser of the desired depth, or the depth where the borehole squeezes shut. For cases where the borehole remains open (to depths of approximately 2 to 3 *m*), the piston is fixed at the bottom of the Shelby tube, which is lowered into the borehole and set on the soil at the desired depth. The piston is then released and the Shelby tube is then pushed gradually into the ground while the piston is held stationary. When the Shelby tube is filled with soil, water is added to the top of the piston to maintain suction over the sample (Fig 4.7) when the tube is extracted from the ground. Finally, the Shelby tube is extracted with the piston locked in place. For cases where the borehole does squeeze shut (i.e., below a depth of 3 *m*), the piston was locked in place near the end of the Shelby tube using a locking nut (Fig. 4.8), and the sampler was pushed by hand through the peat to the desired depth.

This is only possible in extremely soft soil, and would be unimaginable in sand or even in normally consolidated clay. However, the Sherman Island peat is so soft that two people could easily push the sampler as deep as about 6 m with the piston locked near the end of the Shelby tube. When the sampler had been pushed to the desired depth, the piston was unlocked, the sampler was pushed, water was poured on top of the piston, and the sampler was extracted with the piston again locked in place.

The piston provides suction to the sample when the Shelby tube is pulled out of the ground, and results in sample recovery without significant disturbance. We obtained full recovery for every sample using this technique. Other researchers who have not used piston samplers had to push the Shelby tube a distance that was longer than the tube in order to compress the peat inside the tube so it would stay in the tube during extraction (e.g., Tim Wehling personal communication 2001). This approach results in compression of the peat and sample disturbance. The present piston sampler configuration was designed to avoid this problem.

Figure 4.6. Hand auger

Figure 4.7. The rod is filled with water to keep suction over the sample. The all thread rod is attached to the piston at the bottom of the borehole.

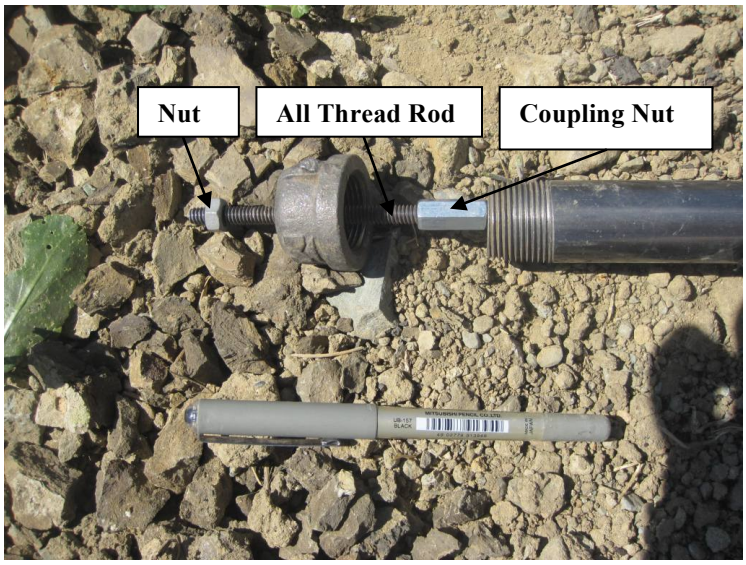

Figure 4.8. All thread rod fixed in-place by a nut and a coupling nut

4.4 INDEX PROPERTIES AND IN-SITU WATER CONTENT

Index tests performed on the peat samples include organic content and specific gravity. Atterberg limits tests could not be performed on the peat due to its fibrous nature. Organic content was measured in the UCLA lab by burning peat in a muffle furnace up to $440^{\circ}C$ according to the ASTM D 2974-00 (ASTM 2010) test method *C*. Organic content versus depth is plotted in Fig. 4.9, which shows that the organic content is highest at a depth of 2*m*, ranging from 60 to 80%, and decreases with depth, becoming as low as 8% at a depth of 5.5*m*. Photos of peat with high organic content and low organic content are shown in Figs. 4.10 and 4.11. The highly organic content peat is black in color, and has visible fibers. The peat transitions to a grey color at 5.5*m* similar to Bay Mud.

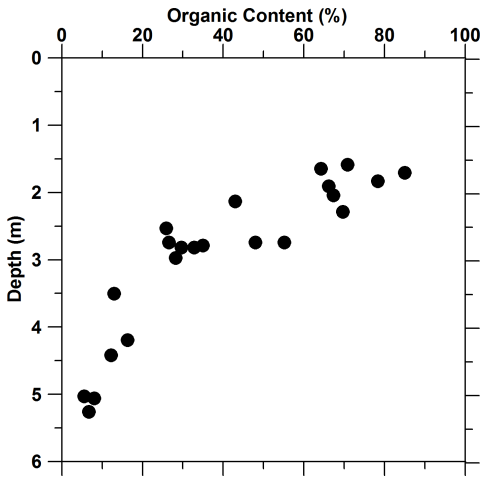

Figure 4.9. Organic content profile in Sherman Island

Figure 4.10. High organic content peat with visible fibers

Figure 4.11. Low organic content peat

The specific gravity (G_s) of the peat was measured based on ASTM D 854-06 (ASTM 2010), while the entrapped air in the soil was removed by boiling. There are some errors associated with this method. For example, some amount of the peat floats in the pycnometer, but the specific gravity test assumes the solids are denser than water. Furthermore, the peat likely consists of cell structures with entrapped water, and this water may contribute to the specific gravity measurement. As shown in Fig.4.12, G_s decreases as organic content increases, and varies from 1.8 to 2.6. Fig. 4.13 also presents water content (w_0) and bulk unit weight (γ) profiles at the Sherman Island site measured from the undisturbed specimens used in oedometer testing. These results show that water content decreases and bulk unit weight increases with depth, reflecting the effects of decreasing organic content and void ratio.

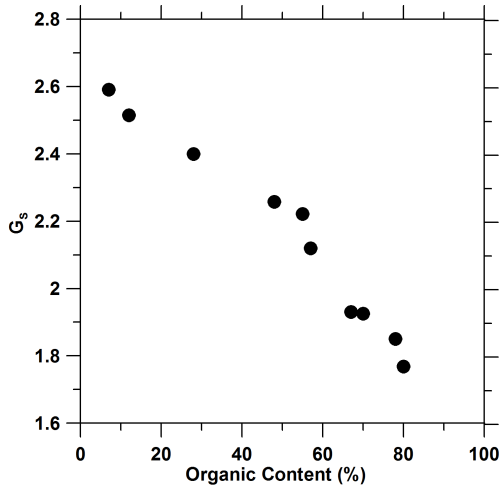

Figure 4.12. Specific gravity of the Sherman Island peat

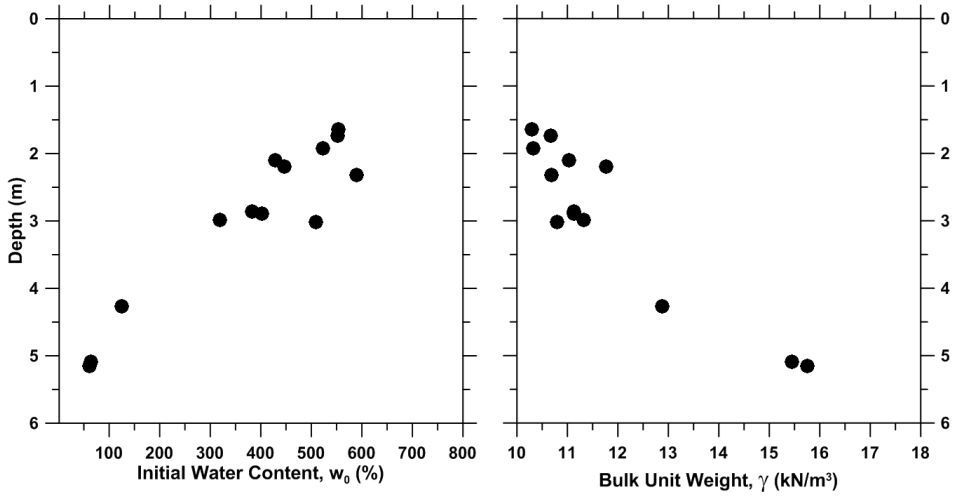

Figure 4.13. Water content and bulk unit weight profile in the Sherman Island

4.5 LABORATORY EXPERIMENTS OF MECHANICAL PROPERTIES

The principle purpose of obtaining tube samples of peat was for high quality laboratory testing of relatively undisturbed as well as reconstituted Sherman Island peat specimens. Results of these tests are presented in Chapters 5 and 6. The test sequence included:

1. Consolidation testing with Load Increment Ratios (*LIR*=load increment/current vertical load on the soil, $\Delta\sigma_v/\sigma_{vo}'$) of 1 and less than 1 to evaluate compressibility parameters (C_c, C_r), coefficient of consolidation (c_v), and secondary compression index (C_α). Tests with *LIR*<1 were performed to establish a fundamental problem with the traditional interpretation of secondary compression, and set the stage for an alternative stress-space based interpretation. An innovative consolidation cell was developed to facilitate this work in which it is possible to measure pore water pressure at the bottom of the specimen while drainage occurs through the top. Measuring pore pressure is important for distinguishing the "end" of primary consolidation, and therefore distinguishing the volume change fraction associated with primary consolidation from that associated with secondary compression.

2. Monotonic consolidated-undrained simple shear testing of specimens consolidated to various vertical stresses of approximately $1.5\times\sigma_p'$, $2.5\times\sigma_p'$, and $4.0\times\sigma_p'$ (where σ_p' =preconsolidation pressure from consolidation test) to check whether undrained strengths and mobilized pore water pressures normalize with effective vertical consolidation stress (e.g., Ladd and Foot, 1974; Ladd, 1991). These tests were run under constant height conditions on the UCLA Digitally Controlled Simple Shear (UCLA-DCSS) apparatus as described in Chapter 2 of this dissertation.

3. Cyclic constant volume simple shear tests of specimens consolidated as described in (2) subject to strain-controlled cycles of shear strain amplitudes as large as 10%. These tests comprise one of the critical contributions of this study. Tests on specimens consolidated to consistent vertical stress levels but subject to varying cyclic strain amplitudes enable evaluation of the relationship between shear strain amplitude (γ) and residual pore water pressure ratio (r_{ur}, defined as excess pore pressure at the end of cyclic loading normalized by the initial consolidation stress) as well as shear strain amplitude and post-cyclic volume change (ε_v). Following undrained cyclic shear, specimens were monitored as they re-consolidated to the initial vertical effective stress for a sufficient period of time to evaluate primary consolidation and secondary compression.

4. Cyclic stress-controlled constant volume simple shear tests with $\alpha = \frac{\tau_s}{\sigma_{v0}} > 0$, where τ_s =static shear stress, and σ_{v0}'=initial vertical effective stress. The influence of static shear stress on the excess pore pressure, post-cyclic volume change and secondary compression, and post-cyclic deviatoric creep was investigated through these tests.

5. Post-cyclic monotonic constant volume simple shear tests to investigate the effect of cyclic shear straining on the undrained shear strength.

5 Static Compressibility of Sherman Island Peat

5.1 INTRODUCTION

The compression behavior of peat differs from the compression behavior of other types of soils in two important ways: 1) peat is much more compressible than inorganic soils, and 2) the creep portion of settlement often plays a more significant role in determining the total settlement of peat than of other soil types. As described previously in Chapter 3, the dominant factors controlling the compressibility characteristics of peat include the fiber content, natural water content, void ratio, initial permeability, nature and arrangement of soil particles, and inter-particle chemical bonding in some of the soils (Mesri and Ajlouni, 2007). Primary consolidation of fibrous peat occurs rapidly because its hydraulic conductivity tends to be much larger than inorganic fine-grained mineral deposits. Secondary compression can be large enough to obscure the transition from primary consolidation to secondary compression that is apparent in measurements of height change versus log(time) for inorganic mineral soils.

Oedometer tests were carried out on Sherman Island peat to evaluate its compressibility properties including compression index (C_c), recompression index (C_r), secondary compression index (C_α), coefficient of consolidation (c_v), and hydraulic conductivity (k). A consolidation test with LIR =1 was performed on one specimen from each Shelby tube. Some consolidation tests with $LIR \leq 1$ were also carried out to establish a fundamental problem with the traditional

interpretation of secondary compression, and set the stage for an alternative stress-space-based interpretation. Consolidation tests on reconstituted specimens were performed as well to verify if they could replicate the compressibility properties obtained from testing on undisturbed specimens. In total, 22 consolidation tests were carried out in this study. Tables 5.1 and 5.2 present the consolidation test matrix.

Table 5.1. Consolidation test matrix for undisturbed specimens

Specimen ID	Specimen Depth (m)	LIR	w_0[a] (%)	OC[b] (%)	C_c	C_r	σ'_p[c] *(kPa)*	C_α	C_k[d] (k_{ref}, $e_{k,ref}$)[e]
BH3S1_1.65[f]	1.65	1	553.1	64	6.70	0.57	19.0	0.32	1.98 $(2.87\times10^{-6}, 8.29)$
BH6S2_2.10	2.10	1	429.3	67	2.96	0.17	19.0	0.24	2.03 $(1.12\times10^{-6}, 5.96)$
BH6S5_3.00	3.00	1	509.4	48	3.04	0.30	?	0.29	2.78 $(6.85\times10^{-7}, 7.43)$
BH6S1_4.25	4.25	1	125.4	16	1.20	0.09	10.0	0.10	1.02 $(3.21\times10^{-7}, 2.65)$
BH7S1_2.85	2.85	1	383.0	28	2.20	0.13	?	0.26	1.37 $(2.85\times10^{-7}, 4.77)$
BH7S2_2.90	2.90	≤ 1	402.7	28	N.A.	N.A.	N.A.	N.A.	1.66 $(1.53\times10^{-6}, 6.65)$
BH7S1_5.10	5.10	1	64.2	8	0.49	0.06	12.0	0.03	0.45 $(1.01\times10^{-7}, 1.36)$
BH7S2_5.15	5.15	≤ 1	61.0	8	N.A.	N.A.	N.A.	N.A.	0.43 $(1.00\times10^{-7}, 1.12)$
BH8S1_1.75	1.75	1	551.5	66	5.59	0.47	35.0	0.28	1.73 $(2.85\times10^{-6}, 5.78)$
BH8S2_1.80	1.80	≤ 1	491.2	66	N.A.	N.A.	N.A.	N.A.	1.46 $(3.66\times10^{-8}, 6.25)$
BH8S2_2.20	2.20	1	446.4	69	3.16	0.13	19.0	0.21	1.22 $(2.85\times10^{-6}, 5.78)$
BH9S3_1.90	1.90	1	523.6	78	5.9	0.82	19.0	0.35	2.20 $(2.64\times10^{-7}, 6.56)$
BH9S7_2.30	2.30	1	589.3	57	6.1	0.43	19.0	0.40	2.08 $(1.70\times10^{-7}, 7.67)$
BH9S3_3.00	3.00	1	318.6	30	2.56	0.12	19.0	0.29	1.36 $(1.04\times10^{-7}, 4.23)$

[a]Initial (Natural) Water Content (ASTM D2216-10)

[b]Organic Content (ASTM D2974-14)

[c]Preconsolidation Pressure (ASTM D2435-04)

[d,e]See Fig. 5.1 (k_{ref} in cm/s)

[f]Borhole No.3, Specimen No.1, Depth=1.65 m

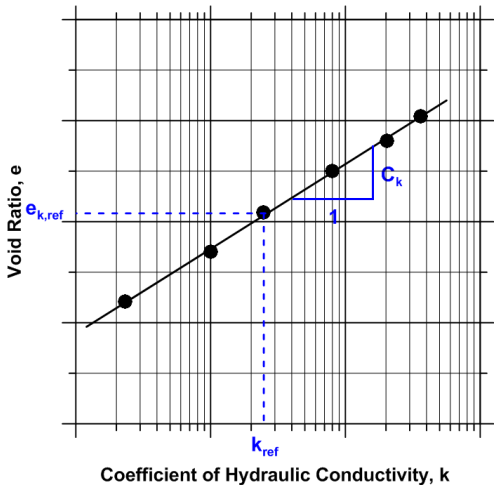

Figure 5.1. Definition of C_k, k_{ref}, and $e_{k,ref}$

Table 5.2. Consolidation test matrix for reconstituted specimens

Specimen ID	Specimen Depth (m)	LIR	w_0 (%)	OC (%)	C_c	C_r	σ'_P *(kPa)*	C_α	C_k (k_{ref}, $e_{k,ref}$)
BH7S8_R	2.75-3.20	1	315.6	28	1.39	0.10	N.A.	0.23	1.64 $(1.38\times10^{-7}, 4.88)$
BH7S9_R	2.75-3.20	≤ 1	318.1	28	2.85	0.20	N.A.	N.A.	1.73 $(2.87\times10^{-6}, 8.29)$
BH7S1_R	5.00-5.50	1	56.7	8	0.42	0.05	N.A.	0.02	0.50 $(8.17\times10^{-8}, 1.15)$
BH8S1_R	1.70-2.15	1	539.1	66	4.2	0.42	N.A.	0.25	1.80 $(5.11\times10^{-6}, 7.26)$
BH8S2_R	1.70-2.15	≤ 1	501.7	66	N.A.	N.A.	N.A.	N.A.	1.46 $(3.66\times10^{-8}, 6.25)$
BH9S1_R	2.60-3.05	1	329.5	30	3.25	0.25	N.A.	0.34	2.12 $(5.07\times10^{-7}, 5.46)$
BH9S2_R	2.60-3.05	≤ 1	339.0	30	N.A.	N.A.	N.A.	N.A.	2.35 $(3.17\times10^{-7}, 4.50)$
BH9S3_R	2.60-3.05	1	312.7	30	N.A.	N.A.	N.A.	N.A.	1.53 $(3.30\times10^{-7}, 5.20)$

5.2 DEVELOPMENT OF NEW CONSOLIDOMETER THAT PERMITS PORE PRESSURE MEASUREMENT DURING CONSOLIDATION

To facilitate accurate evaluation of the end of primary consolidation, we designed and fabricated a new consolidometer that provides single drainage through the top of the specimen, while pore pressure is measured at the bottom (Fig. 5.2). A similar device was utilized for peat by Fox and Edil (1999). This is different from a traditional consolidation device in which drainage is provided at both the top and bottom of the specimen. The measurement of pore pressure at the bottom of the specimen is facilitated by an o-ring seal at the bottom of the specimen ring, and a porous stone at the bottom with diameter smaller than the o-ring seal. A hole drilled through the bottom of the consolidometer is attached to an electrical resistance strain gauge piezometer. The hole and bottom porous stones are pre-saturated prior to placement of the specimen. When a load increment is imposed on the top cap, data is recorded simultaneously from the LVDT and piezometer. The peat is not back pressure saturated, so the measured pore pressure is not likely to be equal to the pore pressure in the specimen due to compressibility of gasses trapped inside the peat and/or the porous stones and line leading to the piezometer. Although the pore pressure measurements may not accurately reflect the pore pressure increase in the peat, we believe the device permits accurate measurement of the time rate of pore pressure dissipation, and thereby provides a much more effective means by which to evaluate t_p than the traditional method based on the height change vs log(time) curve.

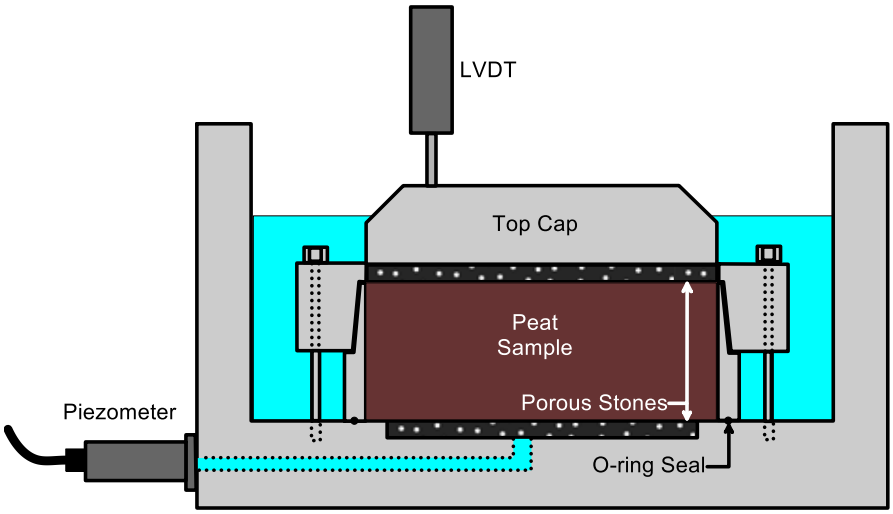

Figure 5.2. Single-drainage consolidometer that permits pore pressure measurement at bottom of specimen

Fig. 5.3 shows an example of data collected using the new consolidation device. In this particular case, a peat sample with an organic content of 66% (BH8S2_1.80) is loaded from an initial vertical effective stress of 52 *kPa* to a final vertical effective stress of 89 *kPa*. The pore pressure increases slowly from about 5 to 11 *kPa* from approximately 0.1s to about 1.0s. The change in pore pressure (Δu) is less than the change in vertical total stress ($\Delta\sigma_v$) because the peat is not completely saturated ($\frac{\Delta u}{\Delta\sigma_v} = \frac{6}{37} = 0.16$; $\frac{\Delta u}{\Delta\sigma_v} = 1.0$ for a fully saturated soil). The pore pressure then dissipates from 1.0 *sec* to about 20 *sec*, when it returns to approximately 4 *kPa*. Although the pore pressure reading provides a clear indication that t_p is near 20 seconds, the LVDT reading (represented here as void ratio rather than displacement) does not show the characteristic "break" in the curve that is traditionally interpreted as the end of primary consolidation in typical consolidation tests. In fact, the rate of void ratio decrease vs log time is actually increasing rather than decreasing at this time (this behavior is common for *LIR* < 1, as explained later). These data clearly demonstrate the benefit of making the pore pressure measurement for the purpose of accurately defining t_p, even though the pore pressure reading

may not be entirely representative of pore pressures within the specimen due to lack of saturation.

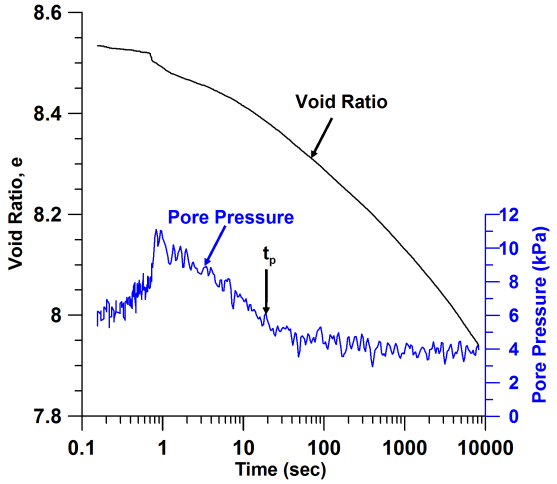

Figure 5.3. Sample data from consolidation device in Fig. 5.1 that clearly shows why pore pressure measurement is necessary for determining end of primary consolidation

5.3 SAMPLE PREPARATION TECHNIQUE AND PROCEDURE FOR OEDOMETER TESTING

Undisturbed specimens for oedometer testing are prepared by extracting the soil sample from the Shelby tube directly into a consolidation ring (Fig. 5.4) with an inside diameter equal to that of Shelby tube (i.e., 72.5 *mm*). During consolidation tests on traditional soil, the sample is often trimmed into a consolidation ring that is smaller than the tube sample to minimize the impact of sample disturbance that invariably occurs at the interface between the soil and the sampling tube. However, the specimens were not trimmed into a smaller ring in this case because the fibrous nature of the peat makes trimming difficult, and less sample disturbance occurred when the specimen was simply extruded directly into the consolidation ring. After extruding the specimen

into the 25.4*mm* tall ring, the top and bottom were leveled with a wire blade, the specimen was carefully placed inside the consolidometer, and consolidation testing was performed.

Figure 5.4. Consolidation ring

Consolidation tests were also performed on reconstituted specimens that were prepared from peat slurry in the lab. Peat trimmings and consolidation specimens that had already been tested were stored in buckets of water, forming a peat slurry. Reconstituted samples were prepared by first pouring the peat slurry into a Shelby tube, and subsequently placing an aluminum piston inside the Shelby tube, exerting a small vertical pressure near 10 *kPa* (Fig. 5.5). Following primary consolidation under this pressure, the sample was carefully extracted into the consolidation ring (Fig. 5.4) in the same manner as the relatively undisturbed field specimens, and then placed inside the consolidometer. The vertical pressure of 10 kPa was found to adequately consolidate the peat so that it could be extruded from the Shelby tube. Lower pressures resulted in peat samples that were too fluid to extrude in a controlled manner.

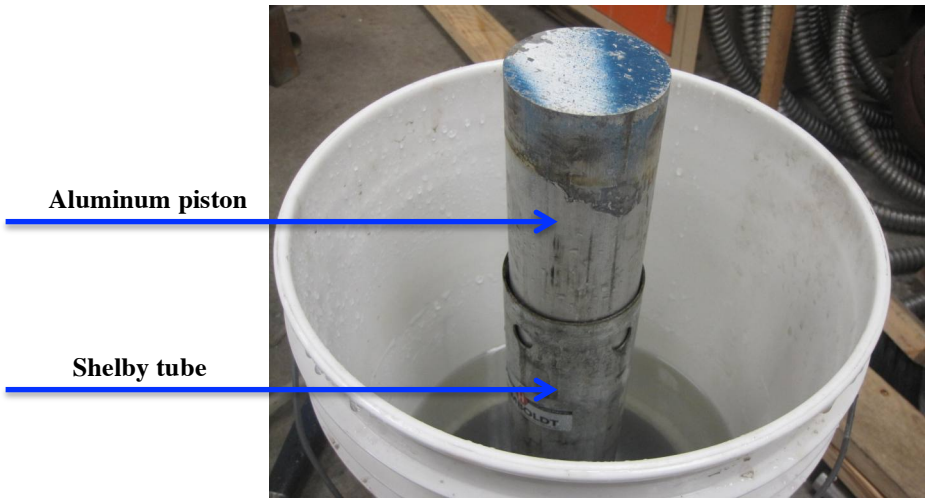

Figure 5.5. Set-up for preparing reconstituted specimens; aluminum piston exerts 10 *kPa* on peat

5.4 CONSOLIDATION TESTS WITH LIR=1

The oedometer tests with LIR=1 were carried out to find static compressibility properties of the Sherman Island peat. Figs. 5.6 to 5.21 summarize the test results, showing void ratio (e) versus vertical effective stress (σ'_v) on a logarithmic ($\log_{10}$) scale, e versus coefficient of hydraulic conductivity (k) on a log scale, and coefficient of consolidation (c_v) versus average vertical effective stress ($\sigma'_{v,avg}$) (log scale) for the stage corresponding to the measurement of c_v. Note that calculation of c_v inherently assumes that the peat follows Terzaghi's one-dimensional consolidation theory, which is subsequently demonstrated to be untrue. Nevertheless, the values of c_v are useful for characterizing the secant behavior of the peat for each load step. The values of k and c_v have been calculated for the loading and unloading stages, and were based on Taylor's method (1948). These values were also verified using Casagrande's method (1940), particularly for the tests in which pore water pressure was measured to enable reliable evaluation

of t_p. The values of e_{avg} and $\sigma'_{v,avg}$ were obtained by taking the average of void ratios and effective vertical pressures at the beginning (prior to loading) and end of the stage.

Values of c_v for normally-consolidated load stages were observed to decrease as vertical effective stress increases, often by more than two orders of magnitude over the stress range tested in the consolidometer. This behavior is the result of a combination of factors. First, the hydraulic conductivity decreases significantly as void ratio decreases, often spanning more than two orders of magnitude. Note that c_v is linearly proportional to k, hence, the decrease in hydraulic conductivity decreases c_v. Second, soil compressibility, $a_v = -de/d\sigma'_v$ tends to decrease as effective stress increases. Note that c_v is inversely proportional to a_v, hence a decrease in a_v would result in an increase in c_v. Within the range of stresses tested in the consolidometer, the permeability response exerts more influence on c_v than the compressibility response, resulting in c_v decreasing as σ_v' increases.

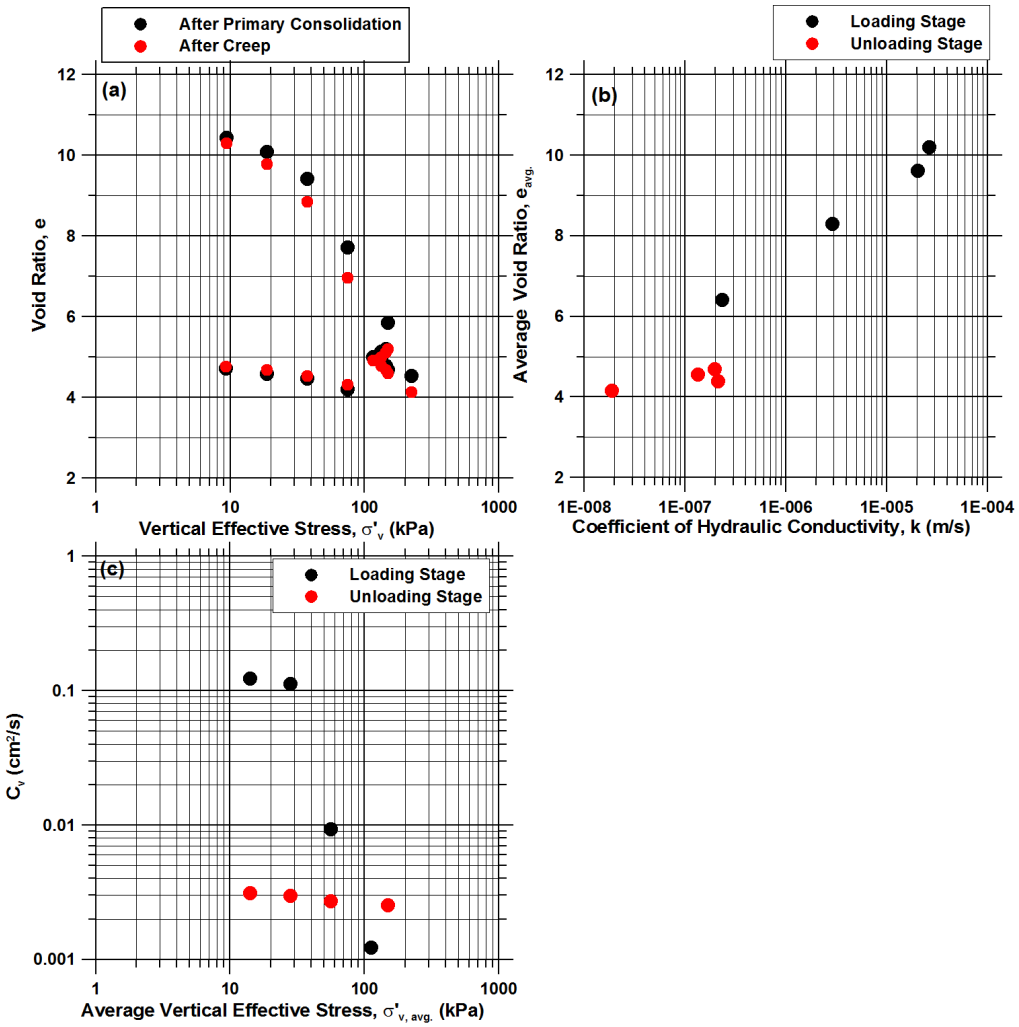

Figure 5.6. Oedometer test results for BH3S1_1.65, OC=64%

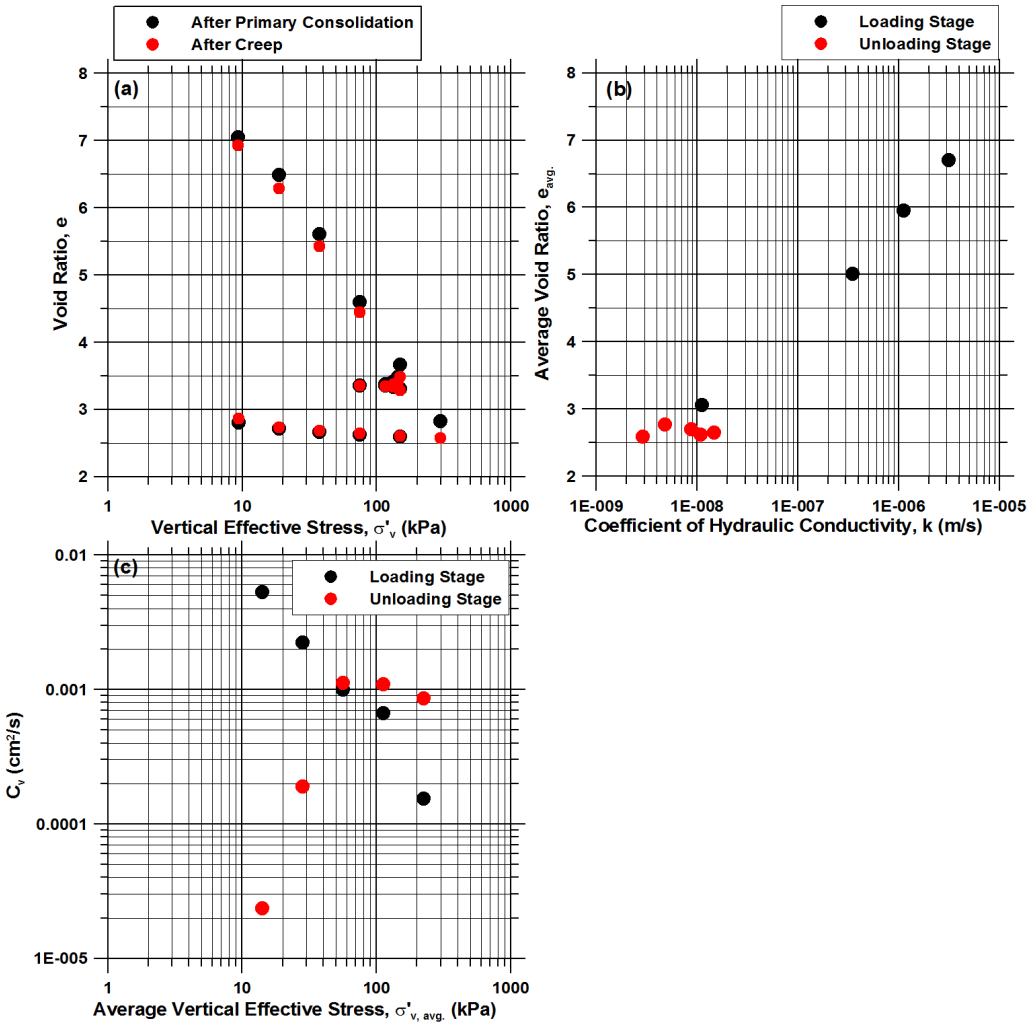

Figure 5.7. Oedometer test results for BH6S2_2.10, OC=67%

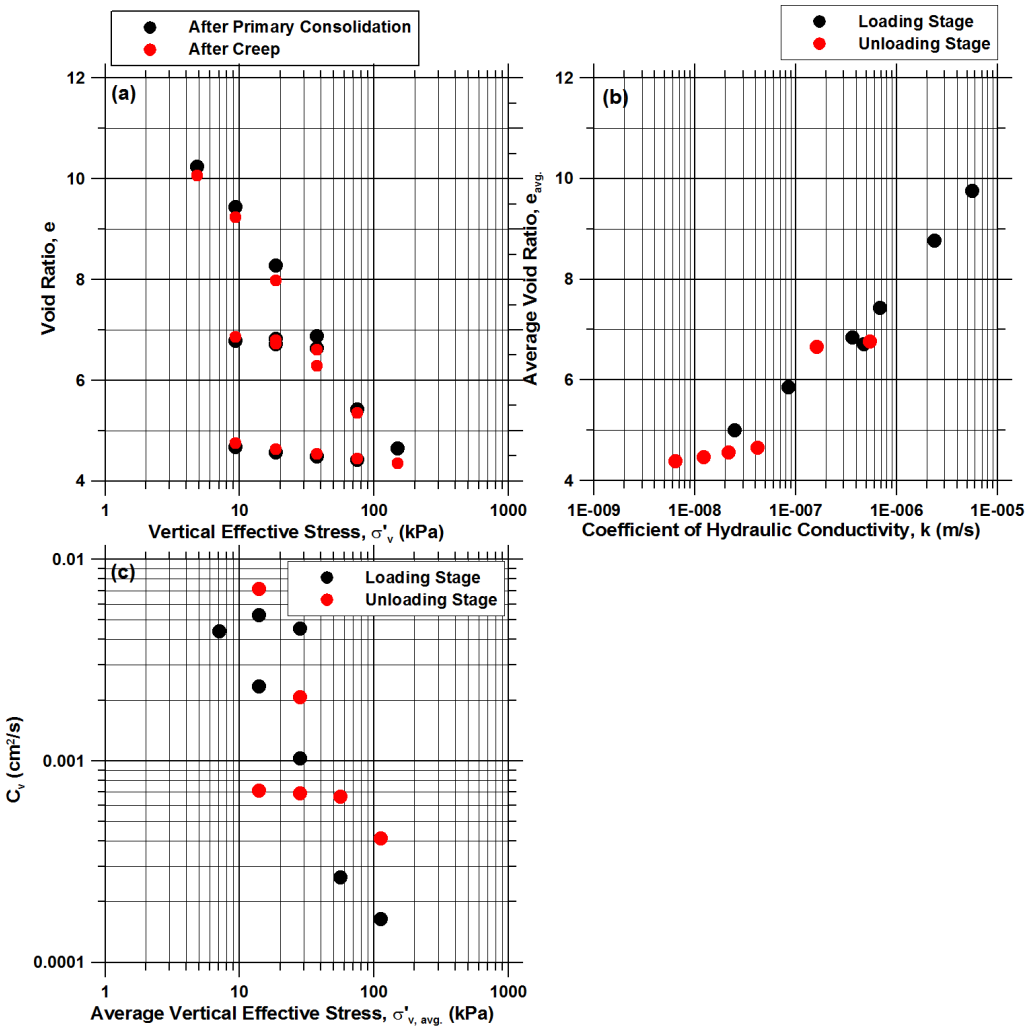

Figure 5.8. Oedometer test results for BH6S5_3.00, OC=48%

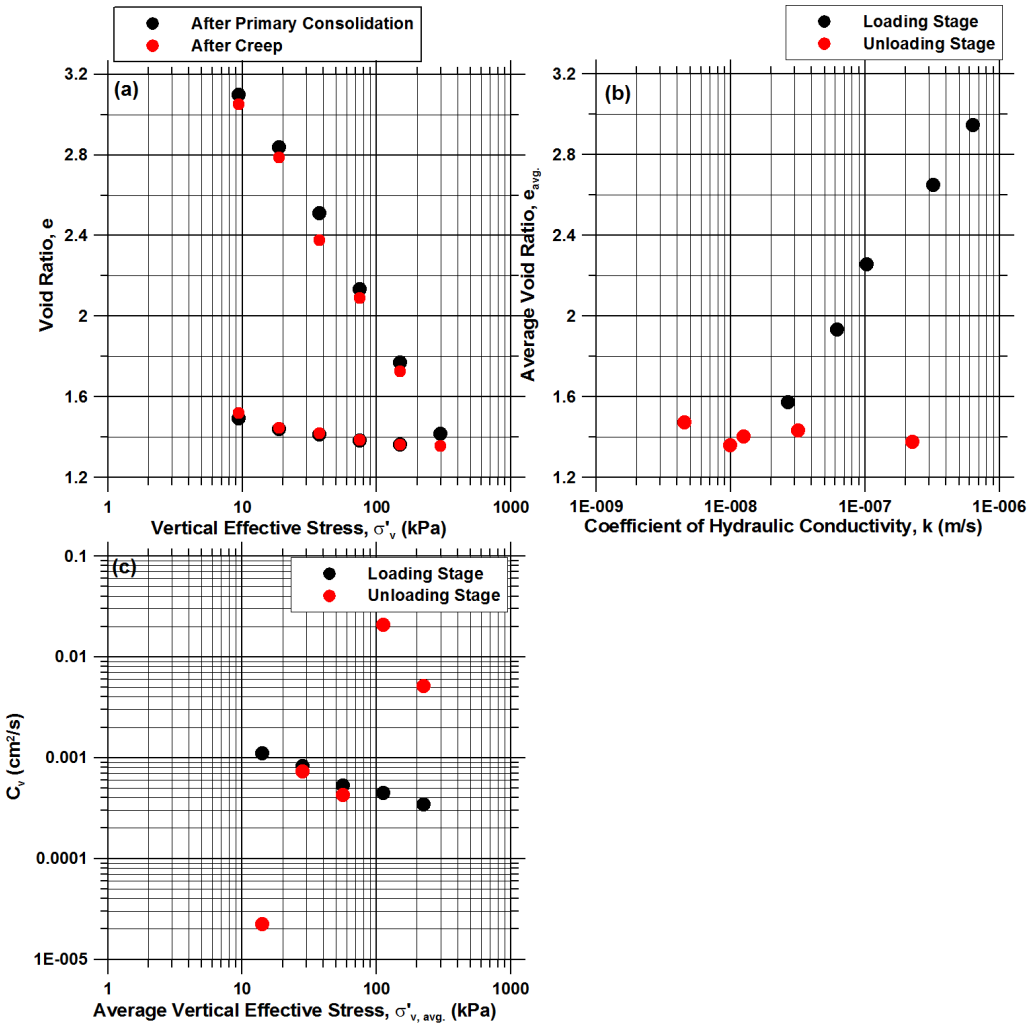

Figure 5.9. Oedometer test results for BH6S1_4.25, OC=16%

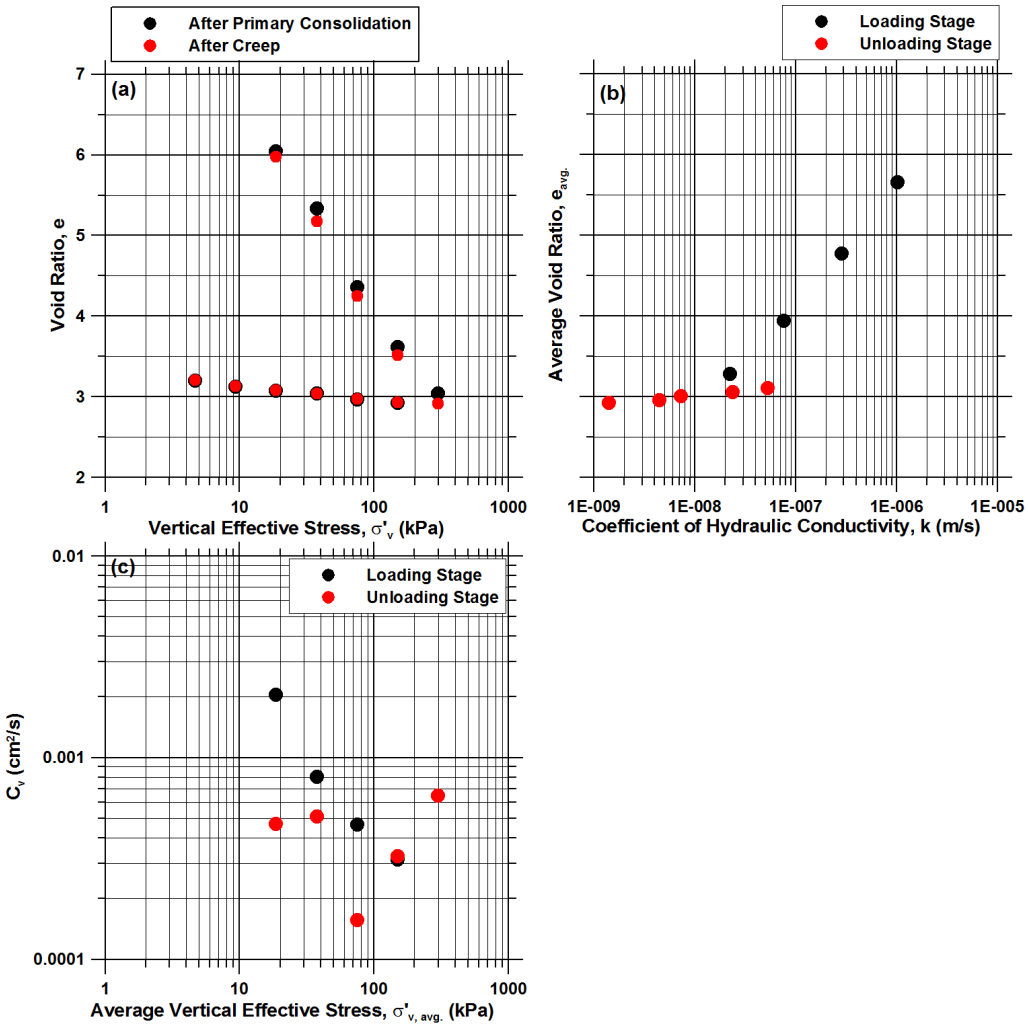

Figure 5.10. Oedometer test results for BH7S1_2.85, OC=28%

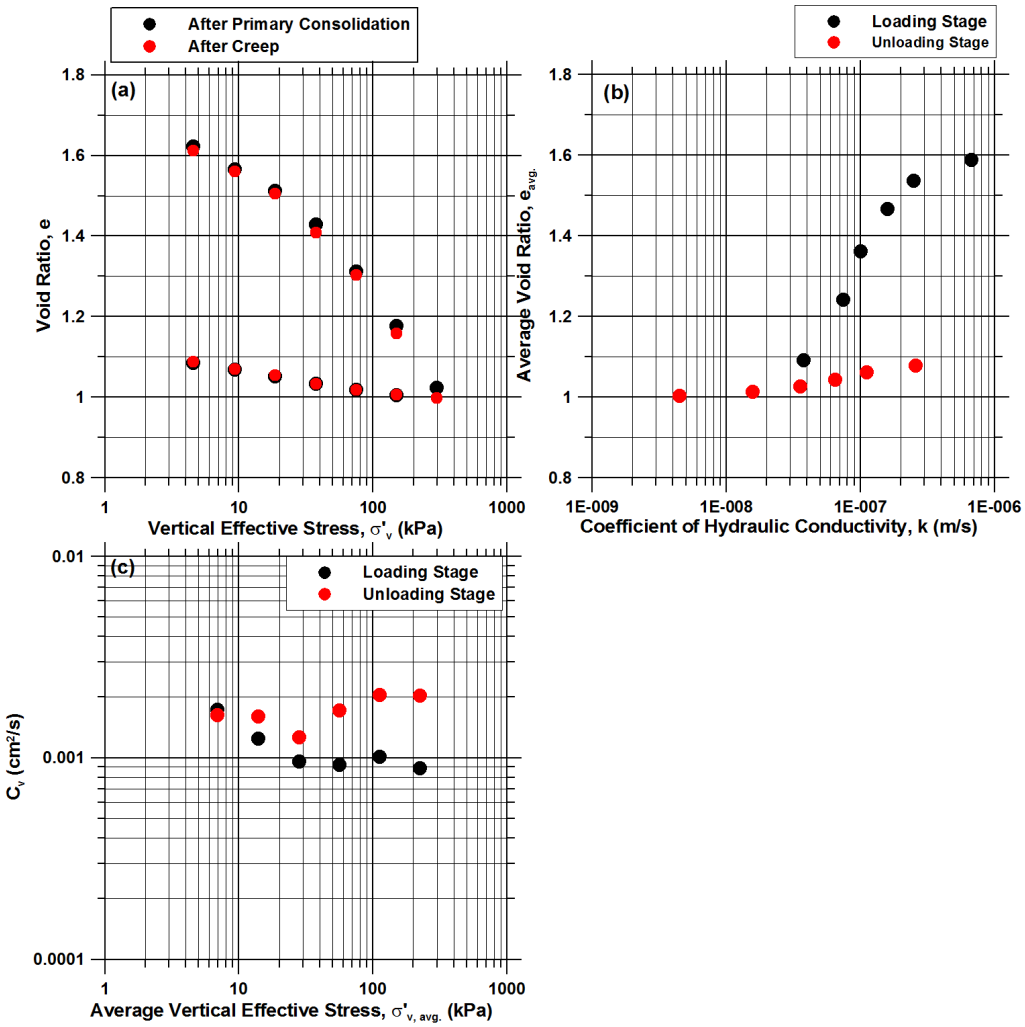

Figure 5.11. Oedometer test results for BH7S1_5.10, OC=8%

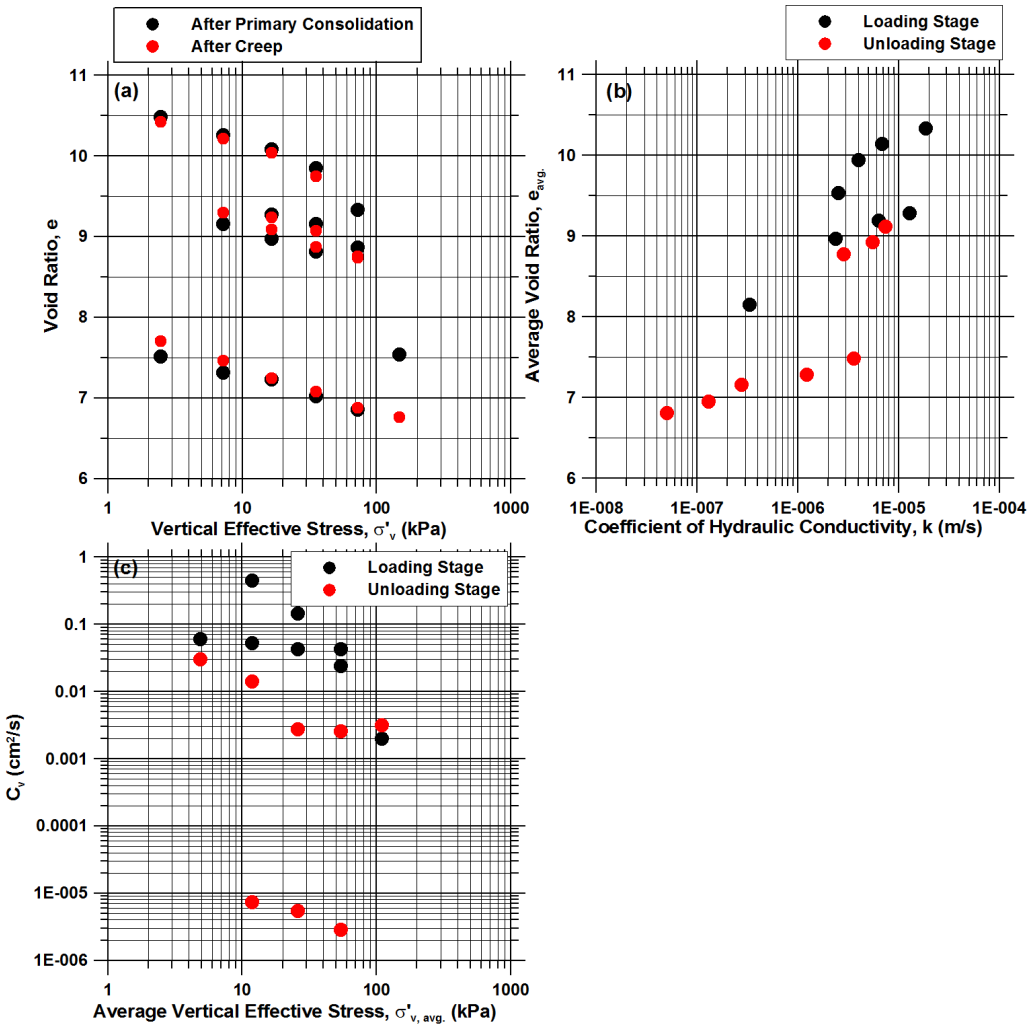

Figure 5.12. Oedometer test results for BH8S1_1.75, OC=66%

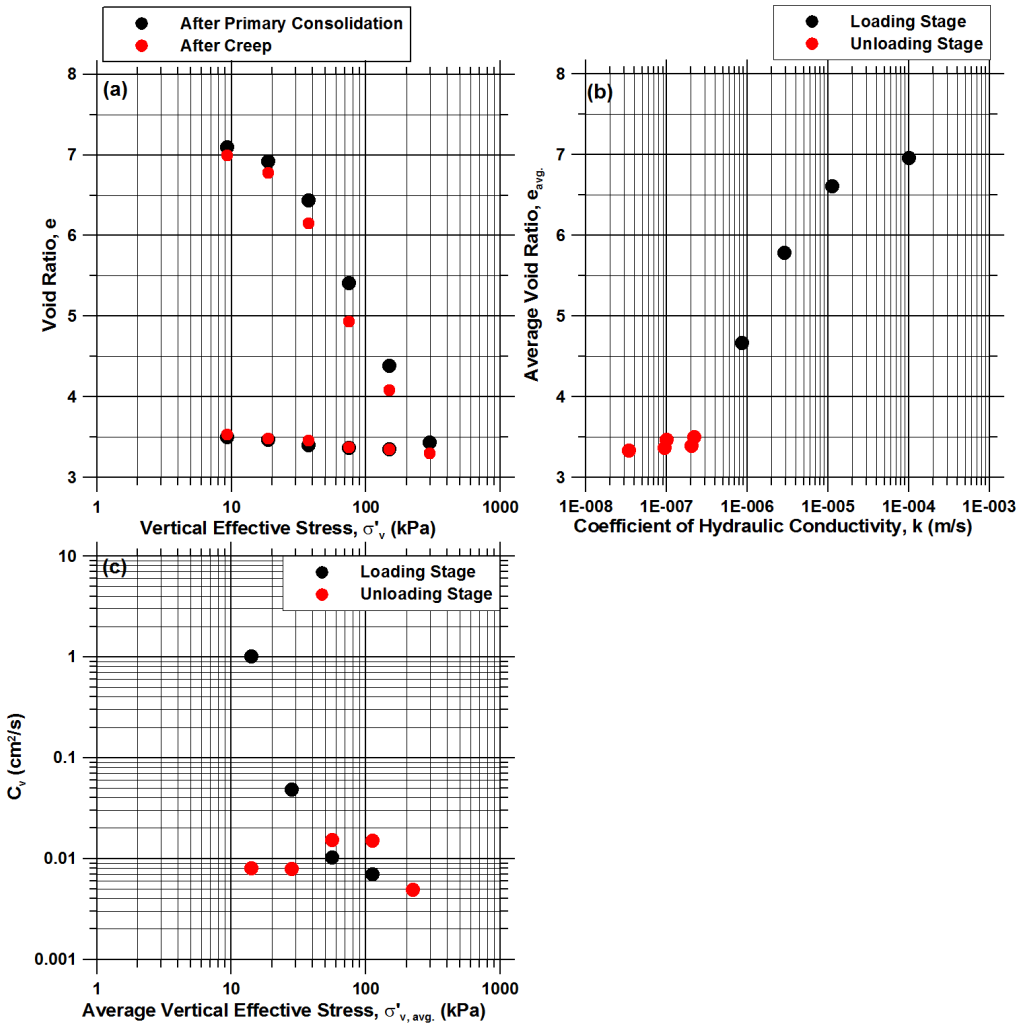

Figure 5.13. Oedometer test results for BH8S2_2.20, OC=69%

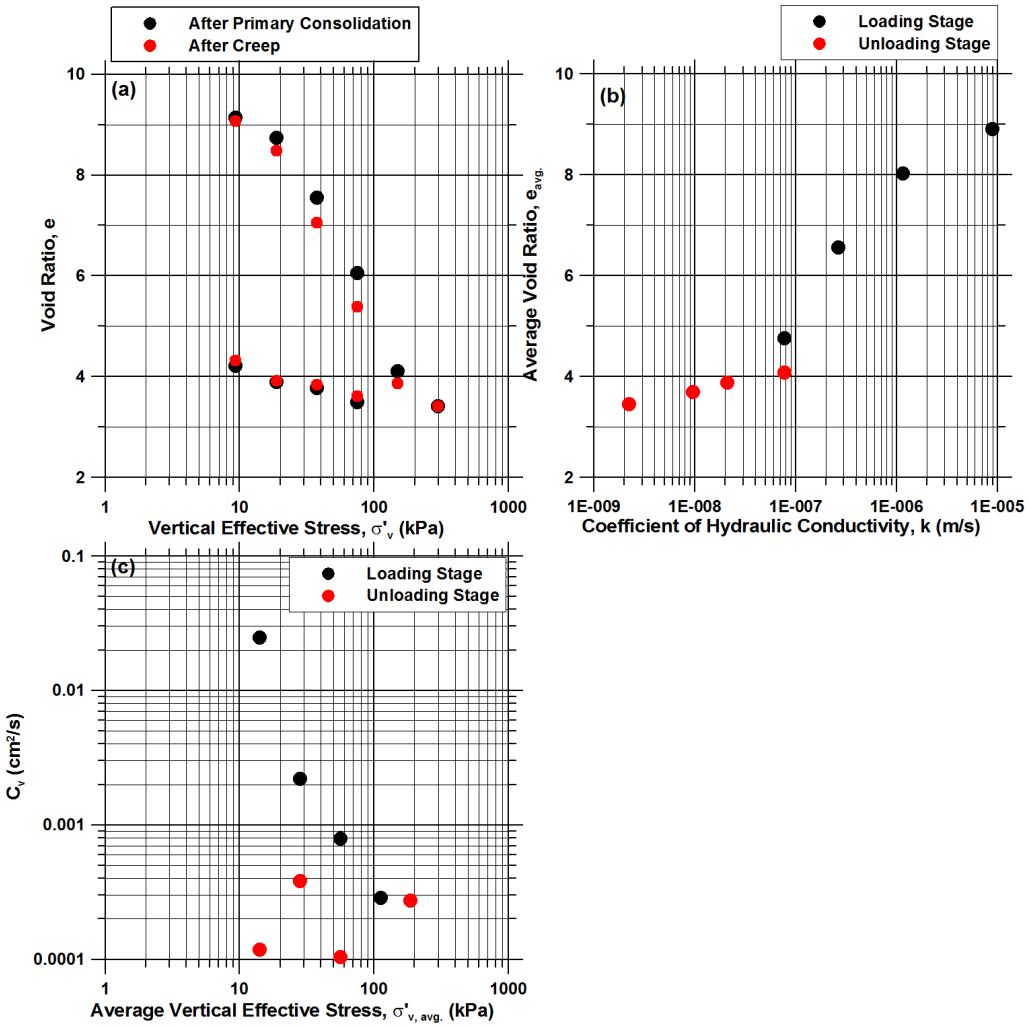

Figure 5.14. Oedometer test results for BH9S3_1.90, OC=78%

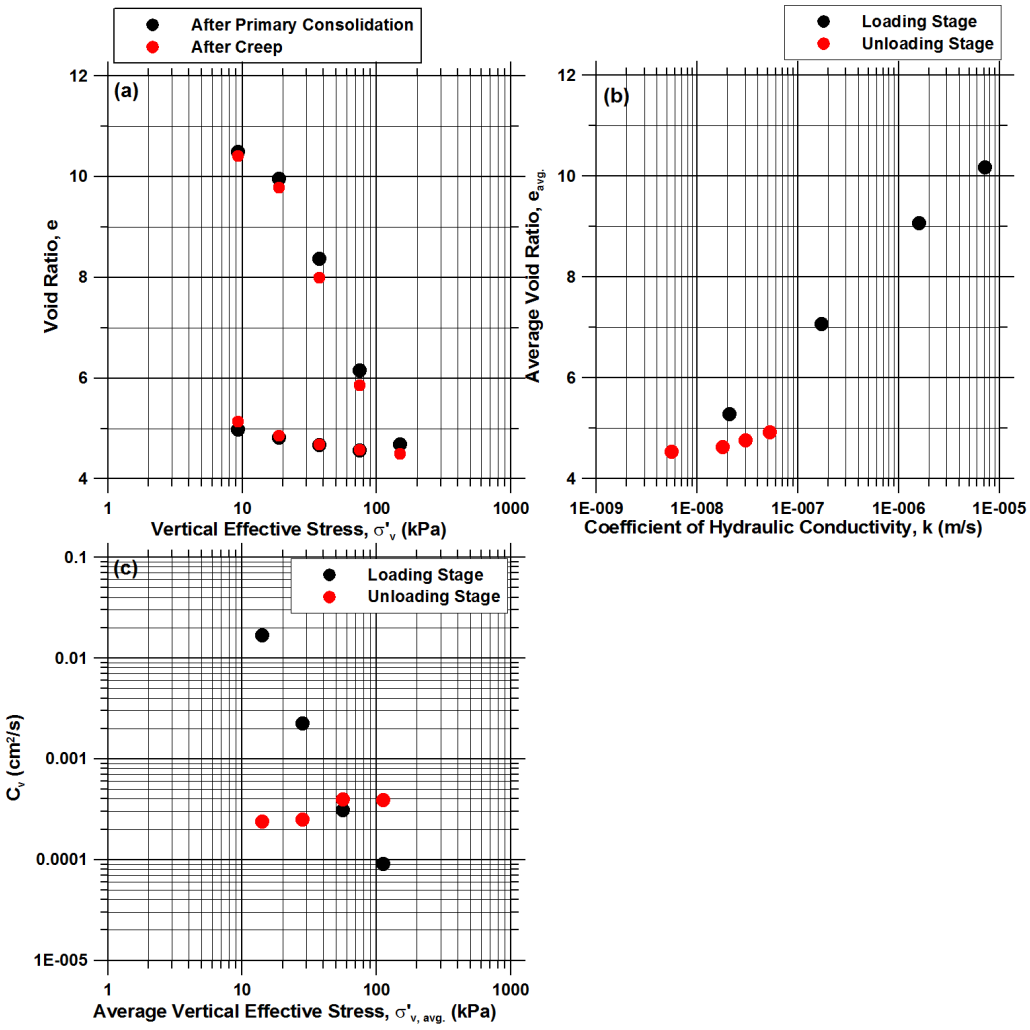

Figure 5.15. Oedometer test results for BH9S7_2.30, OC=57%

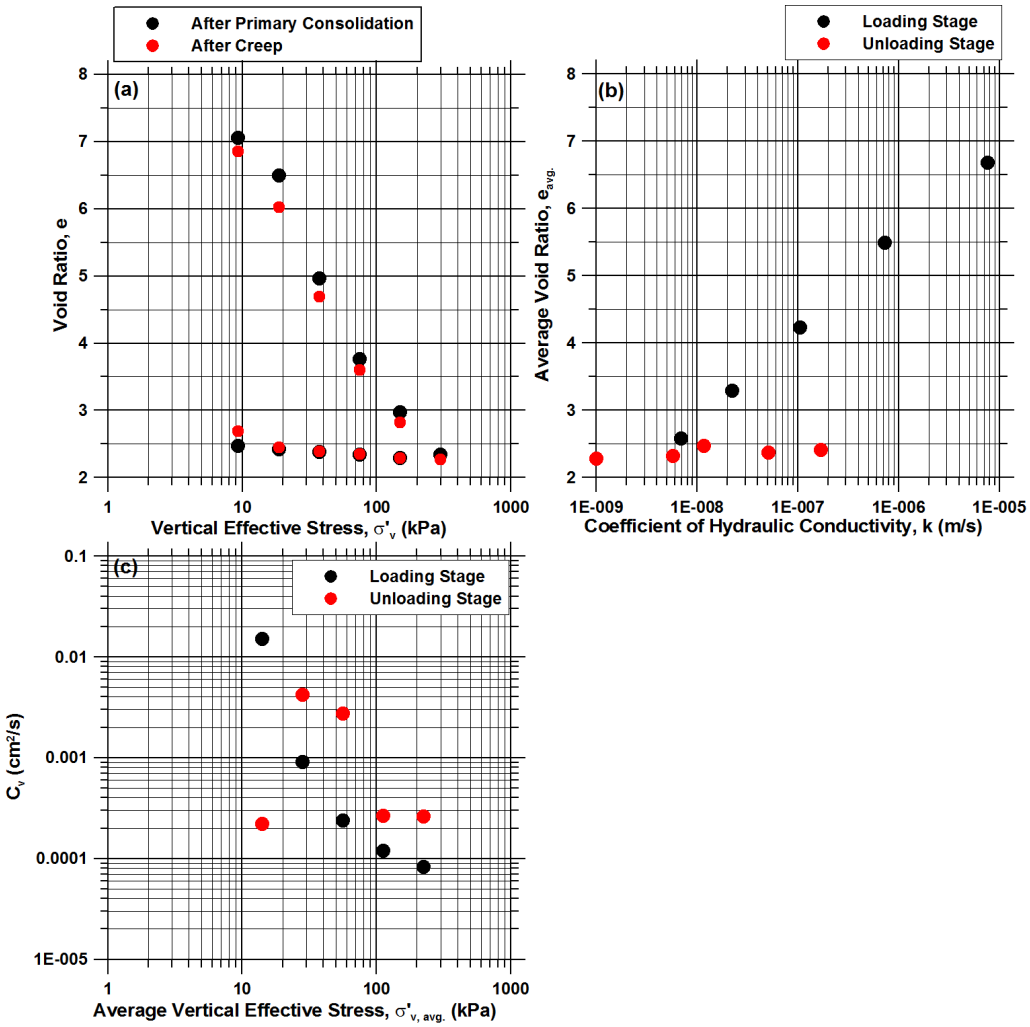

Figure 5.16. Oedometer test results for BH9S3_3.00, OC=30%

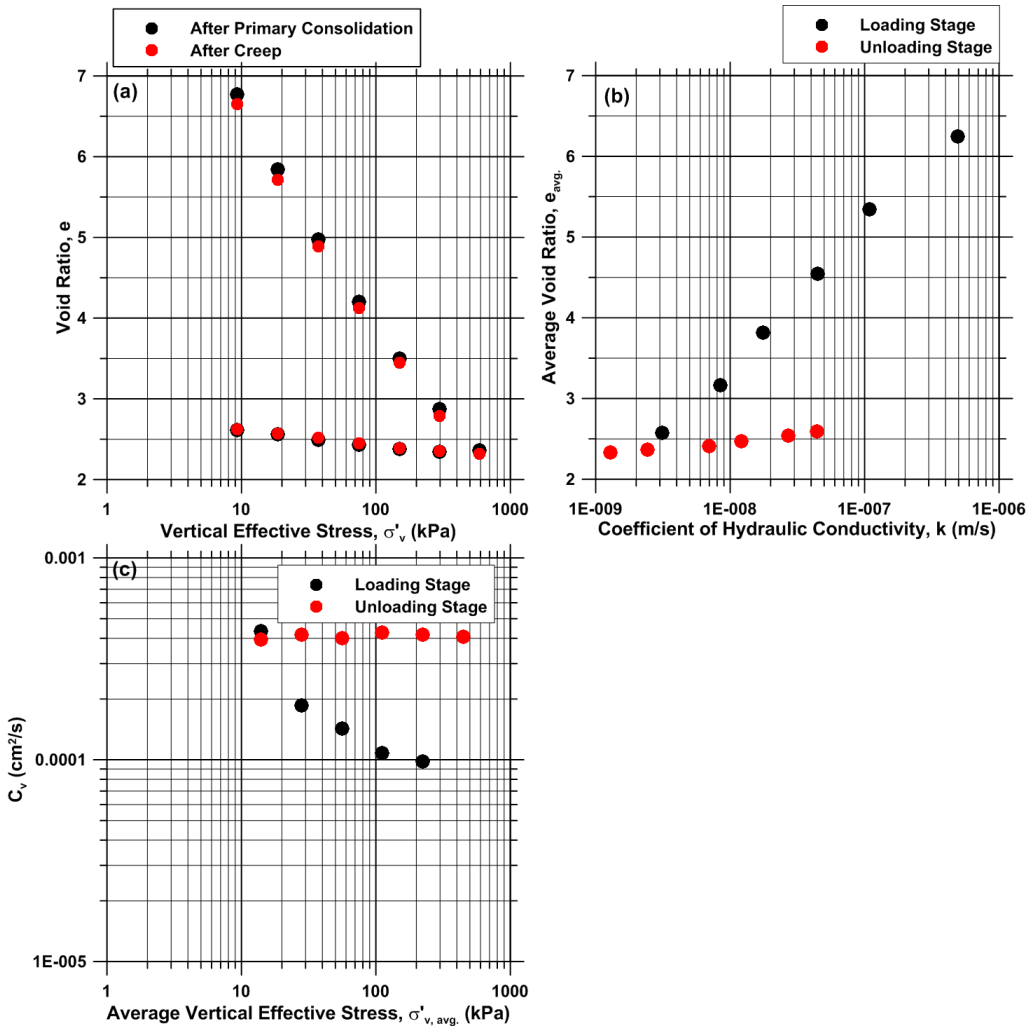

Figure 5.17. Oedometer test results for BH7S8_R, OC=28%

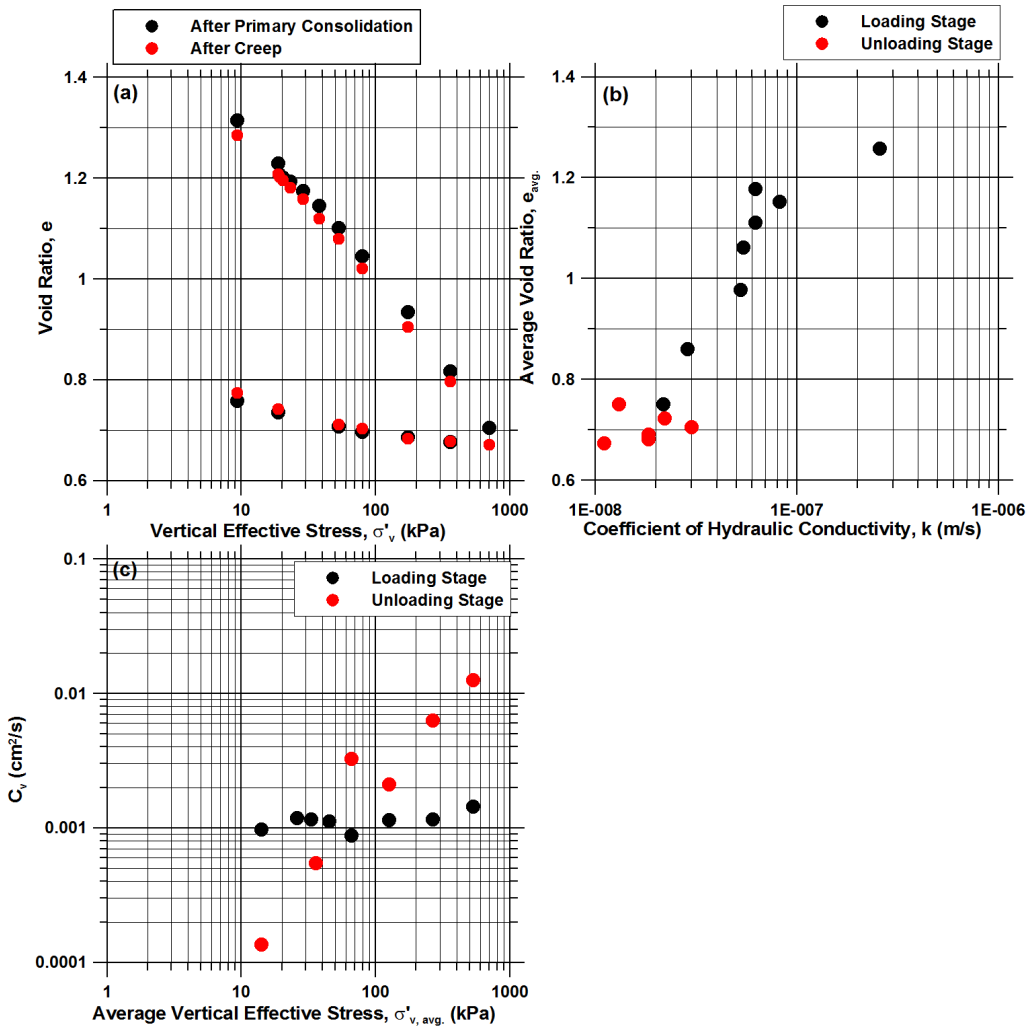

Figure 5.18. Oedometer test results for BH7S1_R, OC=8%

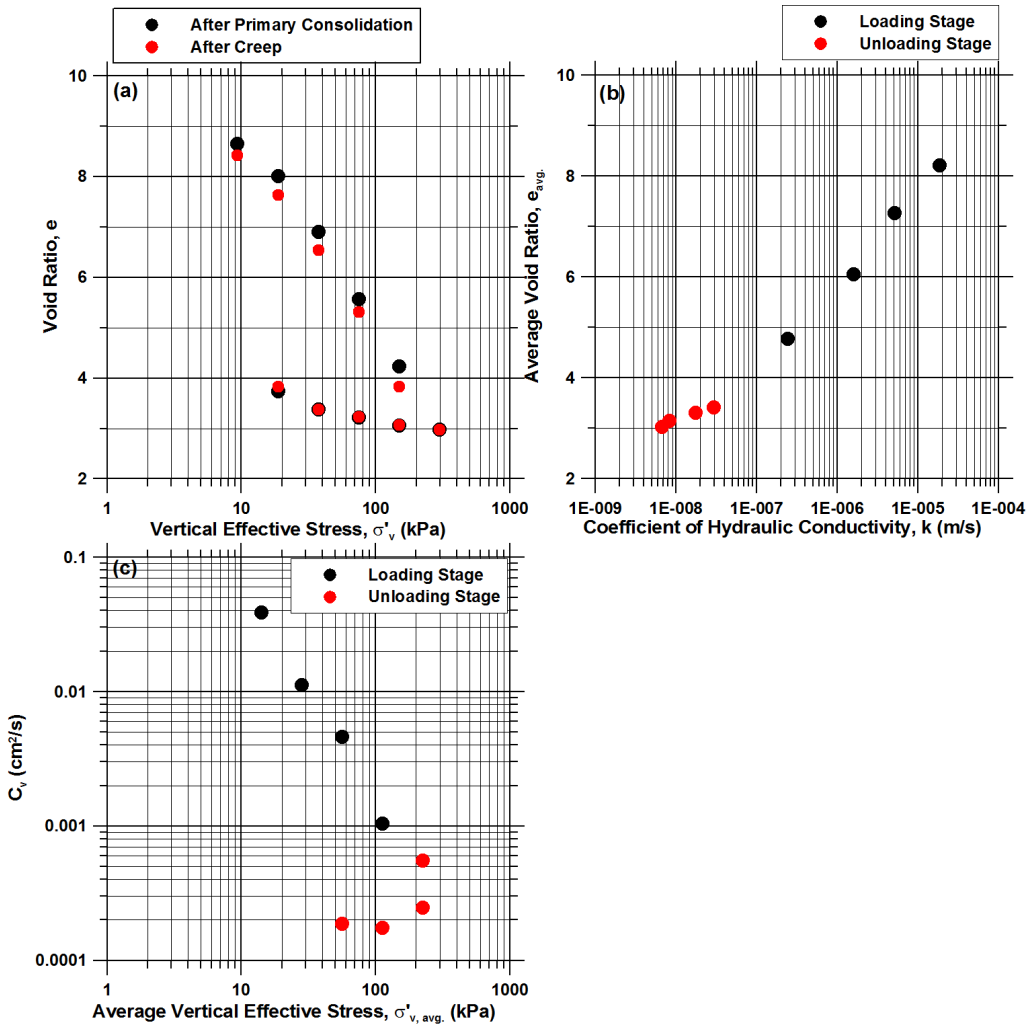

Figure 5.19. Oedometer test results for BH8S1_R, OC=66%

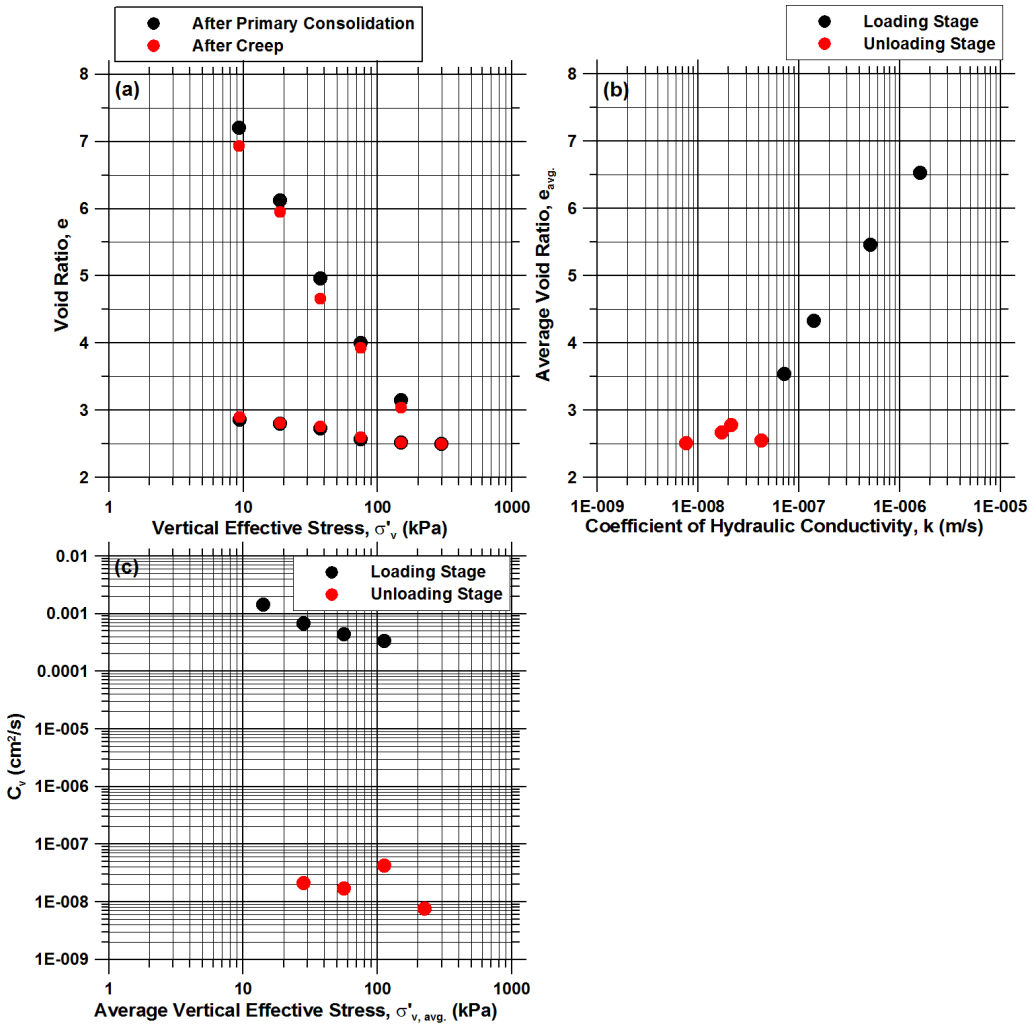

Figure 5.20. Oedometer test results for BH9S1_R, OC=30%

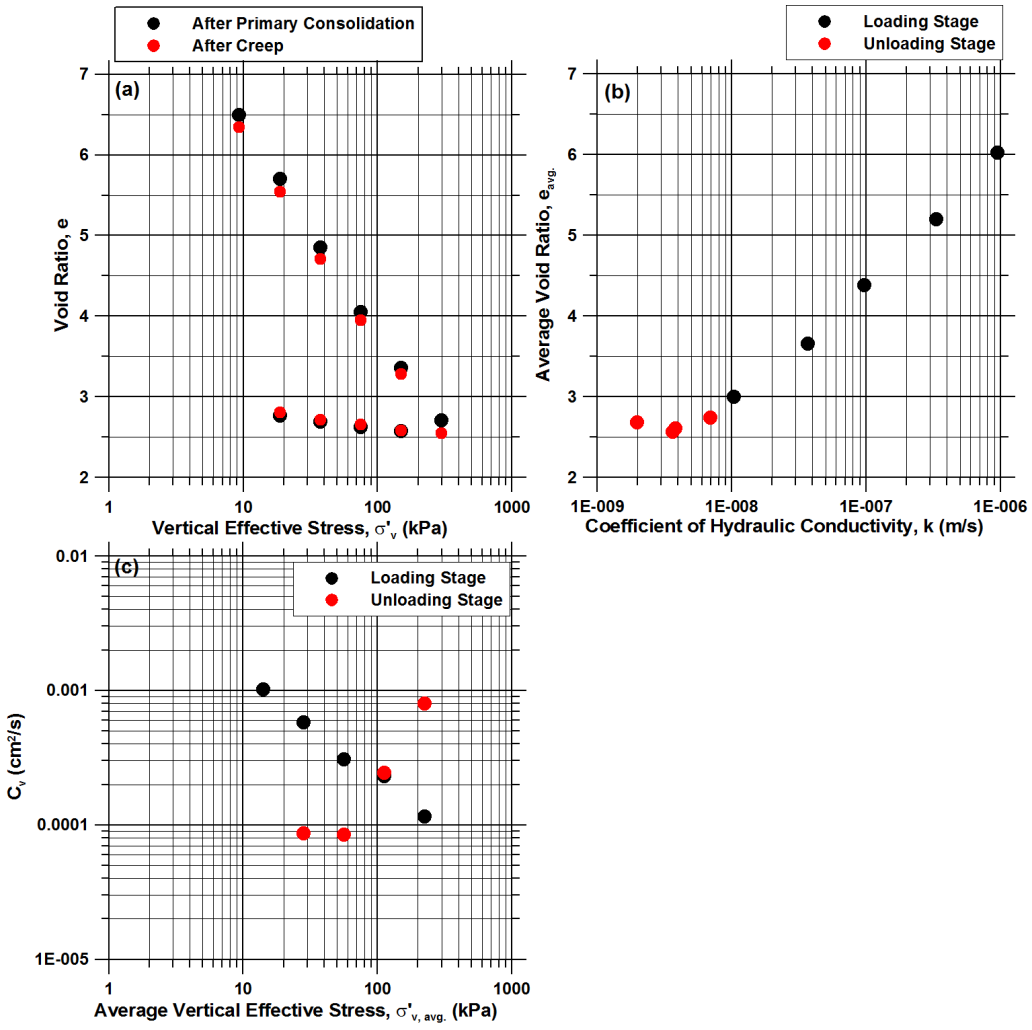

Figure 5.21. Oedometer test results for BH9S3_R, OC=30%

Mesri and Ajlouni (2007) suggest that the virgin compression index can approximately estimated as a function of the natural water content, w_0. Specifically, they found the approximate relation $C_c = w_0/100$ for fibrous peats. Fig. 5.22 shows compression and recompression index versus natural water content for the Sherman Island peat specimens. The trend of compression index confirms the observation by Mesri and Ajlouni (2007) that C_c is positively correlated with

w_0. A linear trend with zero intercept was selected to fit to the data. The best fit is then chosen based on the slope of the model that leads to a lowest value for normalized root mean square error (NRMS):

$$\text{NRMS}=\left[\frac{\sum\left(y_i-y_{model,i}\right)^2}{\sum y_i^2}\right]^{1/2} \tag{5.1}$$

where y_i is the observed value for the ith observation (here refers to C_c or C_r), and $y_{model,i}$ is the predicted value. Results of the linear regression with water content indicate that $C_c=w_0/130$ (NRMS=0.48) and $C_r=w_0/1750$ (NRMS=0.27). It is also possible to fit C_c and C_r with organic content, as shown in Fig. 5.23. As observed, C_c and C_r increase more or less linearly with OC (in percent) as: $C_c=0.07OC$ (NRMS=0.39) and $C_r=0.006OC$ (NRMS=0.39). Hence, the trend with OC is stronger than that with w_0 for C_c, whereas the w_0 trend is stronger for C_r.

As shown in part b of Figs. 5.6 to 5.21, hydraulic conductivity depends on void ratio, with k decreasing as void ratio decreases. The slope of e versus $logk$, that is $C_k = \Delta e/\Delta logk$, is commonly used to quantify this dependence. As shown in Fig. 5.24, C_k increases with initial void ratio (e_0), and the best fit for the data is $C_k = 0.20e_0$. This is reasonably consistent with the findings of Mesri and Ajlouni (2007), who suggest $C_k = 0.25e_0$ based on peat data from the literature as well as tests on James Bay and Middleton peats. In addition, values of C_k from the tests with $LIR \leq 1$ are almost identical to those from LIR=1.

The values of the coefficient of consolidation (c_v) from part c of Figs. 5.6 to 5.21 show that except for the very low organic content peats (OC=8%, Figs. 5.11c & 5.18c), c_v depends on $\sigma'_{v,avg}$ and decreases with the increase in vertical effective pressure. Mesri and Ajlouni (2007) indicate that the maximum value of c_v in the virgin compression range happens at the

preconsolidation pressure (σ_p') and is in the range of 20 to 100 m^2/yr (63 to 317×10^{-4} cm^2/s). As discussed previously, this trend in c_v is driven principally by the decrease of k with increasing consolidation stress. For the Sherman Island peat c_v is as high as 400×10^{-4} cm^2/s at σ_p' (Fig. 5.11).

The values of the secondary compression index (C_α) for Sherman Island peat are also plotted in terms of C_c (Fig. 5.25). Although Mesri and Ajlouni (2007) suggest that C_α/C_c values, on average, vary between 0.05 to 0.07, the values of C_α/C_c for the Sherman Island peat ranges from 0.05 to as high as 0.12 with an average of 0.08.

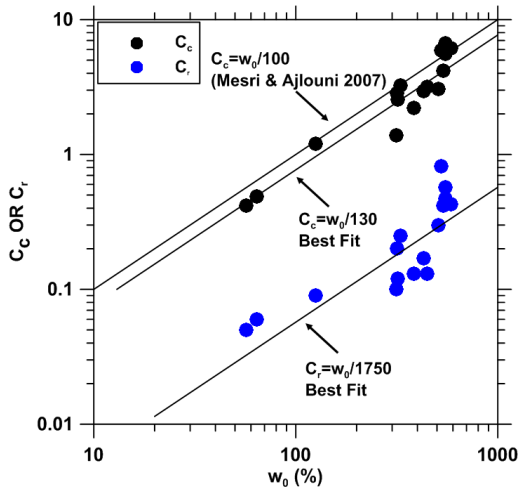

Figure 5.22. Correlation between compression index and natural water content

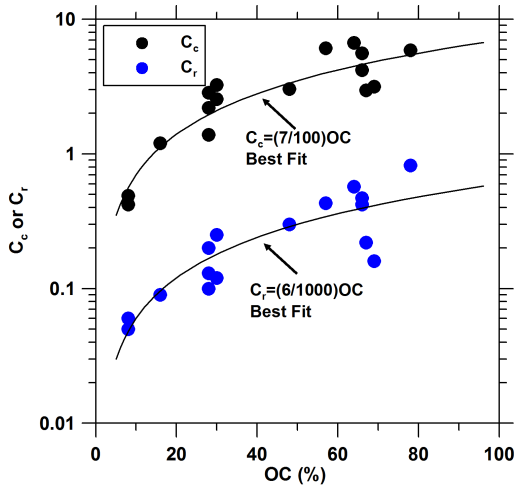

Figure 5.23. Correlation between compression and recompression indices and organic content

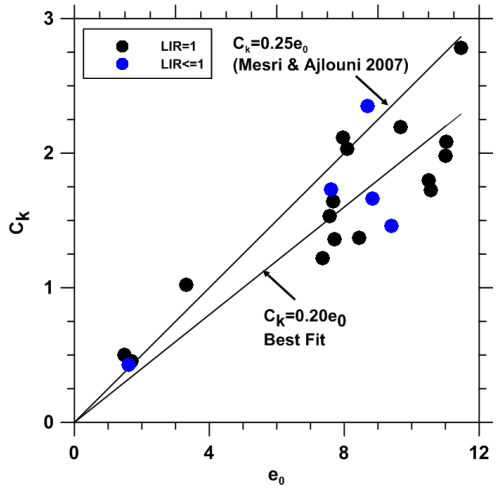

Figure 5.24. Correlation between C_k and initial void ratio

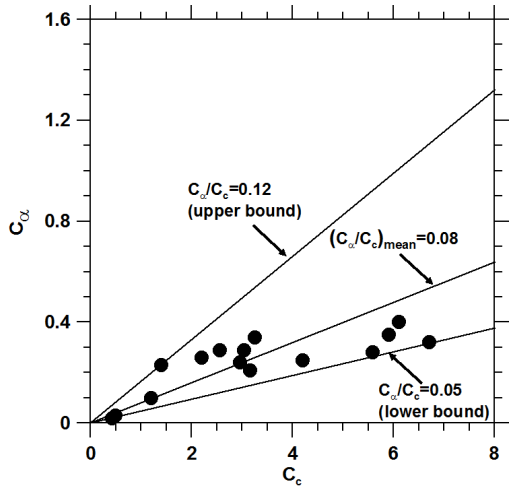

Figure 5.25. Secondary compression index versus compression index for Sherman Island peat

5.5 CONSOLIDATION TESTS WITH LIR<1

Laboratory oedometer tests traditionally use a load increment ratio of 1.0, meaning that the vertical total stress is doubled in each loading stage. Furthermore, the benchtop clock used to keep track of time during the consolidation test is set to zero at the time the load is applied. In this section it is demonstrated that the traditional procedure, in which t=0 corresponds to the time when the load is applied, is inappropriate for identifying the correct value of C_α when *LIR* is less than 1. An alternative stress-space procedure is presented, and shown to provide better agreement with the laboratory test results.

To first demonstrate that the traditional procedure is ineffective for small load increments, consider a test on the specimen BH7S2_2.90 for a load stage in which a 9.3 *kPa* vertical stress increment is imposed first (Stage 2, σ'_{v0}= 9.3 kPa, σ'_{vf} = 18.6 kPa, *LIR* = 1.0), followed by a very small 0.6 *kPa* load increment (Stage 3, σ'_{v0}= 18.6 kPa, σ'_{vf} = 19.2 kPa, *LIR* = 0.03). Fig. 5.26 shows the results recorded from this test plotted with t=0 corresponding to the beginning of

Stage 2. The load increment imposed in Stage 3 is so small that only a very small change in void ratio due to consolidation is apparent in the few seconds after load application at time t=22895 sec (relative to the start of Stage 2). The slope of the secondary compression line remains essentially unchanged from Stage 2 to Stage 3, with only a minor increase in secondary compression rate. This makes sense because the loading imposed during Stage 3 was so small that it had very little influence on the soil fabric, and therefore on the factors that control secondary compression.

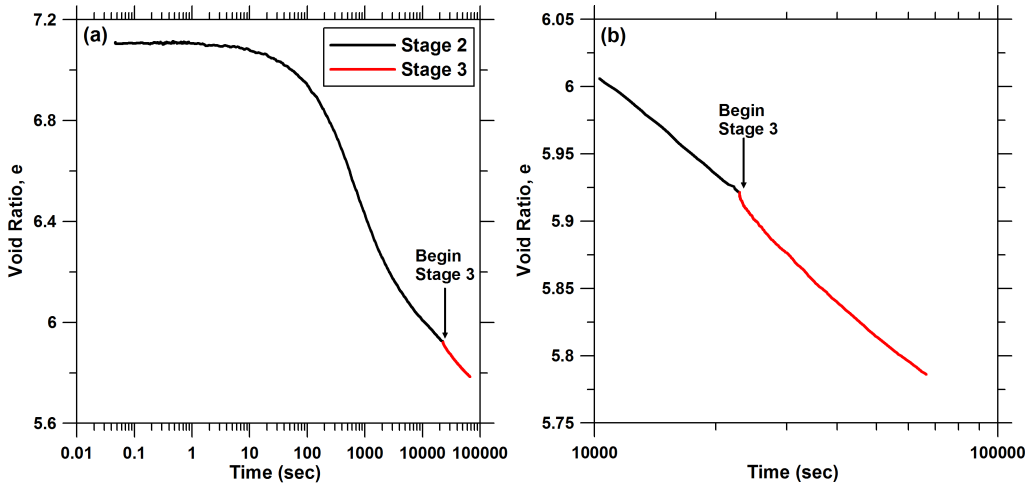

Figure 5.26. Consolidation test on peat specimen BH7S2_9.5. In Stage 2, a vertical load increment of 9.3 *kPa* was imposed, and in Stage 2, an additional 0.6 *kPa* load increment was imposed.

Although the data presented in Fig. 5.26 make sense, the time reference used in the plots for the Stage 3 data is actually the beginning of Stage 2, which is a violation of the traditional procedure in which the clock is reset at the time of load application. The Stage 3 data from Fig. 5.26 is plotted again in Fig. 5.27, except that the clock is reset at the time when the load is applied at the beginning of Stage 3. Bearing in mind that excess pore pressure dissipated after

only a few seconds, traditional secondary compression theory would dictate that the settlement plot would be a straight line in e-log *t* space after a few seconds. However, plotted in the traditional manner in which the clock is reset when the load is applied, the secondary compression behavior exhibits a nonlinear trend with slope increasing over time. A secondary compression slope, C_α, cannot be accurately derived from Fig. 5.27, and it is unclear how to utilize this sort of curve in a secondary compression analysis.

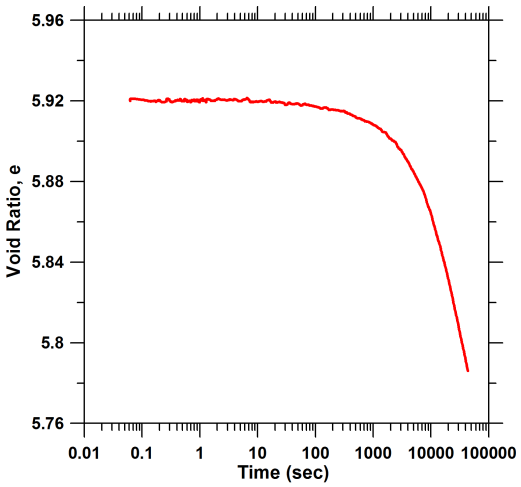

Figure 5.27. Void ratio versus time for the Stage 3 data plotted in Fig. 5.26, except with the clock reset at the time of application of the 0.6 *kPa* load increment.

The explanation of the behavior illustrated in Fig. 5.27 is simple: a line in *e*-log *t* space becomes a curve when the time reference is adjusted. If *t*=0 is set to be later than the actual time reference, the curve will be concave down as shown in Fig. 5.27. Conversely, if *t*=0 is set to be earlier than the actual time reference, the curve will be concave up. A straight line will only arise when the correct time reference is utilized. The traditional theory of secondary compression is therefore correct when a large load increment adequately remolds the fabric of the soil to fully

restart the secondary compression mechanism. However, it may not be correct for load stages that generate smaller strains (e.g., *LIR* < 1, and/or overconsolidated load stages).

Figs. 5.28 and 5.29 show two examples of oedometer tests on Middleton peat, one from Fox et al. (1994) on a normally consolidated specimen with *LIR*<1 (Fig. 5.28), and one from Mesri et al. (1997) on an overconsolidated specimen (Fig. 5.29). These results from the literature show that C_α increases with time in a manner similar to what we have shown in Figs. 5.26 and 5.27, when that behavior was clearly associated with inappropriate selection of the reference time. It may be that these same features as observed by Fox et al. and Mesri et al. can also be explained by inappropriate selection of reference time.

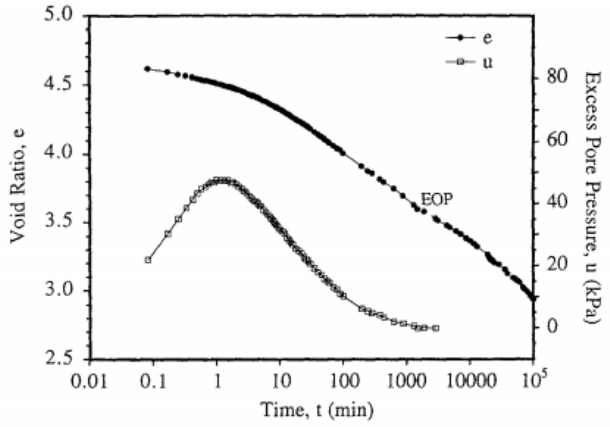

Figure 5.28. Oedometer test on a normally consolidated specimen of Middleton peat with LIR=0.1 (Fox et al. 1994)

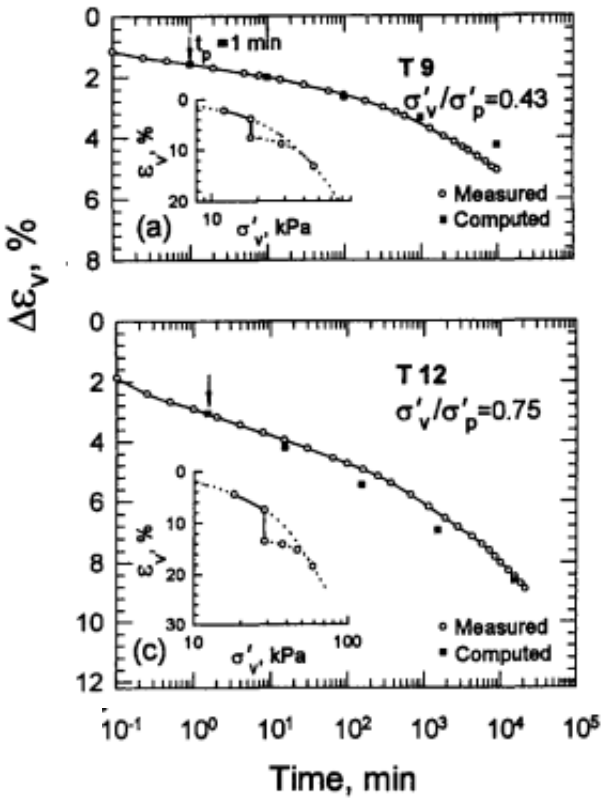

Figure 5.29. Oedometer tests on overconsolidated specimens of Middleton peat (Mesri et al. 1997)

Earthquake ground shaking represents a condition that can potentially impose small load increments by developing modest cumulative excess pore pressures (this aspect of the soil behavior is the subject of Chapter 6). Understanding the secondary compression response for small load increments is therefore a subject of considerable practical importance. To study this behavior in a controlled manner without the complexity of cyclic loading, six oedometer tests were run with *LIR*<1. Figs. 5.30 to 5.35 show a summary of the test results.

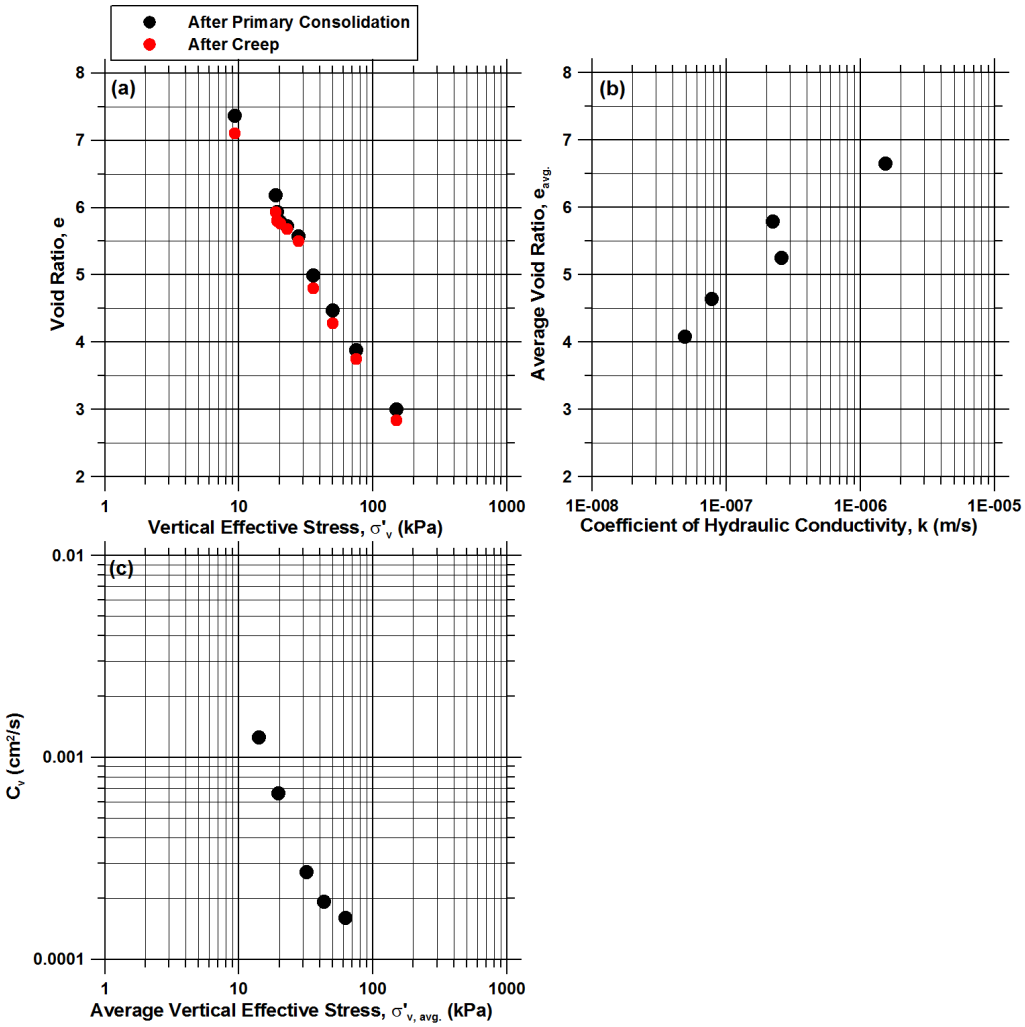

Figure 5.30. Oedometer test results for BH7S2_2.90, OC=28%, LIR=[1.0, 0.03, 0.05, 0.12, 0.22, 0.30, 0.39, 0.50, 1.0]

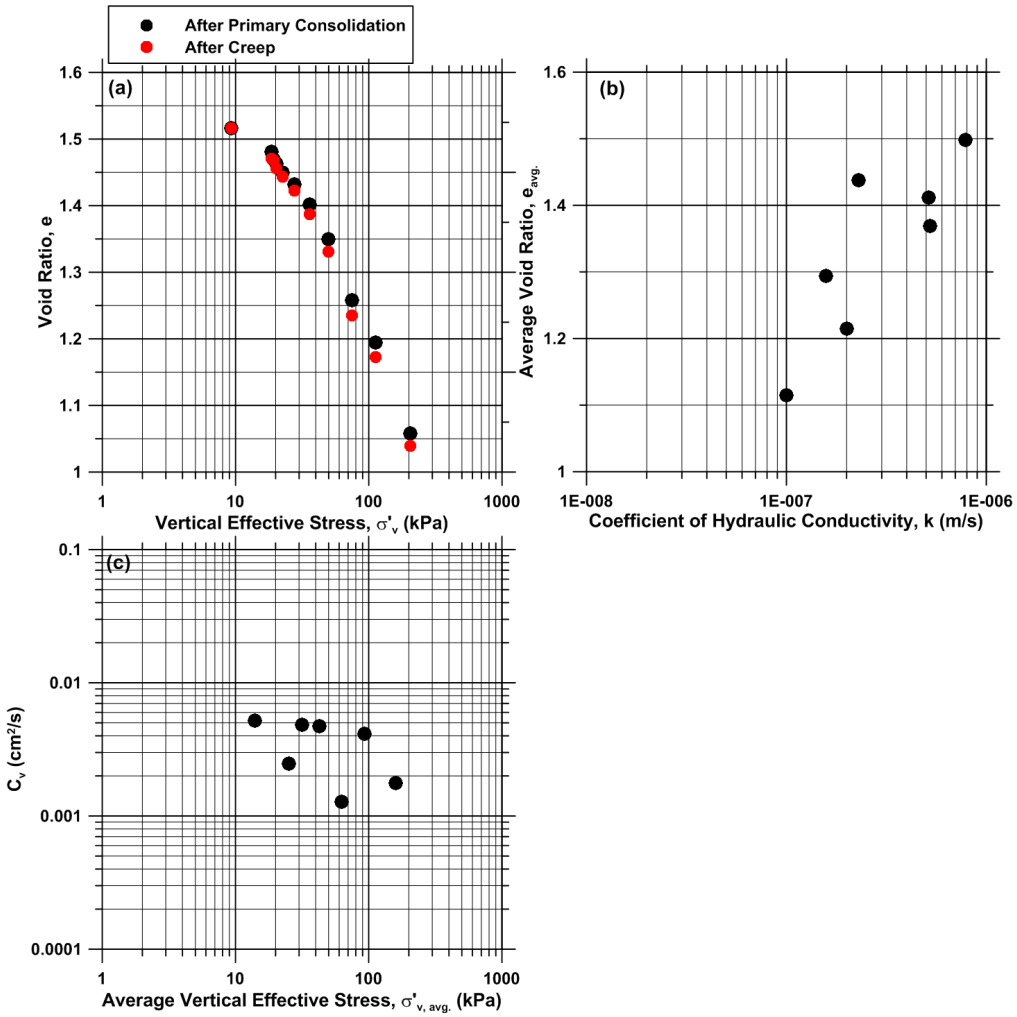

Figure 5.31. Oedometer test results for BH7S2_5.15, OC=8%, LIR=[1.0, 0.03, 0.05, 0.12, 0.21, 0.30, 0.39, 0.50, 0.50, 0.83]

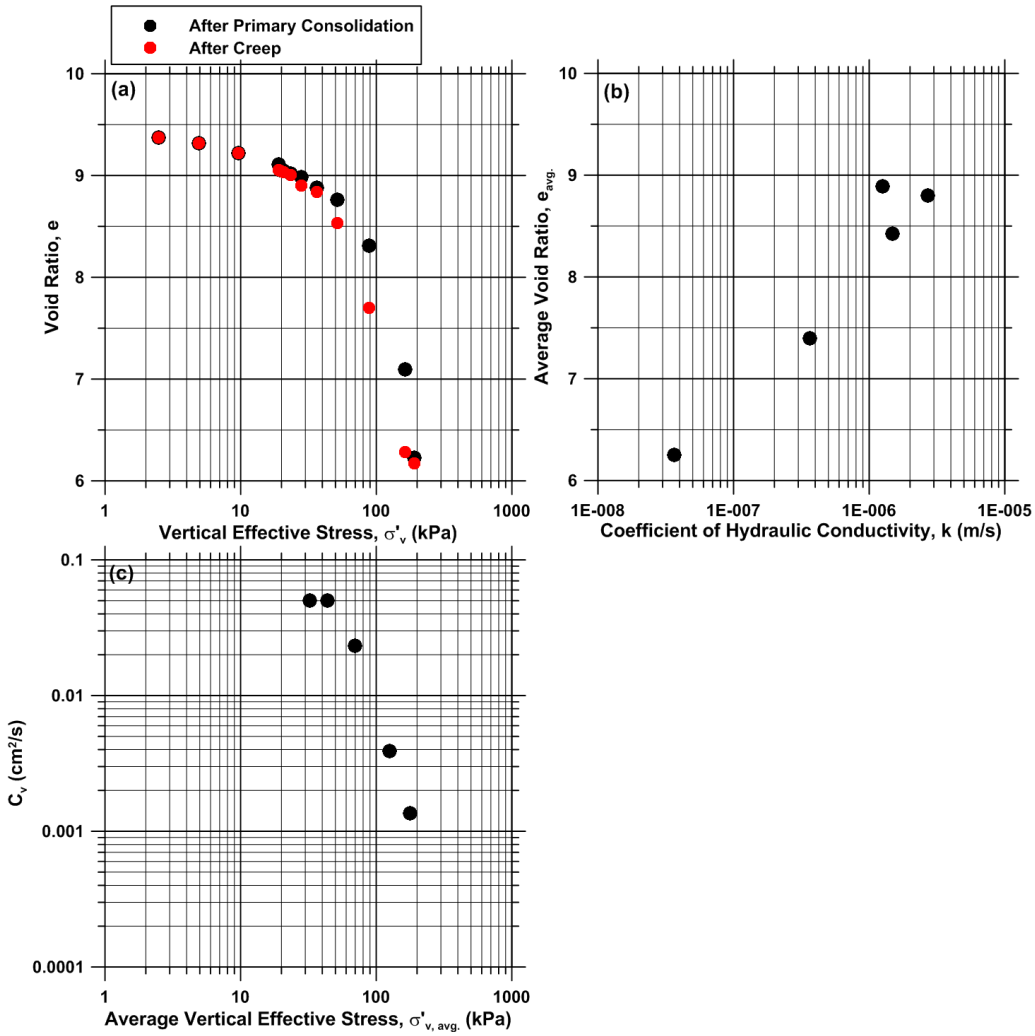

Figure 5.32. Oedometer test results for BH8S2_1.80, OC=66%, LIR=[1.0, 0.96, 0.96, 0.03, 0.06, 0.13, 0.20, 0.29, 0.42, 0.72, 0.84, 0.17]

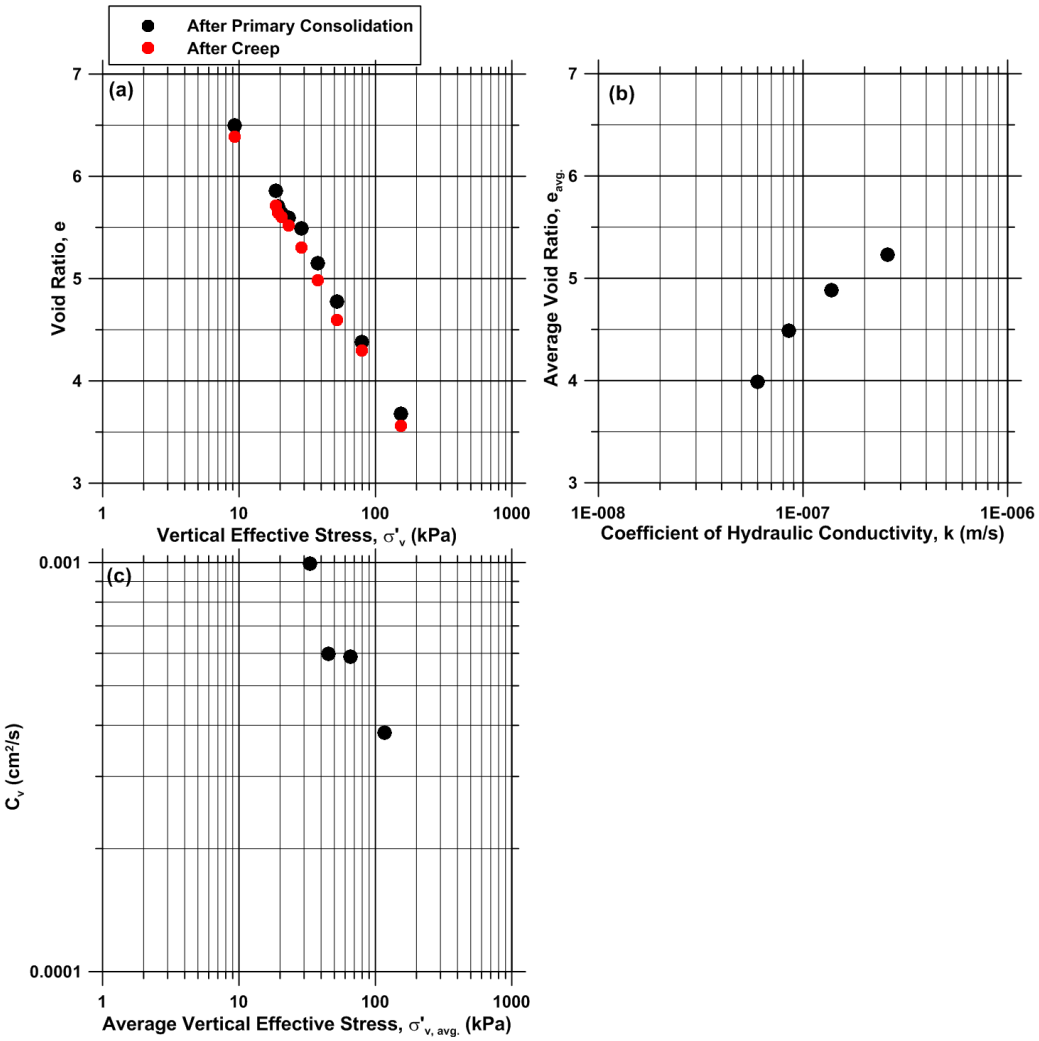

Figure 5.33. Oedometer test results for BH7S9_R, OC=28%, LIR=[1.0, 0.03, 0.06, 0.13, 0.24, 0.31, 0.40, 0.51, 0.94]

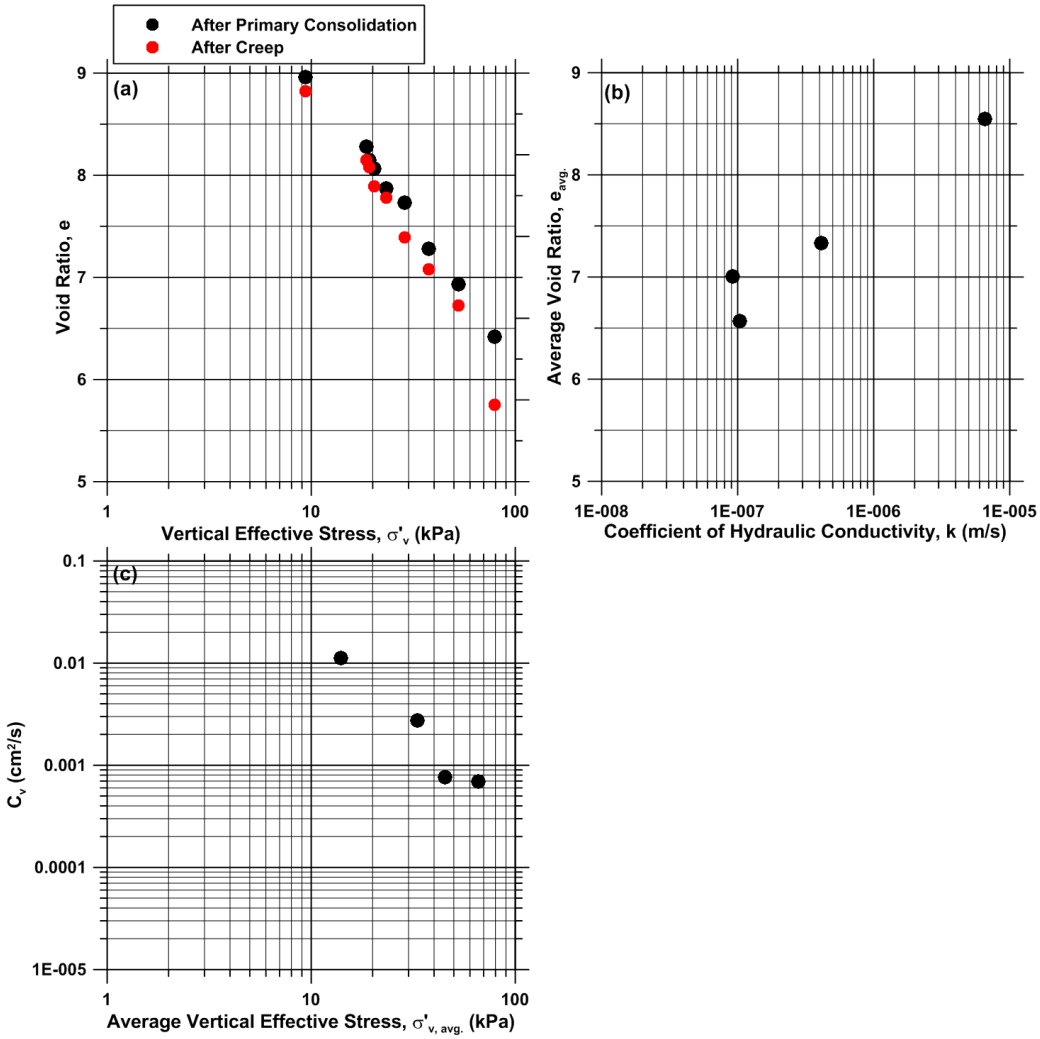

Figure 5.34. Oedometer test results for BH8S2_R, OC=66%, LIR=[1.0, 0.03, 0.06, 0.14, 0.23, 0.31, 0.40, 0.51, 0.94]

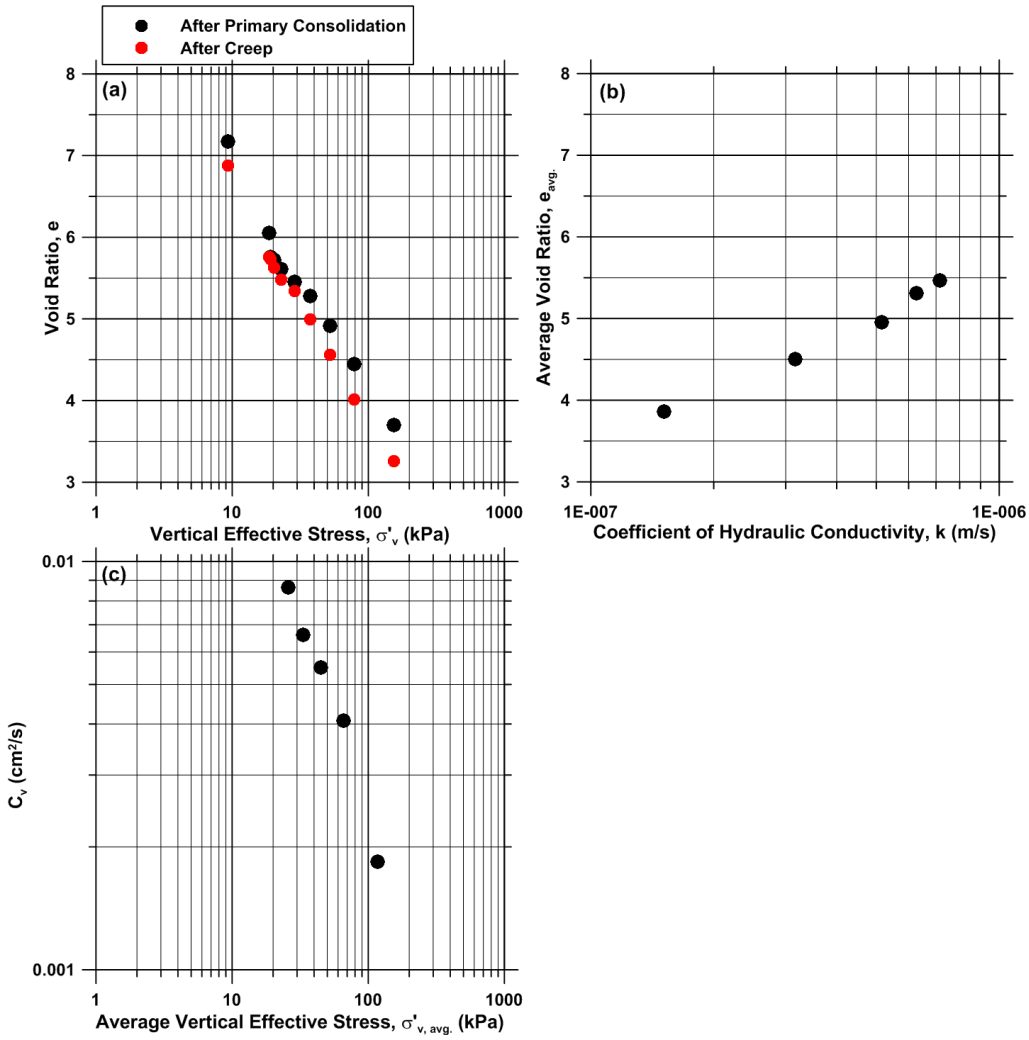

Figure 5.35. Oedometer test results for BH9S2_R, OC=30%, LIR=[1.0, 0.03, 0.06, 0.13, 0.24, 0.31, 0.40, 0.51, 0.94]

5.6 AN ALTERNATIVE INTERPRETATION OF SECONDARY COMPRESSION

To solve the secondary compression problem for small load increments, either the correct time reference must somehow be defined, or an alternative approach must be adopted. Identifying the correct time reference is non-trivial. For example, in Fig. 5.26, the correct time reference for Stage 2 is the beginning of Stage 2 because the load increment was large. The correct time reference for Stage 3 is also approximately the beginning of Stage 2 because the load increment was so small. However, how would the time reference be identified for the case of an intermediate load increment being applied? In such a case, a time between the onsets of Stage 2 and 3 loading would be needed. A framework could conceivably be developed in which the time reference is related to *LIR* following an extensive laboratory testing program, although this would leave unanswered the question of how to treat cases involving stress increases on over-consolidated soil or pore pressure generation from undrained cyclic loading. In other words, it is difficult to conceptualize a fully general procedure for evaluating the time reference for secondary compression.

Accordingly, an alternative simpler approach is explored here. The idea is to formulate the secondary compression strain rate as a function of distance to a secondary compression reference line (SCRL) in e-logσ_v' space. This is a fundamental departure from traditional theory in which the secondary compression rate (in e-t space) is defined as exponentially decaying as a function of time (t). It also has the benefit of eliminating an arbitrary time reference from the secondary compression calculation, instead conditioning secondary compression rate on soil state.

The theoretical underpinning of this approach was presented in the Rankine lecture by Bjerrum (1967), who postulated a unique relationship between void ratio, vertical effective

stress, and time that can be represented by families of parallel lines in e – log σ_v' space. In this figure, each line corresponds to a different elapsed time since load application (Fig. 5.36). The "time-lines" in Fig. 5.36 are associated with logarithmic time increments; therefore, the distance between adjacent time-lines is equivalent to C_α.

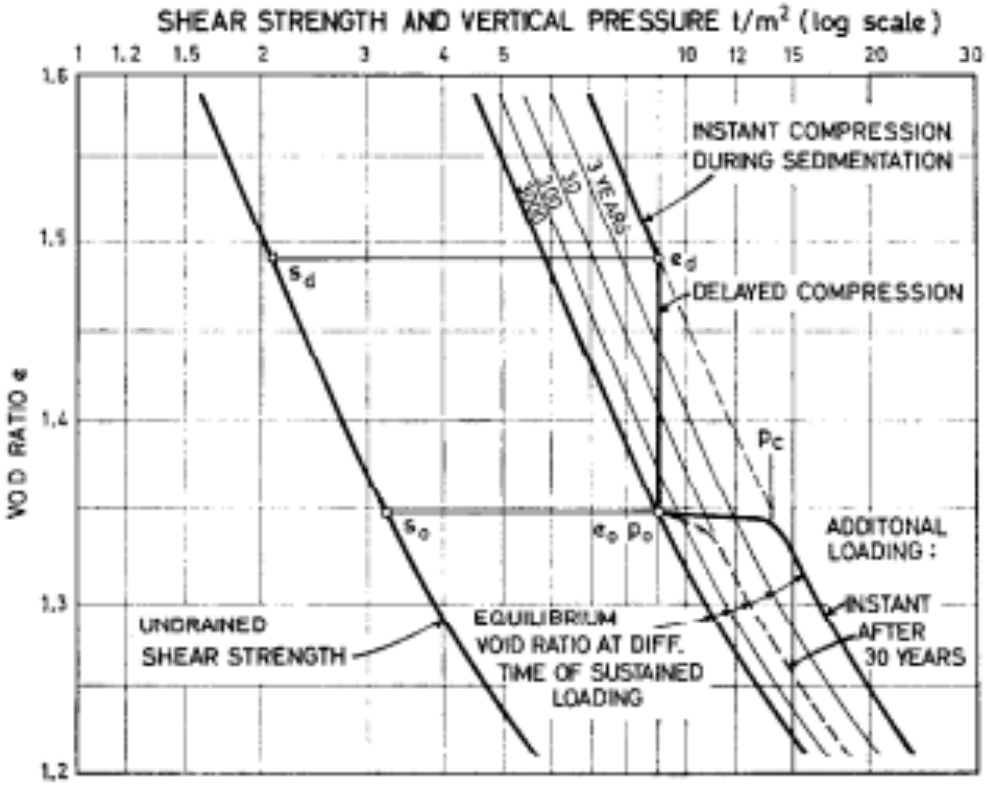

Fig. 5.36 Relationships between between *e*, log σ_v', and *time* corresponding to virgin compression and various levels of pseudo-overconsolidation from secondary compression. The e- log σ_v' relationships marked as 'delayed compression' are separated by log increments of time and comprise parallel "time-lines" described in the text. Also shown for reference purposes is the relationship between undrained shear strength and effective stress for normally consolidated clay.

Kutter and Sathialingam (1992) extended Bjerrum's time-line concept to derive an expression for the plastic volumetric strain caused by secondary compression as a function of the vertical distance in *e*-ln p' space from a reference time-line. The reference time line they selected was the normal consolidation line (NCL) measured in a laboratory oedometer test. The resulting expression for secondary compression volumetric strain rate ($\dot{\varepsilon}_v^{sc}$) is:

$$\dot{\varepsilon}_v^{sc} = \frac{a}{(1+e_0)t_{ref}}\left(\frac{\sigma_v'}{\sigma_s'}\right)^{(C_c-C_r)/C_\alpha} \tag{5.2}$$

in which $a = C_\alpha/ln10$, σ_s' is the effective stress on the SCRL that is encountered when the soil is consolidated along the recompression line from σ_v' to the SCRL, and t_{ref} is the time since load application associated with the reference time-line (i.e., $t_{ref} = t_p$ if the reference time-line is the NCL). Note that in the case where the SCRL and the NCL are coincident, $\sigma_s' = \sigma_p'$. An outcome of Eq. (5.2) is that $\dot{\varepsilon}_v^{sc}$ decreases as the soil state falls further below the SCRL, which in most applications involves OCR increases. For example, $\dot{\varepsilon}_v^{sc}$ is lower at point A than at point B in Fig. 5.37.

For comparison, if the rate of secondary compression is evaluated using the traditional approach, it depends only on C_α and t_{ref} as:

$$\dot{\varepsilon}_v^{sc} = \frac{C_\alpha/\ln 10}{(1+e_0)t_{ref}} \tag{5.3}$$

This framework is unable to account for the effects of overconsolidation and has an irremovable dependence on time through t_{ref}, which in this case is the time since load application. As discussed previously, this time definition produces bias when *LIR* < 1 (and similar situations not

producing substantive pore pressure generation and soil deformations). The removal of this bias necessarily depends on identifying the 'correct' reference time, which is generally unknown.

A benefit of Eq. (5.2) relative to Eq. (5.3) is that the former holds the potential for removing time entirely from the evaluation of $\dot{\varepsilon}_v^{sc}$. It is this potential that we seek to develop in the present work, extending the work of Kutter and Sathialingam (1992). We seek to define $\dot{\varepsilon}_v^{sc}$ solely from the 'state' of soil as defined by its position in *e*-log σ_v' space. This soil state is time-dependent in classical consolidation problems where total stress on a soil deposit is increased, and must be time-integrated to derive an expression for settlement. Moreover, by linking $\dot{\varepsilon}_v^{sc}$ to state, there is no need for the arbitrary division of settlement into separate primary consolidation and secondary compression phases. This is desirable because secondary compression and primary consolidation occur simultaneously for $t < t_p$. However, these benefits come at the expense of requiring a solution tool for solving the governing differential equation for flow of pore water from the soil matrix, both as a result of pore pressure dissipation and secondary compression.

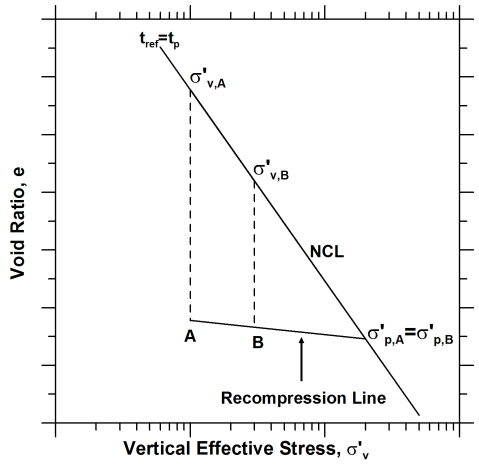

Figure 5.37. Description of Kutter and Sathialingam (1992) model for calculating volumetric secondary compression rate

The proposed framework can be used to predict the variation of secondary compression void ratio (e^{sc}) with time following loading/unloading. Referring to Fig. 5.38(a), consider point B, which represents a state in $e - log\sigma'_v$ space achieved by some arbitrary combination of loading/unloading (which is not marked in Fig. 5.38a). In the present derivation, we seek $e^{sc}(\tau)$ following secondary compression from point B to point C, where τ represents time elapsed after the soil reaches the state at Point B (hence $\tau = t - \Delta t$, where Δt is the arbitrary time required for the soil state to change from the SCRL to Point B). Point A represents a point on the SCRL having the same effective stress as Points B and C, void ratio e_{ref}, and time t_{ref}. Keeping in mind the concept presented by Bjerrum (Fig 5.36), one can imagine many lines parallel to and below the SCRL (not shown in Fig. 5.38a) corresponding to times $t > t_{ref}$. It follows therefore, that the void ratio at point C can be defined as follows:

$$e^{sc}(\tau) = e^{sc}(t) = e_{ref} - C_\alpha log\left(t/t_{ref}\right) \tag{5.4}$$

where $t=\tau+\Delta t \geq t_{ref}$. Note that in the common case (for non-seismic problems) where the SCRL and NCL are coincident, t_{ref} would be taken as t_p as indicated in Fig. 5.37. By differentiating with respect to time:

$$\dot{e}^{sc}(\tau) = \frac{-a}{t} \tag{5.5}$$

On the other hand:

$$t = t_{ref} exp\left[\frac{e_{ref} - e^{sc}(\tau)}{a}\right] \tag{5.6}$$

Entering t from Eq. (5.6) into Eq. (5.5), taking $\dot{e}^{sc}(\tau) = de^{sc}/d\tau$, and re-arranging, we obtain:

$$exp\left[\frac{e_{ref} - e^{sc}(\tau)}{a}\right] de^{sc} = \frac{-a}{t_{ref}} d\tau \tag{5.7}$$

Note that with this substation, time as variable t disappears. If we integrate both sides with respect to time τ, and define $e^{sc}(\tau) = e_0$ at τ=0, then:

$$e^{sc}(\tau) = e_{ref} - aln\left[\frac{\tau}{t_{ref}} + exp\left(\frac{e_{ref} - e_0}{a}\right)\right] \tag{5.8}$$

However:

$$e_0 = e_{ref} - (C_c - C_r)\log(OCR) \tag{5.9}$$

If e_0 from Eq. (5.9) is entered into Eq. (5.8), then:

$$e^{sc}(\tau) = e_{ref} - aln\left\{\frac{\tau}{t_{ref}} + exp\left[\frac{(C_c - C_r)\log(OCR)}{a}\right]\right\} \tag{5.10}$$

Fig. 5.38(b) presents the variation of e^{sc} in terms of $\frac{\tau}{t_{ref}}$ for a case in which e_{ref}=1.4, C_α=0.10, C_c=0.5, C_r=0.05, and OCR=[1,2,4,8, 16]. Eq. (5.4) is the equation used for the asymptote and is plotted in Figure 5.38(b) for Δt=0.

As shown in Figure 5.39, Eq. (5.8) can now be used with $e_{ref} = 6.72$, $e_0 = 5.919$, $t_{ref} = 250\,sec$, and $C_\alpha = 0.29$ to predict variation of e^{sc} versus time for the case that was already shown in Fig. 5.27 (corresponding to a very small load increment of 0.60 *kPa*). In this case, the reference to define e_{ref} and t_{ref} is the onset of Stage 2 consolidation.

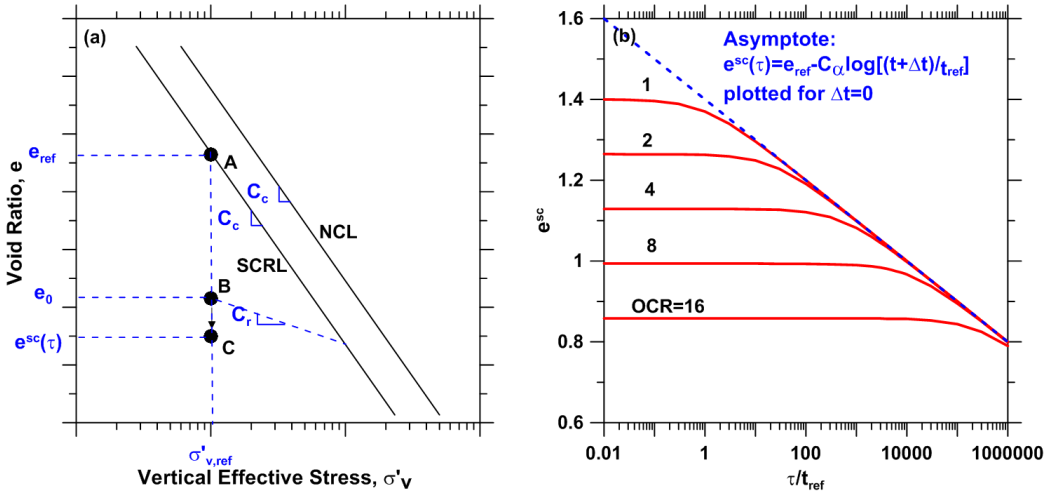

Figure 5.38 Physical interpretation of new framework for secondary compression: (a) description of the framework in $e - log\sigma'_v$ space; (b) an example of variation of e^{sc} as a function of time after the soil reaches the reference condition at Point B and OCR

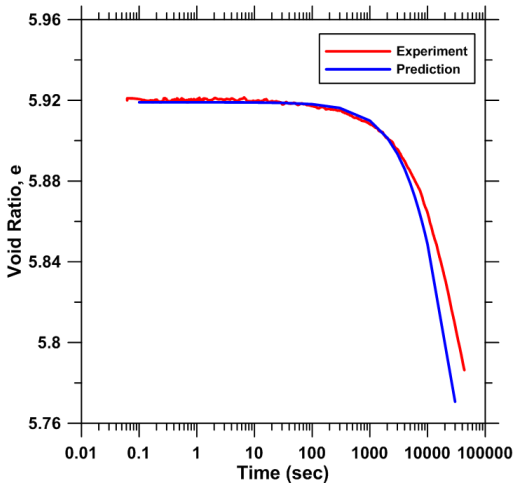

Figure 5.39 Use of new secondary compression framework to predict secondary compression following a very small load increment of 0.60 *kPa*

The proposed stress-based framework was integrated into a nonlinear consolidation code by professor Brandenberg (hereafter called "non-linear consolidation code") that permits secondary compression to occur simultaneously with primary consolidation. The code (which is available at www.uclageo.com/software.php) adopts the new terminology "secondary compression reference line (SCRL)" as shown in Fig. 5.40. The SCRL is assumed parallel to the NCL, as observed by Bjerrum (1967). As shown in Chapter 6, cyclic straining can cause the SCRL to move downward, which is the reason why we have chosen to uncouple the SCRL and NCL.

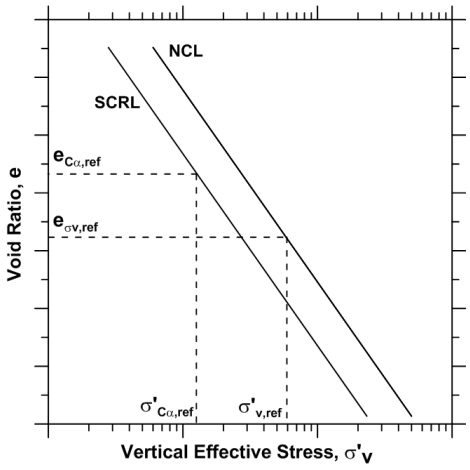

Figure 5.40. Definition of secondary compression reference line (SCRL)

Fig. 5.41 displays a screen shot of the code. User inputs include compressibility properties (C_c, C_r, $\sigma'_{v,ref}$, $e_{\sigma v,ref}$, G_s), permeability properties (k_{ref}, $e_{k,ref}$, C_k), secondary compression properties (C_α, t_{ref}, $\sigma'_{C\alpha,ref}$, $e_{c\alpha,ref}$), and loading conditions (layer thickness, initial overburden pressure, vertical total stress change, initial excess pore pressure ratio, void ratio or OCR, number of elements, number of time steps, and the maximum time needed to plot the results (for definition of $\sigma'_{v,ref}$, e_{ref}, $\sigma'_{C\alpha,ref}$, and $e_{c\alpha,ref}$ see Fig. 5.40). The code assumes perfect drainage boundary conditions as being either impermeable or free-draining (permitting double drainage, single drainage through the top, or single drainage through the bottom). The soil layer is assumed to be "uniform", which means that the material constants apply to the entire layer. In this context, "uniform" does not mean that the entire layer must have the same void ratio and OCR. In fact, a constant void ratio implies that the OCR must vary with depth, and a constant OCR implies that the void ratio must vary with depth. Outputs from the program include excess pore water pressure isochrones (user-adjustable) and settlement versus time at the top of the soil

deposit. An example of the use of the code to calculate post-earthquake settlement based on the lab tests data is presented in Chapter 6.

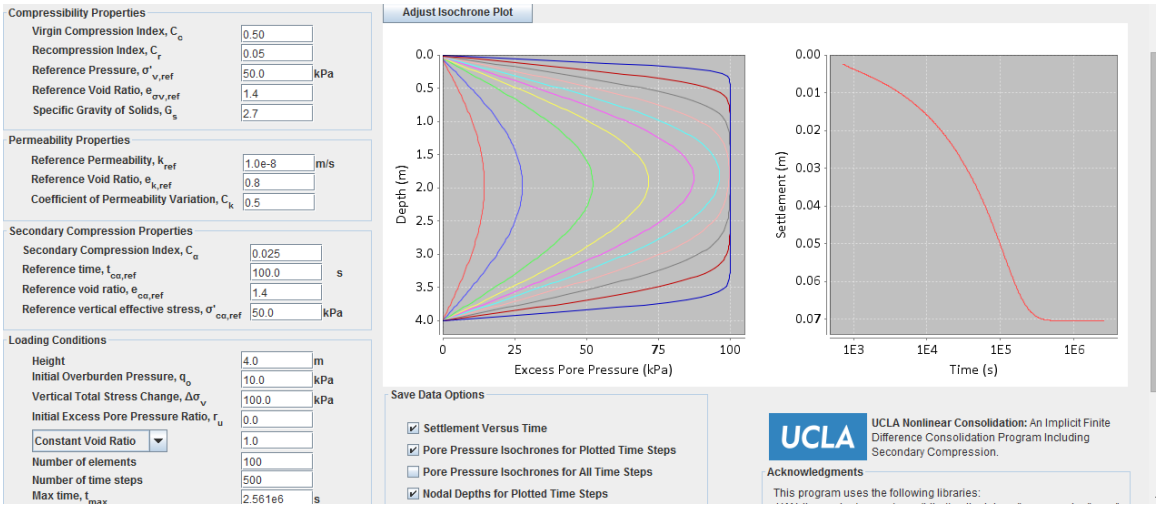

Figure 5.41 Input windows and screen shots of results from nonlinear consolidation code

6 Monotonic, Cyclic, and Post-Cyclic Shearing Behavior of Sherman Island Peat

6.1 INTRODUCTION

This chapter is concerned with the shear behavior of Sherman Island peat as investigated using the UCLA digitally-controlled direct simple shear device for the following test types: (1) strain-controlled constant-height monotonic tests, (2) strain-controlled constant-height cyclic tests with post-cyclic volume change measurements, (3) strain-controlled constant-height cyclic tests with post-cyclic constant-height monotonic shearing, and (4) stress-controlled constant-height cyclic tests conducted with a finite static driving shear stress with post-cyclic volume change measurements. This chapter first presents the specimen preparation procedures, followed by examples of each test type, summary plots, and discussions of lessons learned. Results from all of the cyclic experiments are plotted in Appendix A.

6.2 SPECIMEN PREPARATION

Direct simple shear (DSS) tests were run on reconstituted and relatively undisturbed specimens of Sherman Island peat retrieved from the field in the manner described in Chapter 4. The reconstituted specimens were prepared from peat slurry in the lab as explained in Sec. 5.3. The preparation of test specimens from relatively "undisturbed" samples began by cutting a short length from the Shelby tube using a manual pipe cutter. The diameter of the reinforced

membrane is less than the diameter of the Shelby tube, therefore the samples (either reconstituted or undisturbed) cannot be directly extruded into the wire-reinforced membrane, and must first be trimmed. The short length of the Shelby tube sample is extruded into a 28 mm tall ring having the same diameter as the Shelby tube, i.e., 72.5 mm. The sample is then cut to the desired height using the ring as a guide.

The specimen is then placed on the bottom cap of the simple shear device, which is placed inside the trimming device (Fig. 6.1a). A top cap is lowered onto the specimen and locked into place without placing significant vertical stress on the specimen, and the ring is removed from the specimen. The specimen is then trimmed to achieve a diameter of 67.8 mm (Fig. 6.1b), which is the same as the reinforced membrane. The reinforced membrane is then stretched around a 68.3 mm diameter ring, and placed on top of the specimen (Fig. 6.1b). The membrane is then gently pulled down around the specimen, and the non-wire-reinforced portion of the membrane is unfolded onto the top and bottom caps (Fig. 6.1c). Finally, the ring is removed, o-ring seals are placed around the top and bottom portions of the membrane, and the specimen inside the reinforced membrane is ready for testing (Fig. 6.1d).

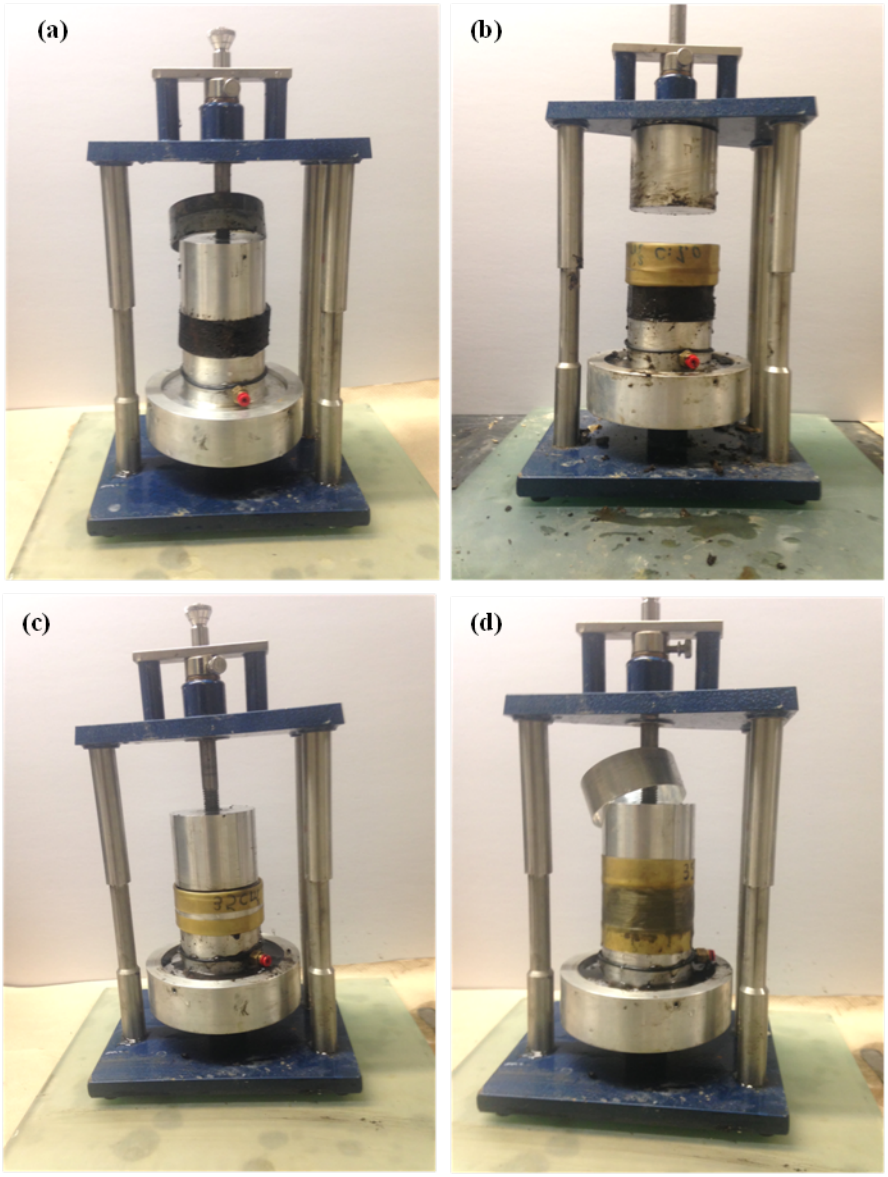

Figure 6.1 Specimen preparation in trimming device (a) specimen (72.5 mm diameter) on the simple shear device's bottom cap prior to trimming (b) specimen (67.8 mm diameter) after trimming, ready to be placed inside the reinforced membrane (c) specimen inside the reinforced membrane and 68.3 mm diameter ring (d) specimen inside the reinforced membrane after ring removal

Following specimen preparation, the soil specimen and bottom cap are placed inside the simple shear device, and the top cap is fixed in place maintaining a small gap between the specimen surface and top cap to avoid disturbance. The top cap is then connected to the drainage

line, while the bottom cap is connected to a pore water pressure transducer installed to determine the end of primary consolidation during initial consolidation to a desired effective stress, and also for post-cyclic re-consolidation measurements. As described previously in Section 5.2, although the specimens are not fully saturated, they nevertheless exhibit a measureable pore pressure response during consolidation that permits evaluation of the end of primary consolidation, which is not always obvious from displacement measurements alone. The top cap is lowered until it just touches the specimen using servo-hydraulic control of the vertical actuator using a string potentiometer (the range of the LVDT's used to measure vertical deformation is inadequate for this stage of specimen preparation). The vertical LVDTs are then mounted, and the transducer used to control the vertical axis is switched from the string potentiometer to the vertical LVDTs.

Consolidation is performed under stress-controlled conditions until reaching the desired vertical pressure. The specimen is then overconsolidated by unloading. Some overconsolidation is desired because (i) Sherman Island peat is overconsolidated due primarily to secondary compression, and (ii) there is a high rate of secondary compression in normally consolidated peats that leads to significant relaxation and excess pore pressure before and during the constant volume testing, which can be significantly reduced by overconsolidating the specimens prior to shearing in constant-height mode. The specimens tested in this study had OCRs ranging from 1.1 to 5. Some of the specimens were consolidated to a maximum past pressure of 80 *kPa* in the simple shear device, and then unloaded to the desired pressure, while others were loaded up to 210 *kPa* outside the device to model peat underlying tall levees. These samples cannot be consolidated to such high pressures inside the simple shear device because the limit of the LVDTs is 12.7 mm, and the amount of settlement under high pressures can exceed this limit.

These samples were first preconsolidated in Shelby tubes (outside the simple shear device) up to 210 *kPa*, then placed inside the simple shear device, and consolidated to the desired pressure to achieve the desired OCR.

Secondary compression can increase excess pore water pressure under constant-height conditions due to stress-relaxation. To demonstrate this process for a case in which no shear is applied, Fig. 6.2 shows the accumulation in time of excess pore water pressure under conditions of zero applied shear stress. This pore pressure increase is caused by stress relaxation due to secondary compression. The rates of pore water pressure accumulation ($\dot{u}$) (i.e., the slopes of the curves in Fig. 6.2) have peak values on the order of 1.82 to 3.22 *kPa/min*, which subsequently decreases with time to values as low as 0.20 *kPa/min* after 5*min*. All of the specimens in this study were tested after achieving $\dot{u} \leq 0.20$ *kPa/min* prior to shear.

The pore pressure accumulation process under constant-height conditions described above is problematic during shear, because it becomes very difficult to distinguish pore pressure generation caused by shear from pore pressures that develop from the aforementioned stress relaxation. One way to mitigate this problem is to shear the soil at sufficiently fast strain rates (i.e., as might be associated with earthquake shaking) that stress relaxation and its associated pore pressures are insignificant. Hence, a relatively fast rate of loading was used in monotonic and cyclic tests to minimize the effect of secondary compression during shearing. The monotonic tests were carried out at a shear strain rate ($\dot{\gamma}$) of 3%/min, and cyclic tests were performed at a frequency (*f*) of 1.0 *Hz*. When the relatively short test durations associated with fast strain rates are combined with initiation of shear after achieving $\dot{u} \leq 0.20$ *kPa/min*, we anticipate secondary

compression-induced pore pressures during shear to be ≤1.67 kPa (monotonic loading up to 25% shear strain), and ≤0.05 kPa (cyclic loading for 15 cycles at 1 Hz).

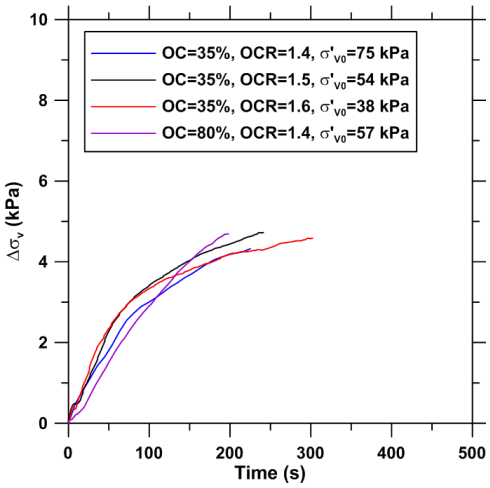

Figure 6.2. Stress relaxation during constant height "consolidation" experiment on reconstituted specimens due to secondary compression.

6.3 MONOTONIC SHEAR BEHAVIOR

Constant volume monotonic simple shear tests were conducted on relatively undisturbed specimens of Sherman Island peat with different organic contents and overconsolidation ratios to investigate their contractive/dilative behavior and to see if their monotonic undrained shear strengths, stress-strain behavior, and pore pressure-strain behavior normalize with respect to pre-shear consolidation stress in a similar manner to that observed previously for clays (e.g., Ladd and Foot, 1974; Ladd, 1991). As described in the previous section, the monotonic tests were performed at a shear strain rate of 3%/min to minimize the effects of secondary compression during shear. They were continued until achieving a shear strain of at least 25% (except for specimens BH7S3_2.95 and BH7S9_5.25, for which the tests were terminated at shear strains of 19.7% and 9.8%, respectively). Table 6.1 presents the test matrix for the monotonic tests.

Table 6.1. Monotonic simple shear test matrix for specimens of Sherman Island Peat.

Specimen ID	Sample Depth (m)	Specimen Depth (m)	OC (%)	Target pre-shear OCR	σ_{v0} [a] *(kPa)*	e_c [b]
BH6S2_4.30	4.10-4.55	4.30	10	3.2	51.5	1.200
BH6S3_4.35	4.10-4.55	4.35	10	1.05	190.5	1.129
BH7S3_2.95	2.75-3.20	2.95	35	1.25	40.0	3.542
BH7S5_3.00	2.75-3.20	3.00	35	1.4	71.4	2.964
BH7S6_3.00	2.75-3.20	3.00	35	1.5	104.2	2.532
BH7S7_3.05	2.75-3.20	3.05	35	3.4	17.2	3.641
BH7S8_3.10	2.75-3.20	3.10	35	1.6	39.5	3.458
BH7S9_3.10	2.75-3.20	3.10	35	1.5	55.9	3.174
BH7S8_5.20	5.05-5.50	5.20	8	1.1	46.3	1.759
BH7S9_5.25	5.05-5.50	5.25	8	1.15	87.0	1.270
BH7S11_5.30	5.05-5.50	5.30	8	4.9	23.4	1.423
BH8S6_2.00	1.70-2.15	2.00	80	4.3	14.8	9.650
BH8S7_2.05	1.70-2.15	2.05	80	1.4	56.3	8.740
BH9S2_1.85	1.70-2.15	1.85	85	3.4	26.2	8.690
BH9S2_1.95	1.70-2.15	1.95	85	1.2	82.9	8.140
BH9S2_2.00	1.70-2.15	2.00	85	3.4	48.8	7.170

[a]Initial vertical stress

[b]Post-consolidation void Ratio

Figs. 6.3 to 6.5 show shear stress (τ_{hv})-shear strain (γ), normalized excess pore pressure (r_u)-shear strain (γ), and stress path in $\tau_{hv} - \sigma'_v$ (vertical effective stress), for three groups of Sherman Island peat specimens with 8-10%, 35%, and 80-85% organic content. Lightly overconsolidated peat with OCR < 2 shows contractive behavior, while higher OCR's respond dilatively. The pore pressures in these plots are based on the change in vertical stress required to maintain constant height, not on a piezometer. Although the simple shear device has the capability of measuring pore pressures through the bottom cap, this feature was not utilized during shearing so as to speed up consolidation during the application of static loads prior to the onset of shear.

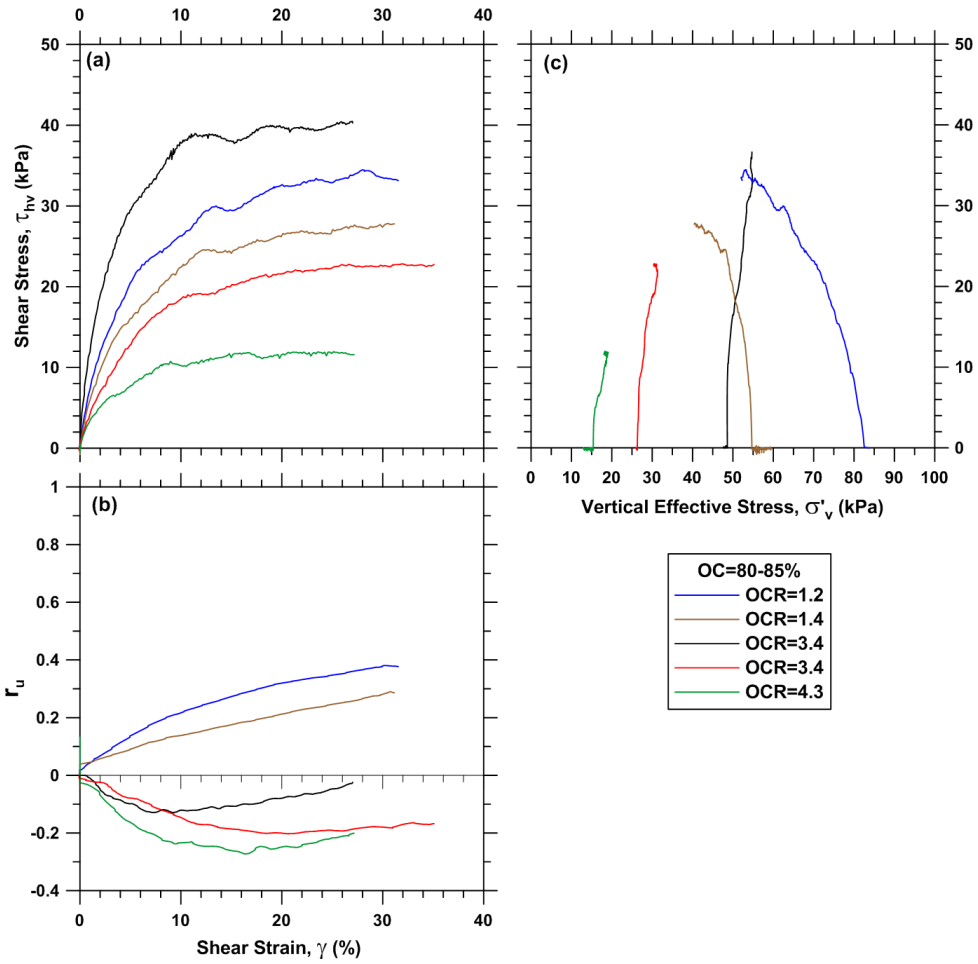

Figure 6.3 Constant volume DSS test on Sherman Island peat, organic content=80-85%

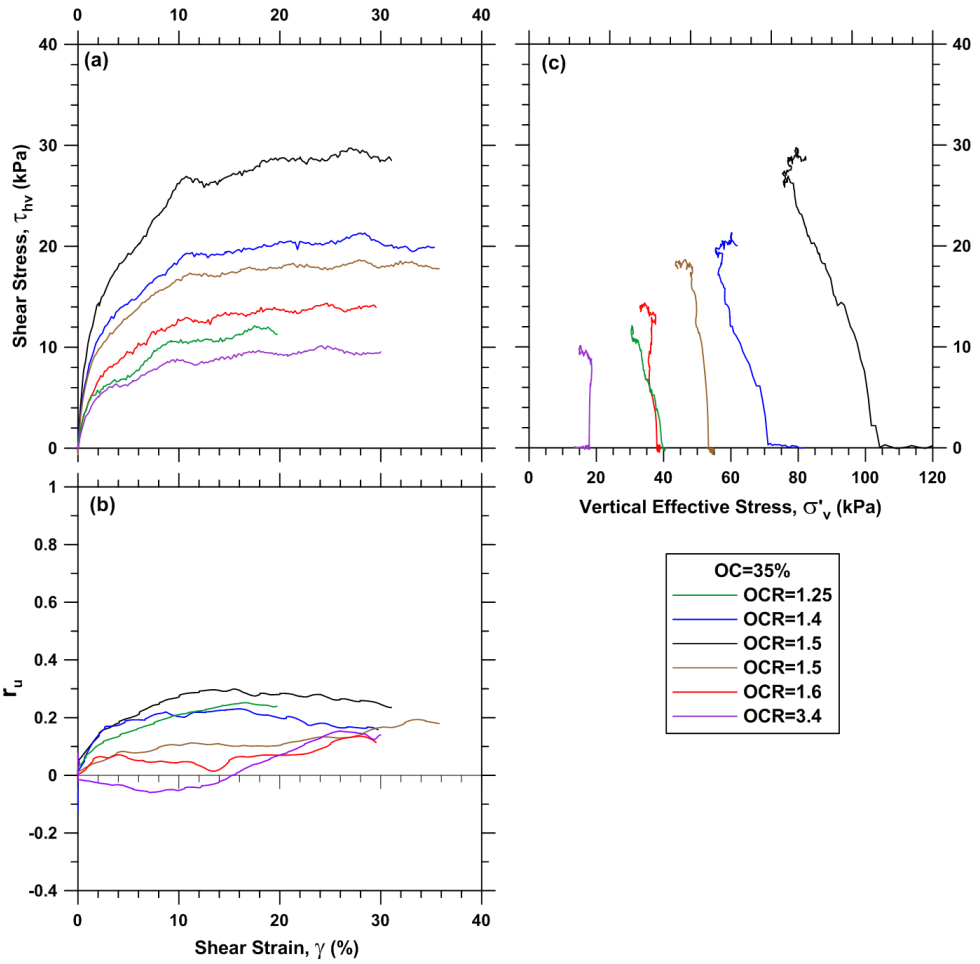

Figure 6.4 Constant volume DSS test on Sherman Island peat, organic content=35%

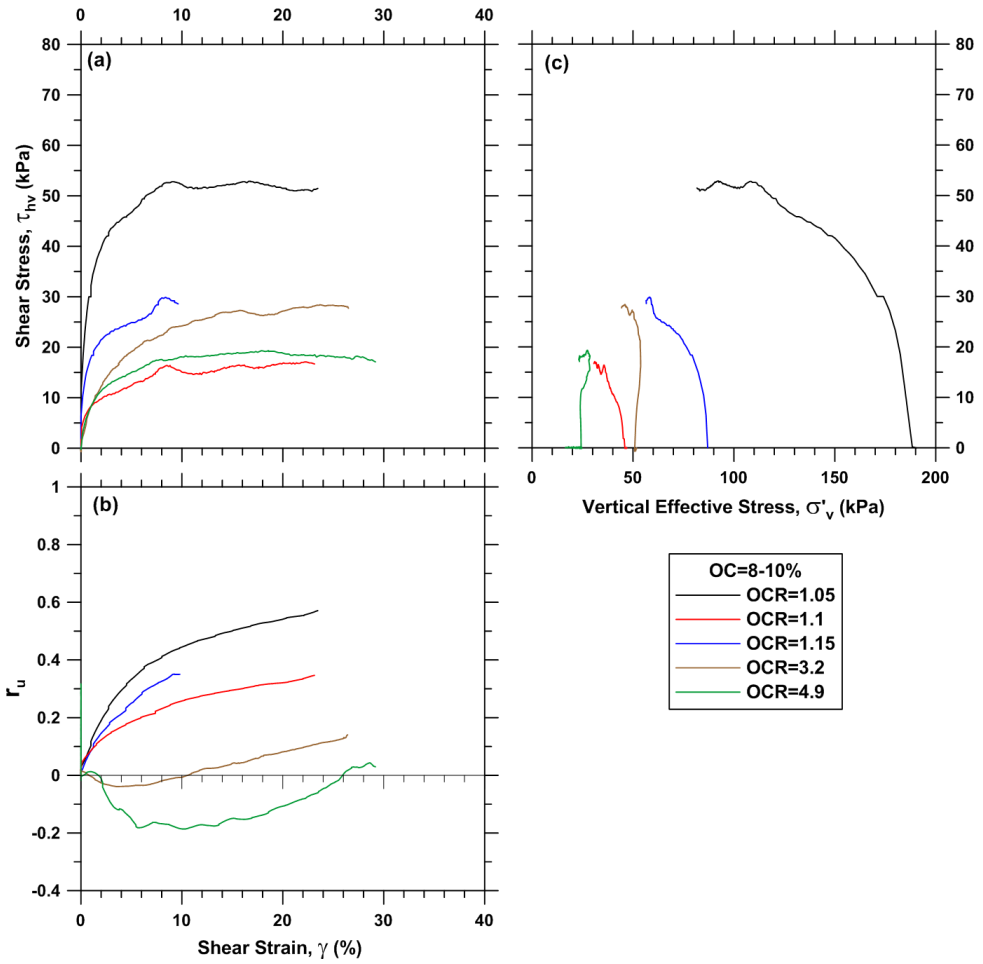

Figure 6.5 Constant volume DSS test on Sherman Island peat, organic content=8-10%

Fig. 6.6 shows final states of the specimens (at $\gamma = 25\%$) in $e - log\sigma'_v$ space along with the normal consolidation line (NCL) as established from the consolidation testing described in Section 5.4. As shown by the blue lines in Fig. 6.6, we fit a failure state line (FSL) to the data representing the final states of the testing specimens (at $\gamma = 25\%$). The 95% confidence intervals (CI) are also shown on Fig. 6.6. The standard error (SE) of the slope of the FSL is shown in Table 6.2. The NCL and FSL seem to be parallel straight lines for OC = 8 to 10%, and for OC = 35%, but not for OC = 85% (Fig. 6.6a). However, based on the small number of data points and the relatively large standard errors of the slopes, we cannot reject the null hypothesis that the slopes of NCL and FSL are not equal.

The NCL for OC = 85% may be steeper than the FSL due to the influence of secondary compression during consolidation, and hence an over-prediction of C_c (because secondary compression would affect high void ratio portions of the NCL to a greater extent that low void ratio portions). If the NCL and FSL are parallel straight lines, the undrained strength normalizes with consolidation stress and overconsolidation ratio as follows (Ladd, 1991):

$$\frac{S_u}{\sigma'_{v0}} = sOCR^m \tag{6.1}$$

On the basis of DSS tests on clays with different plasticity, Ladd and DeGroot (2003) showed that *s* varies from 0.20 to 0.25 when plasticity index changes from 5 to 80%, while *m* can be taken as 0.8 ± 0.1. Fig. 6.7 shows the data from this study along with the best fit line, and trends suggested by Ladd and DeGroot (2003). Peat with OC=80-85% exhibits the highest normalized shear strength while the peat with OC=35% and OC=8-10% have almost the same normalized shear strength.

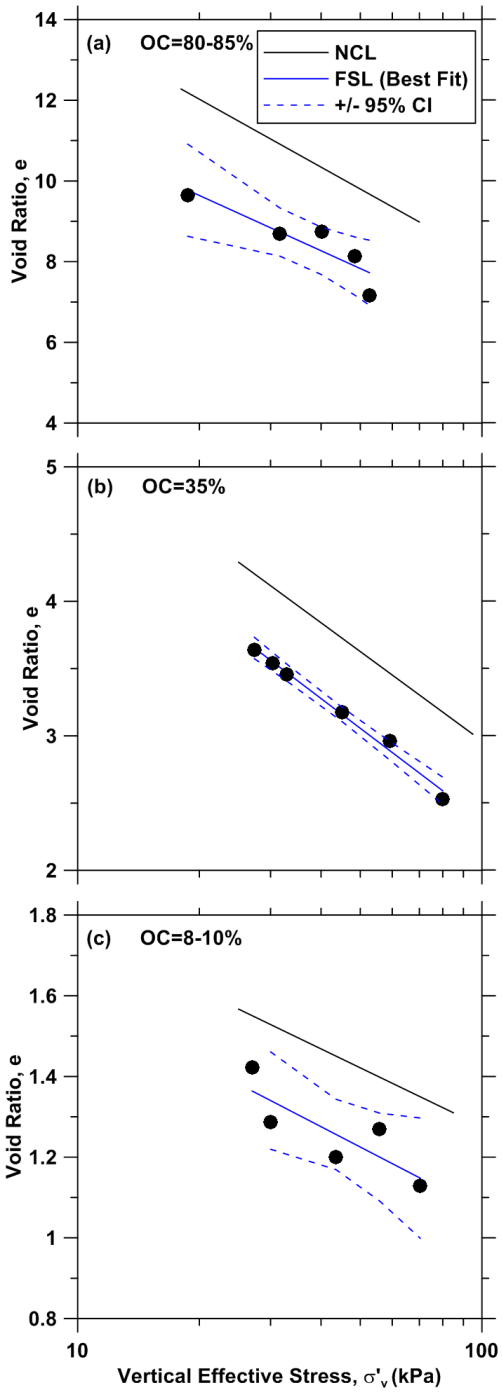

Figure 6.6 Failure states of the specimens from constant volume monotonic DSS tests

Table 6.2. Slopes of NCL and FSL

OC (%)	Slope of NCL	Slope of FSL±SE
80-85	2.43	1.98±0.55
35	0.96	0.99±0.05
8-10	0.21	0.23±0.09

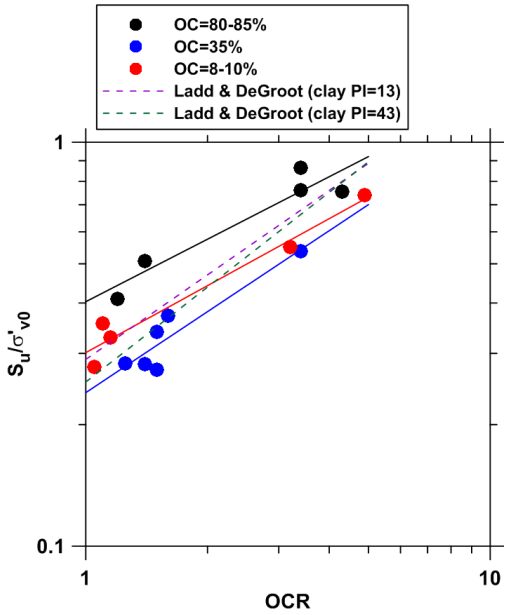

Figure 6.7 Normalized shear strength from constant volume DSS tests along with the trends suggested by Ladd and DeGroot (2003) for clays with different PI

Table 6.3. Regression parameters from Eq. (6.1)

OC (%)	s±SE	m±SE
80-85	0.40±0.04	0.51±0.10
35	0.24±0.02	0.67±0.13
8-10	0.30±0.02	0.55±0.07

6.4 STRAIN-CONTROLLED CONSTANT-HEIGHT CYCLIC DSS TESTS WITH POST-CYCLIC VOLUME CHANGE MEASUREMENTS

Following consolidation, strain-controlled multi-stage cyclic DSS testing was performed under constant volume conditions, in stages having shear strain amplitudes ranging from 0.01 to ≥10%. Each stage of loading consisted of either 5, 15, or 30 uniform strain cycles with various amounts of static shear stress at a loading frequency of 1.0 *Hz*. Most tests were performed under 'base-line' conditions consisting of 15 uniform strain cycles and zero static shear stress. No piezometric measurements were made either during the static load application phase or during the cyclic shearing phase. During consolidation, the static loads are applied for a time interval sufficient to complete consolidation and reduce secondary compression-induced pore pressure increments below target values, as described in Section 6.2. The times required to achieve these objectives are based on experience from consolidation testing. During cyclic shear, pore pressures are inferred based on the change in vertical stress required to maintain constant height.

Following each stage of cyclic shearing, specimens were allowed to reconsolidate to their initial consolidation stress and volume changes were monitored. Strain-controlled cyclic shearing was preferred to stress-controlled tests because we believe post-cyclic volume change is more fundamentally related to the cyclic shear strain amplitude. To evaluate the effect of number of loading cycles on the post-cyclic behavior of the peat, a few tests were performed under 5 and 30 uniform strain cycles. To evaluate the effects of non-zero static shear stresses, some tests were carried out under stress-controlled conditions with $\alpha = 0.1, 0.2, \text{and } 0.3$, where $\alpha = {}^{\tau_s}/_{\sigma_{v0}}$ is the ratio of static shear stress to initial total vertical stress. Note that in applications elsewhere α is defined using the pre-shear vertical effective stress, but in the present case the total stress is used. The use of total stress is motivated by it being the measured quantity (due to piezometers not

having been used during the pre-shear application of static loads). However, for practical purposes pore pressures are expected to be very small, so that the effective and total stresses should be nearly identical. Table 6.4 presents test matrix for the cyclic DSS tests.

Figs. 6.8 to 6.10 show results of a typical DSS test sequences on a peaty specimen under shear strain amplitudes (γ_c) of 0.4%, 1.2% and 4.0% respectively. For γ_c= 0.4%, the cyclic pore pressure ratio $r_u = \Delta u/\sigma_{v0}$ is almost zero (Fig. 6.8c). Although hysteresis loops form, no degradation occurs (Fig. 6.8b), and the stress path in $\sigma'_v/\sigma_{v0} - \tau/\sigma_{v0}$ space is essentially vertical, similar to the stress path of a drained test (Fig. 6.8a). When γ_c is increased to 1.2%, excess pore pressures develop during cyclic shearing, and residual pore pressure (r_{ur}) is slightly larger than zero (Fig. 6.9c). Hysteretic damping also increases with low degradation (Fig. 6.9b). On the other hand, when γ_c is increased to 4%, r_u increases with each cycle and r_{ur} reaches 0.1 after 15 cycles (Fig. 6.10c). The soil stiffness degrades slightly as evidenced by reductions in the shear stress (Figs. 6.10b) to achieve the uniform strain amplitude. Interestingly, the specimen initially exhibits dilative behavior until achieving the maximum shear stress, followed by contractive behavior during unloading until shear stress becomes zero. The next half cycle again starts with a dilative behavior followed by contractive behavior. Appendix A presents all the cyclic DSS test results from this study.

Table 6.4. Cyclic direct simple shear test matrix

Specimen ID	Sample Depth (m)	Specimen Depth (m)	OC (%)	OCR	σ_{v0} *(kPa)*	N	α	NLS[a]	e_c[b]
BH3S2_1.70	1.60-1.75	1.70	65	1.14	39.4	15	0	3	5.371
BH6S4_2.25	2.00-2.45	2.25	67	4.83	12.1	15	0	3	4.862
BH6S2_2.85	2.75-3.20	2.85	48	4.49	13.4	15	0	7	5.048
BH6S8_3.15	2.75-3.20	3.15	48	1.33	67.5	15	0	3	4.352
BH6S4_4.35	4.10-4.60	4.35	10	1.25	84.0	15	0	4	2.082
BH7S1_2.20	2.15-2.60	2.20	58	1.18	34.0	15	0.1	3	5.262
BH7S2_2.25	2.15-2.60	2.25	58	1.18	34.0	15	0.3	3	5.262
BH7S10_3.15	2.75-3.20	3.15	35	4.92	12.2	15	0	7	3.555
BH8S1_2.20	2.15-2.60	2.20	70	1.75	100.0	15	0	6	4.037
BH8S3_2.25	2.15-2.60	2.25	70	2.04	32.7	5	0	3	5.371
BH8S4_2.30	2.15-2.60	2.30	70	2.32	72.7	30	0	5	4.104
BH9S1_2.20	2.15-2.60	2.20	60	3.60	16.7	15	0.2	2	7.215
BH9S2_2.25	2.15-2.60	2.25	60	3.46	17.0	15	0.2	2	7.211
BH9S4_2.30	2.15-2.60	2.30	60	1.18	34.0	15	0.1	3	8.190
BH9S5_2.35	2.15-2.60	2.35	60	1.18	34.0	15	0.2	3	8.190
BH9S6_2.40	2.15-2.60	2.40	60	1.18	34.0	15	0.3	3	8.190
BH9S8_2.45	2.15-2.60	2.45	60	1.18	34.0	15	0	6	8.194
BH9S9_2.50	2.15-2.60	2.50	60	1.18	34.0	15	0.2	3	8.189

[a]Number of Loading Stages

[b]Post-Consolidation Void Ratio

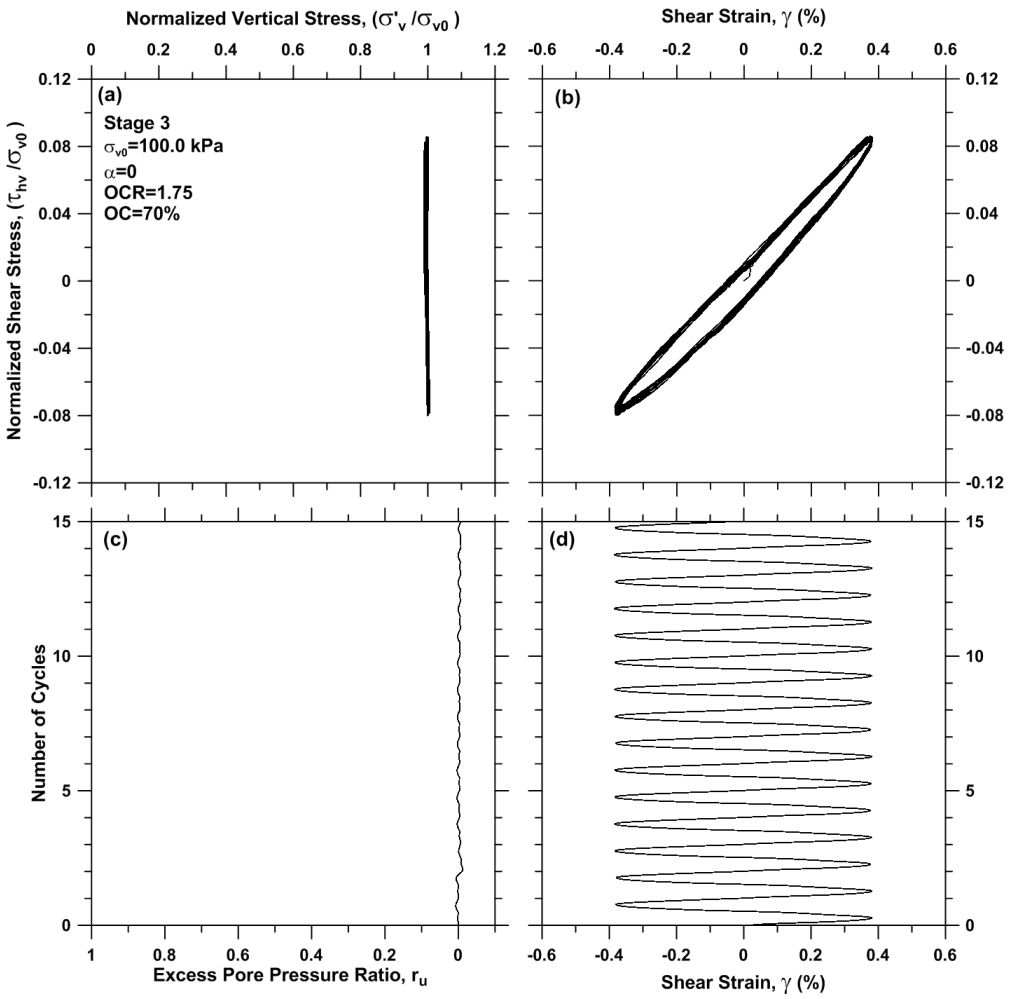

Figure 6.8 Typical cyclic DSS test results when shear strain amplitude is low (specimen: BH8S1_2.20)

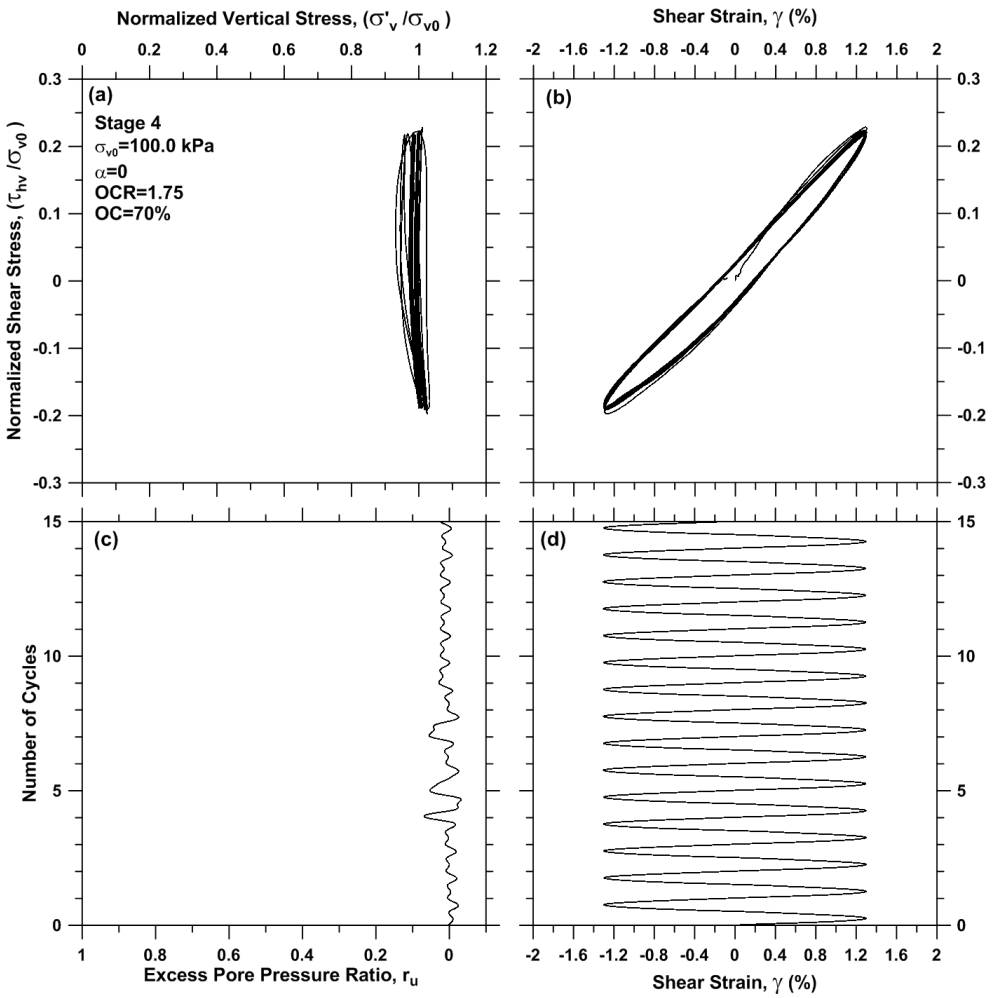

Figure 6.9 Typical cyclic DSS test results when shear strain amplitude is medium (specimen: BH8S1_2.20)

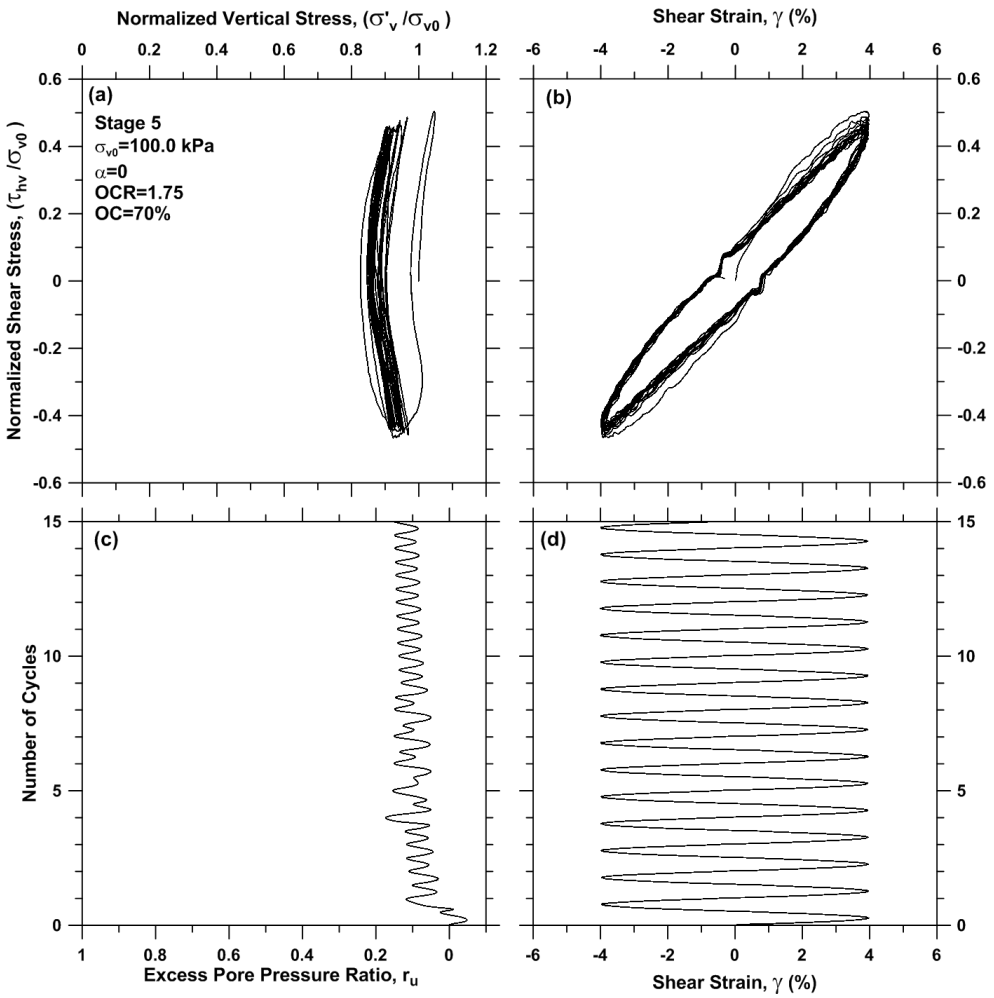

Figure 6.10 Typical cyclic DSS test results when shear strain amplitude is high (specimen: BH8S1_2.20)

Fig. 6.11 shows the residual pore pressure at the end of cycle 15, which is denoted $r_{ur,15}$ as a function of the shear strain amplitude, for all the specimens tested in this study with an organic content ranging between 35 to 70%. Part a of the figure shows the data over the full range of $r_{ur,15}$ that was observed in the tests. Part b of the figure zooms in on the lower end of the $r_{ur,15}$ range so as to more clearly indicate the strain level where $r_{ur,15}$ begins to exceed zero. Based on Fig. 6.11b, the threshold shear strain (γ_{tp}) below which no residual pore pressure develops is

around 0.7%. The pore pressure generation markedly increases for cyclic shear strain amplitudes larger than 1.0% and reaches values as high as 0.4. For comparison, initial liquefaction of sand is defined as r_u = 1.0 (e.g., Seed, 1979), so the pore pressure generation in peat is much smaller. Normally consolidated clays that are cyclically sheared sufficiently to achieve cyclic softening have been observed to have pore pressure ratios within the range 0.30 to 0.80, which develop for shear strain amplitudes varying from 1 to 9.5% (Boulanger and Idriss 2006; Chu et al. 2008; Dahl et al. 2014).

Pore pressure readings from piezometers installed in Sherman Island peat underlying a model levee subject to forced-vibration testing (Reinert et al. 2015) are also plotted in Fig. 6.11. Shear strains were computed from displacement gradients obtained from subsurface acceleration measurements. Field data are in accordance with the lab data, and do not show any remarkable pore pressure build-up when shear strain is less than 1%.

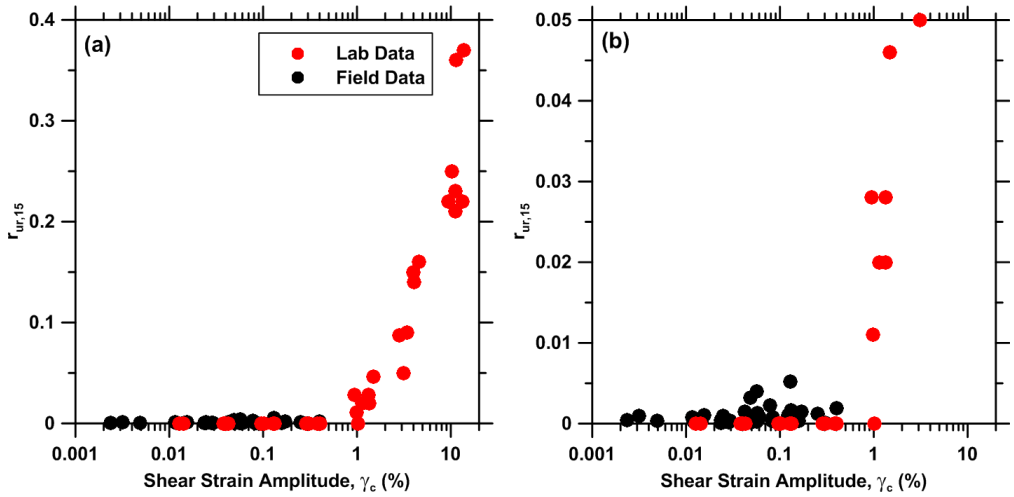

Figure 6.11 Excess pore pressure build-up in Sherman Island peat as a function of shear strain amplitude

6.4.1 Post-Cyclic Shear Behavior: Reset of Secondary Compression Clock by Cyclic Straining

Following the end of cyclic loading, volume change was allowed to occur by enabling drainage through the top cap, which in turn lowered pore pressures and restored the vertical effective stress to its original value in place prior to the start of cyclic loading. Water was allowed to drain from the top of the specimen while pore pressure was monitored at the bottom. The end of primary consolidation (t_p) was found to occur after about 1 min., and consolidation was monitored for at least 20 minutes following each stage to measure secondary compression. Volume change that occurred for $t > t_p$ is attributed to secondary compression, although I recognize that some fraction of the volume change that occurs during $t < t_p$ is likely also affected by secondary compression.

Test results for a peat specimen with 70% organic content, σ_{v0}=100 *kPa*, and OCR = 1.75 is shown in Fig. 6.12, which show that volumetric strain (ε_v) increases with γ_c. Residual pore pressure ratio ($r_{ur,15}$) is nonzero when $\gamma_c > 0.7\%$, with $r_{ur,15} = 0.37$ for γ_c=13.69% (Fig. 6.11b). As shown in Fig. 6.12(a), although these $r_{ur,15}$ values are modest, postcyclic volumetric strains are significant when $\gamma_c > 0.7\%$, because of the peat's high compressibility. Fig. 6.12(c) shows that the secondary compression rate, which is related to the difference between post-cyclic volumetric strain ($\varepsilon_{v,pc}$) at 1 and 20 min, increases with γ_c. This suggests that cyclic straining can increase the secondary compression rate, which has not been previously recognized. Similar increases in secondary compression rate are routinely observed when total stress is increased in laboratory odometer tests (as explained in Sec. 5.5), which can be viewed as resetting the secondary compression clock to zero at the time the load is applied. The data in Fig. 6.12 indicate that cyclic straining can at least partially reset the secondary compression clock without

total stress increase. All the test results from the post-cyclic volumetric strain measurements are shown in Appendix A.

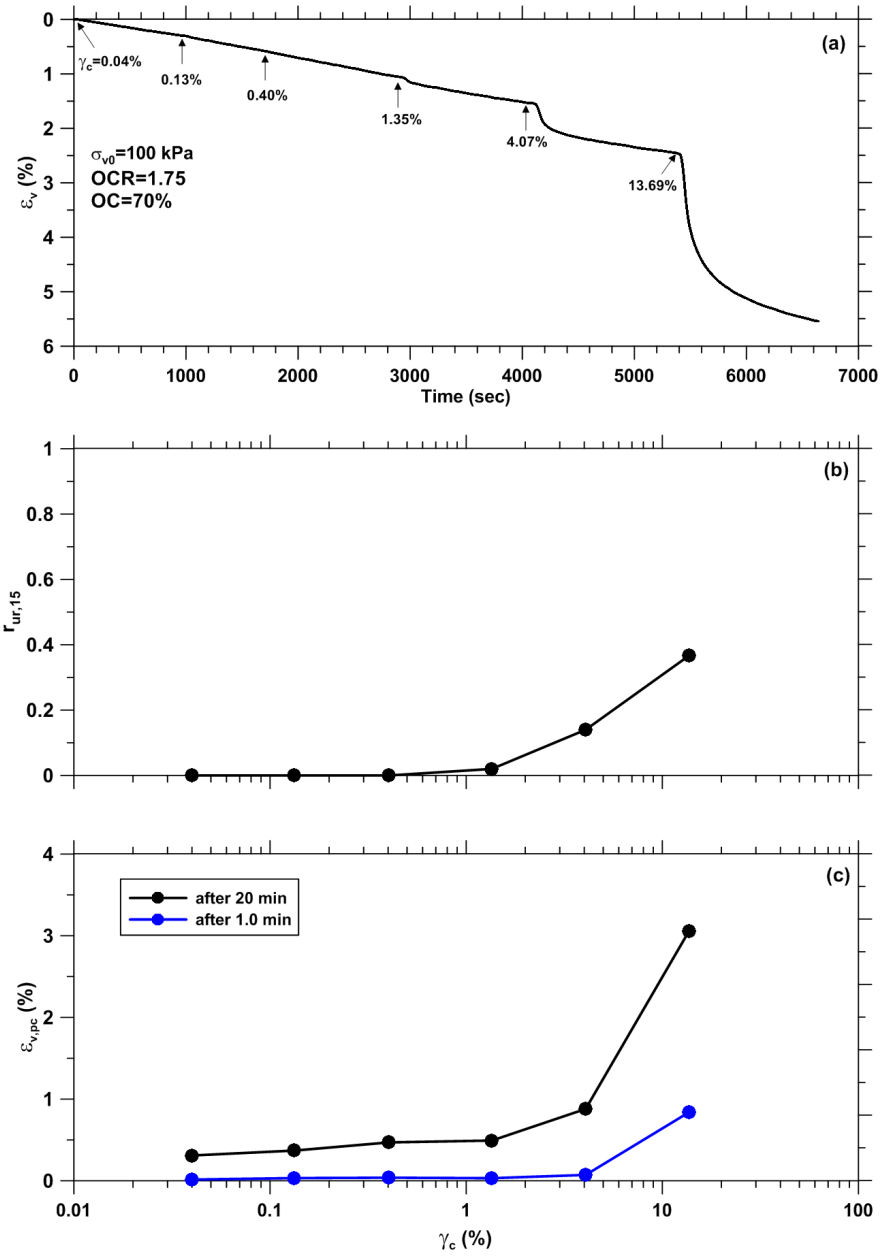

Figure 6.12. Cyclic DSS test results of Sherman Island peat (a) volumetric strain (ε_v) versus time (t); (b) residual pore pressure ratio after 15 cycles ($r_{ur,15}$) versus cyclic shear strain amplitude (γ_c); (c) ε_v versus γ_c

Fig. 6.13 shows the loading path in $e - log\sigma'_v$ space followed during and after cyclic DSS testing. The initial state of the overconsolidated peat is at point A. Cyclic shearing builds up pore pressure in the specimen and causes σ'_v to decrease (while void ratio remains constant) as indicated by path A-B. Post-cyclic reconsolidation happens through path B-C followed by secondary compression through path C-D. Based on Eq. (5.2), the rate of secondary compression at point C should be less than the rate at point A ($\dot{\varepsilon}_{v,C}^{sc} < \dot{\varepsilon}_{v,A}^{sc}$) because point C is farther below the SCRL. However, as shown on Figs. 6.12 (a) and (c), $\dot{\varepsilon}_{v,C}^{sc}$ is greater than $\dot{\varepsilon}_{v,A}^{sc}$. This means that secondary compression has been reset (at least partially) following cyclic loading. This can be modeled as a downward shift in the secondary compression reference line from A' to A''.

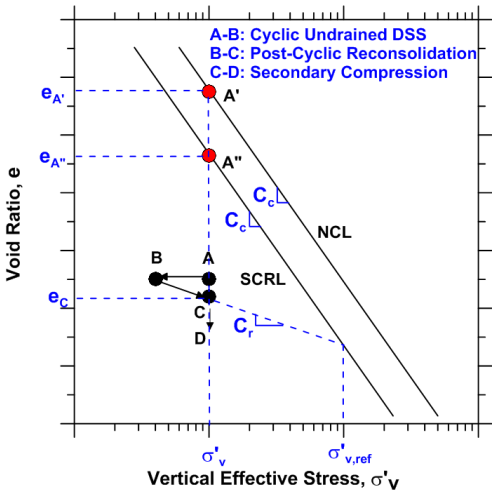

Figure 6.13 Reset of secondary compression clock

The approach adopted herein is to measure the rate of void ratio change during post-cyclic reconsolidation, and subsequently compute the value of $e_{A''}$ that matches the measured rate. The equation for rate of change of void ratio is given by Eq. 6.2.

$$\dot{e}^{sc} = \frac{-a}{t_{ref}} exp\left(\frac{e_C - e_{A"}}{a}\right) \tag{6.2}$$

where $a = C_\alpha / ln10$, and t_{ref} is the time since load application associated with the reference time-line (i.e., $t_{ref} = t_p$ if the reference time-line is the NCL).

The amount of reset can be quantified by introducing a dimensionless reset index (I_R), which is defined as follows (see Fig. 6.13):

$$I_R = \frac{\overline{A'A''}}{\overline{A'C}} = \frac{e_{A'} - e_{A''}}{e_{A'} - e_C} \tag{6.3}$$

The value of I_R varies between 0 (no reset) to 1 (full reset). For classical consolidation tests with *LIR*=1.0, we assume that I_R is equal to zero.

An example of how to compute I_R is described here. Fig. 6.14 presents post-cyclic void ratio following stage 2 of cyclic strain-controlled shearing on the specimen BH6S4_2.25 (see Table 6.4). Fig. 6.15 presents the location of the NCL in $e - log\sigma'_v$ space along with the required values of void ratios to calculate reset index. For this specimen: C_c=2.96, C_r=0.17, C_α=0.24 (see Table 5.1), t_{ref}=t_p=190 *s* (Fig. 6.16), σ'_v=12.1 *kPa*, e_c=4.862 (see Table 6.4), and $\dot{e}^{sc} = \dot{\varepsilon}_v^{sc} \times (1 + 4.862) = 1.90 \times 10^{-6}$ s^{-1} (see Fig. 6.14 for the value of $\dot{\varepsilon}_v^{sc}$). After plugging the appropriate values of C_c, C_r, C_α, t_{ref}, σ'_v and $\dot{e}_v^{sc}$ in Eq. (6.1), $\sigma'_{v,ref}$=19.9 *kPa* is obtained (see Fig. 6.15). Then, the value of $e_{C\alpha,ref}$ can be calculated from Eq. (6.3): $e_{C\alpha,ref} = 4.860 + (2.96 - 0.17) \log\left(\frac{12.1}{19.9}\right) = 5.461$. In addition, $e_{NCL} = 6.827$ (see Fig. 6.15). Finally, from Eq. (6.4): $I_R = \frac{6.827 - 5.461}{6.827 - 4.860} = 0.69$.

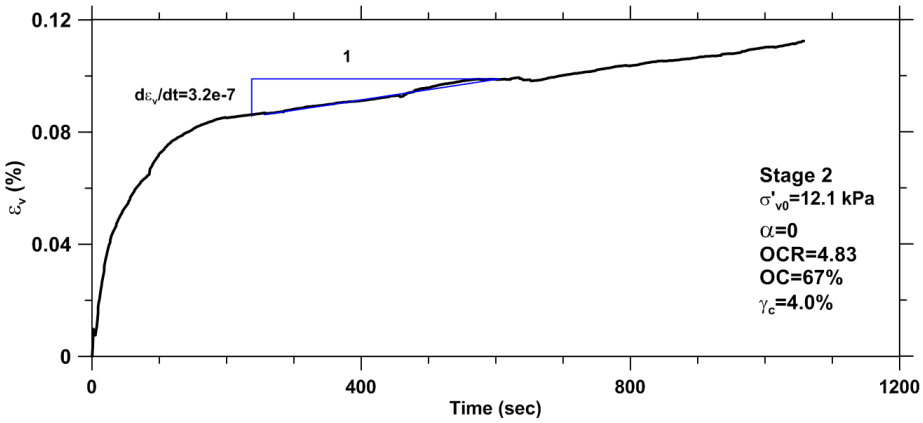

Figure 6.14 Post-cyclic volume change for specimen BH6S4_2.25 following strain-controlled test with γ_c=4%

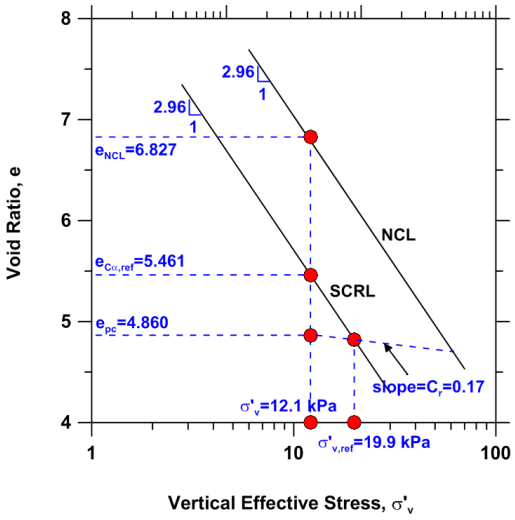

Figure 6.15 An example of reset index computation from cyclic straining: specimen BH6S4_7.3 (OC=67%, OCR=4.83 and γ_c=4%)

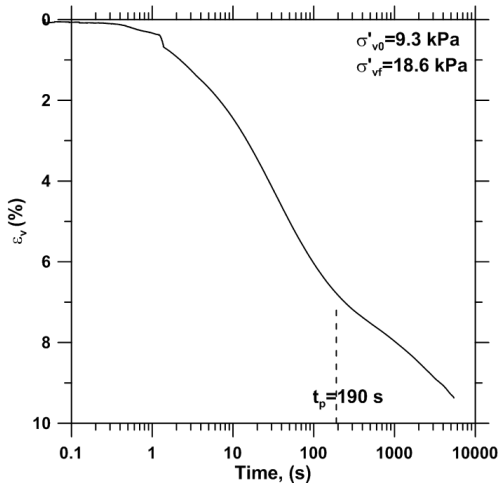

Figure 6.16 Oedometer test result for specimen BH6S2_6.9

Fig. 6.17 shows I_R as a function of γ_c from cyclic DSS testing with *N*=15 and α=0. As shown, I_R increases with γ_c, and can reach as high as 0.96 when γ_c is 11.2%. In addition, cyclic loading can reset the secondary compression clock even if $\gamma_c < \gamma_{tv}$. For $\gamma_c < 1\%$ the value of I_R can be as large as 0.4, despite the absence of cyclic pore pressure build-up.

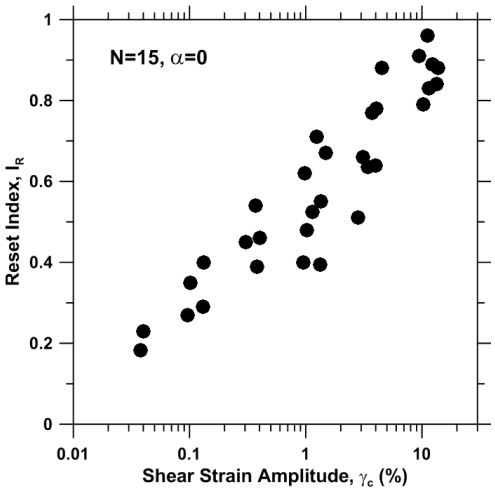

Figure 6.17 Reset index as a function of shear strain amplitude

6.4.2 Effect of Static Shear Stress

Levees induce static shear stresses in the peat. Boulanger (2003) has shown how static shear stress can affect liquefaction triggering resistance in sands, which was extended for applications to cyclic softening of clays by Boulanger and Idriss (2007). To evaluate the effects of static shear stress on the post-cyclic behavior of peat, five multi-stage cyclic constant-volume DSS tests were carried out under stress-controlled conditions (see Table 6.3). Strain-controlled conditions cannot be utilized while maintaining a constant static shear stress.

Fig. 6.18 shows results of a typical DSS test sequence with static shear stress on a peaty specimen. Shear strain amplitude accumulates in the direction of static shear stress during the test (Fig. 6.18d). As evidenced from Fig. 6.18(b), the specimen exhibits mild degradation in stiffness with a degradation index (Idriss et al. 1978) of 0.06 (degradation index=$\frac{Log\left(G_N/G_1\right)}{logN}$, in which G_1 and G_N are shear modulus at the first and *N*th cycles of loading). As shown in Fig. 6.18c, the residual excess pore pressure ratio increases quickly in the first few cycles, then increases more gradually for the remaining cycles until reaching a peak value of 0.20 at the end of cyclic shearing. Fig. 6.18d shows that the specimen demonstrates viscous behavior in the direction of applied static shear stress (Fig. 6.18b), as indicated by the rounded ends of the stress-strain loops.

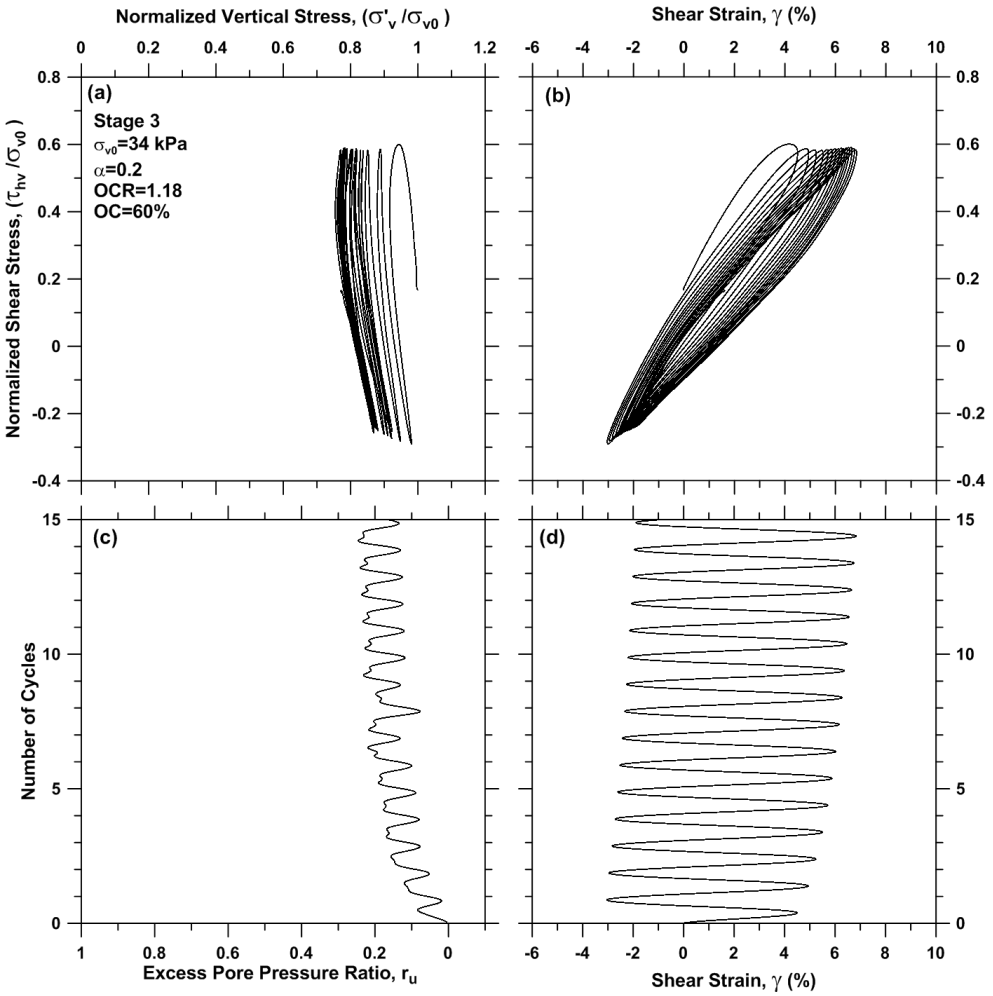

Figure 6.18 Typical cyclic stress-controlled DSS test results on Sherman Island peat in the presence of static shear stress

Fig. 6.19 presents post-cyclic volume change ($\varepsilon_{v,pc}$) in term of post-cyclic shear strain (γ_{pc}), which is the shear strain that accumulates under constant static shear stress while drainage and secondary compression develop upon the conclusion of cyclic loading. Fig. 6.19 indicates that $\varepsilon_{v,pc}$ increases nearly proportionately with γ_{pc}, which is the case for all the tests with finite static shear stress (see Appendix A). For comparison with the strain-controlled tests with zero static shear stress, an average value of γ_c is computed over the 15 loading cycles from the measured strain history (γ_c= 4.88% in this example). The reset index was computed for all of the tests with static shear stress and are plotted in Fig. 6.20 with the data collected without a static shear stress. The value of I_R increases as α increases. All the cyclic and post-cyclic test results are shown in Appendix A.

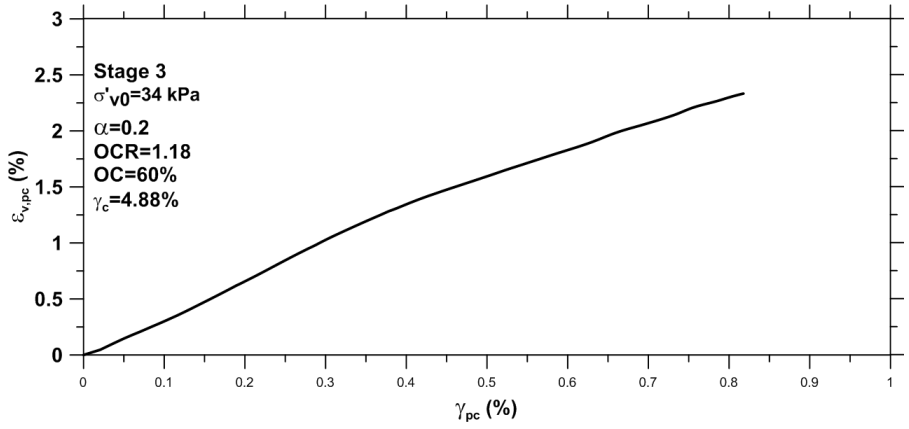

Figure 6.19 Effect of static shear stress on the post-cyclic strains

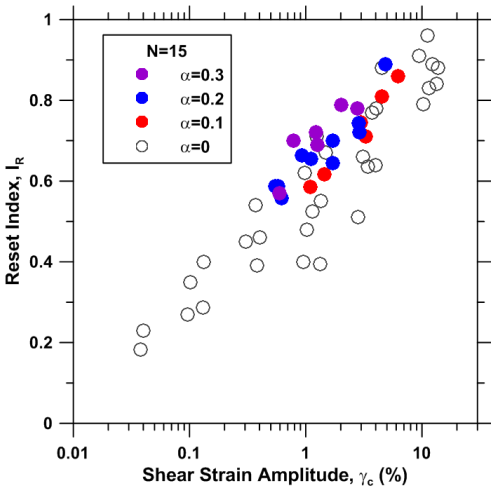

Figure 6.20 Effect of static shear stress on reset index

6.4.3 Effect of Number of Uniform Loading Cycles (*N*)

Most of the tests in this study were conducted with N=15. The influence of number of loading cycles on liquefaction triggering evaluation is well-understood and can be expressed using a magnitude scaling factor, C_M (e.g., Youd et al. 2001; Idriss and Boulanger 2008). Scaling factor C_M takes on a reference value of unity for **M** 7.5 earthquakes. Earthquakes that produce larger numbers of cycles (typically involving **M** > 7.5) for the same stress amplitude are more demanding on the soil, which is reflected through a capacity reduction (i.e., the capacity at 15 cycles is normalized by C_M, which is > 1 in this case). The scaling factor C_M can alternatively be related directly to the number of cycles, for which available GMPEs indicate dependence on **M**, source to site distance and site conditions (e.g., Liu et al. 2001; Bommer et al. 2009).

Relations for C_M, or equivalently the effect of N on cyclic degradation, have been developed for liquefaction problems (e.g., Seed et al. 1975; Liu et al. 2001; Idriss and Boulanger 2008) and cyclic softening problems (Boulanger and Idriss 2007). However, no such relations exist for secondary compression reset or excess pore pressure development in peat. For this reason, we

compile test results at *N*=5 and *N*=30 to observe the influence of number of cycles (see Table 6.3). Fig. 6.21 presents the effect of *N* on I_R, and indicates that I_R increases with *N*.

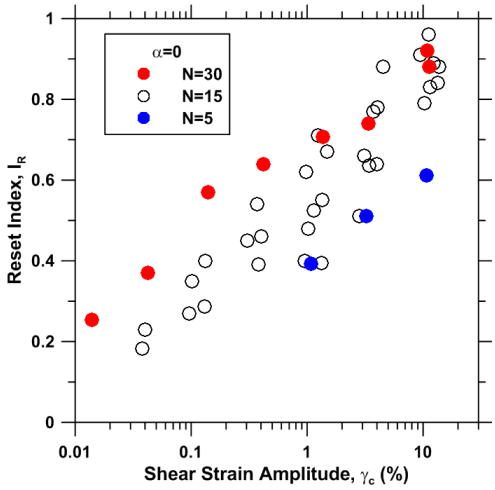

Figure 6.21 Effect of number of uniform loading cycles on reset index

6.5 POST-CYCLIC SHEAR STRENGTH

Cyclic loading in cohesive soils has been observed to cause a reduction in post-cyclic undrained stiffness and shear strength for sensitive soils (e.g., Thiers and Seed 1969; Yasuhara 1994) (other tests have shown a lack of post-cyclic strength reduction for non-sensitive soils; Castro and Christian, 1976). Two cyclic constant-volume DSS tests (with *f*=1 *Hz* and *N=15*) followed by constant volume monotonic shear tests (with no change in volume allowed between cyclic and monotonic loading) were performed on Sherman Island peat at different organic contents to investigate this aspect of soil behavior (Figs 6.22 and 6.23). Test results from monotonic constant-volume DSS tests are superimposed on Figs. 6.22 and 6.23 for reference purposes. As evidenced from Fig. 6.22(a), a specimen with OC=58% subjected to cyclic loading with $\gamma_c = 11.9\%$ experienced an undrained shear strength decrease of 24%. As shown in Figure

6.22c, this specimen had reached $r_{ur,15}$ = 0.37. Figure 6.23 shows results for a specimen with OC=35%, which exhibited 26% undrained strength decrease following cyclic shearing (γ_c = 9.9%, $r_{ur,15}$ = 0.37). In our testing program, we did not shear the soil to sufficiently large strains to observe possible soil sensitivity.

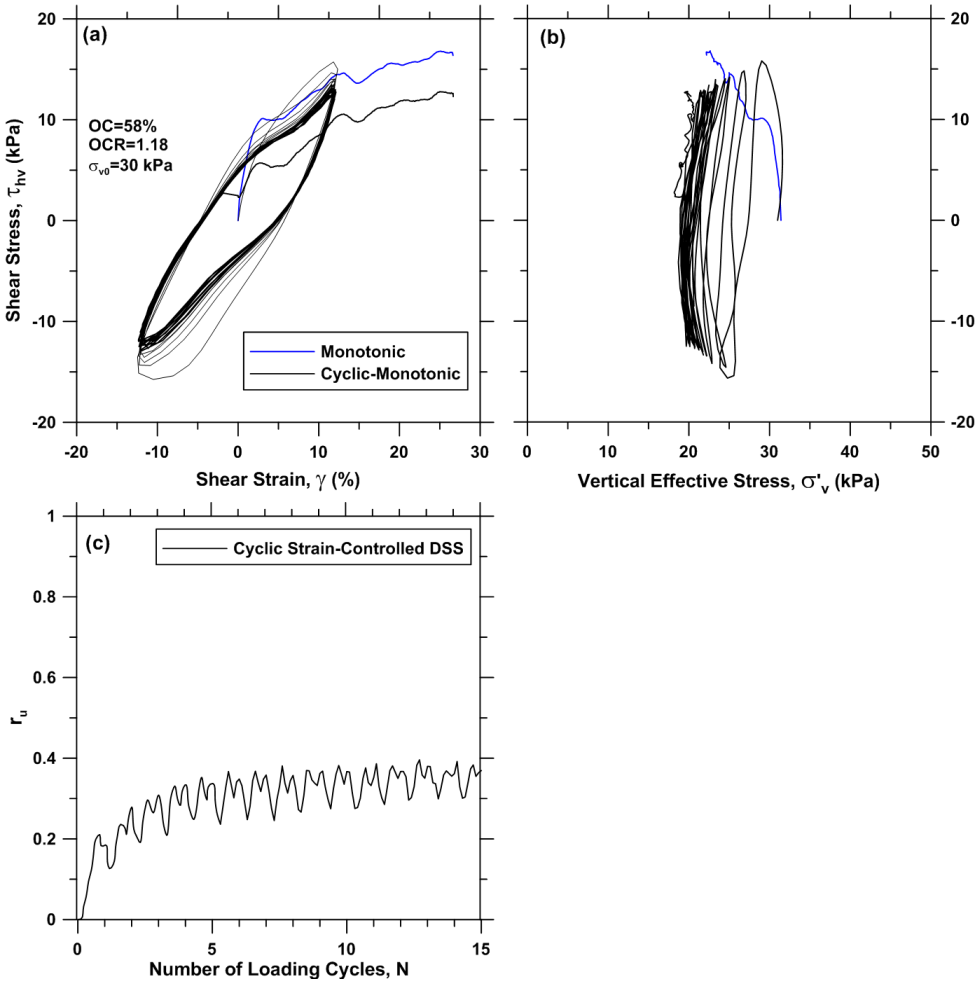

Figure 6.22 Effect of cyclic loading on the undrained shear strength of peat with OC=58%

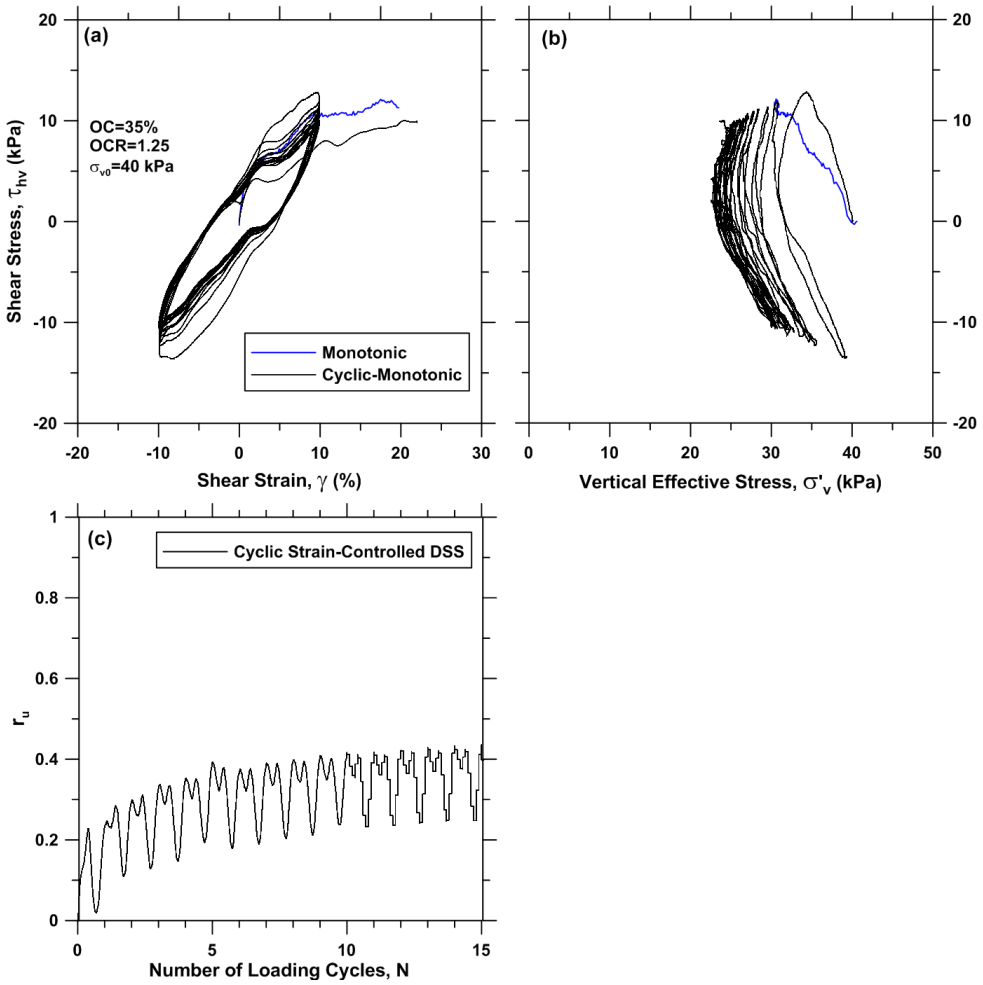

Figure 6.23 Effect of cyclic loading on the undrained shear strength of peat with OC=35%

6.6 EMPIRICAL MODEL FOR RESET INDEX

The results of cyclic DSS tests were regressed to develop prediction equations for reset index (I_R). Variables considered in the regression are: cyclic shear strain amplitude (γ_c) number of cycles (N), organic content (OC), vertical effective consolidation stress prior to the onset of cyclic shear (σ'_{v0}), overconsolidation ratio, (OCR), and static shear stress ratio (α). Vertical effective stress σ'_{v0} is used here because the model is intended for field applications, where effective stresses are distinct from total stresses. In the development of the model, as explained previously, the vertical total consolidation pressure (σ_{v0}) applied to the specimen is taken as equivalent to σ'_{v0}. Various forms for the regression equation were explored. The following equation was ultimately selected to represent the reset index:

$$I_R = \gamma_c^{a_1} N^{a_2} (a_3\alpha + a_4)\left(a_5 \frac{OC}{100} + a_6\right)\left(a_7 \frac{\sigma'_{v0}}{p_a} + a_8\right)(a_9 OCR + a_{10}) \qquad 0 \leq I_R \leq 1.0 \qquad (6.5)$$

where p_a is atmospheric pressure, and a_1 to a_9 are the constants obtained from regression analyses as given in Table 6.5 along with the standard deviation ($\sigma_{res.}$) of the residuals. Table 6.6 lists the data set used in the regressions. Residuals of the prediction equations were computed as:

$$Residual = y - \hat{y} \qquad (6.6)$$

where y is the observed value (here refers to test data), and $\hat{y}$ is the predicted value. The residuals are computed in arithmetic units because the data were found to be normally distributed based on the Pearson (1900) test that shows the residuals are normal with 99.2% confidence. The COV for the model, listed in Table 6.5, is computed by normalizing each residual by $\hat{y}$, and then computing the standard deviation of the normalized residuals.

Table 6.5. Constants of the regression model for I_R

a_1	a_2	a_3	a_4	a_5	a_6	a_7	a_8	a_9	a_{10}	$\sigma_{res.}$	COV
0.219	0.261	0.899	0.939	-0.043	0.300	0.192	0.918	0.009	0.980	0.068	0.113

Fig. 6.24 presents the residuals of I_R based on Eq. (6.6), which are plotted relative to N, α, OCR, OC, and σ'_{v0}. The residuals do not show any significant trends with respect to any of the variables. Fig. 6.25 presents the data points along with the model as shown by dashed least squares regression curves for different cases. Reset index increases as both N and α increase.

Table 6.6. Data set used for a mathematical model for I_R

γ_c (%)	OC (%)	OCR	σ'_{V0} (kPa)	α	N	I_R
0.95	65	1.14	39.4	0	15	0.40
2.82	65	1.14	39.4	0	15	0.51
9.5	65	1.14	39.4	0	15	0.91
1.33	67	4.83	12.11	0	15	0.40
4.0	67	4.83	12.11	0	15	0.64
13.33	67	4.83	12.11	0	15	0.84
0.096	48	4.49	13.37	0	15	0.27
0.99	48	4.49	13.37	0	15	0.62
1.49	48	1.33	67.5	0	15	0.67
4.55	48	1.33	67.5	0	15	0.88
11.16	48	1.33	67.5	0	15	0.96
0.102	35	4.92	12.2	0	15	0.35
0.307	35	4.92	12.2	0	15	0.45
1.02	35	4.92	12.2	0	15	0.48
3.12	35	4.92	12.2	0	15	0.66
10.24	35	4.92	12.2	0	15	0.79
0.04	70	1.75	100	0	15	0.23
0.133	70	1.75	100	0	15	0.40
0.404	70	1.75	100	0	15	0.46
1.35	70	1.75	100	0	15	0.55
4.07	70	1.75	100	0	15	0.78
13.7	70	1.75	100	0	15	0.88
0.37	10	1.25	84	0	15	0.54
1.235	10	1.25	84	0	15	0.71
3.7	10	1.25	84	0	15	0.77
12.35	10	1.25	84	0	15	0.89
0.04	60	1.18	34	0	15	0.18
0.13	60	1.18	34	0	15	0.29
0.38	60	1.18	34	0	15	0.39
1.145	60	1.18	34	0	15	0.525
3.43	60	1.18	34	0	15	0.635
11.45	60	1.18	34	0	15	0.83
0.014	70	2.32	72.7	0	30	0.25
0.042	70	2.32	72.7	0	30	0.37
0.14	70	2.32	72.7	0	30	0.57
0.42	70	2.32	72.7	0	30	0.64
11.25	70	2.32	72.7	0	30	0.88
1.36	60	2.15	26.7	0	30	0.71
3.4	60	2.15	26.7	0	30	0.74
10.9	60	2.15	26.7	0	30	0.92
1.076	70	2.04	32.7	0	5	0.39
3.23	70	2.04	32.7	0	5	0.51
10.764	70	2.04	32.7	0	5	0.61
3.28	60	1.18	34	0.1	15	0.71
4.53	60	1.18	34	0.1	15	0.81
6.215	60	1.18	34	0.1	15	0.86

Table 6.6. Continued

1.10	58	1.18	34	0.1	15	0.59
1.45	58	1.18	34	0.1	15	0.62
2.98	58	1.18	34	0.1	15	0.75
0.62	60	1.18	34	0.2	15	0.56
0.55	60	1.18	34	0.2	15	0.59
2.9	60	1.18	34	0.2	15	0.72
1.105	60	3.46	17.3	0.2	15	0.65
1.71	60	3.46	17.3	0.2	15	0.64
0.58	60	3.6	16.7	0.2	15	0.59
0.934	60	3.6	16.7	0.2	15	0.66
0.78	60	1.18	34	0.3	15	0.70
1.23	60	1.18	34	0.3	15	0.72
2.8	60	1.18	34	0.3	15	0.78
0.594	58	1.18	34	0.3	15	0.57
1.254	58	1.18	34	0.3	15	0.69
2.025	58	1.18	34	0.3	15	0.79

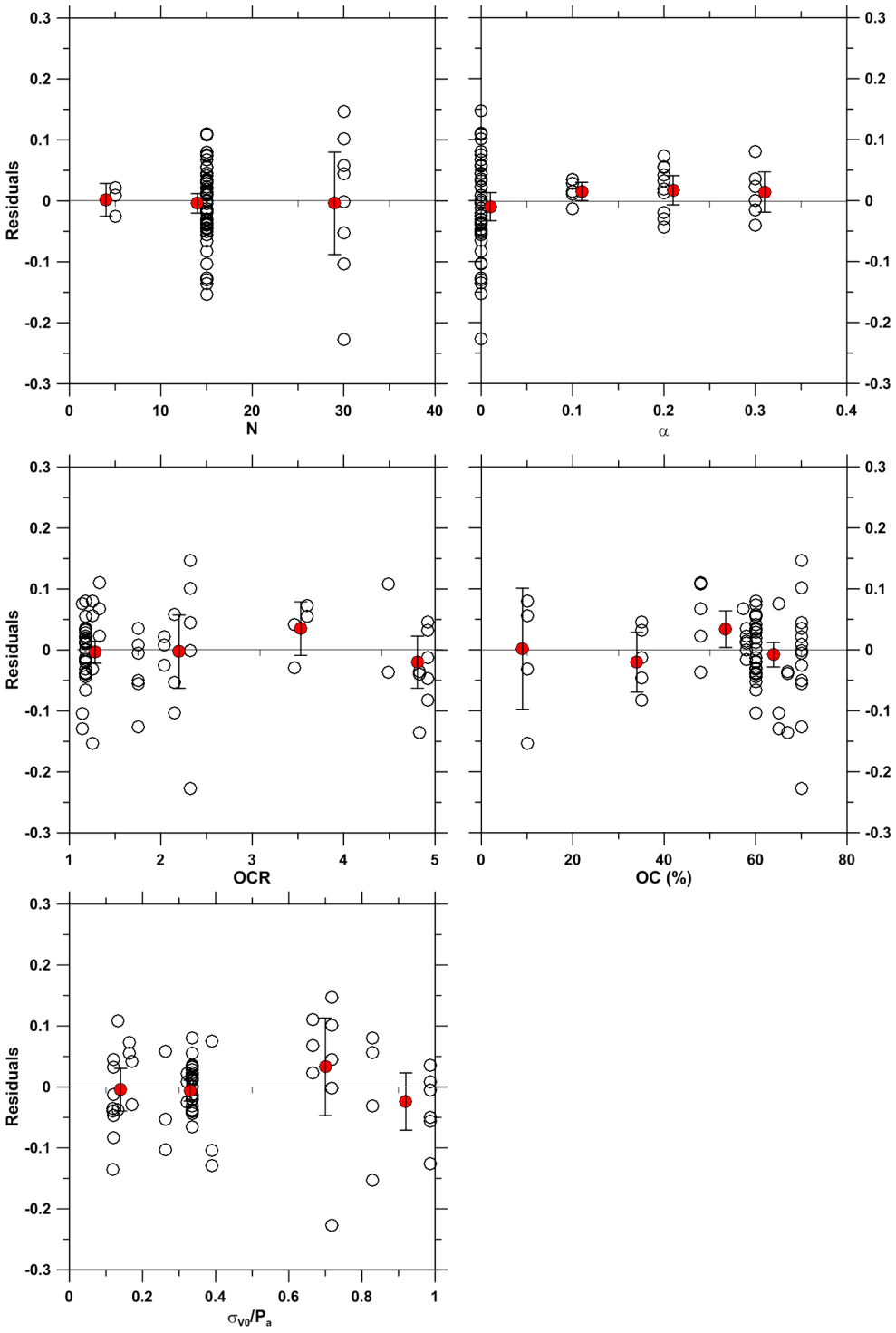

Fig.6.24 Residuals in reset index along with binned means± 95% confidence interval in terms of different variables

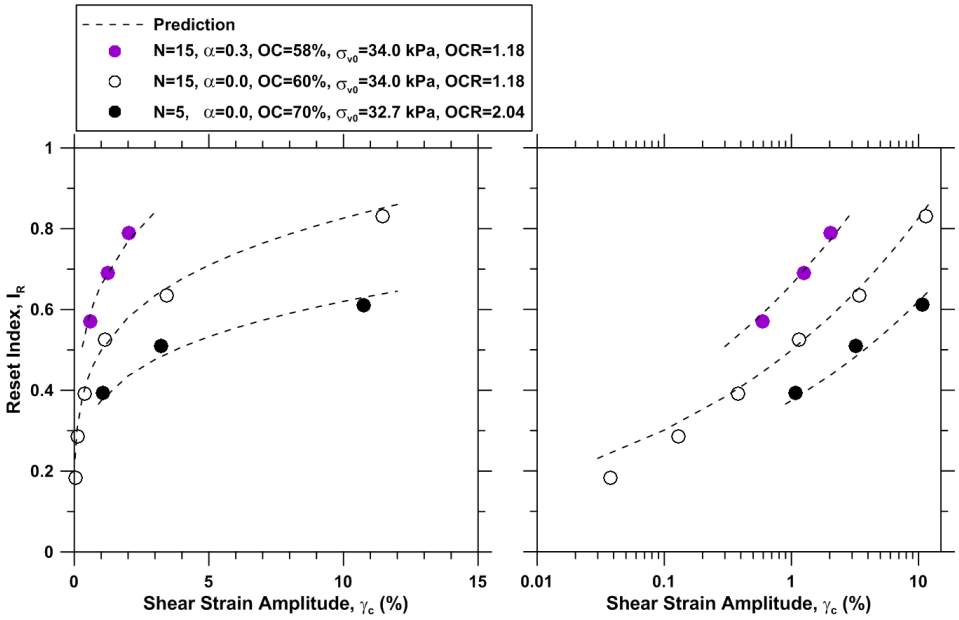

Fig.6.25 Trends of reset index with cyclic strain amplitude and number of cycles. Figure shows both the model predictions and relevant data points.

6.7 EMPIRICAL MODEL FOR RESIDUAL PORE PRESSURE RATIO

The results of cyclic strain-controlled DSS tests were regressed to develop prediction equations for residual pore pressure ratio (r_{ur}), defined as the cumulative increase in pore pressure ratio following cyclic shearing. Transient fluctuations of pore pressure during cyclic shearing result in peak values of r_u that are larger than r_{ur}, but r_{ur} was selected because it is more pertinent to post-cyclic reconsolidation. Variables considered in the regression are: γ_c, N, OC, and OCR. Table 6.5 lists the data set used in the regressions. Various forms for the regression equation were

explored, and the residuals were analyzed to identify any biases with respect to the regression variables. The following equation was ultimately selected to represent the pore pressure ratio:

$$r_{ur} = b_1(\gamma_c - \gamma_{tp})^{\,b_2}\, N^{b_3}\, OCR^{b_4}\, [b_5(\ln(OC) + b_6)] \quad if\ \ \gamma_c > \gamma_{tp} \tag{6.7}$$

$$r_{ur} = 0 \quad if\ \ \gamma_c \le \gamma_{tp}$$

where:

γ_{tp}= threshold shear strain below which no excess pore pressure develops (in percent)

b_1 to b_5= curve fitting parameters

Regression analysis yields the coefficients for use with Eq. (6.7) shown in Table 6.7 along with the COV and standard deviation of the predictions. The COV in Table 6.7 was computed as described in Section 6.6. Table 6.8 also lists the data set used in the regressions.

Table 6.7. Constants of the regression model for r_{ur}

b_1	b_2	b_3	b_4	b_5	b_6	$\sigma_{res.}$	COV
1.210	0.619	0.187	-0.264	-0.035	0.173	0.062	0.429

The value of γ_{tp} was anticipated to be a function of organic content as it transitions from a value appropriate to clay at low OC to a higher value at high OC. Therefore, non-linear regression analyses were performed introducing γ_{tp} as an independent variable. As shown in Figs. 6.26 and 6.27, γ_{tp} does indeed depend on OC, and is taken as 0.70 when $35\% \le OC \le 70\%$, and 0.10% for $OC \le 10\%$. The value of 0.10% at OC = 10% is consistent with prior results for clay (Hsu and Vucetic, 2006), which indicates that the behavior of this soil is dominated by

the clay matrix. Because of the lack of the data for 10% < OC <35%, it is assumed that γ_{tp} varies linearly with OC. The recommended procedure for analysis of γ_{tp} is as follows:

$$\gamma_{tp} = 0.024OC - 0.14 \quad 10\% \leq OC \leq 35\% \tag{6.8}$$
$$\gamma_{tp} = 0.10\% \quad 10\% > OC$$
$$\gamma_{tp} = 0.70\% \quad 35\% < OC$$

The r_{ur} residuals are computed using Eq. (6.6) in arithmetic units because the data were found to be normally distributed based on the Pearson (1900) test that shows the residuals are normal with 99.0% confidence.

Fig. 6.28 presents the residuals of r_{ur}, in terms of *N*, OCR, and OC. The residuals do not show significant trends with respect to *N*, OCR, or OC. Data at *N*=30 are somewhat sparse. More measurements at a high number of cycles would be needed to further study potential bias. Fig. 6.29 shows how the model trends with respect to cyclic shear strain amplitude and OC.

Table 6.8. Data set used for a mathematical model for r_{ur}

γ_c (%)	OC (%)	OCR	σ'_{V0} (kPa)	N	r_{ur}
0.95	65	1.14	39.4	5	0.027
2.82	65	1.14	39.4	5	0.078
9.5	65	1.14	39.4	5	0.19
0.95	65	1.14	39.4	15	0.028
2.82	65	1.14	39.4	15	0.087
9.5	65	1.14	39.4	15	0.22
1.33	67	4.83	12.11	5	0.02
4.0	67	4.83	12.11	5	0.12
13.33	67	4.83	12.11	5	0.17
1.33	67	4.83	12.11	15	0.028
4.0	67	4.83	12.11	15	0.15
13.33	67	4.83	12.11	15	0.22
0.014	48	4.49	13.37	15	0
0.043	48	4.49	13.37	15	0
0.096	48	4.49	13.37	15	0
0.286	48	4.49	13.37	15	0
0.99	48	4.49	13.37	5	0.01
0.99	48	4.49	13.37	15	0.011
1.49	48	1.33	67.5	5	0.03
4.55	48	1.33	67.5	5	0.11
11.16	48	1.33	67.5	5	0.17
1.49	48	1.33	67.5	15	0.046
4.55	48	1.33	67.5	15	0.16
11.16	48	1.33	67.5	15	0.23
0.013	35	4.92	12.2	15	0
0.04	35	4.92	12.2	15	0
0.102	35	4.92	12.2	15	0
0.307	35	4.92	12.2	15	0
1.02	35	4.92	12.2	15	0
3.12	35	4.92	12.2	5	0.05
10.24	35	4.92	12.2	5	0.23
3.12	35	4.92	12.2	15	0.05
10.24	35	4.92	12.2	15	0.25
0.04	70	1.75	100	15	0
0.133	70	1.75	100	15	0
0.404	70	1.75	100	15	0
1.35	70	1.75	100	5	0.01
4.07	70	1.75	100	5	0.12
13.7	70	1.75	100	5	0.27
1.35	70	1.75	100	15	0.012
4.07	70	1.75	100	15	0.14
13.7	70	1.75	100	15	0.37
0.012	10	1.25	84	15	0
0.037	10	1.25	84	5	0.005

Table 6.8. Continued

0.124	10	1.25	84	5	0.006
0.37	10	1.25	84	5	0.048
1.235	10	1.25	84	5	0.169
3.7	10	1.25	84	5	0.308
12.35	10	1.25	84	5	0.538
0.037	10	1.25	84	15	0.01
0.124	10	1.25	84	15	0.012
0.37	10	1.25	84	15	0.095
1.235	10	1.25	84	15	0.262
3.7	10	1.25	84	15	0.462
12.35	10	1.25	84	15	0.615
0.04	60	1.18	34	15	0
0.13	60	1.18	34	15	0
0.38	60	1.18	34	15	0
1.145	60	1.18	34	5	0.016
3.43	60	1.18	34	5	0.09
11.45	60	1.18	34	5	0.32
1.145	60	1.18	34	15	0.02
3.43	60	1.18	34	15	0.09
11.45	60	1.18	34	15	0.36
11.25	70	2.32	72.7	5	0.10
11.25	70	2.32	72.7	15	0.21
11.25	70	2.32	72.7	30	0.226
10.9	60	2.15	26.7	5	0.10
10.9	60	2.15	26.7	15	0.14
10.9	60	2.15	26.7	30	0.15
1.076	70	2.04	32.7	5	0.02
3.23	70	2.04	32.7	5	0.12
10.764	70	2.04	32.7	5	0.225

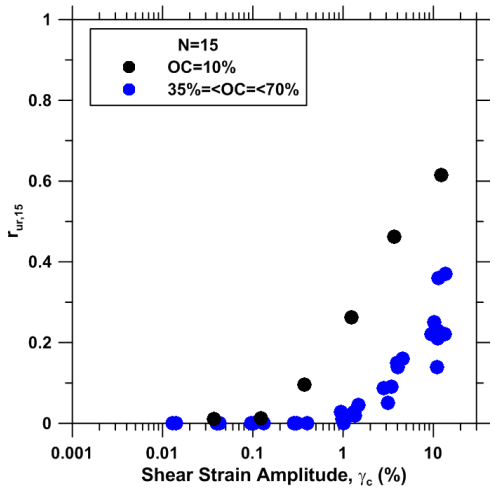

Fig.6.26 Pore pressure build-up in Sherman Island peat

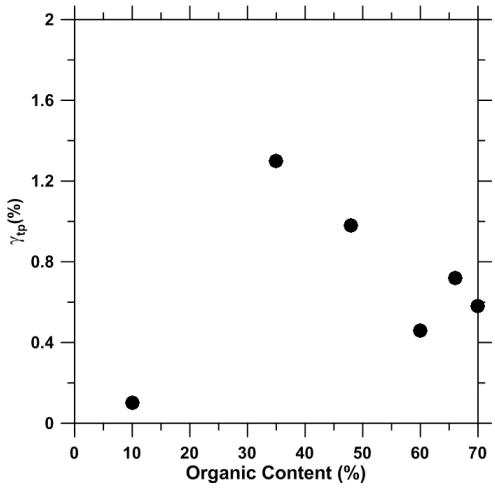

Fig.6.27 Effect of organic content on γ_{tp}

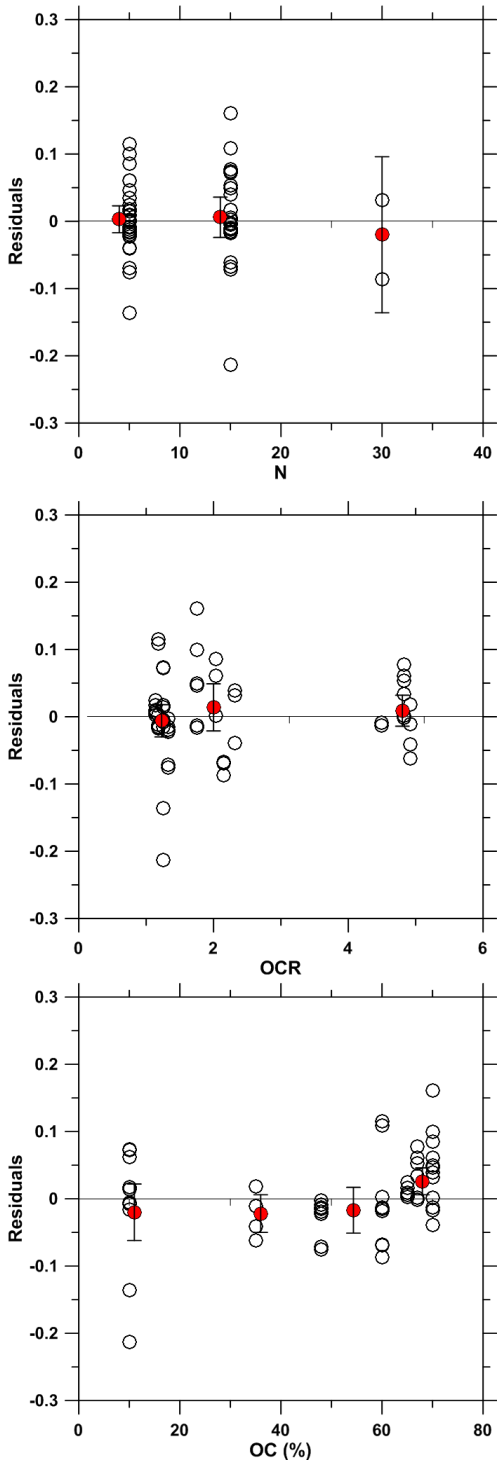

Fig.6.28 Residuals in r_{ur} along with binned means± 95% confidence interval in terms of different variables

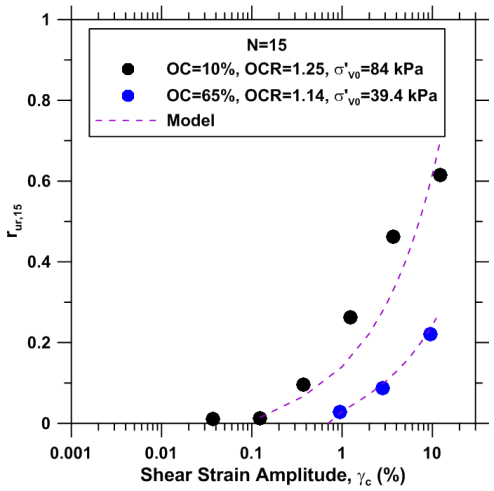

Fig.6.29 A mathematical model for r_{ur}

6.8 SIMPLIFIED PROCEDURE TO ESTIMATE POST-EARTHQUAKE SETTLEMENT IN PEAT

Having obtained the mathematical models for I_R and r_{ur}, post-earthquake settlement can be estimated for levees resting atop Sherman Island peat. An example problem consisting of a 4m levee atop 11m of peat is presented herein (Fig. 6.30). The analyses are performed using one-dimensional ground response analysis even though levees are two-dimensional structures.

Two ground motions consistent with seismic hazard conditions are selected for analysis: one from the 1994 Northridge earthquake and one from the 1995 Kobe earthquake (Table 6.9). Time series are presented in Fig. 6.31 and pseudo-acceleration response spectra (5% damping) are presented in Fig. 6.32. Both motions have a peak horizontal acceleration of 0.23g, but exhibit different durations and the peaks in the response spectra occur at different periods.

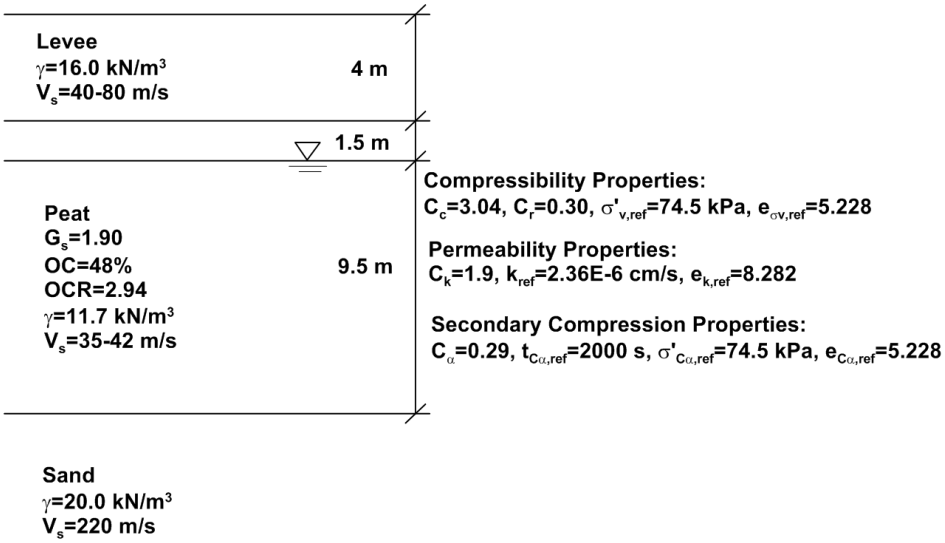

Fig. 6.30 Soil profile in Sherman Island

Table 6.9 Ground motion characteristics

	Motion 1	**Motion2**
Earthquake	1994 Northridge	1995 Kobe
Station	Downey County Maintenance Building	Abeno
M_w	6.7	6.9
R_{jb} (km)	53.2	24.85
V_{s30} (m/s)	272	256
Component	968_180	1100_90
$D_{5\text{-}95}$ (s)	17.2	56.4
PGA (g)	0.23	0.23

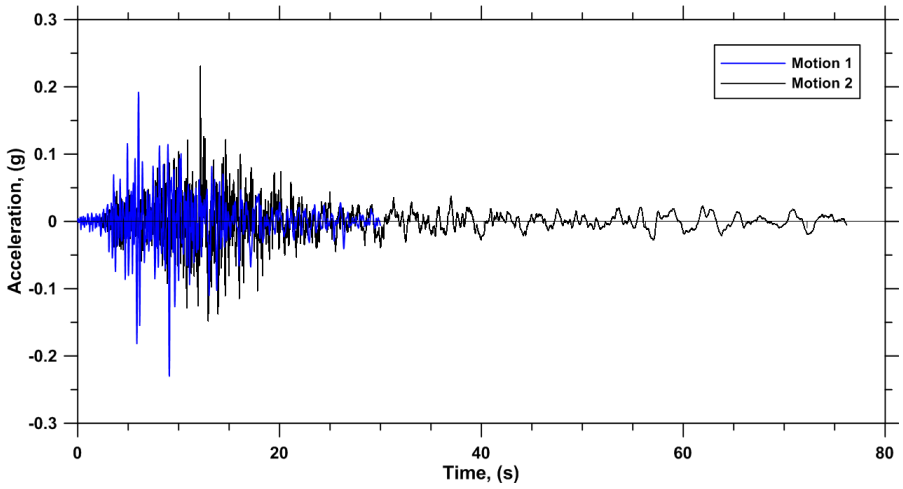

Fig. 6.31 Acceleration time histories applied to the soil profile

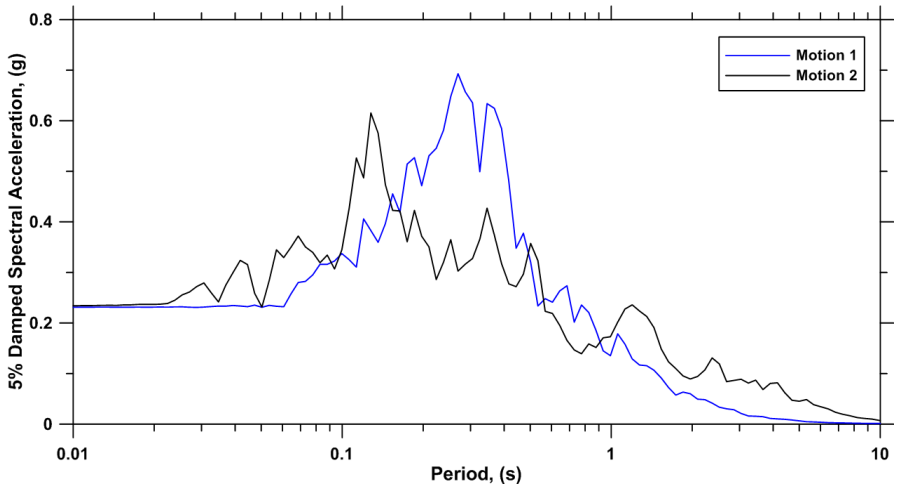

Fig. 6.32 Spectral acceleration for the motions applied to the soil profile

Step 1

Estimating shear strain in the peat:

Equivalent linear 1-D ground response analyses were carried out utilizing the computer program DEEPSOIL version 6.0. Modulus reduction and damping vs. shear strain curves were obtained using the Kishida et al. (2009a) empirical models. It was assumed that the peat has an organic content of 48% on average. The backbone curve was then modified using Yee et al. (2013) method to achieve a normalized shear strength of 0.5 (see Table 3.3). Shear wave velocity in the peat varies from 35 *m/s* beneath the levee and reaches as high as 42 *m/s* at the bottom of the peat (Kishida et al. 2009b).

Distributions of shear strain mobilized in the ground response analyses are plotted in Fig. 6.33. For motion 1, the shear strain profile is relatively constant, whereas for motion 2 it increases with depth. Site response analyses lead to a maximum shear strain (γ_{max}) of 0.44% and 0.82% at the middle of the peat layer when it is subjected to the acceleration time series from motions 1 and 2 respectively (Fig. 6.31). Theses values of shear strains should be multiplied by a magnification factor (MF) accounting for the effects of 2-D shaking and levee-peat interaction effects. Herein, MF=1 is chosen for the sake of simplicity.

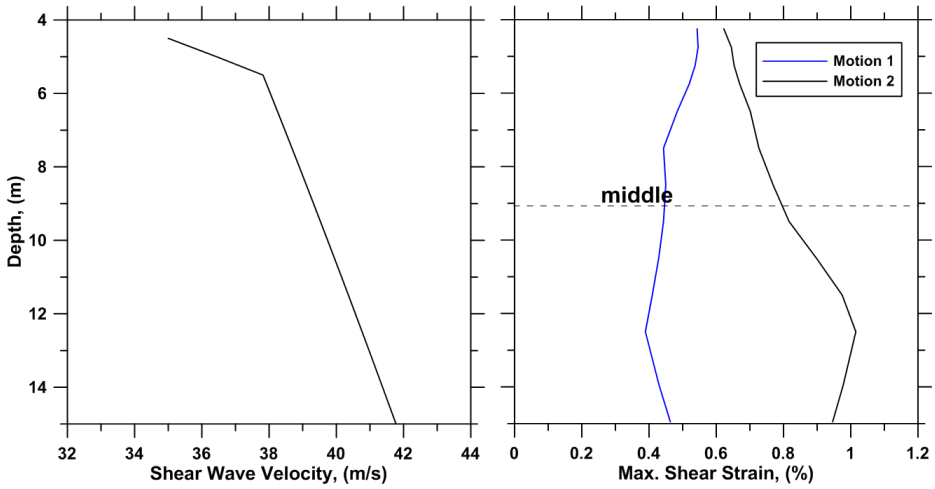

Fig. 6.33 Maximum shear strain profile in the peat

Step 2. Converting Irregular Shear Strain Time Series to Equivalent Uniform Time Series:

To utilize the regression equations for r_{ur} and I_R, an equivalent number of uniform cycles must be computed for the irregular strain time series developed from ground response analysis (Fig. 6.34).

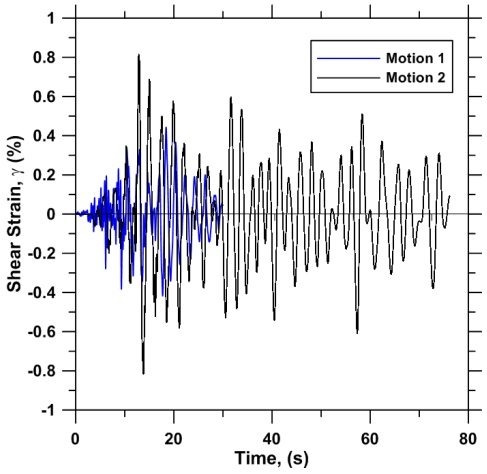

Fig. 6.34 Shear strain time series at the middle of the peat

Rearranging Eq. (6.5) yields to the following equation:

$$\gamma_c = g(I_R, \alpha) N^{-0.675} \tag{6.9}$$

where:

$$g(I_R, \alpha) = \left[\frac{0.300(1.122\alpha + 1)}{I_R}\right]^{\left(-\frac{1}{0.264}\right)}$$

Eq. (6.10) is similar to the equation that relates cyclic resistance ratio (CRR) in sands and clays to the number of uniform loading cycles to failure as:

$$CRR = aN^{-b} \tag{6.10}$$

where a is a material constant, and b is approximately 0.34 for liquefiable sands and 0.135 for clays subject to cyclic softening (Idriss and Boulanger, 2008). This clearly shows the importance of choosing a power function to relate γ_c to the number of cycles N required to induce ground failure (liquefaction or cyclic softening). I use the procedure similar to the one used by Liu et al. (2001) in converting irregular stress histories to equivalent uniform cycles for soil liquefaction. On the basis of Eq. (6.9), the effect of X_A uniform cycles at $\gamma_{c,A}$ can be related to the effect of 1 cycle at $\gamma_{c,B}$ by the following equation:

$$X_A = \left(\frac{\gamma_{c,B}}{\gamma_{c,A}}\right)^{1/0.675} \qquad (1 \text{ cycle at } \gamma_{c,B}) \tag{6.11}$$

Eq. (6.11) is used to convert individual strain cycles into an equivalent number of cycles at a

strain level equal to the peak earthquake-induced shear strain. This leads to *N*=7 and 9 for motions 1 and 2 respectively.

Step 3. Estimate OCR

To estimate the OCR of the peat, we note that the levee has been loaded 1.5 years ago, and the peat layer has been normally consolidated prior to loading. Accordingly, the amount of OCR can obtained from the following equation:

$$\log(OCR) = (C_c - C_r)/\Delta e \tag{6.12}$$

where:

$\Delta e =$ change in void ratio from 1.5 years (=4.73×10^7s) ago up to now owing to secondary compression=$C_\alpha \log\left(\frac{t}{t_{C\alpha,ref}}\right) = 0.29 \log\left(\frac{4.73\times10^7}{1800}\right) = 1.282$.

then:

$OCR = 10^{(3.04-0.30)/1.282}$=2.94

Step 4. Compute Reset Index

Having obtained the values of γ_c (which is equal to γ_{max} from step 1), *N*, OCR, and assuming $\alpha = 0$, OC=48%, and $\sigma_{v0} = 64\ kPa$ (overburden pressure from 4.0 m levee), the value of reset index can be obtained using Eq. (6.5) with the coefficients in Table 6.5, with the result that I_R = 0.40 for motion 1 and 0.49 for motion 2.

Step 5. Estimating Post-Earthquake Settlement

The non-linear consolidation code found at www.uclageo.com/software.php is used to estimate post-earthquake settlement. All the compressibility, permeability, and secondary compression properties are obtained from an oedometer test on a specimen with organic content of 48%. Values of the parameters needed to introduce to the code are obtained as follows:

(1) The compressibility properties including virgin compression index (C_c), recompression index (C_r), reference pressure ($\sigma'_{v,ref}$), and reference void ratio ($e_{\infty v,ref}$) are obtained from oedometer test results, as shown in Fig. 6.35.

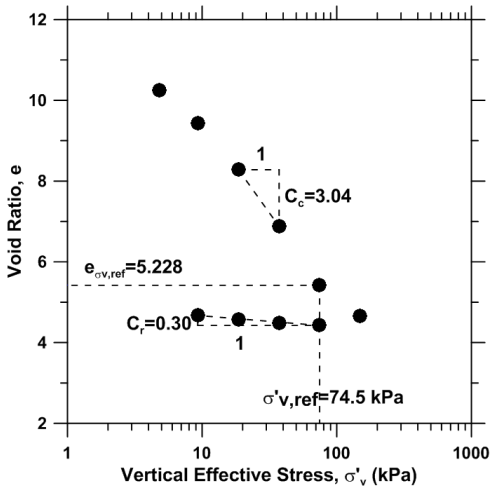

Fig. 6 .35 Compressibility properties for non-linear consolidation code

(2) The permeability properties including reference permeability (k_{ref}), reference void ratio ($e_{k,ref}$), and coefficient of permeability variation (C_k) are obtained from void ratio versus hydraulic conductivity plot, as shown in Fig. 6.36.

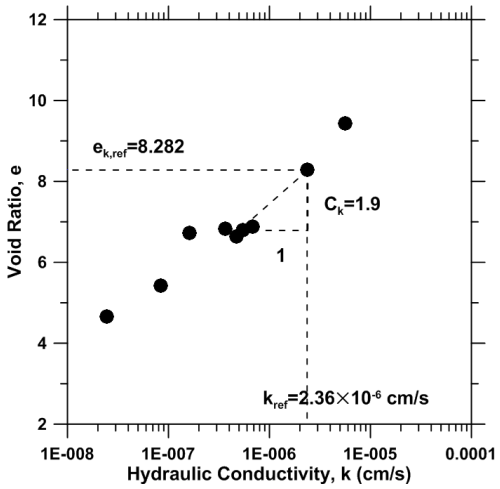

Fig. 6.36 Permeability properties for non-linear consolidation code

(3) The secondary compression properties including secondary compression index (C_α), reference time, ($t_{c\alpha,ref}$), reference void ratio ($e_{c\alpha,}ref$) are obtained from consolidation curve in e-log(t) space pertaining to a loading stage with a final vertical effective stress (=reference vertical effective stress, $\sigma'_{c\alpha,ref}$) of 74.5 kPa, as shown in Fig. 6.37.

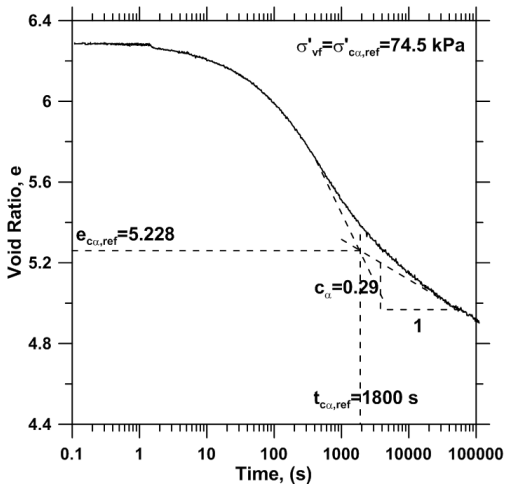

Fig. 6.37 Secondary compression properties for non-linear consolidation code

(4) The value of $e_{C\alpha,ref}$ given in Fig. 6.37, is for the case with I_R=0 (no reset). For the cases in which $I_R \neq 0$, the value of $e_{C\alpha,ref}$ can be obtained as follows:

$$e_{C\alpha,ref} = 5.228 - I_R(C_c - C_r)\log(OCR) \quad (6.13)$$

Then, for the first motion:

$$e_{C\alpha,ref} = 5.228 - 0.40(3.04 - 0.30)\log(2.94) = 4.714$$

similarly for the second motion:

$$e_{C\alpha,ref} = 5.228 - 0.49(3.04 - 0.30)\log(2.94) = 4.599$$

Step 6. Compute Residual Pore Pressure Ratio

Eq.(6.7) along with its coefficients presented in Table 6.7 are used to compute r_{ur} within the peat layer. For the motion1: r_{ur} =0, since $\gamma_{max} = 0.44\% < \gamma_{tp} = 0.70\%$.

For motion 2: $\gamma_{tp} = 0.70\%, \gamma_c = 0.82\%, N = 9, OCR = 2.94,$ and $OC = 48\%$, which results in $r_{ur} = 0.014$.

The remaining parameters of the code are plugged in as shown in Table 6.10:

Table 6.10 Parameters needed to run the non-linear consolidation code

G_s	q_0 [1] (kPa)	$\Delta\sigma_v$ [2] (kPa)	No. of elements	No. of time steps	Maximum time (sec)
1.9	64	0	100	500	3.15×10^7

[1]Initial overburden pressure, (total stress from 4 m height levee)

[2]Total vertical stress change

We also need to increase reference permeability by an order of 100 to account for the 3-D drainage that happens in the field.

Fig. 6.38 shows settlement versus time when the peat is subjected to two motions along with the case for which no reset occurs.

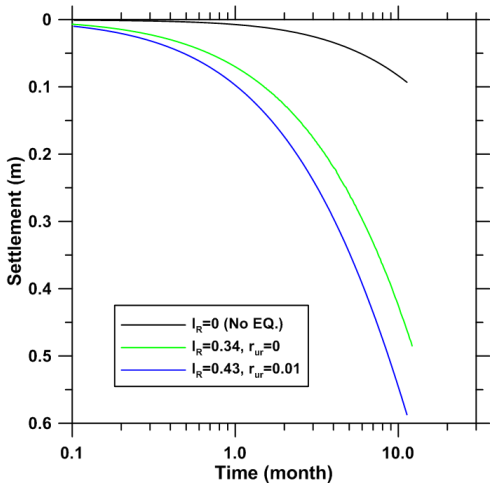

Fig. 6.38 Post-earthquake settlement in peat versus the case in which no clock resetting happens (I_R=0)

7 Summary, Conclusions and Future Work

This research centered around improving fundamental understanding of cyclic and post-cyclic behavior of Sherman Island peat that could affect levee performance. More specifically, a series of monotonic and cyclic tests on consolidated specimens of peaty organic soil was performed to evaluate factors affecting post-cyclic re-consolidation of peat. One of the principle contributions in this dissertation was to demonstrate that evaluation of the rate of secondary compression following primary consolidation is related to the vertical distance in void ratio – effective stress space between soil state and a secondary compression reference line. The framework was then used to explain the increase in rate of secondary compression following cyclic loading.

This chapter is divided into six sections summarizing: 1) modifications performed on the UCLA bi-directional broadband simple shear device, 2) site characterization 3) static compressibility properties of Sherman Island peat, 4) monotonic, cyclic and post-cyclic behavior of Sherman Island peat, 5) development of a framework that can capture secondary compression clock resetting, and 6) recommendations for future research that center around several unresolved issues related to this project.

7.1 UCLA BB-SS DEVICE UPGRADE

UCLA Bi-Directional Broadband Simple Shear (BB-SS) device was upgraded to the capabilities of constant volume and stress-controlled testing features as needed for testing Sherman Island peat under undrained conditions, and static shear stress. Prior to these modifications, the device was useful for constant vertical load (effectively drained) strain-controlled testing. An uncoupled PID control system was adopted to adjust the vertical force using a servo-hydraulic actuator so that the feedback from vertical LVDTs are read and if the displacement during shear is not zero, the vertical load is adjusted to return the vertical displacement to zero. A similar PID algorithm was used for the stress-controlled feature on the horizontal axes.

The performance of the new control system was examined through measurement of vertical strains in constant height testing, top cap rocking, and precision of the stress-control feature under various loading conditions. The procedures introduced to measure these device attributes, along with those of Duku et al. (2007) for constant vertical force testing under displacement control, should be broadly applicable for analysis of the performance of laboratory test devices used for cyclic testing and their control systems. Such performance assessments are rarely performed, but are crucial for understanding the range of conditions over which device performance can be considered reliable.

It was shown that vertical strain errors in constant height testing increase with displacement in horizontal axes. However, high-precision vertical control is achieved even at large horizontal displacement amplitudes such that vertical strain is less than 0.05% when displacement amplitudes are 2.5 *mm* (corresponding to shear strain $\gamma_c = 10\%$ for a 2.5 cm specimen height) for unidirectional shearing and 0.76 *mm* ($\gamma_c = 3\%$) for bi-directional shearing. Top cap rocking increas-

es with horizontal displacement amplitude and is essentially frequency-independent. Top cap rocking is small, with the vertical strain due to rocking at the specimen edge being half or less than averaged vertical strains over the specimen cross section.

The tracking error in stress-controlled tests increases with frequency of loading and decreases with cyclic stress ratio (*CSR*). During constant-volume cyclic stress-controlled tests on liquefiable sands the control system can keep pace with in-cycle contraction/dilation for loading frequencies ≤ 0.5 *Hz*, otherwise, the control system experiences progressively increasing losses of control once initial liquefaction occurs. Similarly, for constant-volume broadband (earthquake-like) testing on liquefiable sands, the feedback signal tracks the command well for $r_u < 0.85$. Tracking errors at higher pore pressures are mitigated by increasing the time step by a factor of 10.

7.2 SITE CHARACTERISATION

A total of 9 boreholes were hand-augered in Sherman Island, and 24 Shelby tube samples were retrieved from depths ranging from approximately 1 to 6 *m* using a special piston sampler fabricated specifically for sampling peat. It was shown that organic content is highest at a depth of 2*m*, ranging from 60 to 80%, and decreases with depth becoming as low as 8% at a depth of 5.5*m*. The highly organic peat is black in color, and has visible fibers or plant material. The peat transitions to a grey color similar to Bay Mud as depth increases to 5.5m. Specific gravity decreases as organic content increases, and varies from 1.8 (organic content=8%) to 2.6 (organic content=80%). Water content decreases and bulk unit weight increases with depth. Water content varies from 50 (at 6.0 *m*) to 600% (at 1.5 *m*), and bulk unit weight varies from 10.2 (at 1.5 *m*) to 16 kN/m^3 (at 6.0 *m*).

7.3 STATIC COMPRESSIBILTY PROPERTIES

Oedometer tests were carried out on Sherman Island peat to evaluate its compressibility properties including compression index (C_c), recompression index (C_r), secondary compression index ($\mathbf{C_\alpha}$), coefficient of consolidation ($\boldsymbol{c_v}$), and coefficient of hydraulic conductivity (k). A consolidation test with load increment ratio (LIR) =1 was performed on one specimen from each Shelby tube. Some consolidation tests with LIR≤1 were also carried out to establish a fundamental problem with the traditional interpretation of secondary compression, and set the stage for an alternative stress-space based interpretation. Consolidation tests on reconstituted specimen were run as well to verify if they could replicate the compressibility properties obtained from testing on undisturbed specimens. In total, 22 consolidation tests were carried out in this study. To facilitate accurate determination of the end of primary consolidation, a new consolidometer was fabricated that provides single drainage through the top of the specimen, while pore pressure is measured at the bottom. The device permits accurate measurement of the time rate of pore pressure dissipation, and provides a much more accurate measure of t_p than the traditional method based on studying the shape of the settlement curve.

Values of $\boldsymbol{c_v}$ for normally-consolidated load stages on specimens with OC ≥28% were observed to decrease as vertical effective stress increases, often by more than two orders of magnitude over the stress range tested in the consolidometer. For the Sherman Island peat $\boldsymbol{c_v}$ is as high as 400×10^{-4} cm^2/s at σ_p'. The trend of compression index, and recompression index confirms that they are positively correlated with in situ water content (w_0) and organic content

(OC). The values of C_α/C_c (where $C_\alpha$is secondary compression index) for the Sherman Island peat ranges from 0.05 to as high as 0.12 with an average of 0.08. Hydraulic conductivity *k* depends on void ratio, and decreases with the decrease in void ratio. The slope of *e* versus $logk$ (i.e., C_k) increases with initial void ratio (e_o), and the best fit for the data is $C_k = 0.20e_0$.

7.4 MONOTONIC, CYCLIC AND POST-CYCLIC SHEARING BEHAVIOR

Shear behavior of the Sherman Island peat was investigated using the UCLA digitally-controlled direct simple shear device for the following test types: (1) strain-controlled constant height monotonic tests, (2) strain-controlled constant-height cyclic tests with post-cyclic volume change measurements, (3) strain-controlled constant-height cyclic tests with post-cyclic constant-height monotonic shearing, and (4) stress-controlled constant-height cyclic tests with static driving shear stress with post-cyclic volume change measurements.

Monotonic test results show that lightly overconsolidated peat with overconsolidation ratio, OCR < 2 shows contractive behavior, while higher OCR's result in dilative behavior. The Normal Consolidation Line (NCL) and Failure State Line (FSL) are approximately parallel for OC ≤ 35%. Normalized shear strength (the normalization is with respect to pre-shear vertical effective stress) has been evaluated as a function of OCR. The soil behavior generally supports the concept of normalization, with the strength ratio being higher for high OC (80-85%) than for low OC (≤35%).

Cyclic strain-controlled tests on the peats with OC ≥ 35% show that for low shear strain amplitude, γ_c (< 0.7%), although hysteretic loops form, cyclic degradation of stiffness does not occur and pore pressures do not accumulate. Accordingly, stress paths are similar to those for a drained test. The threshold shear strain (γ_{tp}) below which no residual pore pressure develops is

around 0.7 % when OC ≥ 35%. The value of γ_{tp} decreases to 0.10% when organic content reaches as low as 10%. In the peaty soils with OC ≥ 35%, pore pressure generation markedly increases for cyclic shear strain amplitudes larger than γ_{tp} and reaches to as high as 0.4 which is lower than those for liquefiable sands but is comparable to those for cyclic softened normally consolidated clays. Field data are in accordance with the lab data, and do not show any remarkable pore pressure build-up when shear strain is less than 1%. An empirical model was also developed for r_{ur} in terms of γ_c, number of uniform loading cycles (N), OCR, and OC.

7.5 SECONDARY COMPRESSION CLOCK RESETTING

It was demonstrated that the traditional procedure, in which t=0 corresponds to the time when the load is applied, is inappropriate for identifying the correct value of C_α when LIR is small. An alternative stress-space procedure was presented, and shown to provide better agreement with the laboratory test results. The secondary compression strain rate was formulated as a function of distance to a secondary compression reference line (SCRL) in void ratio – effective stress space. It also has the benefit of eliminating an arbitrary time reference from the secondary compression calculation, instead basing secondary compression rate on the soil state. The framework was then used to account for the increase in secondary compression rate following cyclic loading.

Post-cyclic volume change measurements show that the secondary compression rate increases with γ_c, which has not been previously recognized, and can be viewed as resetting the secondary compression clock at least partially without change in total stress. To account for the reset of secondary compression clock SCRL was moved downward while keeping reference time, t_{ref} (which could be taken equal to t_p) constant. The amount of reset was then quantified by introducing reset index (I_R), which shows amount of downward movement of SCRL. The value

of I_R varies between 0 (no reset) to 1 (fully reset). An empirical model was then developed for I_R as a function of cyclic shear strain amplitude, number of uniform loading cycles, organic content, initial overburden pressure, and amount of static shear stress.

A simplified procedure was developed to estimate post-earthquake settlement of organic soils in consideration of post-earthquake pore pressure dissipation and accelerated rates of secondary compression. The procedure uses 1-D site response analysis to find representative profiles of peak shear strain and its phasing in time. The irregular shear strain time series is then converted to uniform shear strain cycles at some specified amplitude as a fraction of the peak. Reset index and pore pressure ratio at the conclusion of shaking are then calculated using predictions equations conditioned on strain amplitude, number of cycles, overconsolidation ratio, organic content, and pre-earthquake stress conditions. The resulting values of reset index and pore pressure can be used in a non-linear consolidation code to calculate post-earthquake settlement versus time.

7.6 RECOMMENDATIONS FOR FUTURE RESEARCH

In this study, UCLA BB-SS device was upgraded to the constant volume and stress-controlled testing features, and a new concept for interpretation of post-cyclic volume change behavior of peat in terms of secondary compression clock resetting was developed. In the hardware level, the device can be upgraded to more advanced testing features including set-up for measurement of very low shear strains using non-contact sensors, and use of bender elements to measure dynamic properties at very low shear strains. On the other hand, the secondary compression clock resetting concept can be extended to capture more general cases as discussed here.

- More cyclic strain- and stress-controlled DSS tests under controlled conditions are needed to expand the database and develop more accurate empirical models for I_R and r_{ur}. For example, running some tests on a Shelby tube sample under constant initial vertical stress while OCR varies, or under constant OCR, while initial vertical stress varies can improve the database.

- One of the disadvantages of NGI simple shear device is that it does not provide the value of lateral stress during the test. Triaxial tests can help to investigate the peat behavior while the stress tensor is known, and hence, provide a database that could be eventually implemented in an elasto-plastic model. Cyclic triaxial tests are also helpful to investigate the behavior of peat under rocking motions (beneath the toes of levee).

- All the cyclic tests in this study were carried out under 1-D constant amplitude excitation. To extend the concept of secondary compression clock resetting, more general cases including bi-directional shaking and broadband testing should be investigated. Broadband

tests can also be used to develop a framework to convert irregular time series to equivalent uniform cyclic time series.

- This study revealed the importance of secondary compression on the mechanical behavior of peat. Assuming that secondary compression happens simultaneously with primary consolidation, all the peats in the field/lab are overconsolidated with some amount following primary consolidation. Hence, modulus reduction and damping curves needs to be corrected based on the true value of OCR. The true value of OCR of a specimen can be obtained based on its final void ratio and location of NCL, which has already been corrected for the influence of secondary compression.

- The secondary compression clock resetting framework can be extended to other materials including clays. A series of test performed in this study on Sherman Island peat with OC=10%, showed that clays could have reset indexes as high as peats. A comprehensive testing program similar to what defined here for peat, can be implemented for clays.

APPENDIX A

CYCLIC TEST RESULTS

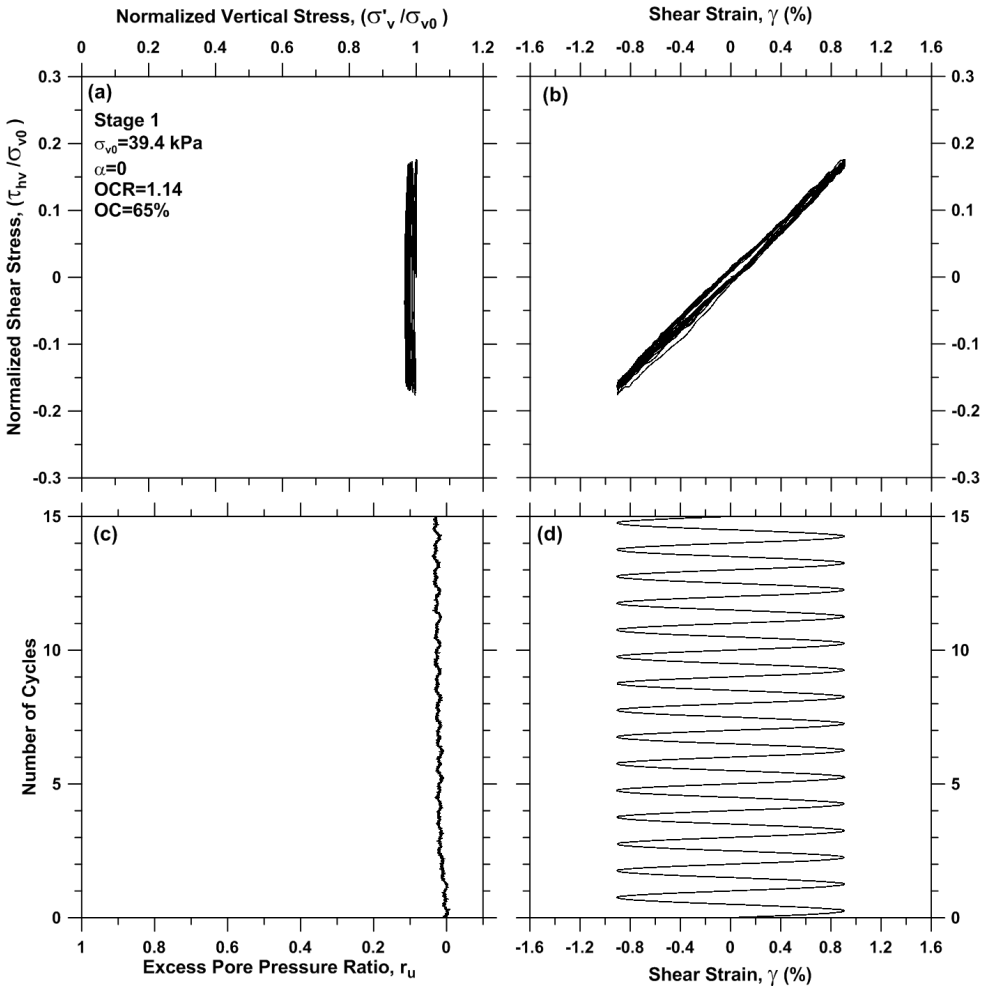

Figure A.1 Cyclic strain-controlled DSS test results on specimen BH3S2_5.6, stage 1

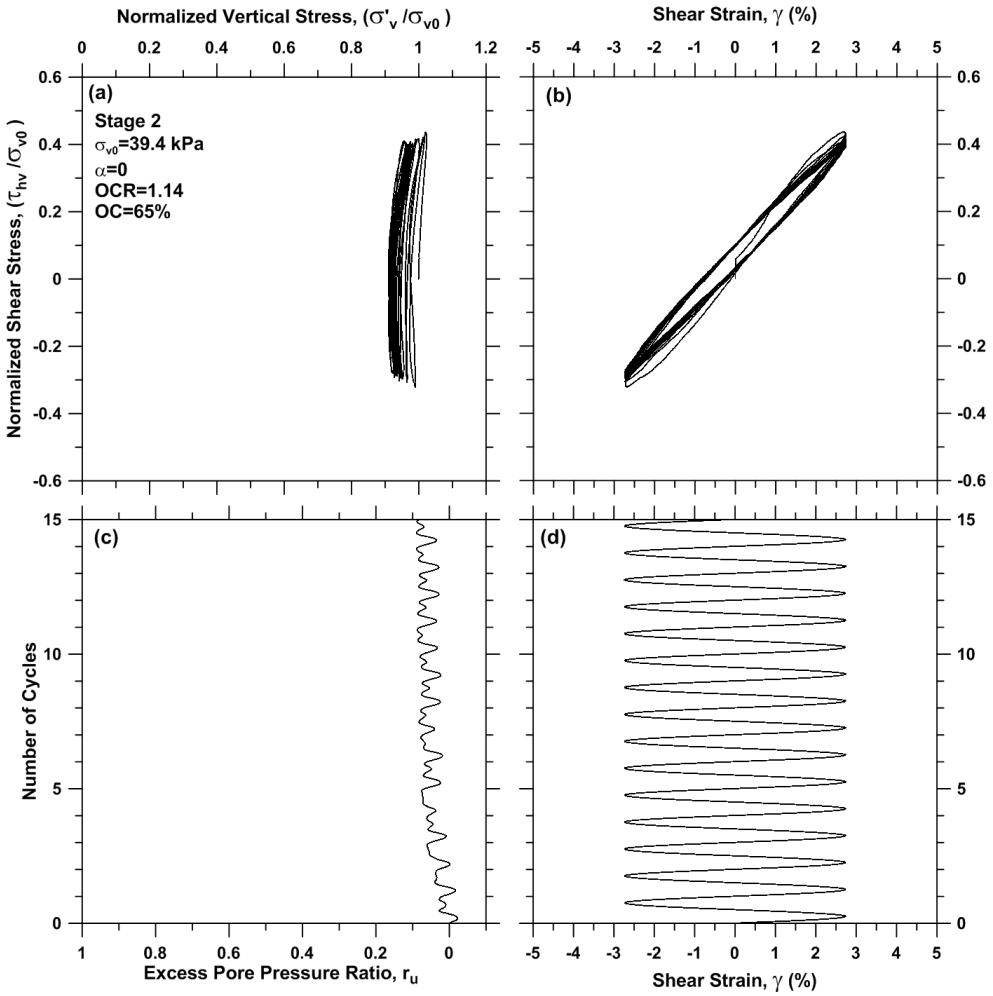

Figure A.2 Cyclic strain-controlled DSS test results on specimen BH3S2_5.6, stage 2

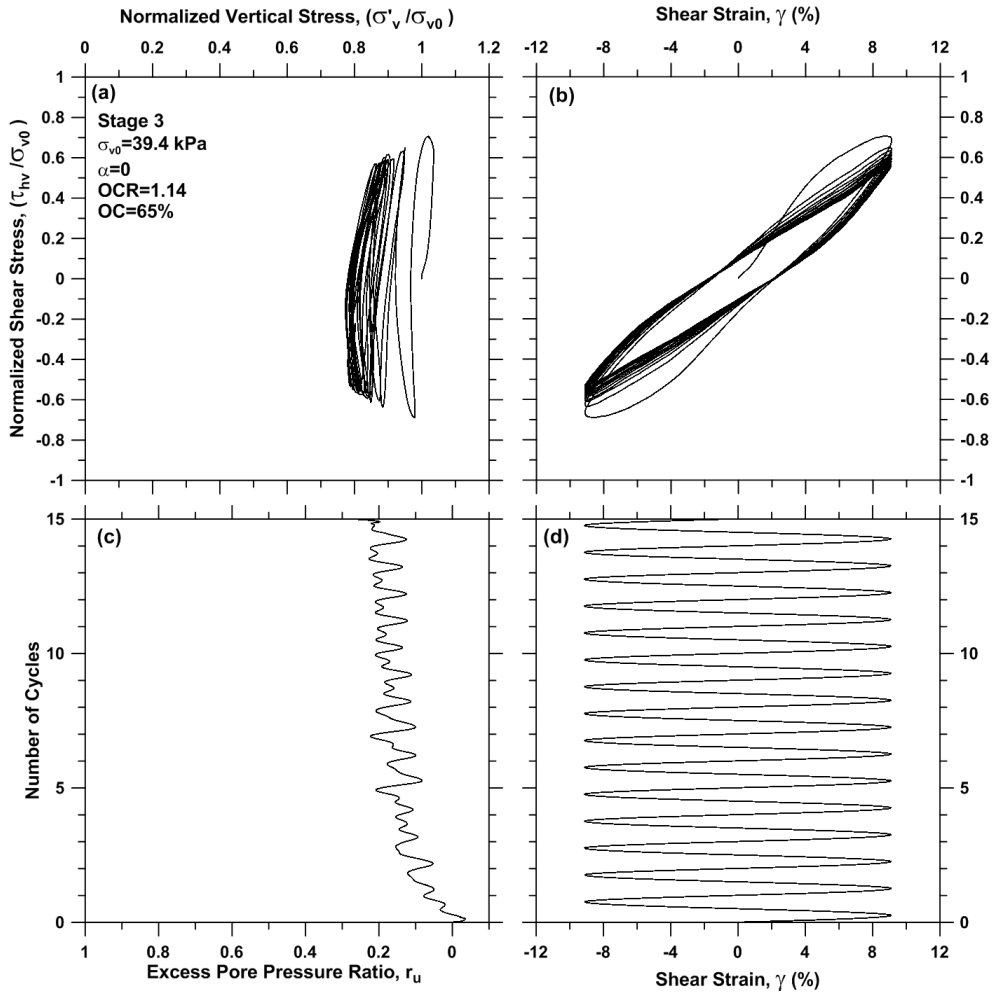

Figure A.3 Cyclic strain-controlled DSS test results on specimen BH3S2_5.6, stage 3

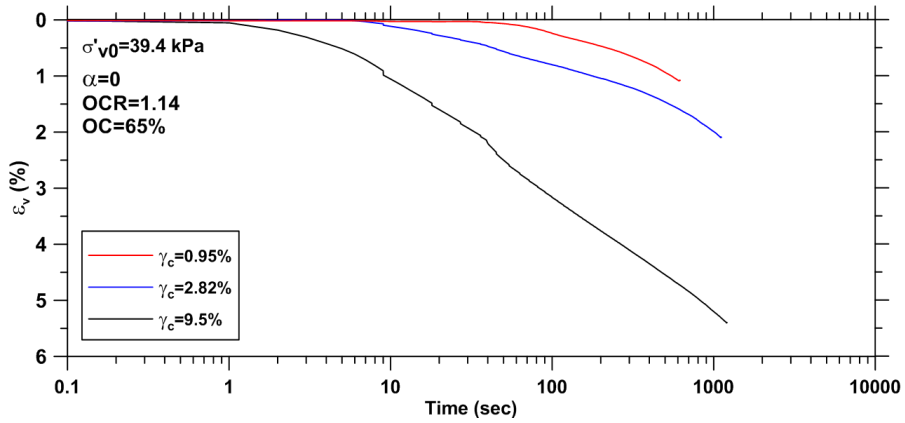

Figure A.4 Post-cyclic volume change following strain-controlled DSS tests on specimen BH3S2_5.6

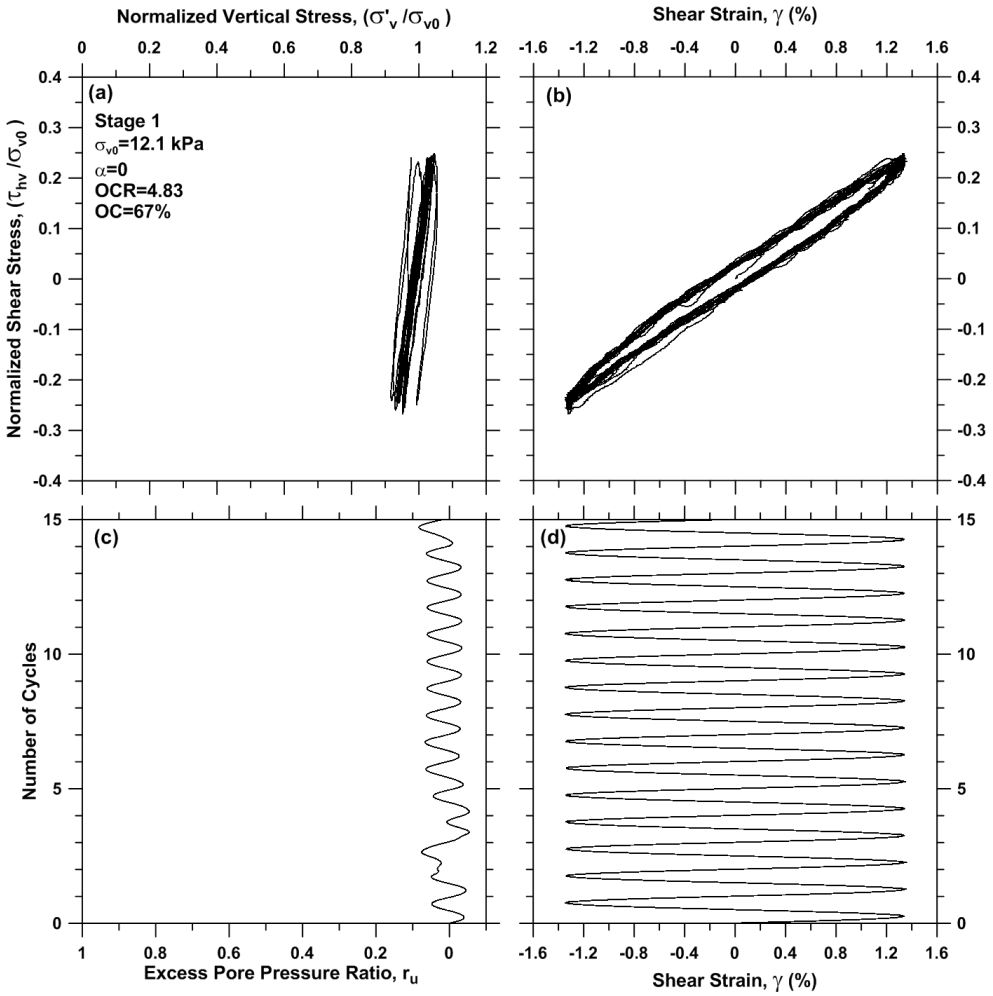

Figure A.5 Cyclic strain-controlled DSS test results on specimen BH6S4_7.3, stage 1

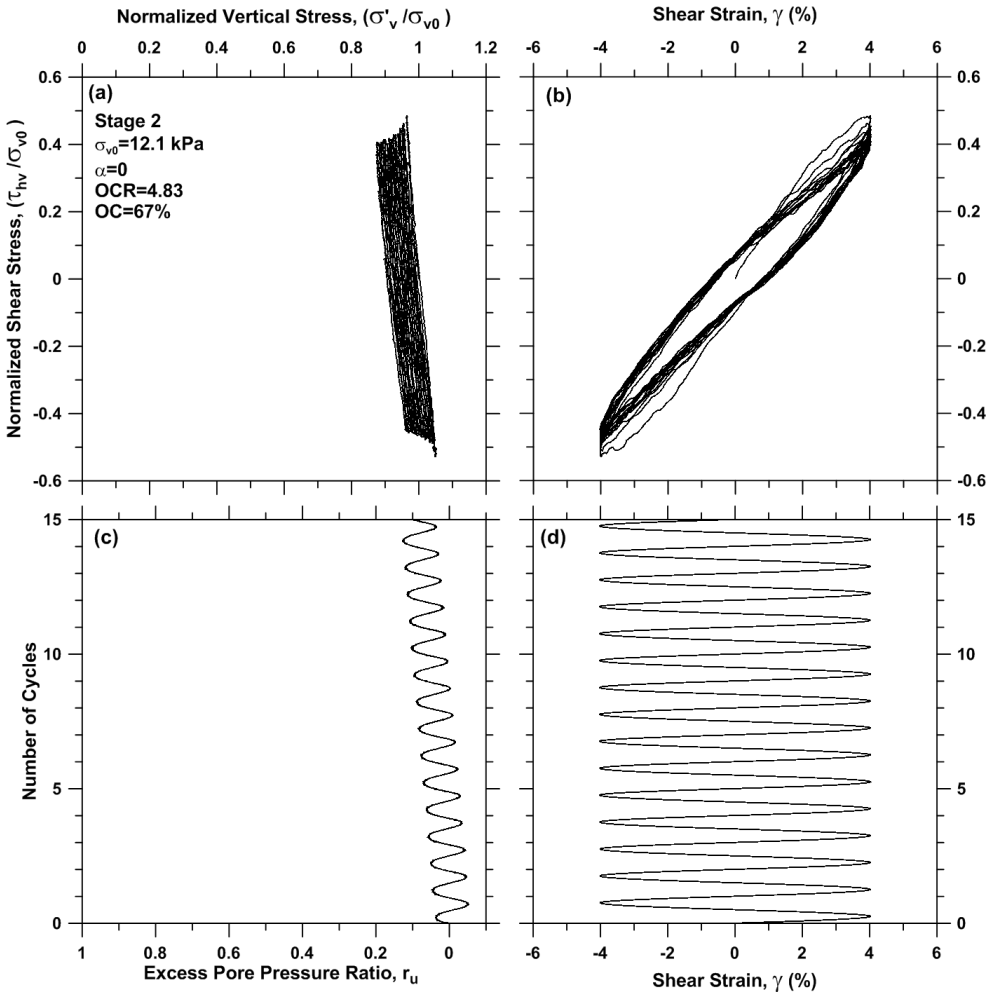

Figure A.6 Cyclic strain-controlled DSS test results on specimen BH6S4_7.3, stage 2

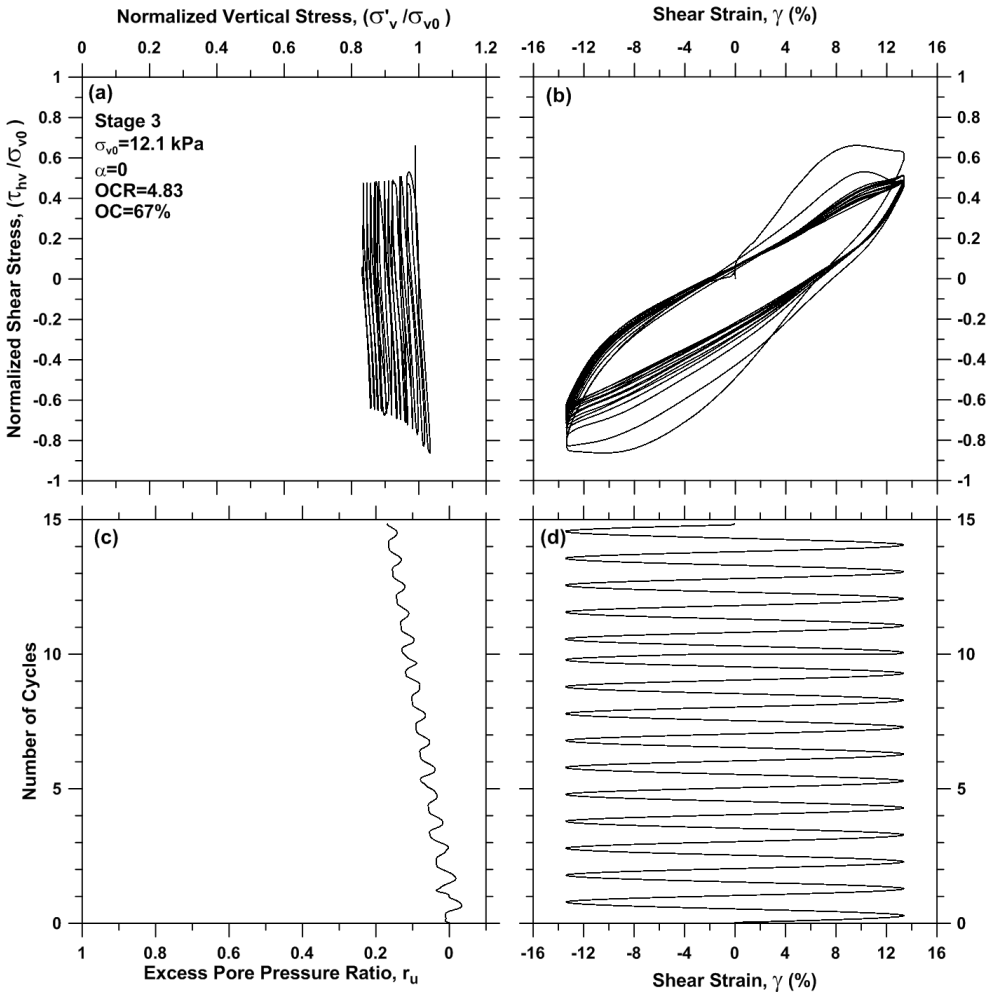

Figure A.7 Cyclic strain-controlled DSS test results on specimen BH6S4_7.3, stage 3

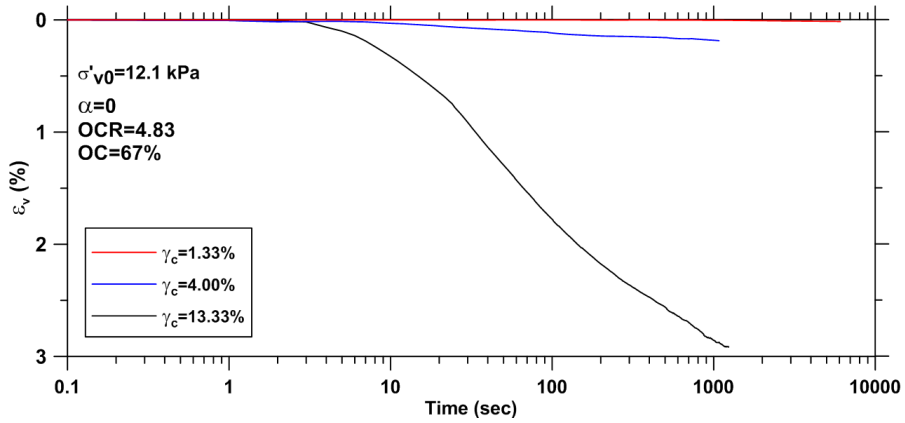

Figure A.8 Post-cyclic volume change following strain-controlled DSS tests on specimen BH6S4_7.3

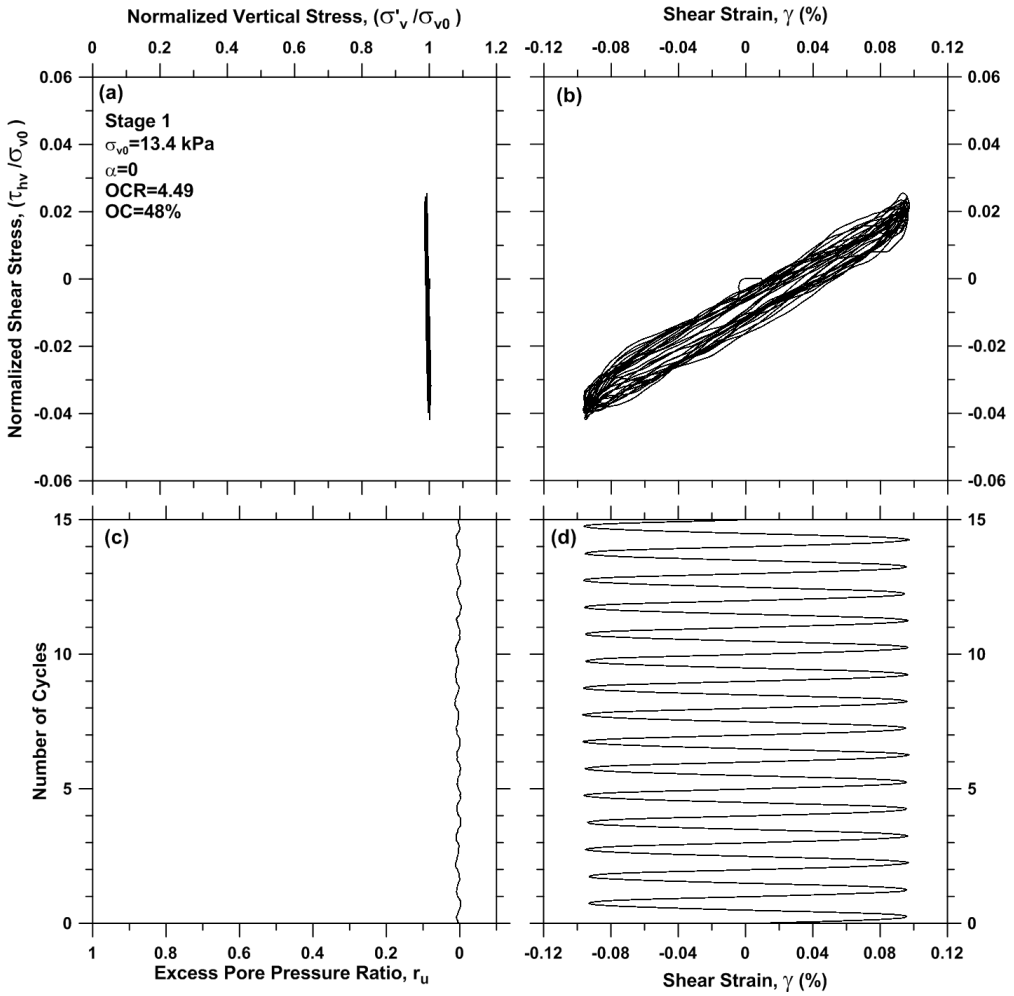

Figure A.9 Cyclic strain-controlled DSS test results on specimen BH6S2_9.3, stage 1

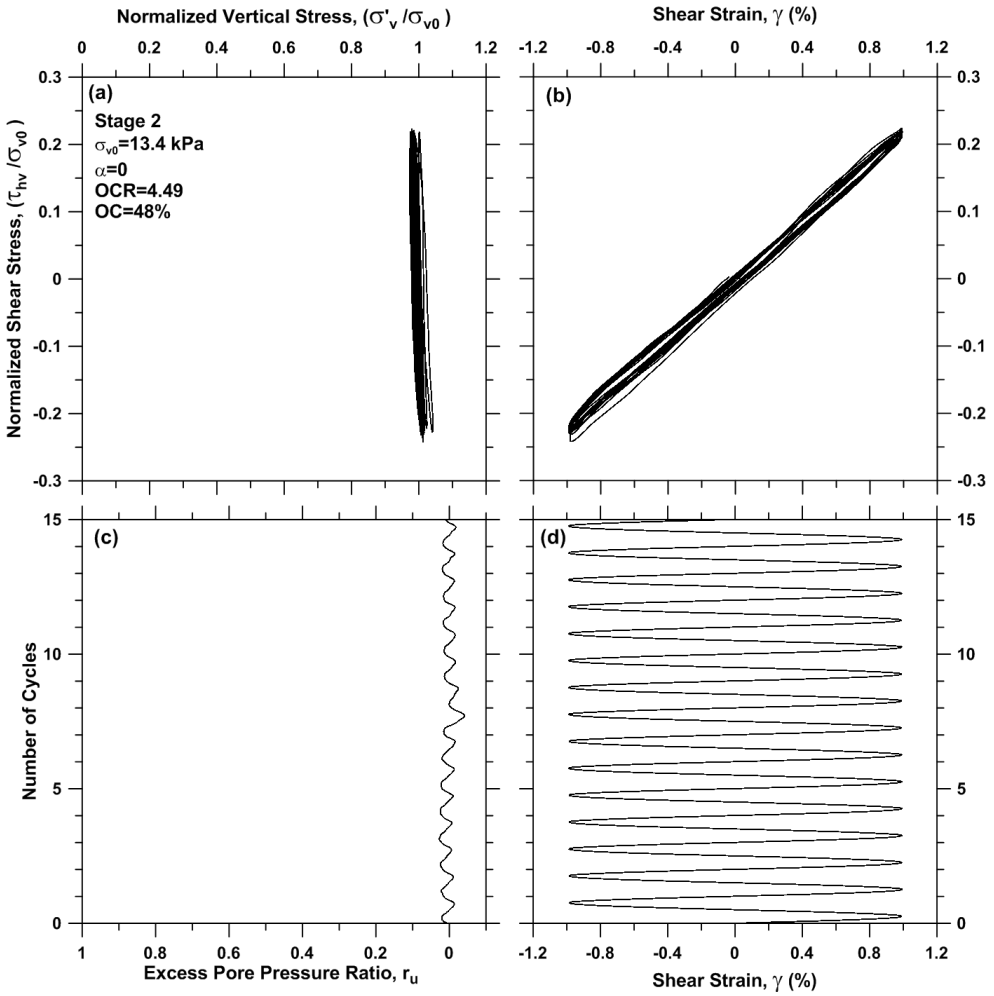

Figure A.10 Cyclic strain-controlled DSS test results on specimen BH6S2_9.3, stage 2

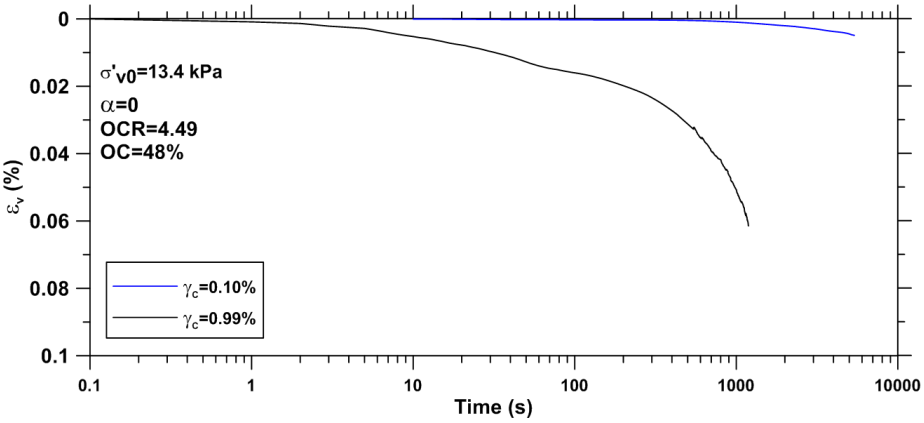

Figure A.11 Post-cyclic volume change following strain-controlled DSS tests on specimen BH6S2_9.3

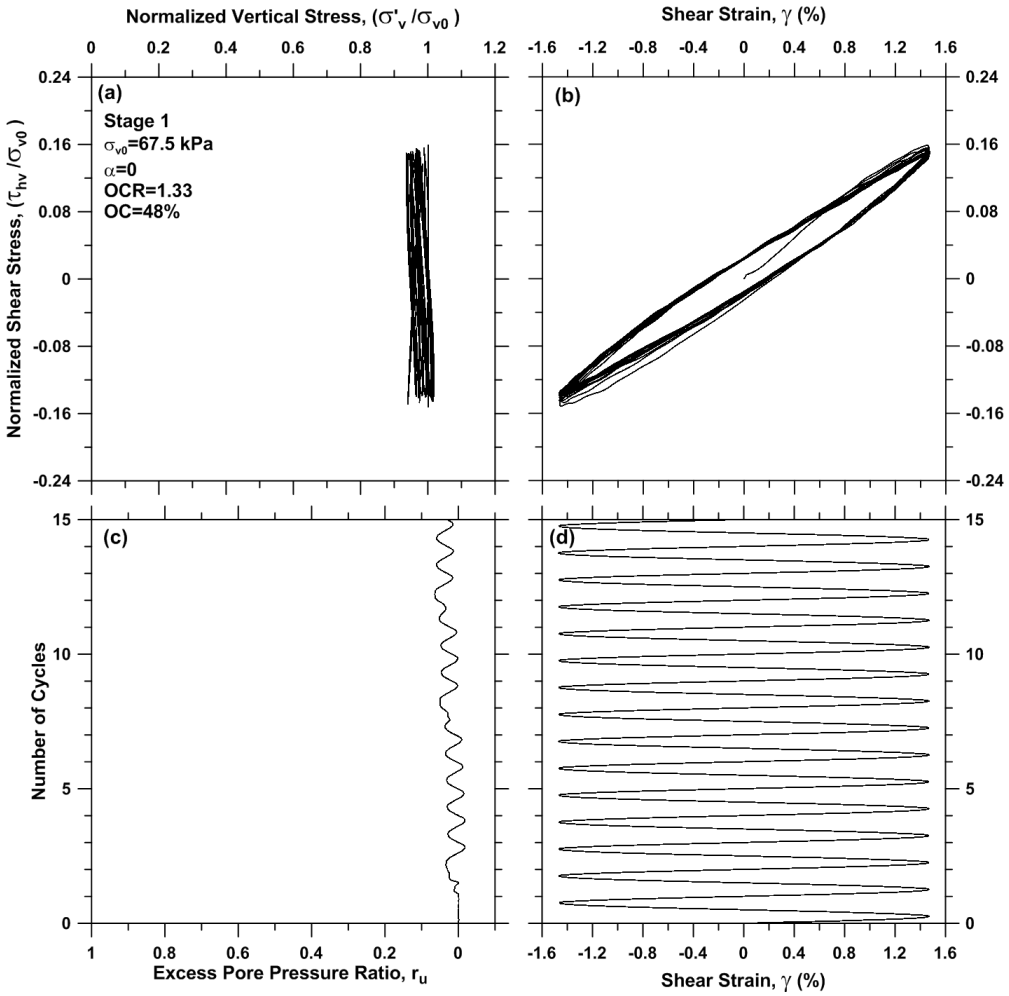

Figure A.12 Cyclic strain-controlled DSS test results on specimen BH6S8_10.3, stage 1

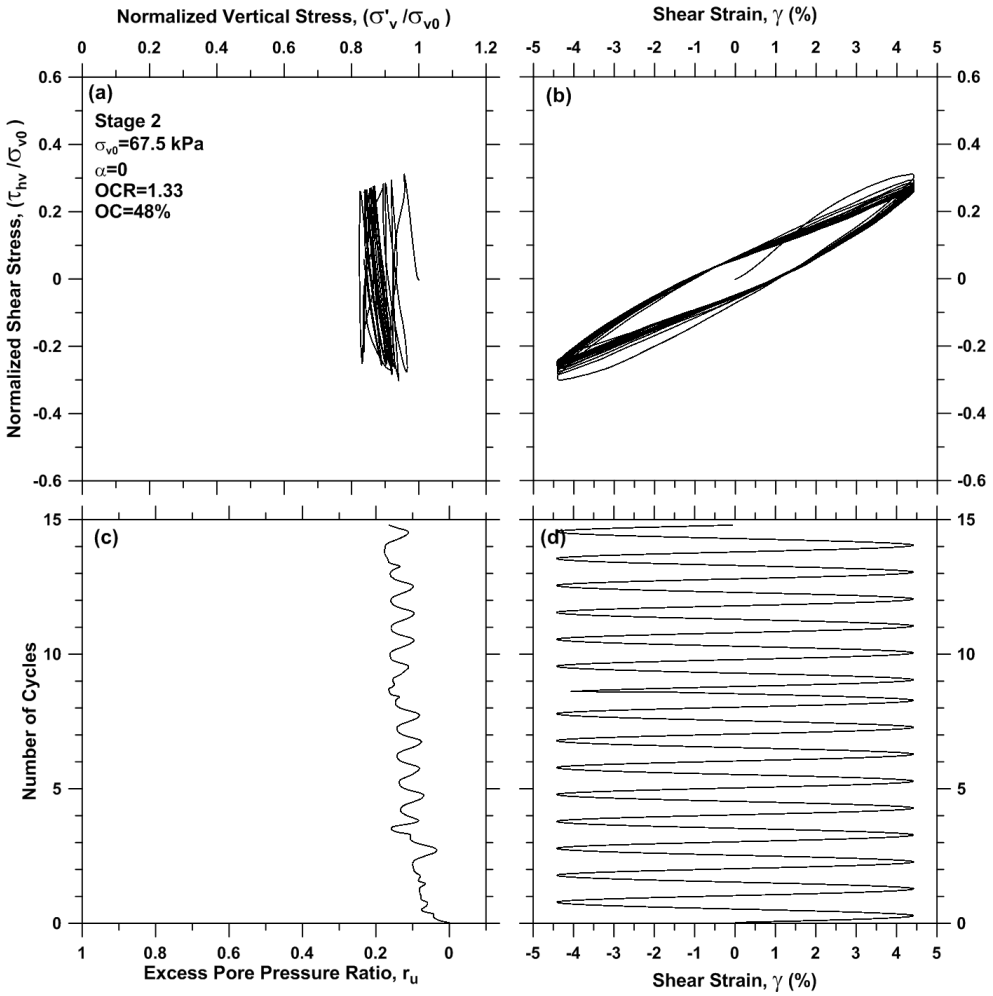

Figure A.13 Cyclic strain-controlled DSS test results on specimen BH6S8_10.3, stage 2

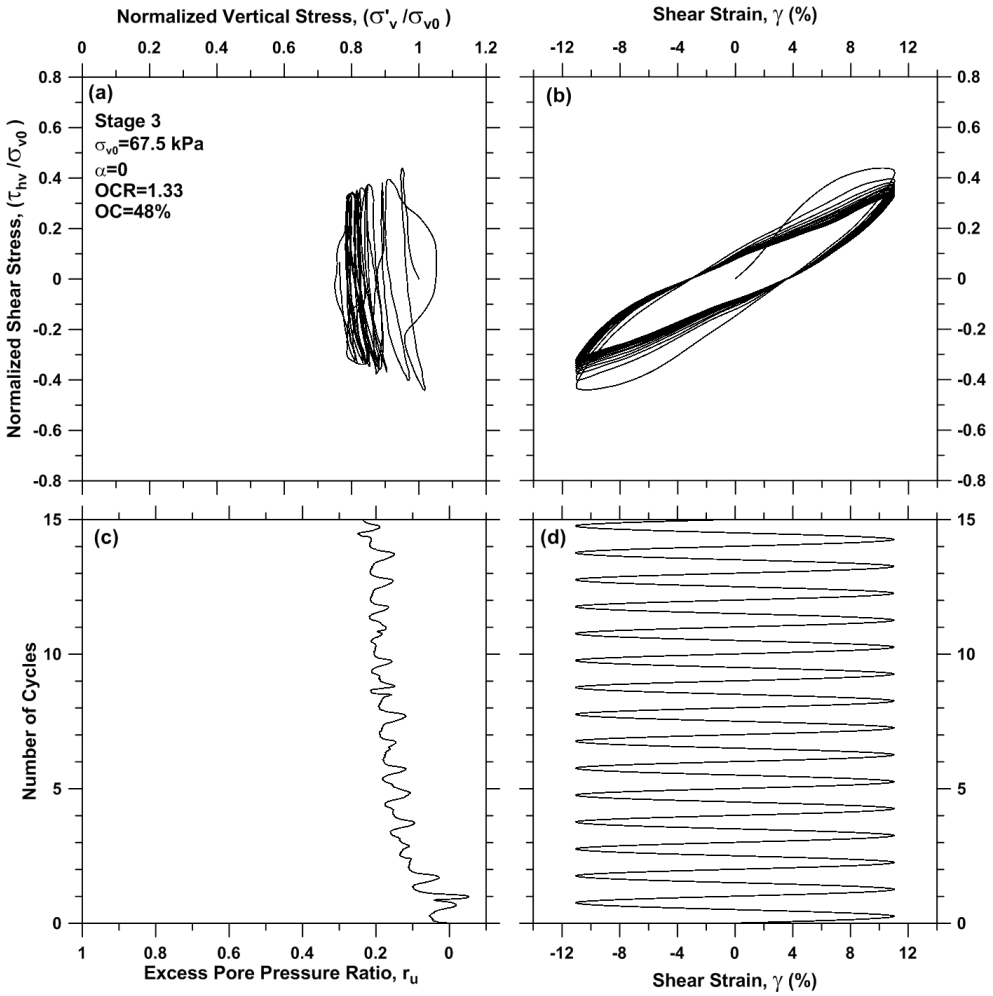

Figure A.14 Cyclic strain-controlled DSS test results on specimen BH6S8_10.3, stage 3

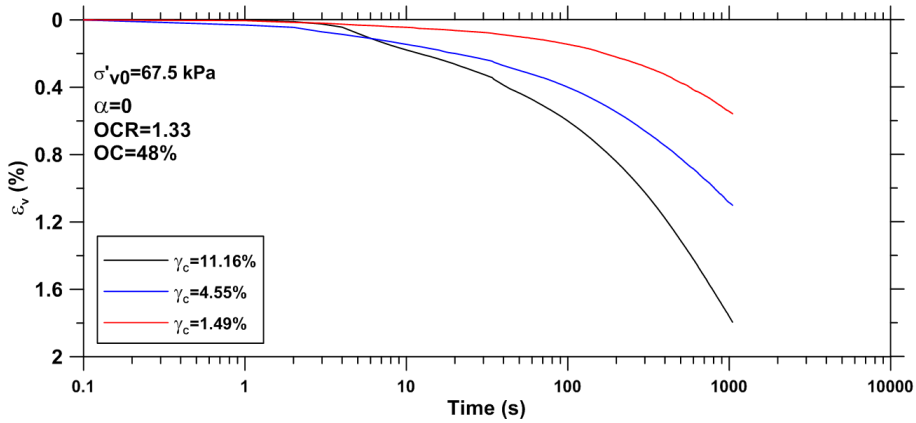

Figure A.15 Post-cyclic volume change following strain-controlled DSS tests on specimen BH6S8_10.3

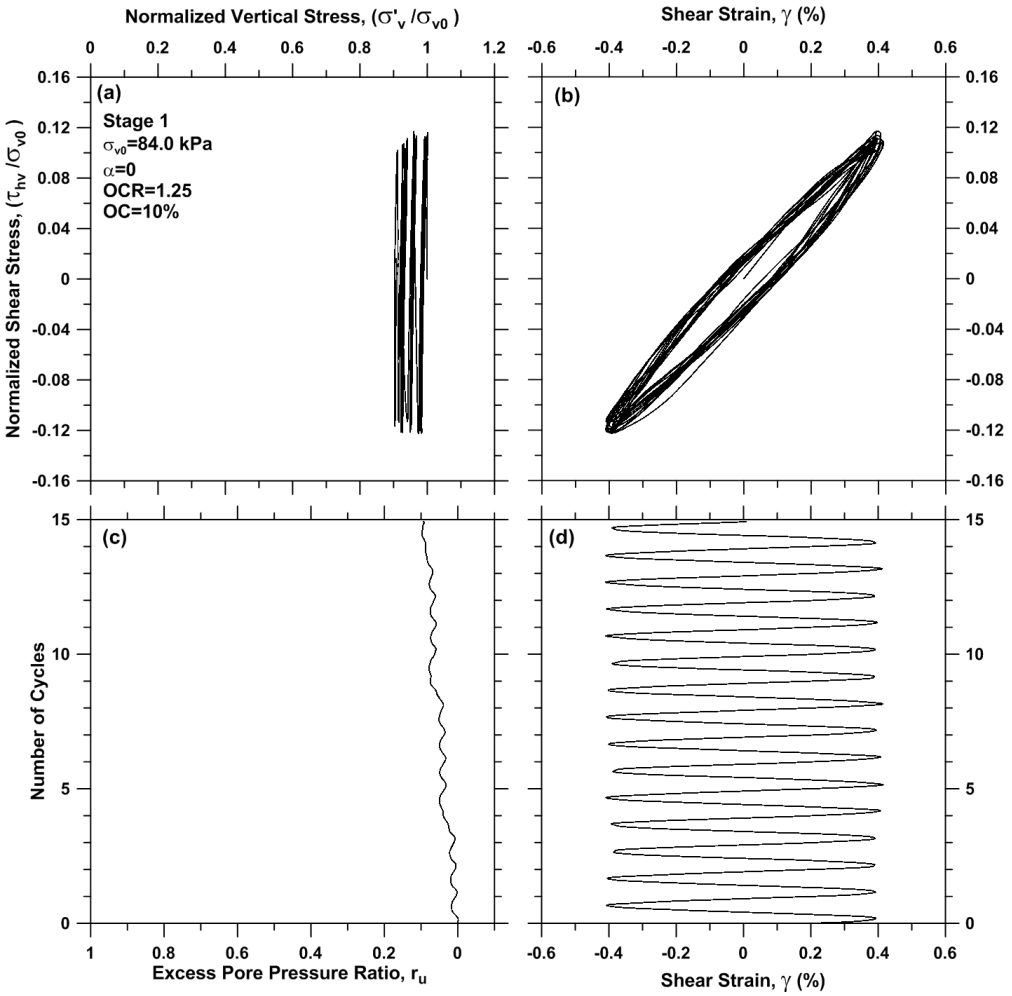

Figure A.16 Cyclic strain-controlled DSS test results on specimen BH6S4_14.3, stage 1

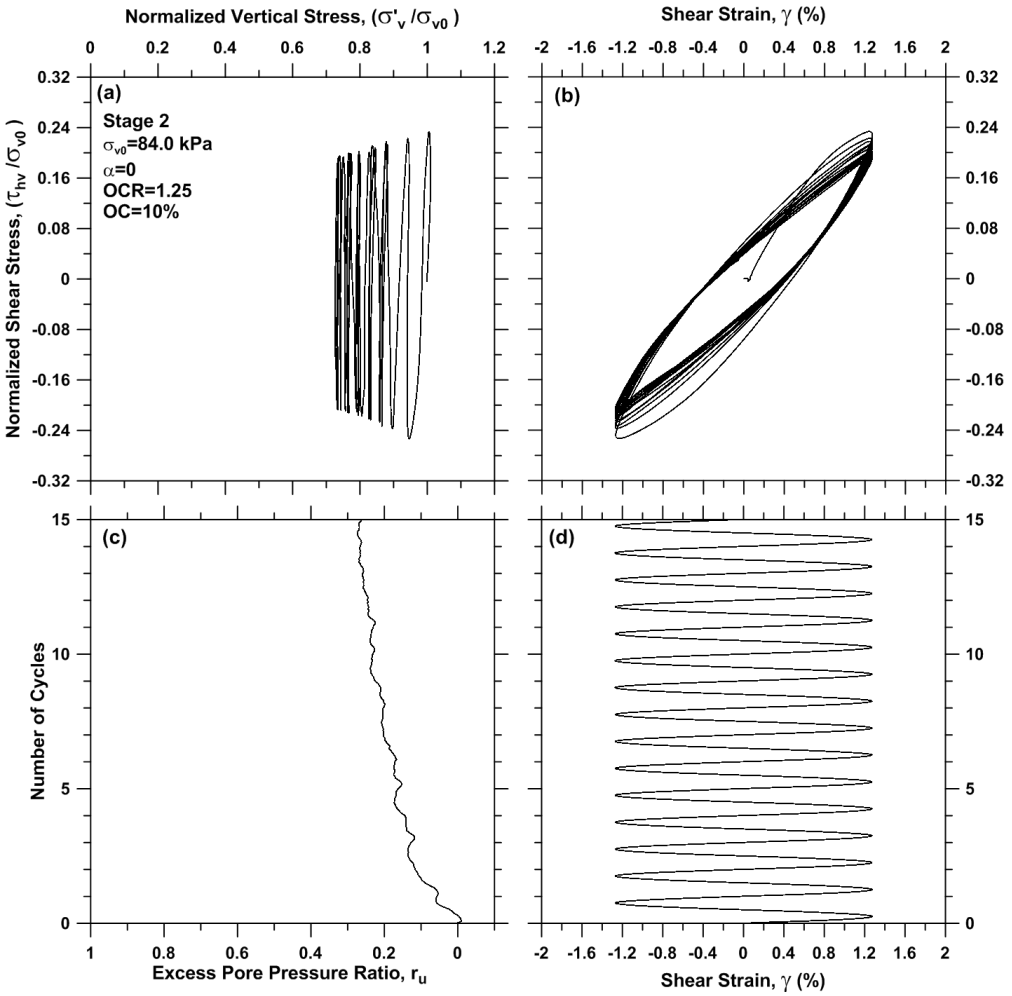

Figure A.17 Cyclic strain-controlled DSS test results on specimen BH6S4_14.3, stage 2

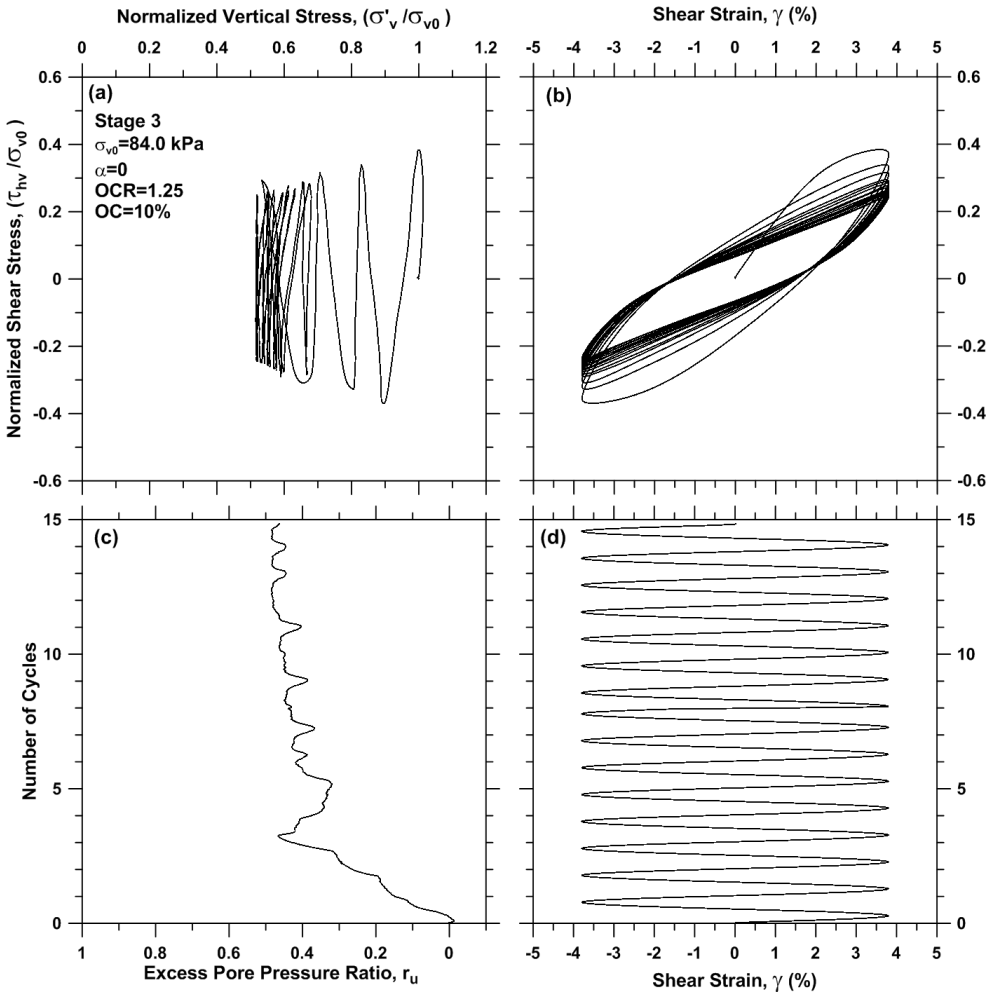

Figure A.18 Cyclic strain-controlled DSS test results on specimen BH6S4_14.3, stage 3

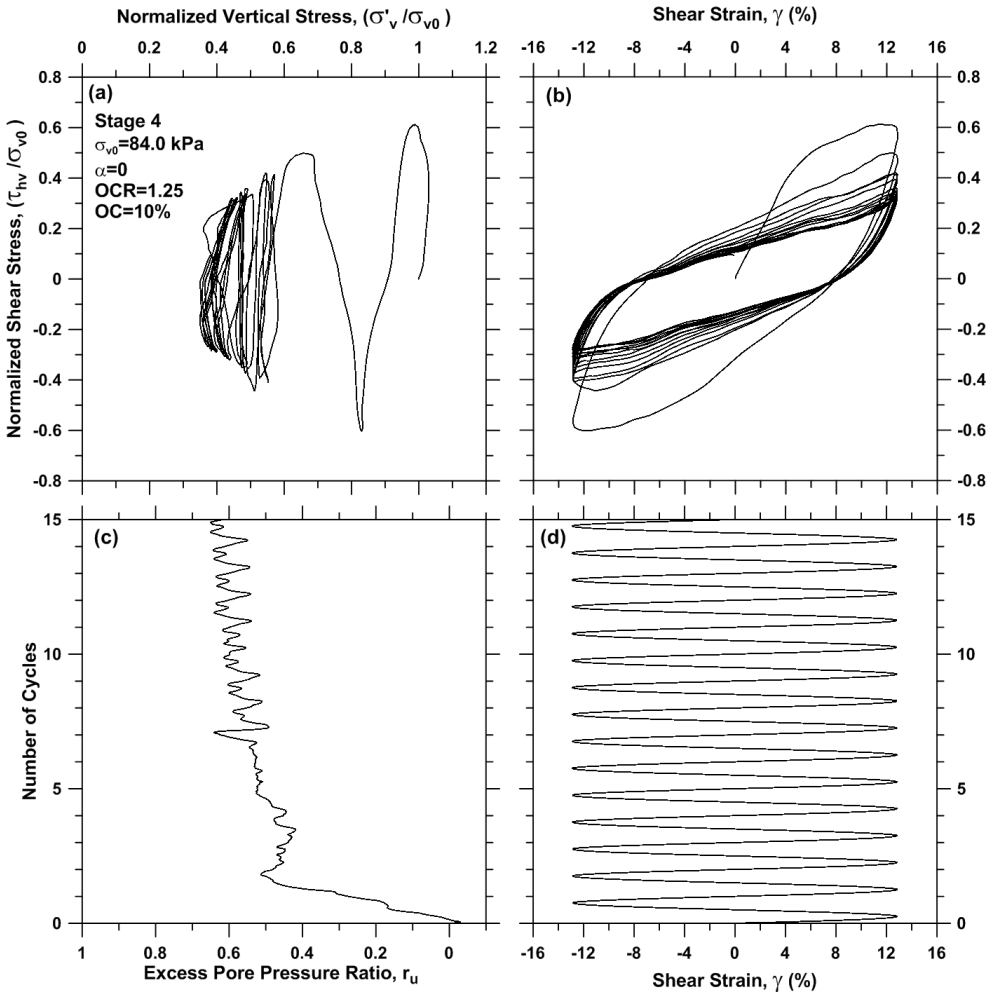

Figure A.19 Cyclic strain-controlled DSS test results on specimen BH6S4_14.3, stage 4

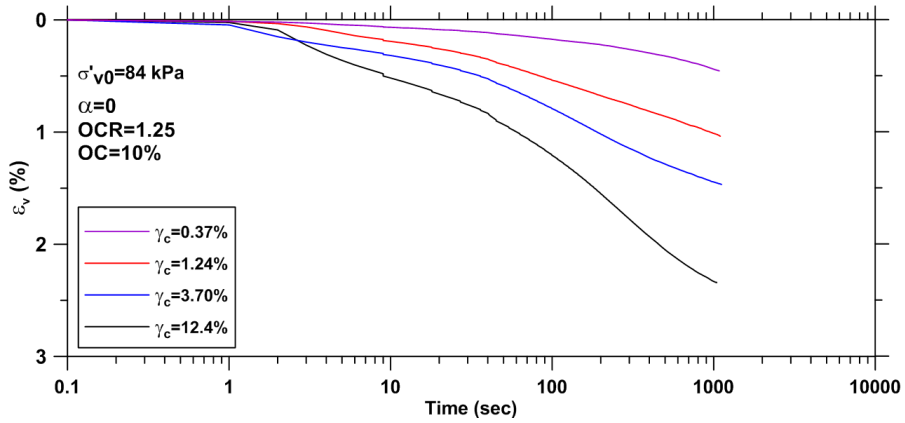

Figure A.20 Post-cyclic volume change following strain-controlled DSS tests on specimen BH6S4_14.3

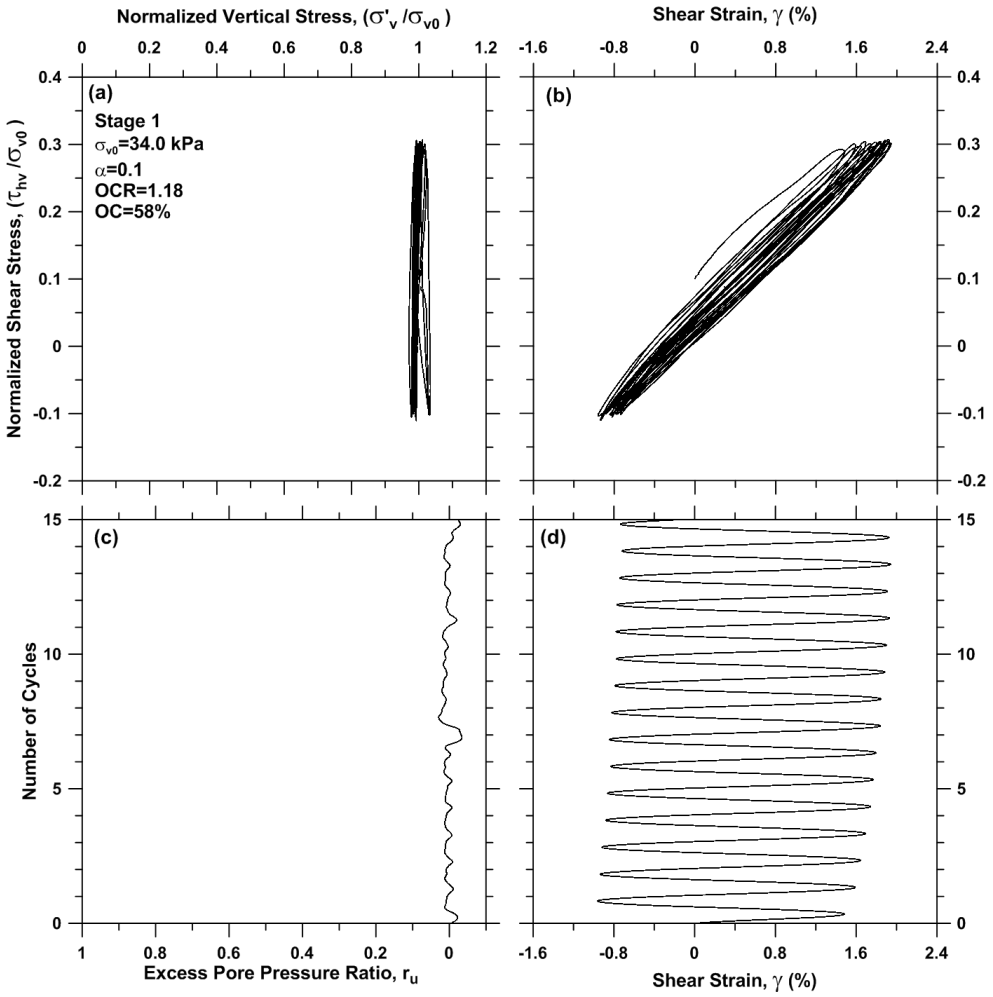

Figure A.21 Cyclic stress-controlled DSS test results on specimen BH7S1_7.1, stage 1

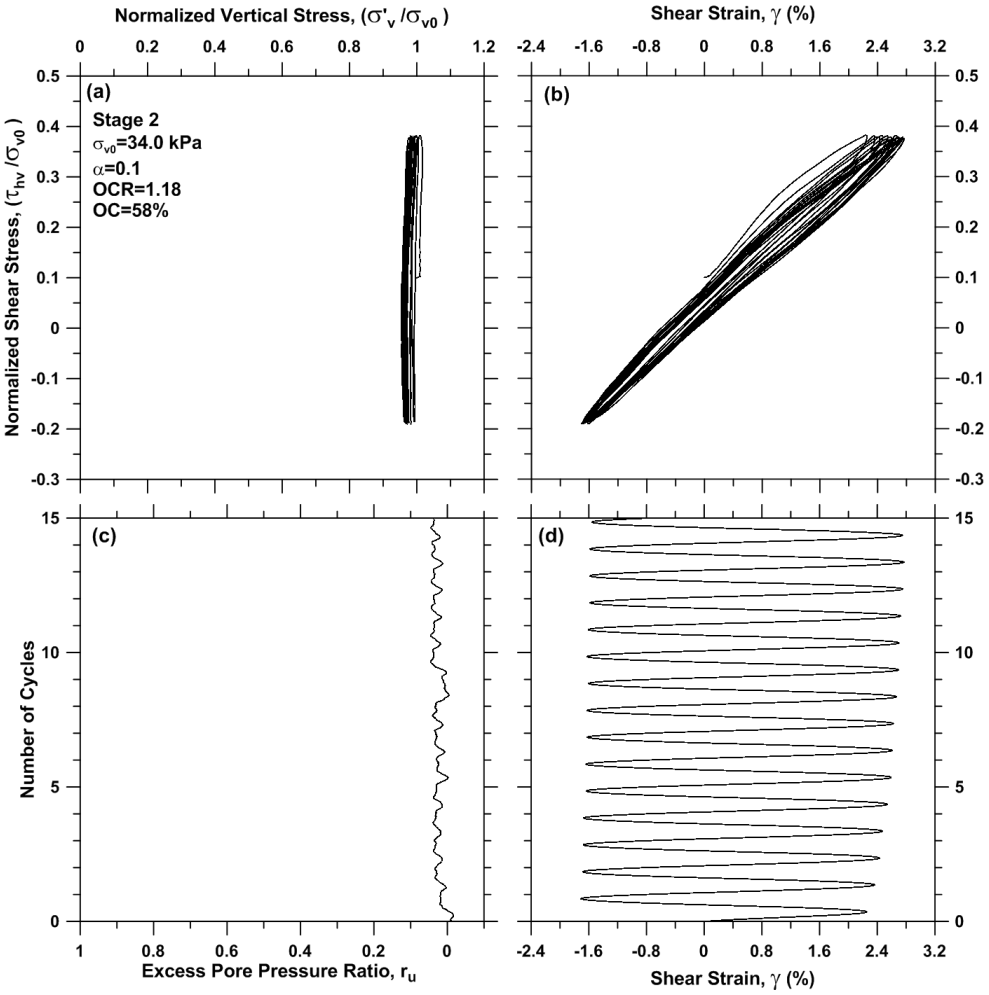

Figure A.22 Cyclic stress-controlled DSS test results on specimen BH7S1_7.1, stage 2

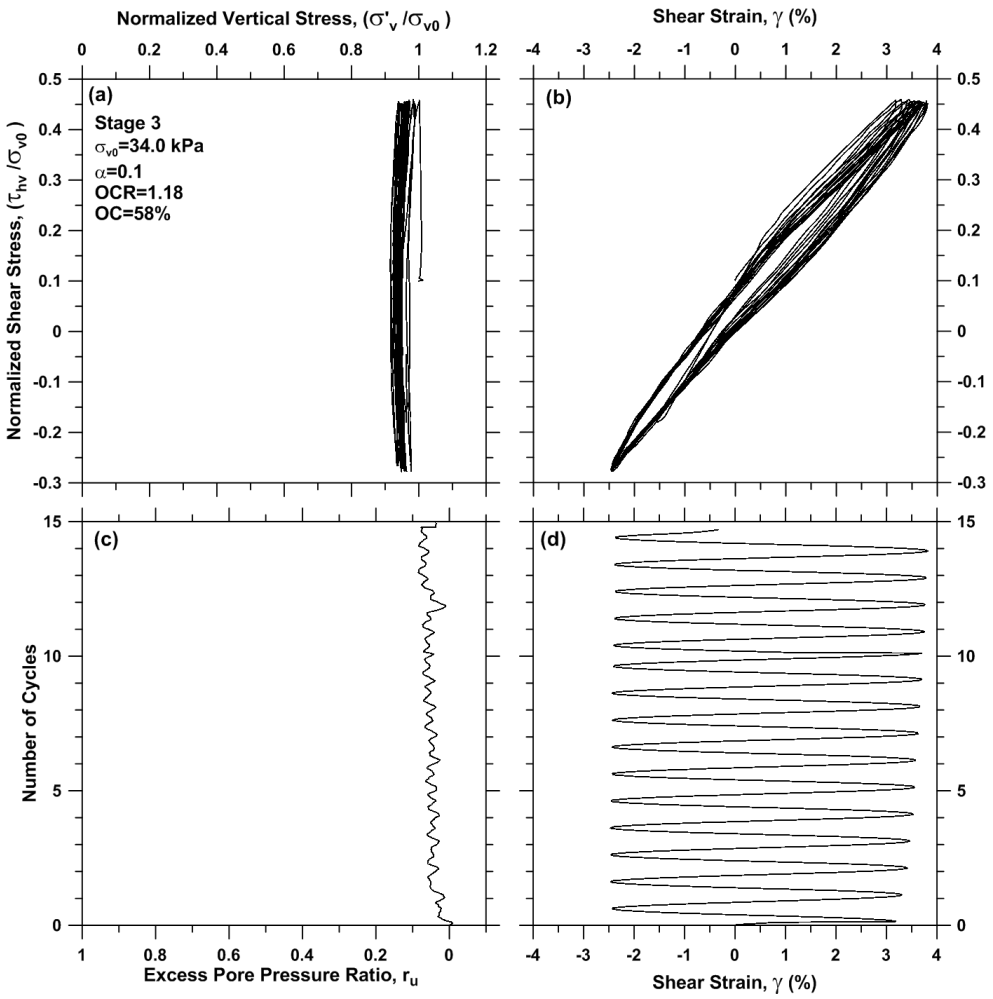

Figure A.23 Cyclic stress-controlled DSS test results on specimen BH7S1_7.1, stage 3

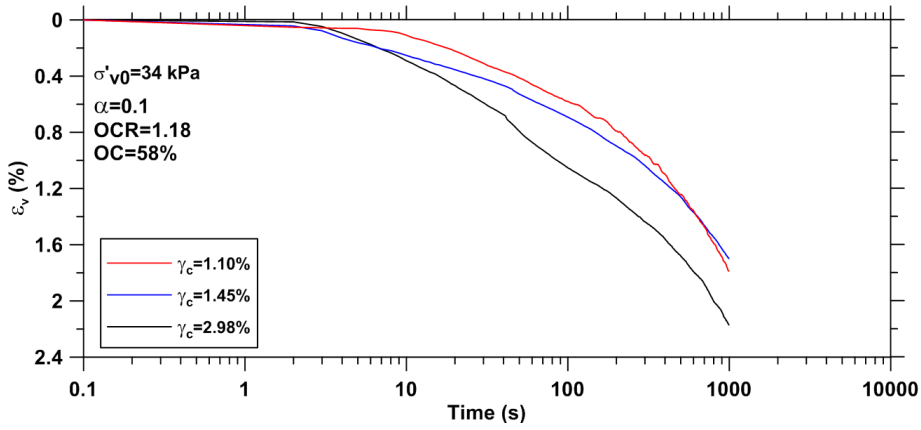

Figure A.24 Post-cyclic volume change following stress-controlled DSS tests on specimen BH7S1_7.1

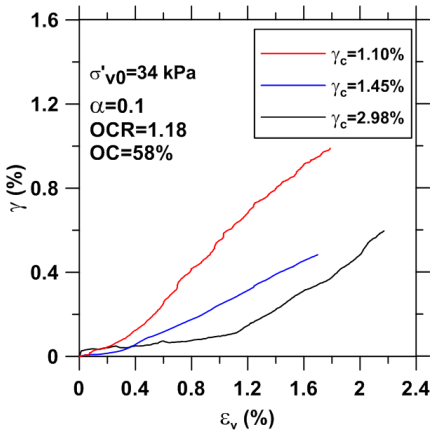

Figure A.25 Post-cyclic shear strain versus post-cyclic volume change for specimen BH7S1_7.1

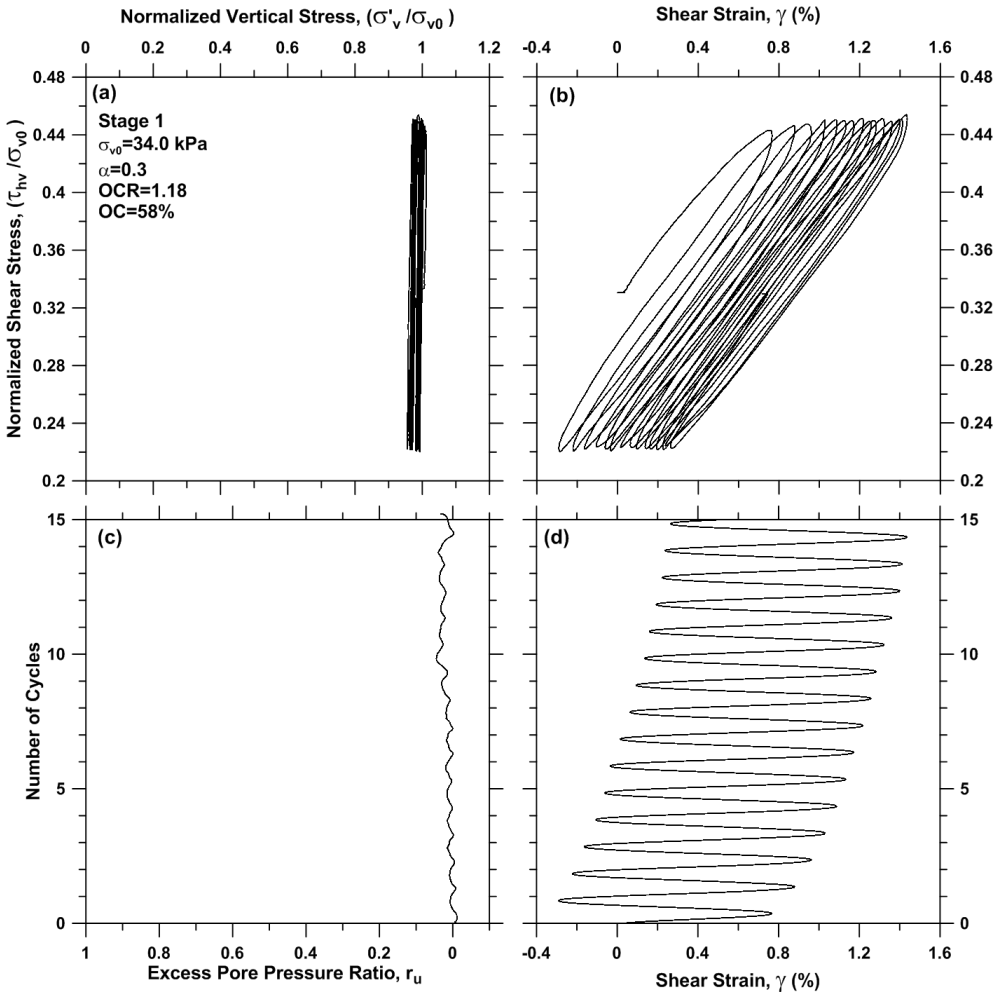

Figure A.26 Cyclic stress-controlled DSS test results on specimen BH7S2_7.2, stage 1

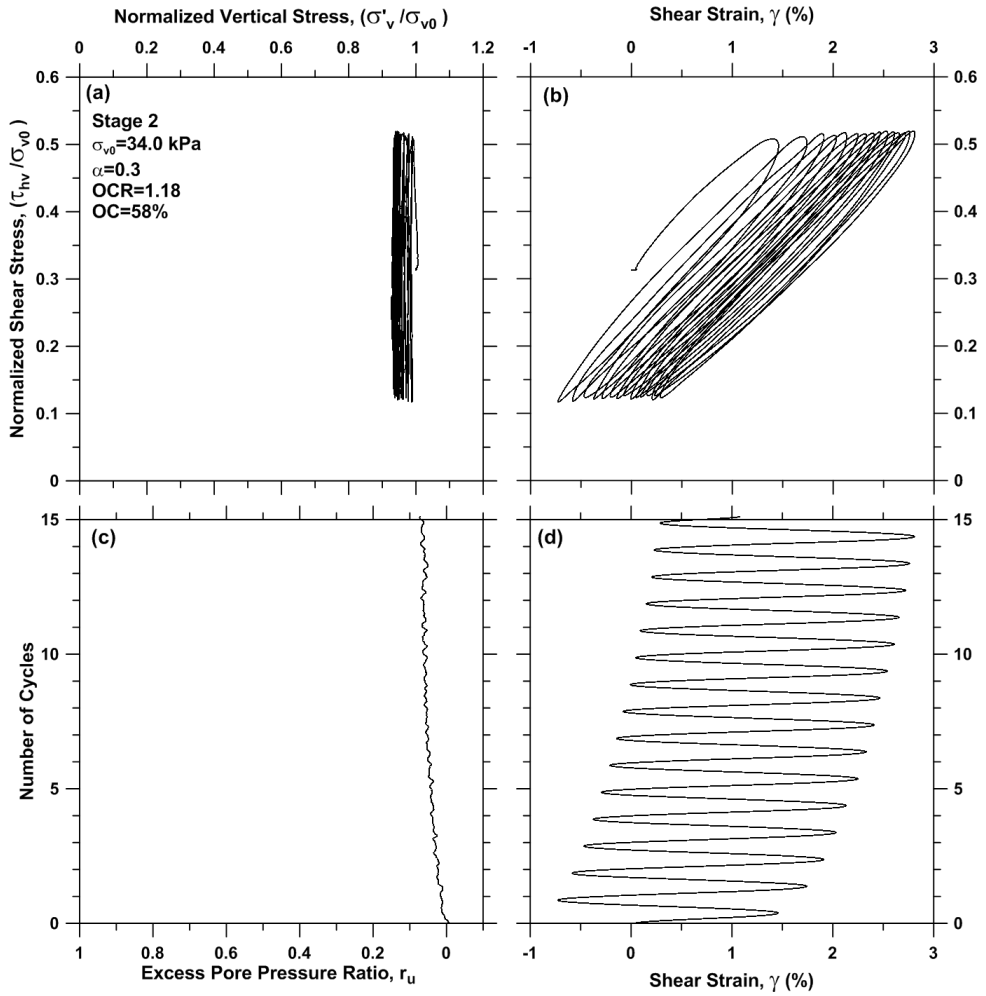

Figure A.27 Cyclic stress-controlled DSS test results on specimen BH7S2_7.2, stage 2

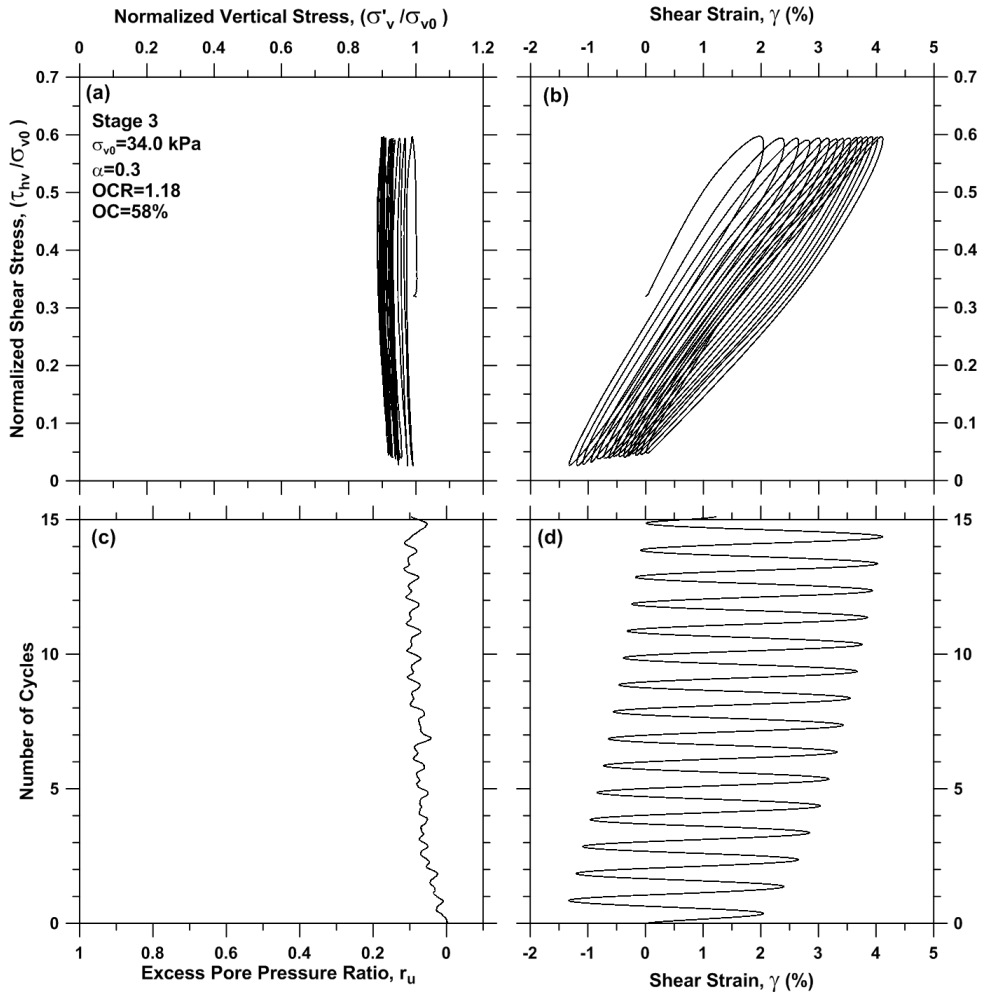

Figure A.28 Cyclic stress-controlled DSS test results on specimen BH7S2_7.2, stage 3

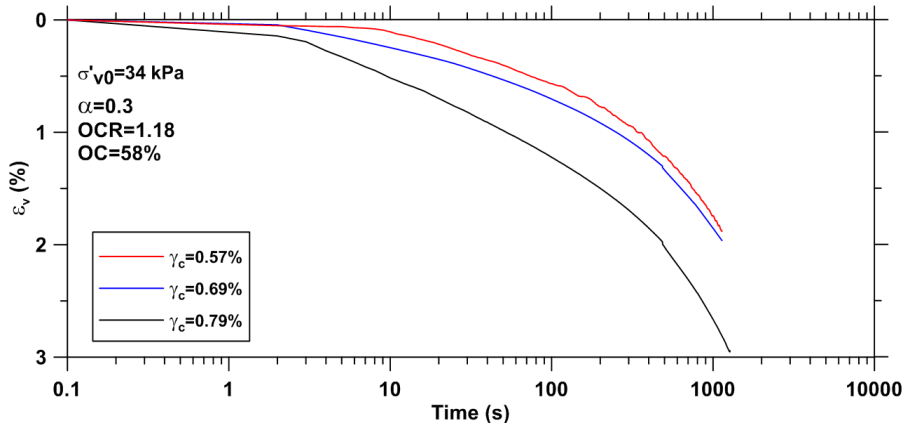

Figure A.29 Post-cyclic volume change following stress-controlled DSS tests on specimen BH7S2_7.2

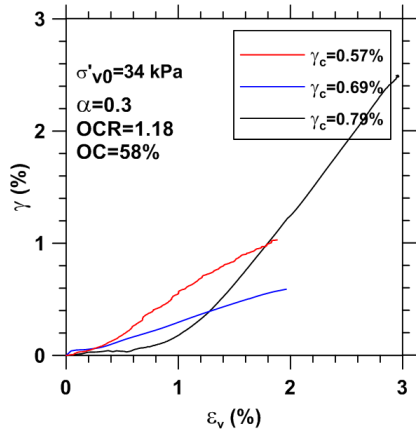

Figure A.30 Post-cyclic shear strain versus post-cyclic volume change for specimen BH7S2_7.2

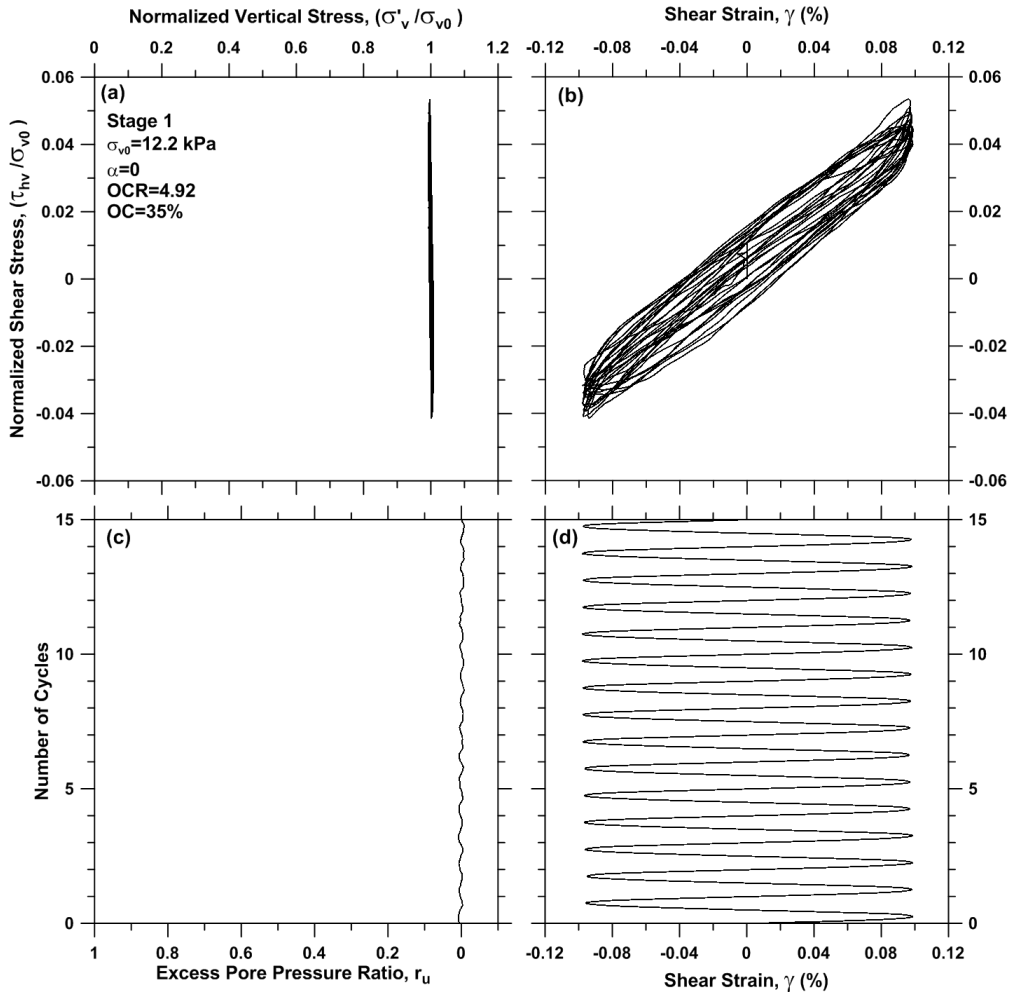

Figure A.31 Cyclic strain-controlled DSS test results on specimen BH7S10_10.3, stage 1

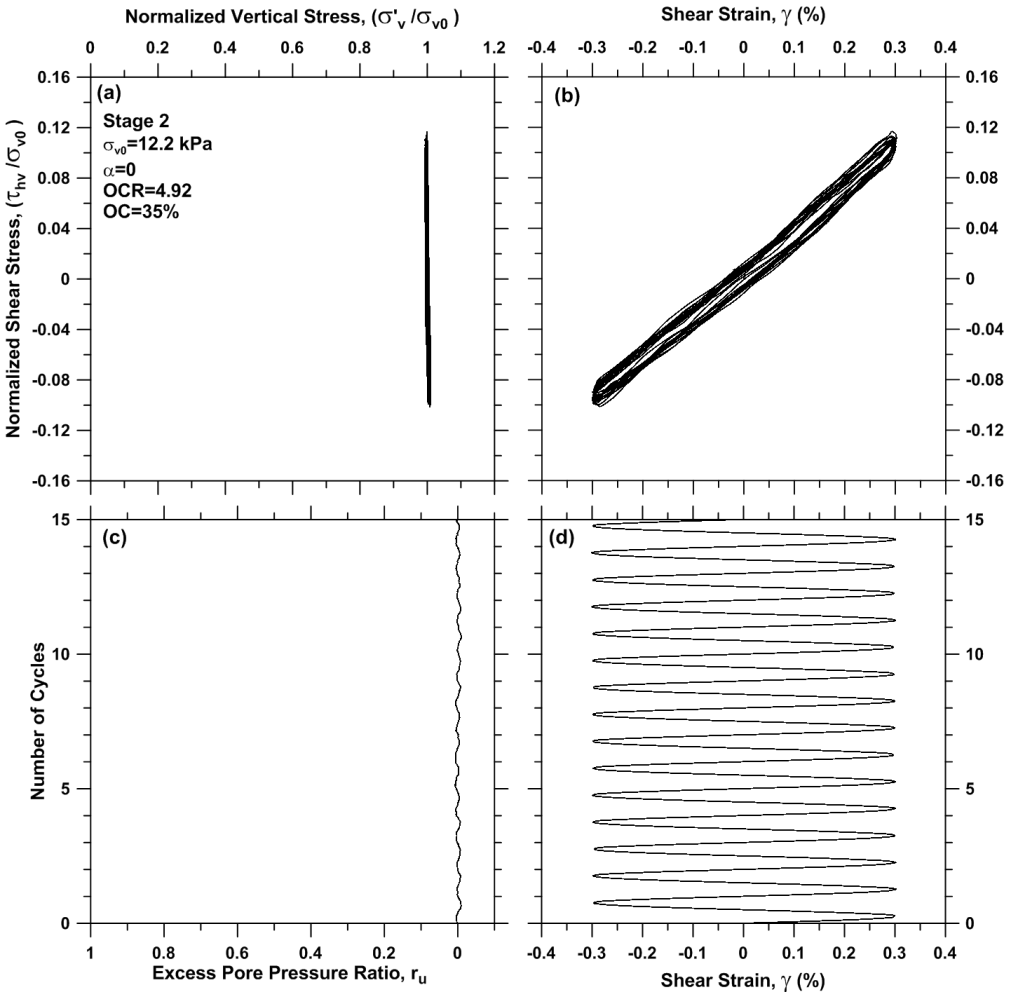

Figure A.32 Cyclic strain-controlled DSS test results on specimen BH7S10_10.3, stage 2

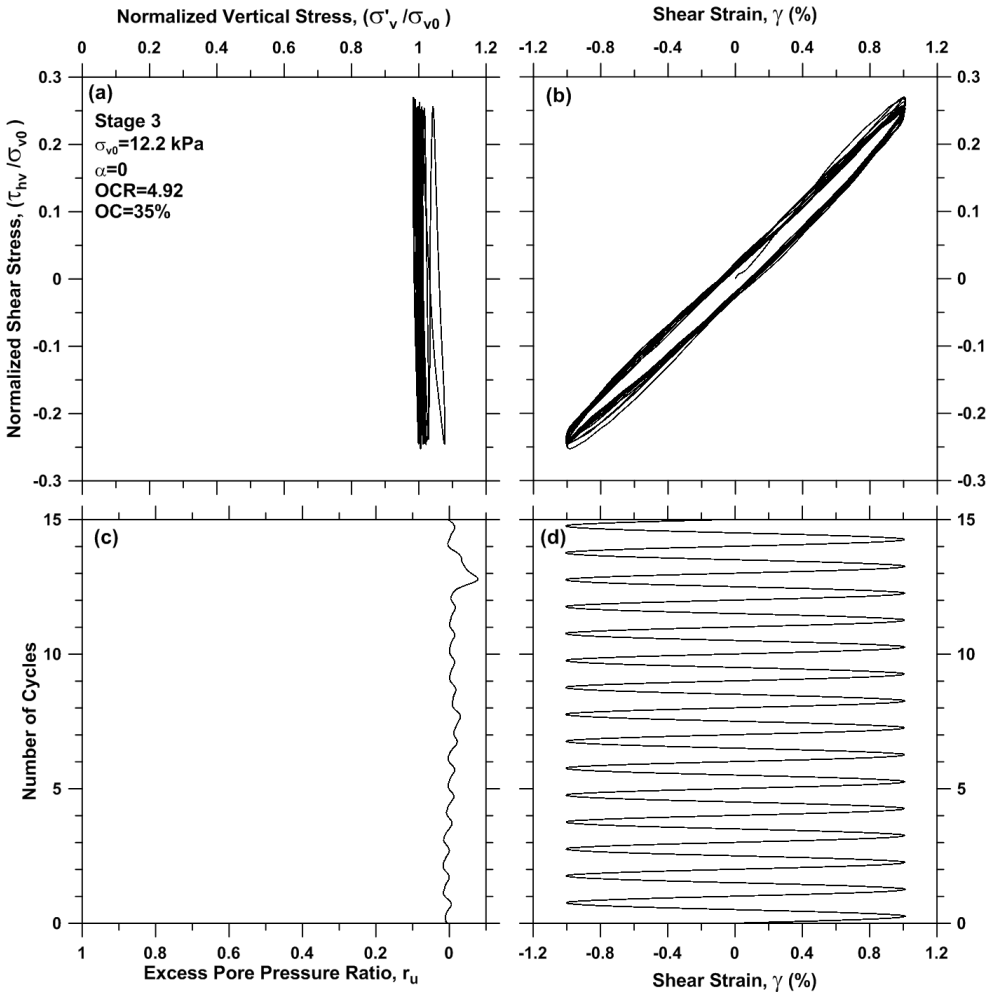

Figure A.33 Cyclic strain-controlled DSS test results on specimen BH7S10_10.3, stage 3

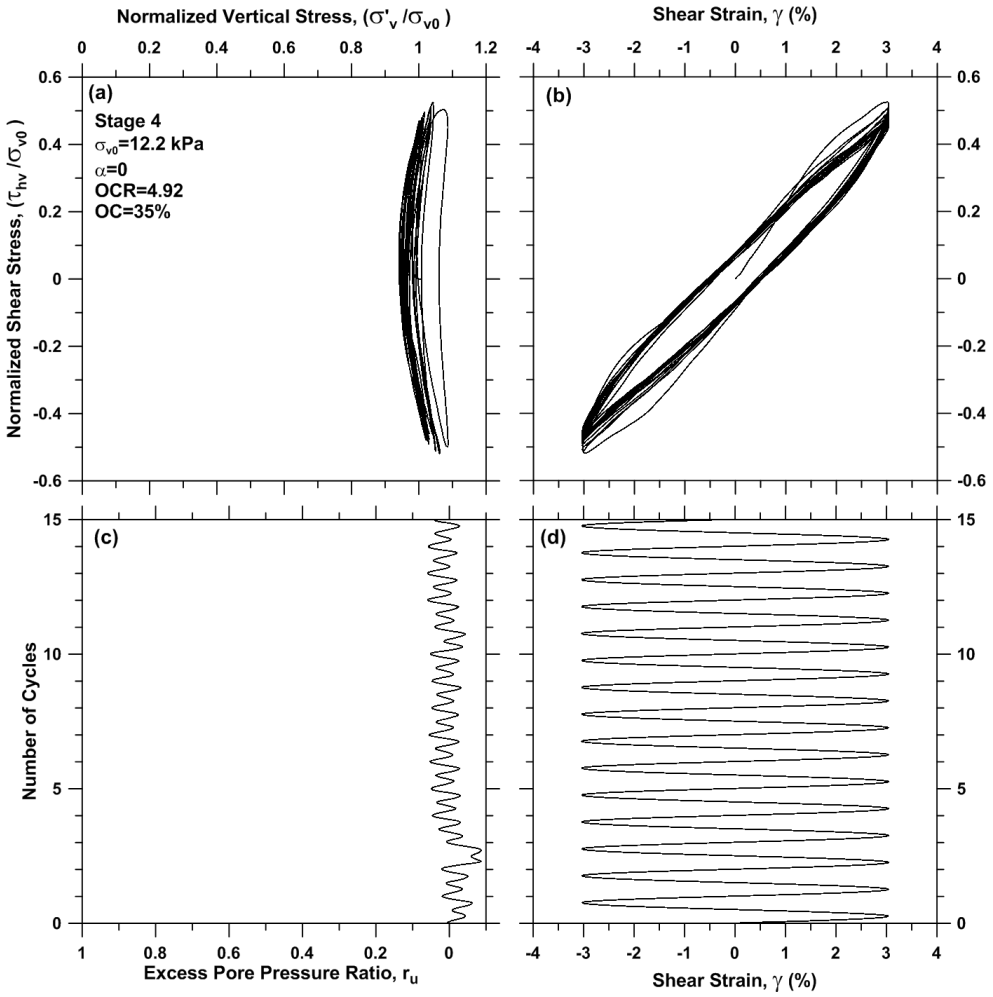

Figure A.34 Cyclic strain-controlled DSS test results on specimen BH7S10_10.3, stage 4

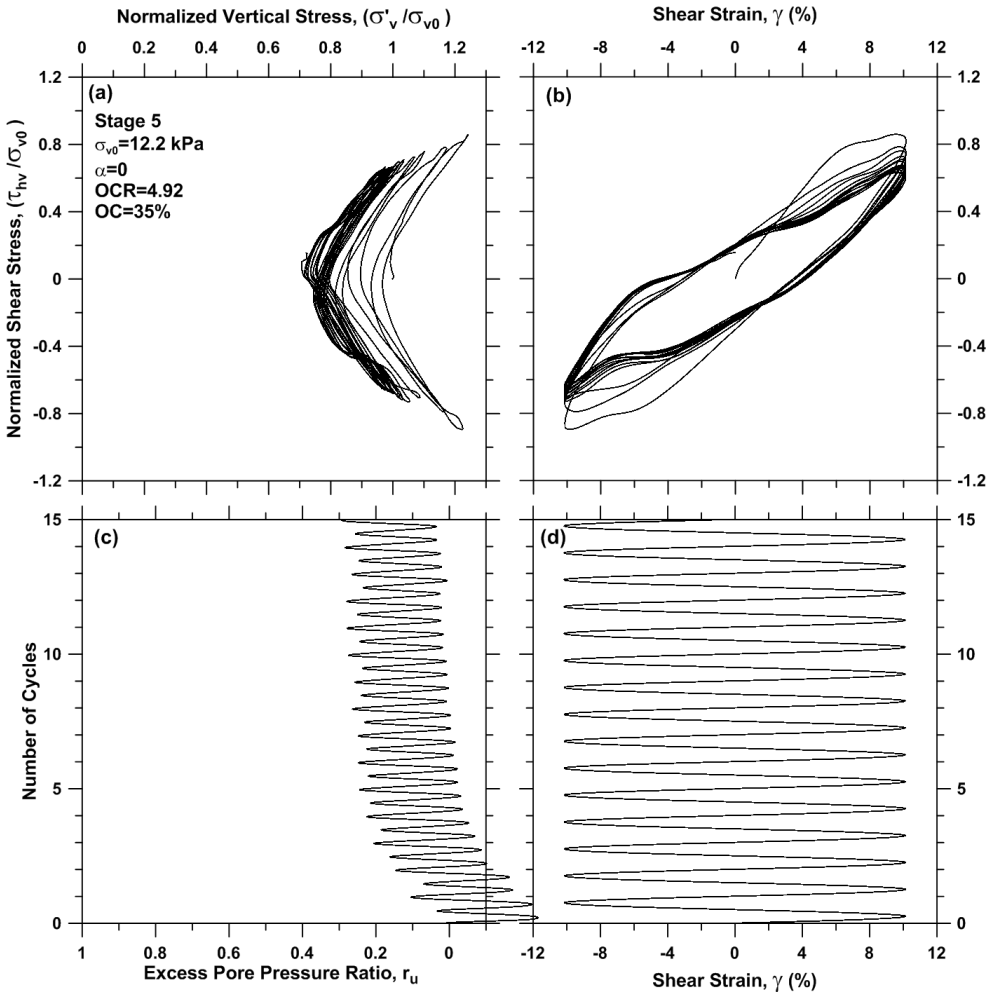

Figure A.35 Cyclic strain-controlled DSS test results on specimen BH7S10_10.3, stage 5

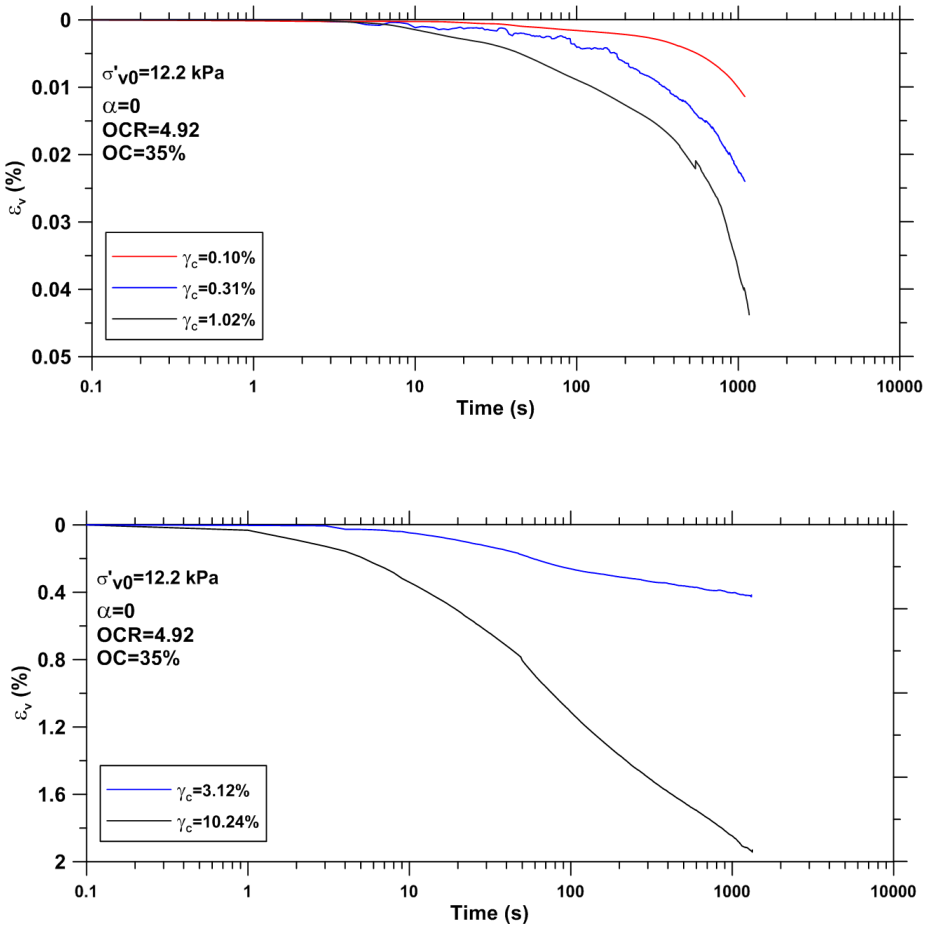

Figure A.36 Post-cyclic volume change following strain-controlled DSS tests on specimen BH7S10_10.3

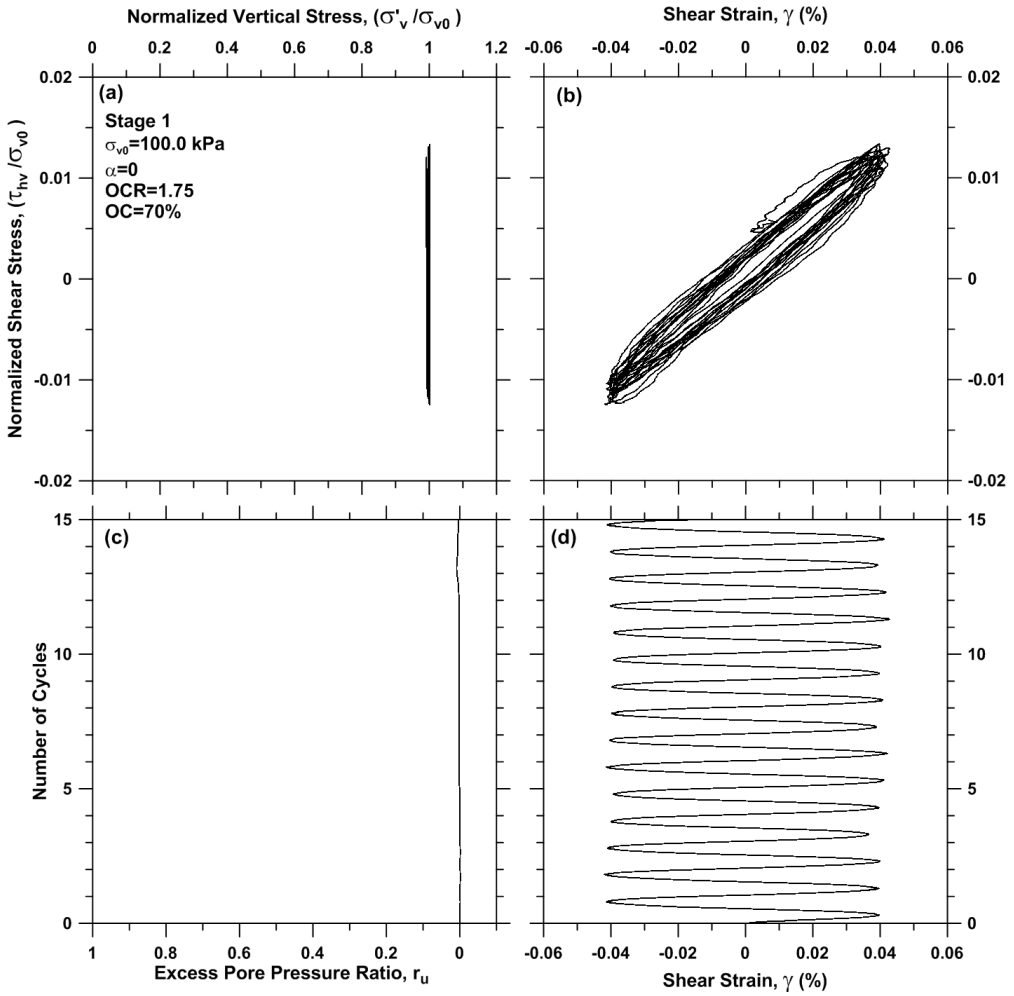

Figure A.37 Cyclic strain-controlled DSS test results on specimen BH8S1_7.1, stage 1

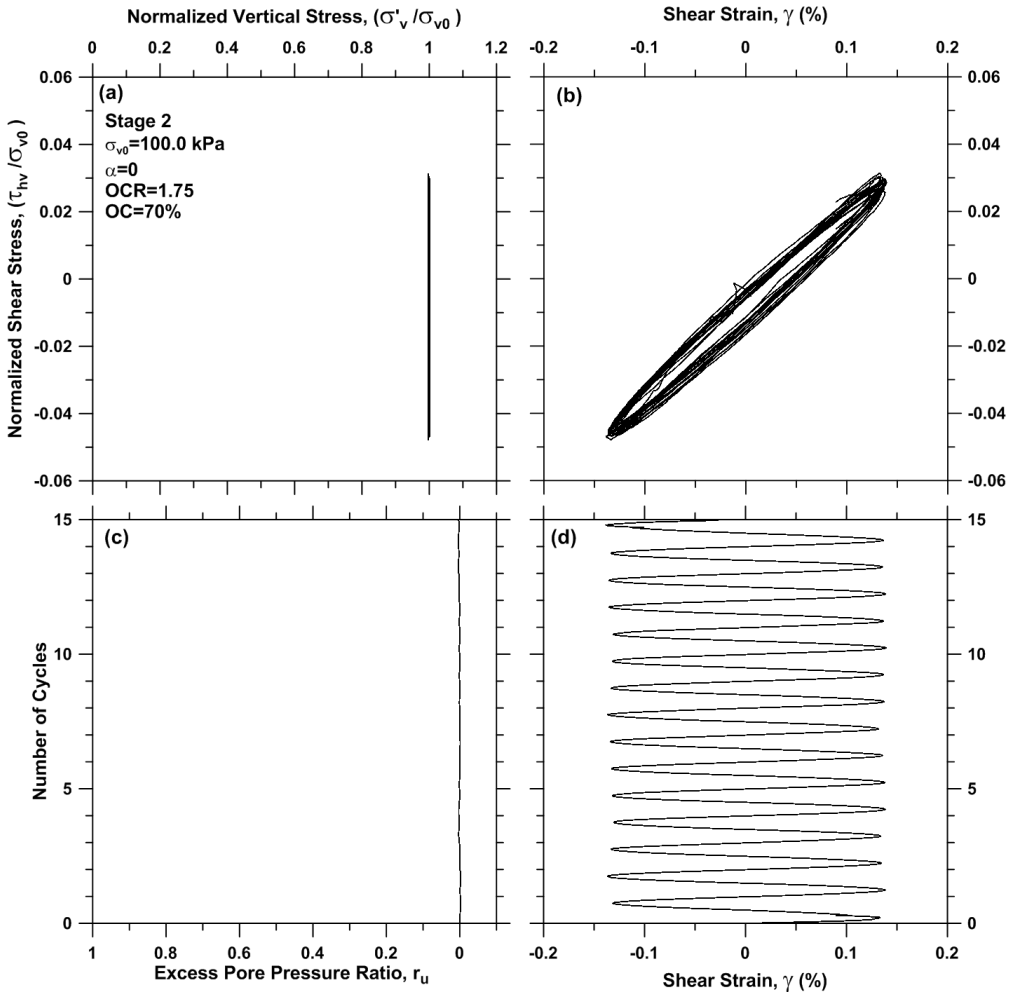

Figure A.38 Cyclic strain-controlled DSS test results on specimen BH8S1_7.1, stage 2

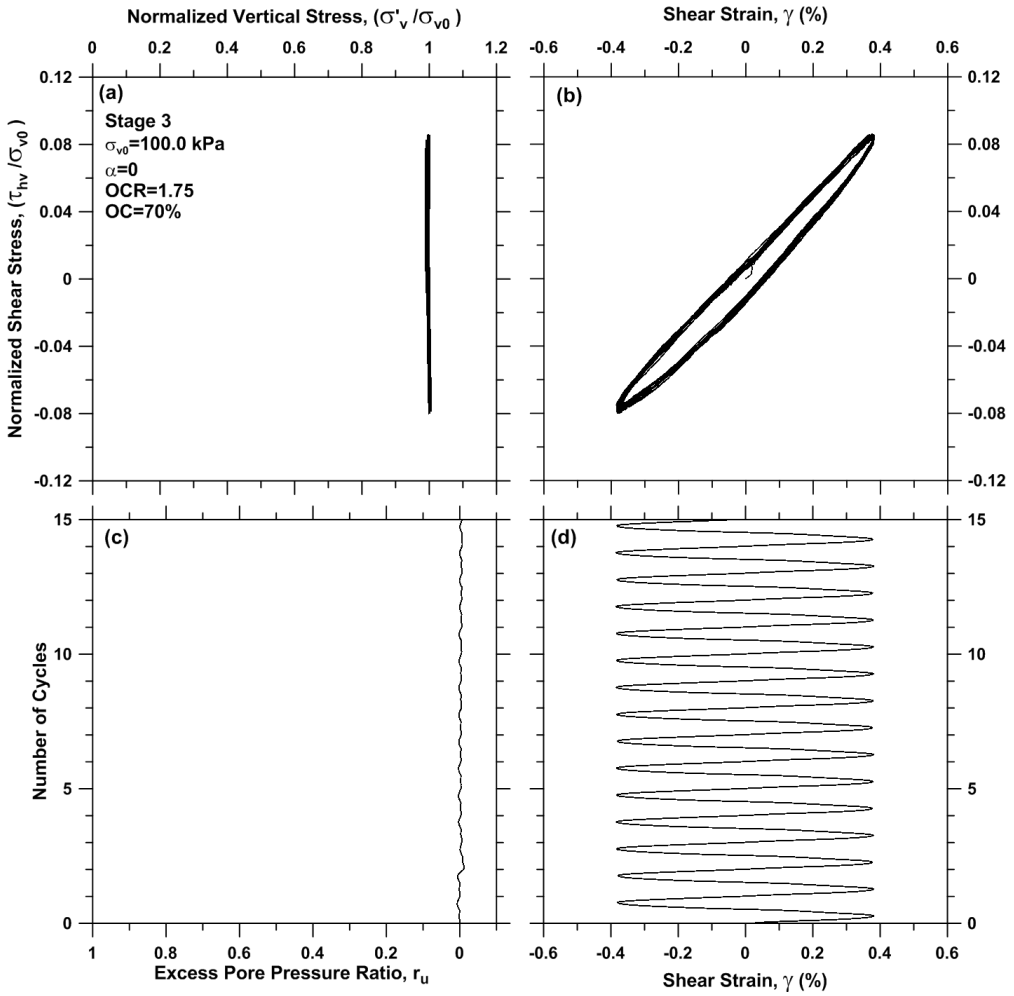

Figure A.39 Cyclic strain-controlled DSS test results on specimen BH8S1_7.1, stage 3

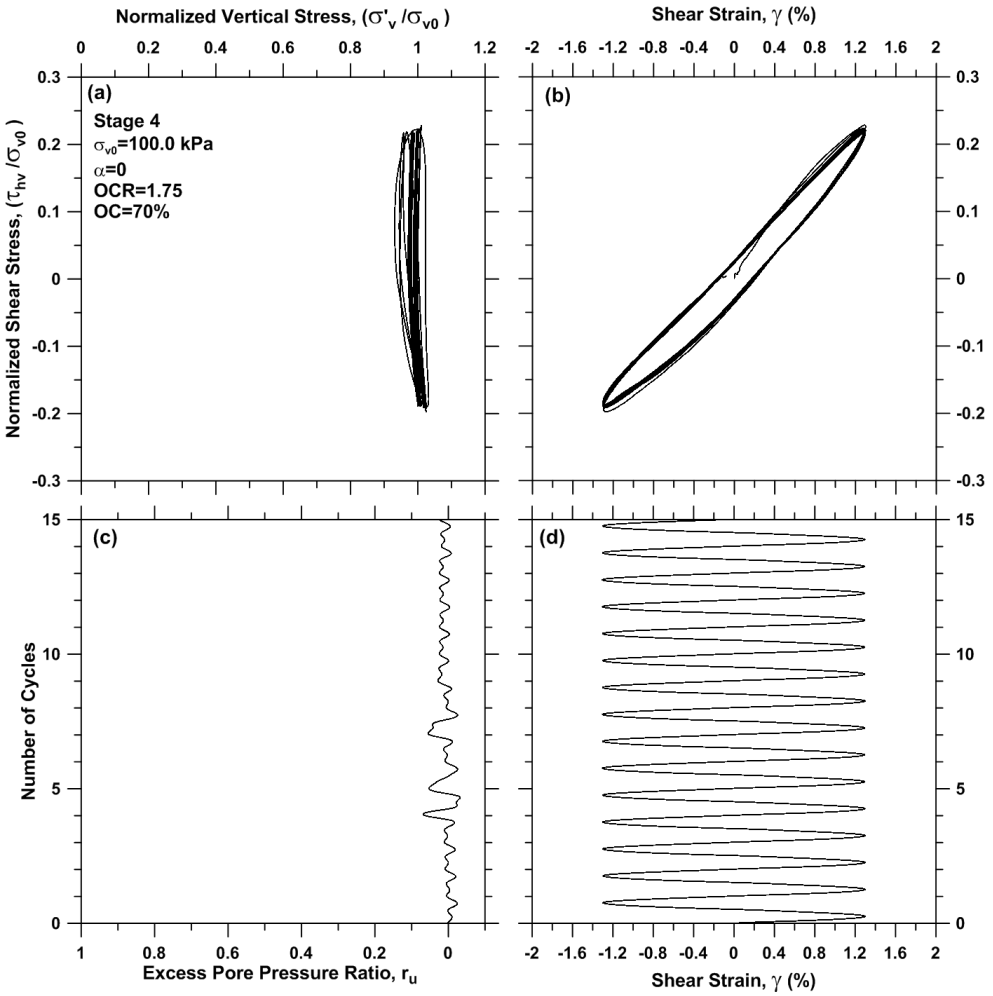

Figure A.40 Cyclic strain-controlled DSS test results on specimen BH8S1_7.1, stage 4

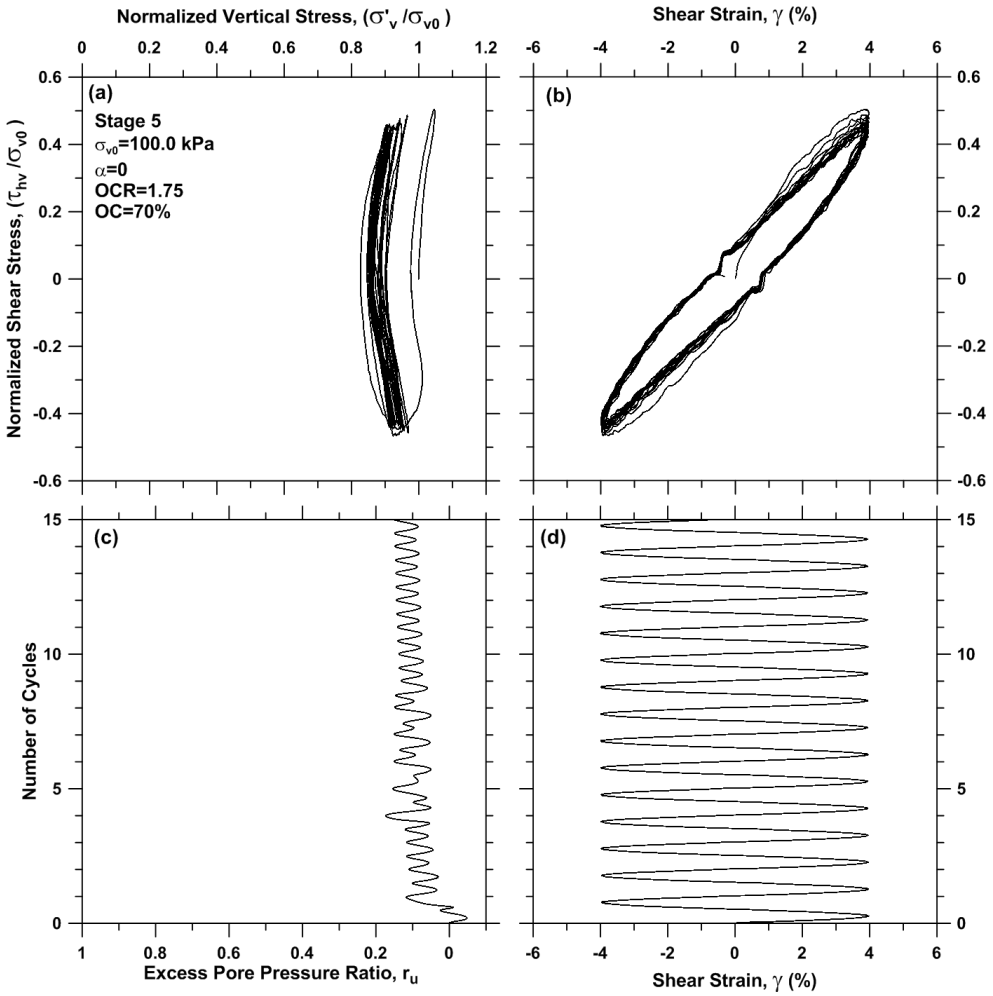

Figure A.41 Cyclic strain-controlled DSS test results on specimen BH8S1_7.1, stage 5

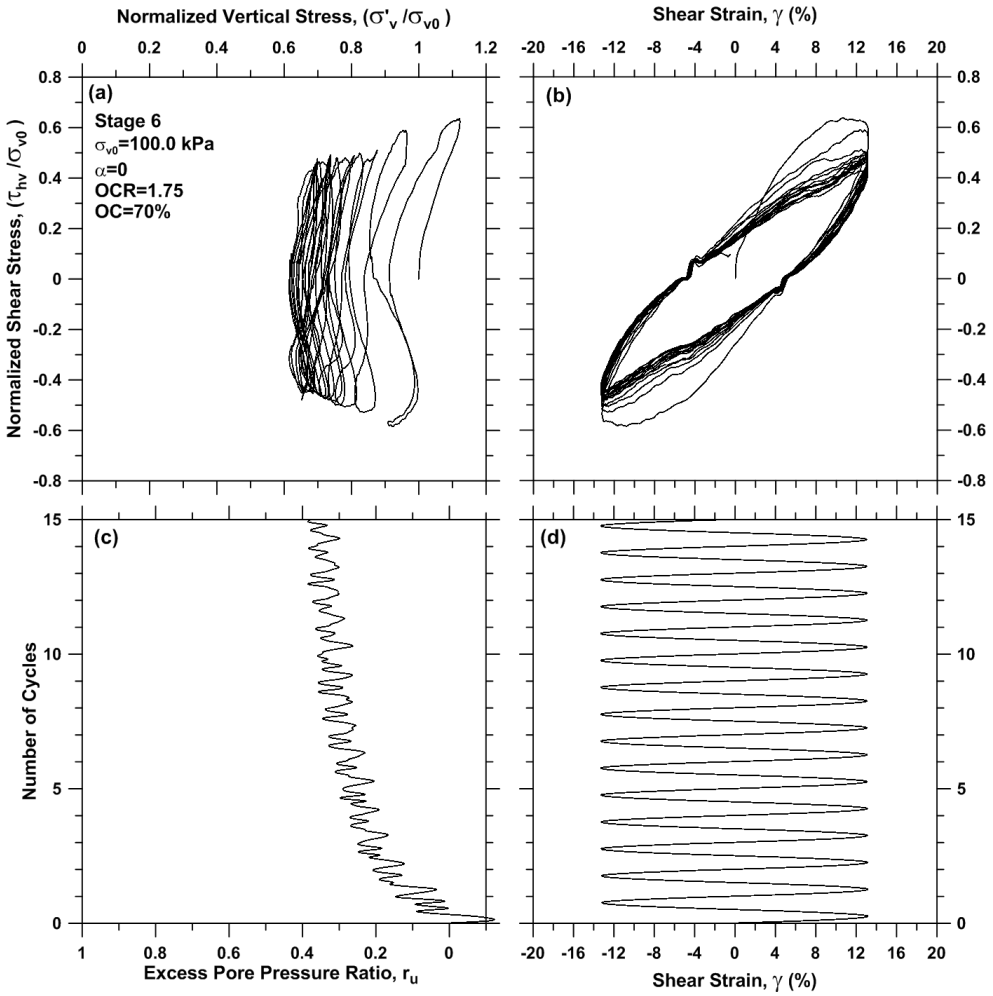

Figure A.42 Cyclic strain-controlled DSS test results on specimen BH8S1_7.1, stage 6

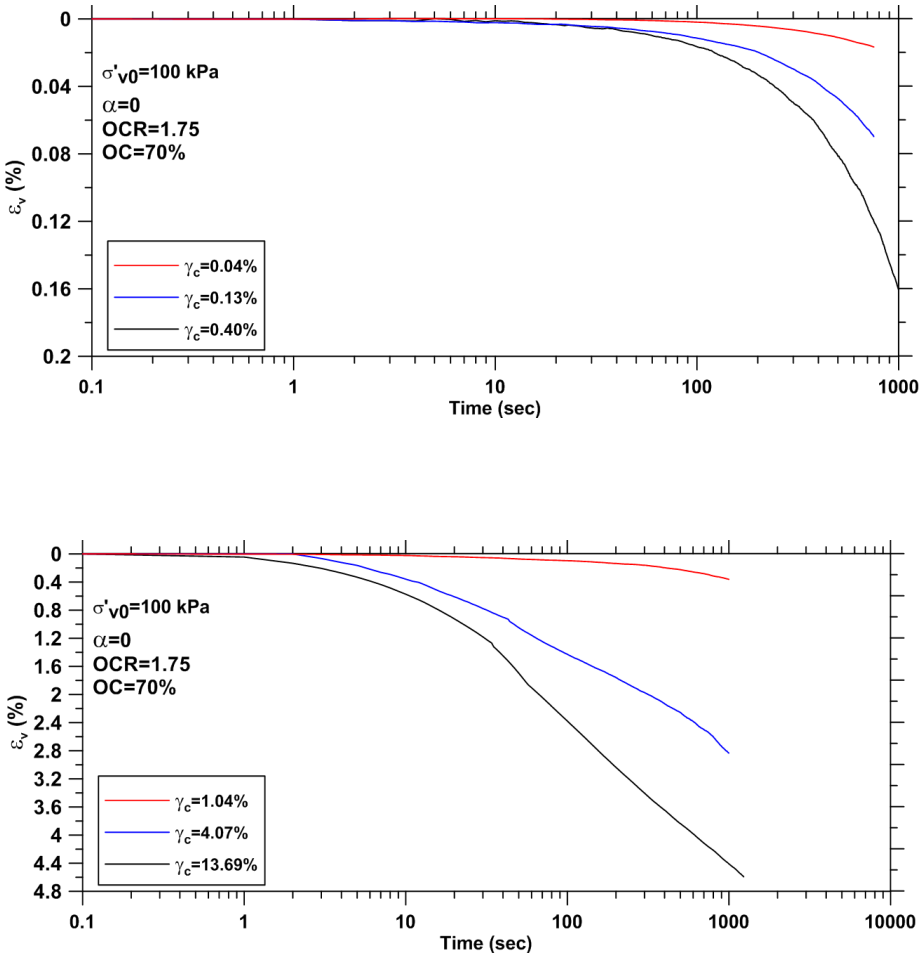

Figure A.43 Post-cyclic volume change following strain-controlled DSS tests on specimen BH8S1_7.1

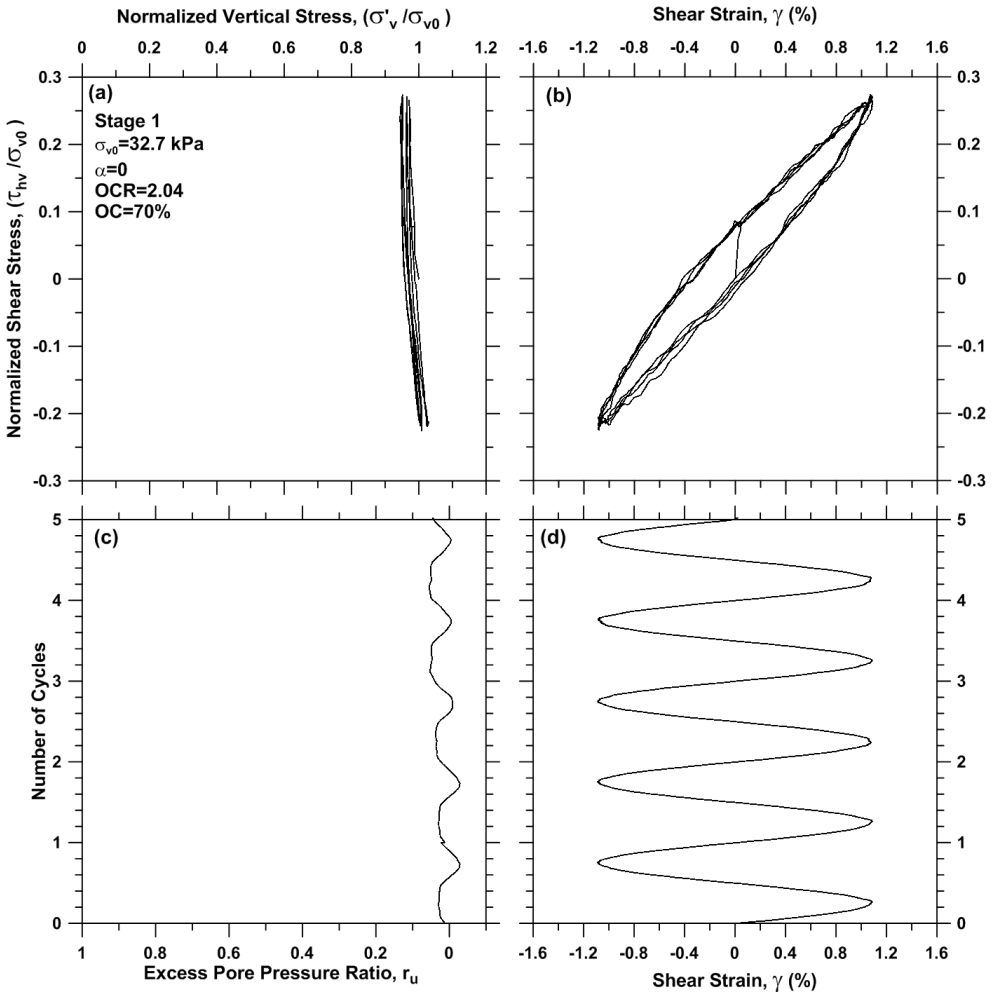

Figure A.44 Cyclic strain-controlled DSS test results on specimen BH8S3_7.4, stage 1

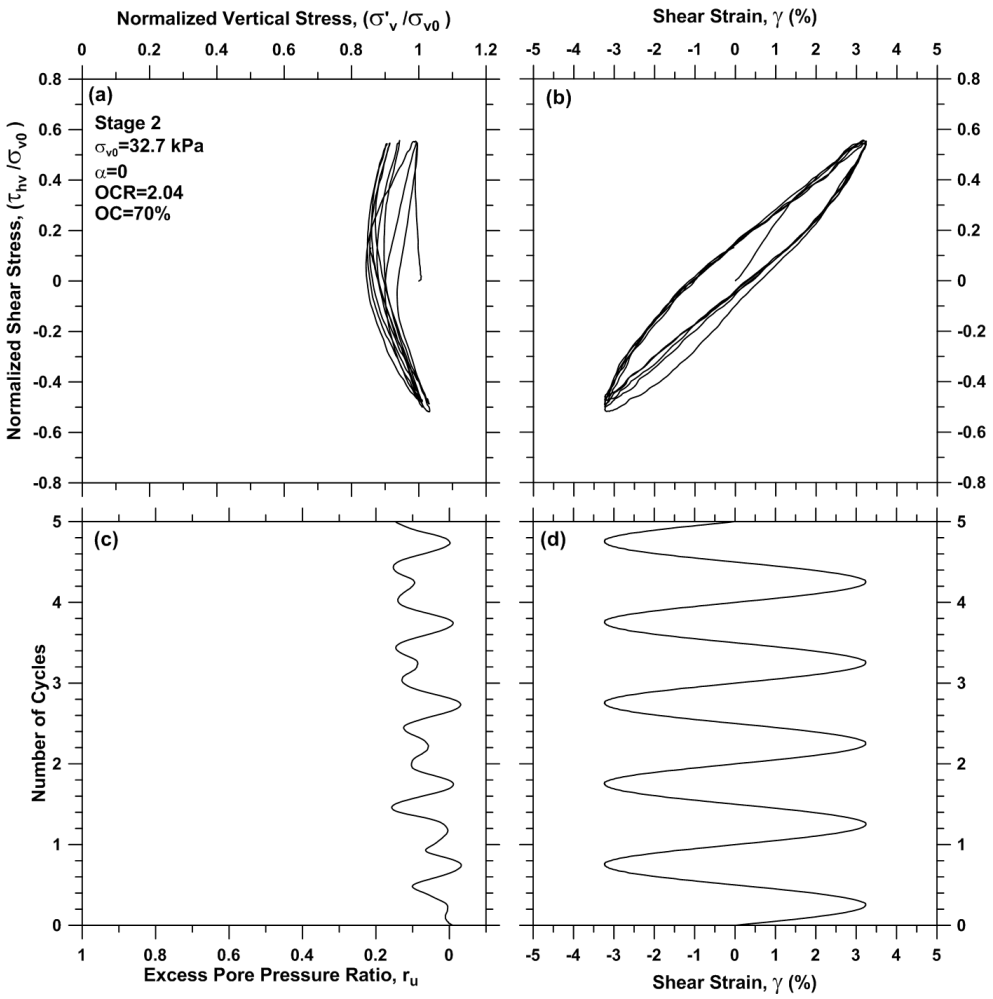

Figure A.45 Cyclic strain-controlled DSS test results on specimen BH8S3_7.4, stage 2

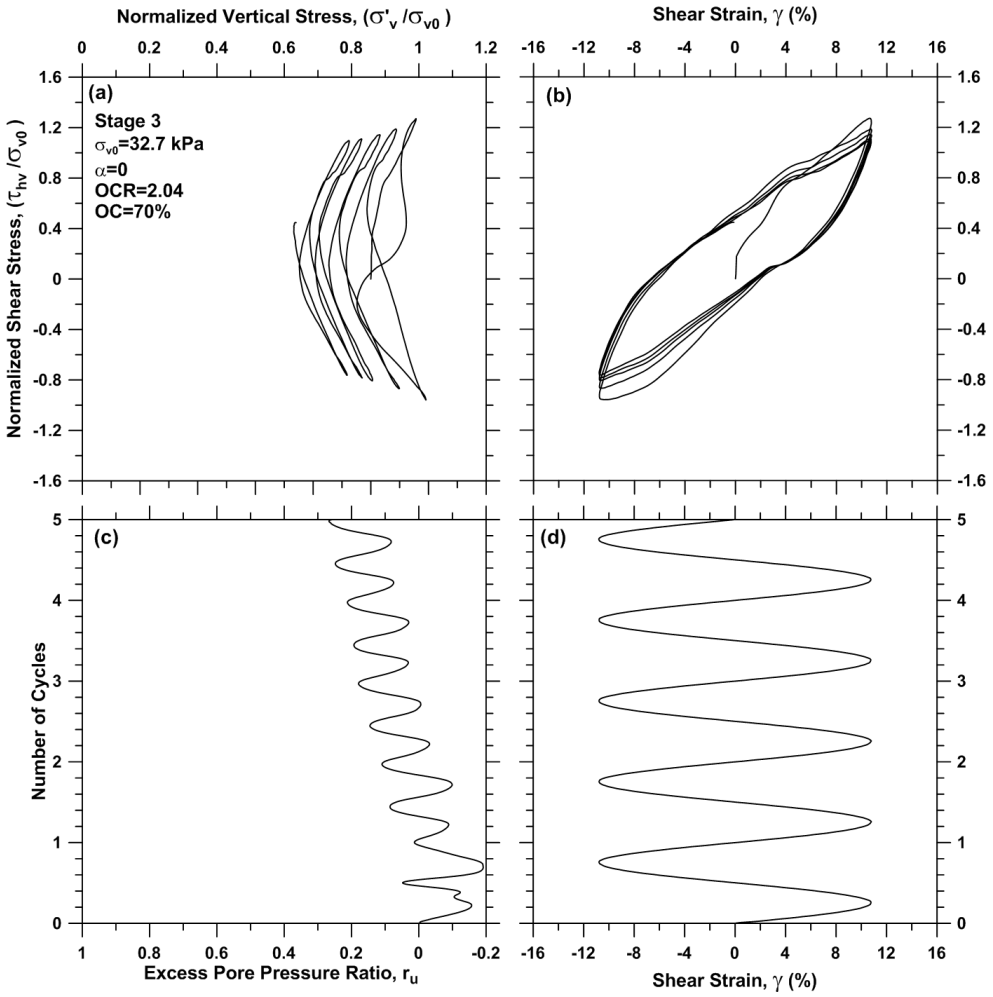

Figure A.46 Cyclic strain-controlled DSS test results on specimen BH8S3_7.4, stage 3

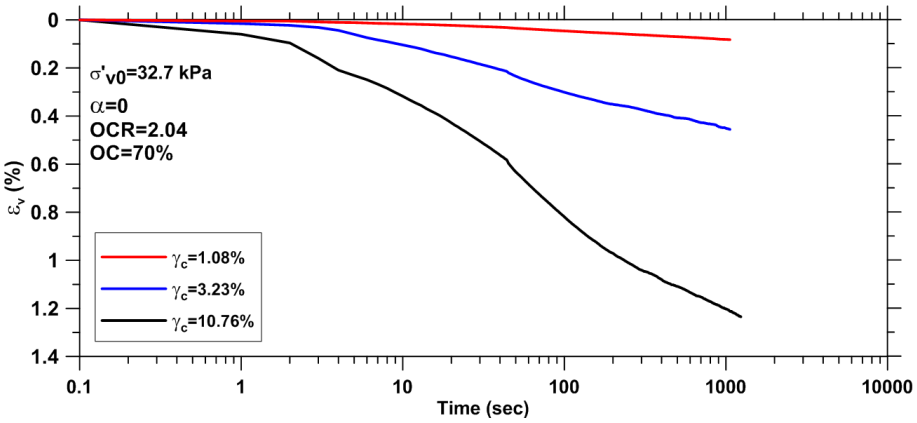

Figure A.47 Post-cyclic volume change following strain-controlled DSS tests on specimen BH8S3_7.4

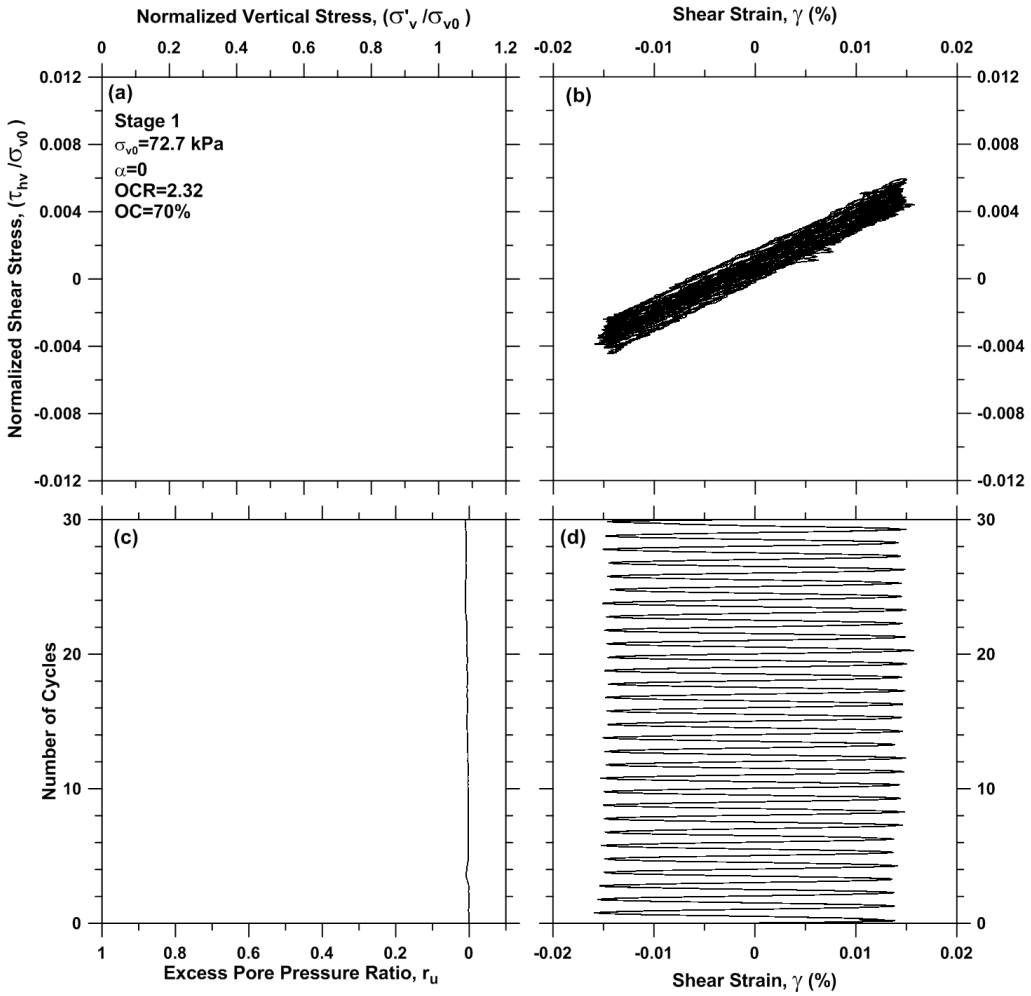

Figure A.48 Cyclic strain-controlled DSS test results on specimen BH8S4_7.5, stage 1

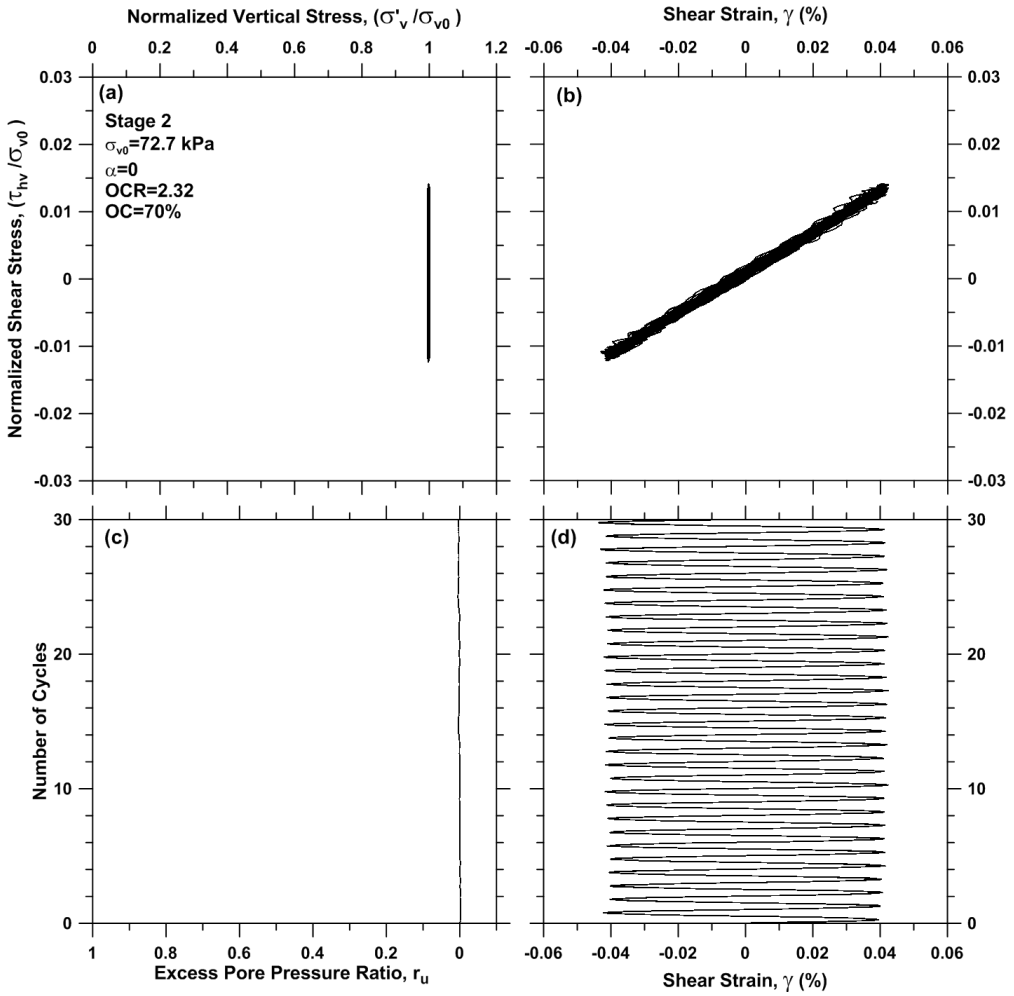

Figure A.49 Cyclic strain-controlled DSS test results on specimen BH8S4_7.5, stage 2

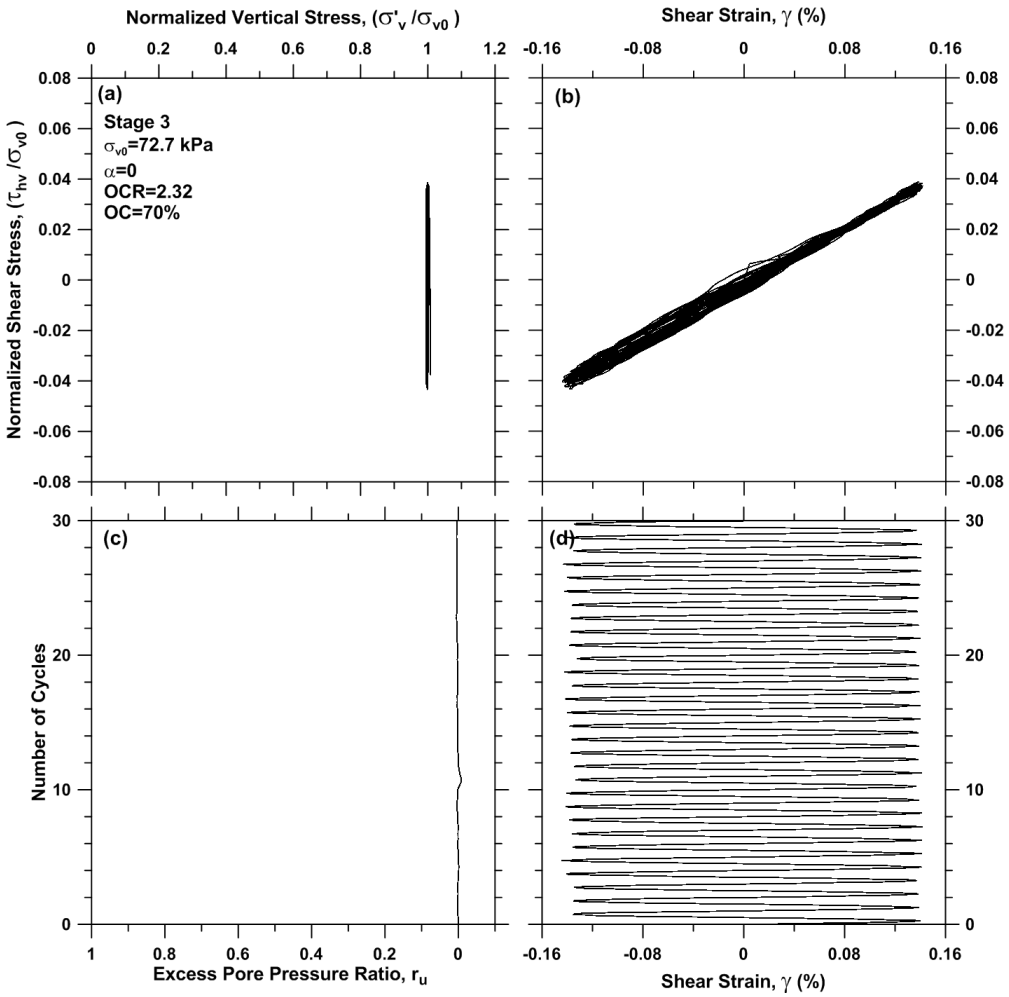

Figure A.50 Cyclic strain-controlled DSS test results on specimen BH8S4_7.5, stage 3

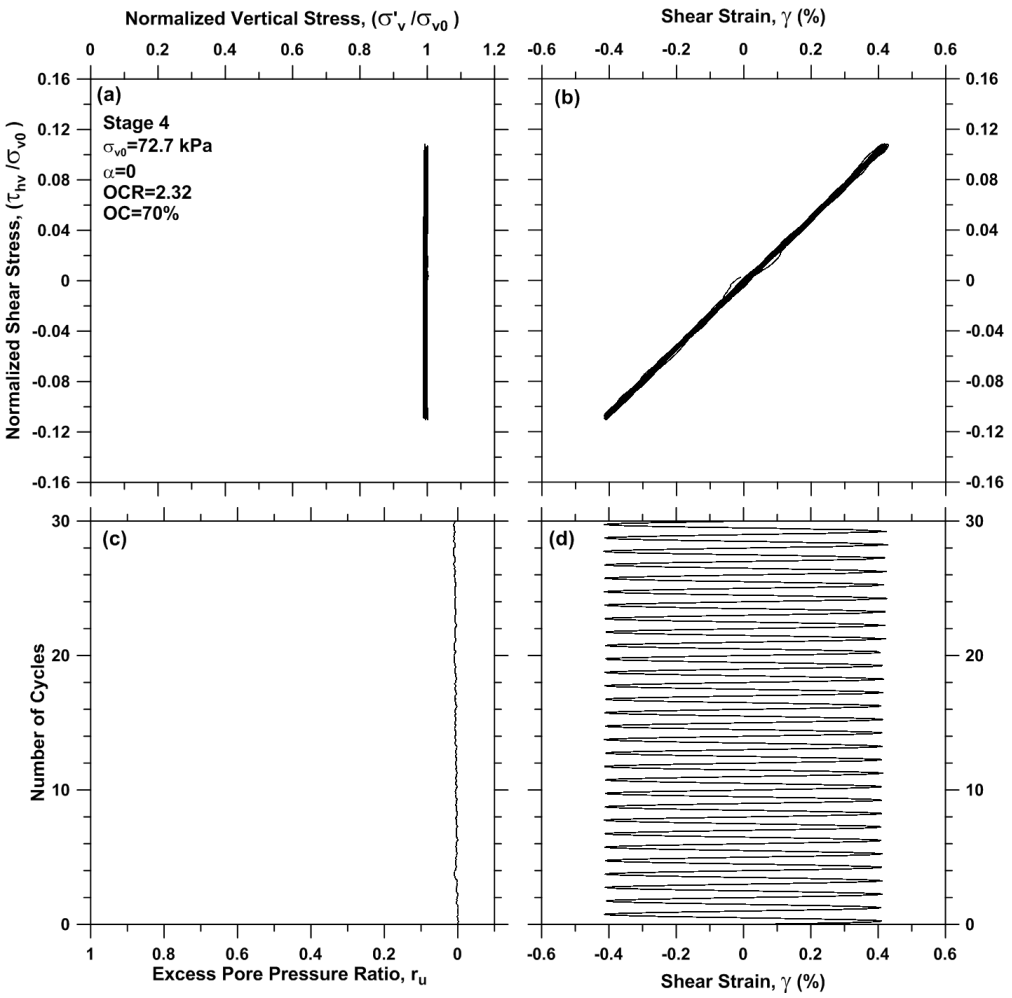

Figure A.51 Cyclic strain-controlled DSS test results on specimen BH8S4_7.5, stage 4

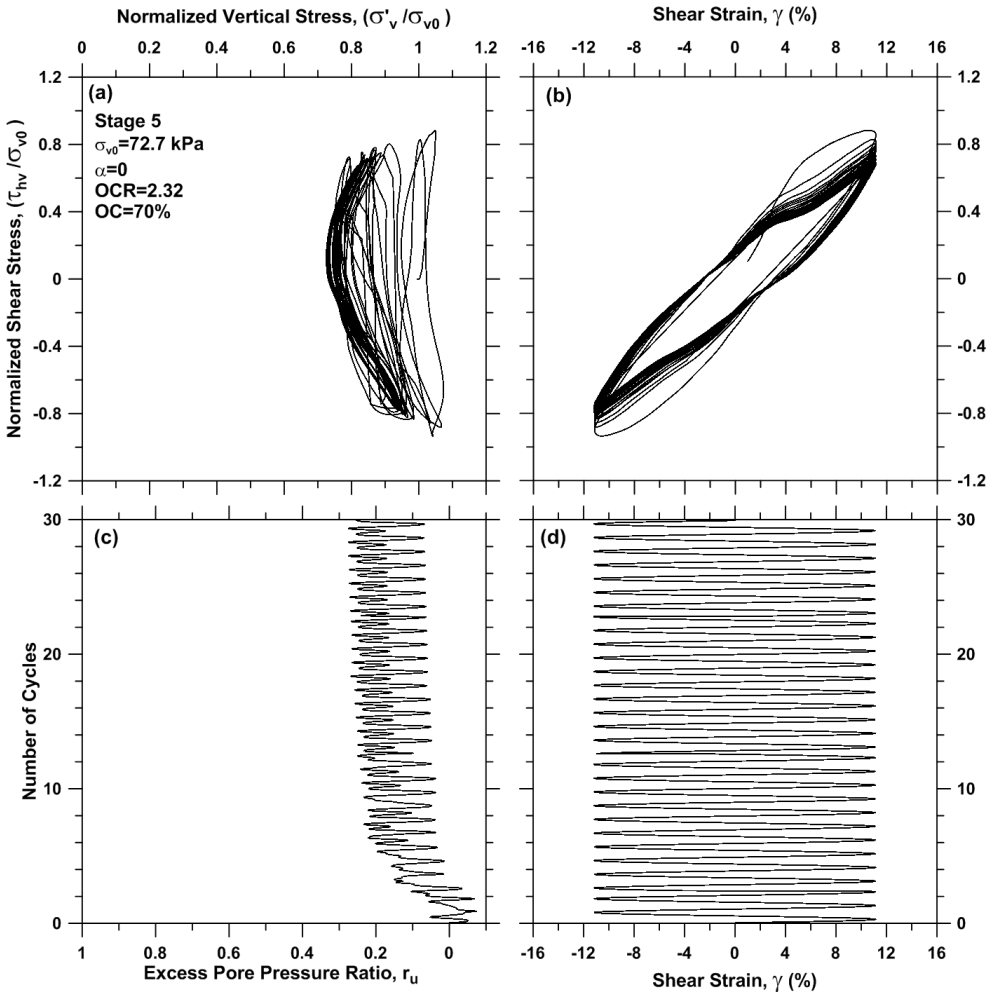

Figure A.52 Cyclic strain-controlled DSS test results on specimen BH8S4_7.5, stage 5

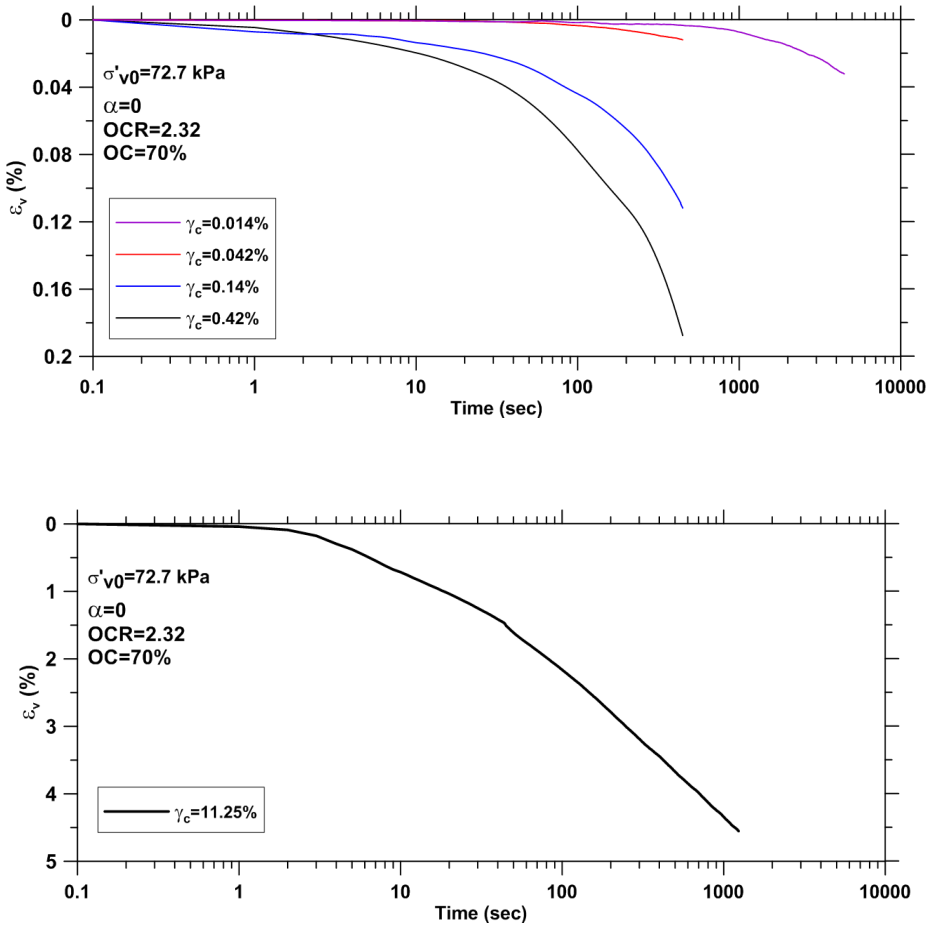

Figure A.53 Post-cyclic volume change following strain-controlled DSS tests on specimen BH8S4_7.5

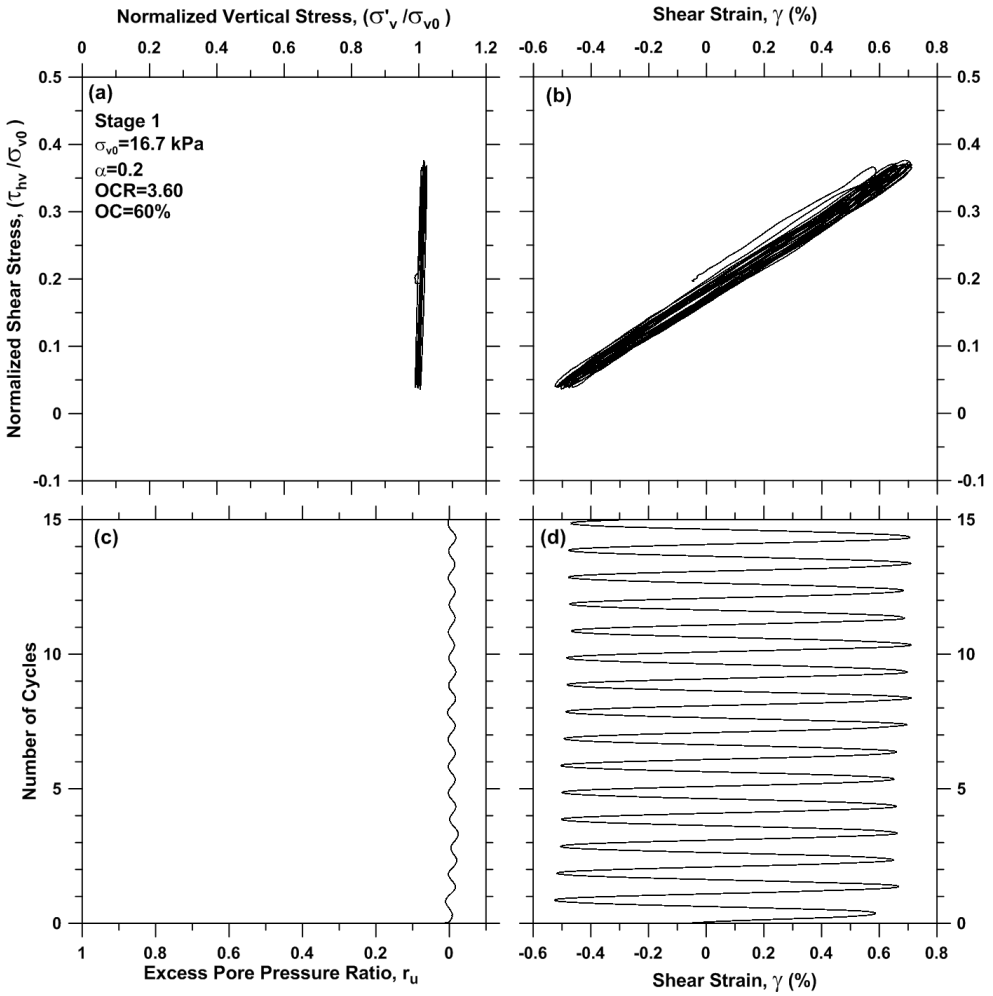

Figure A.54 Cyclic stress-controlled DSS test results on specimen BH9S1_7.0, stage 1

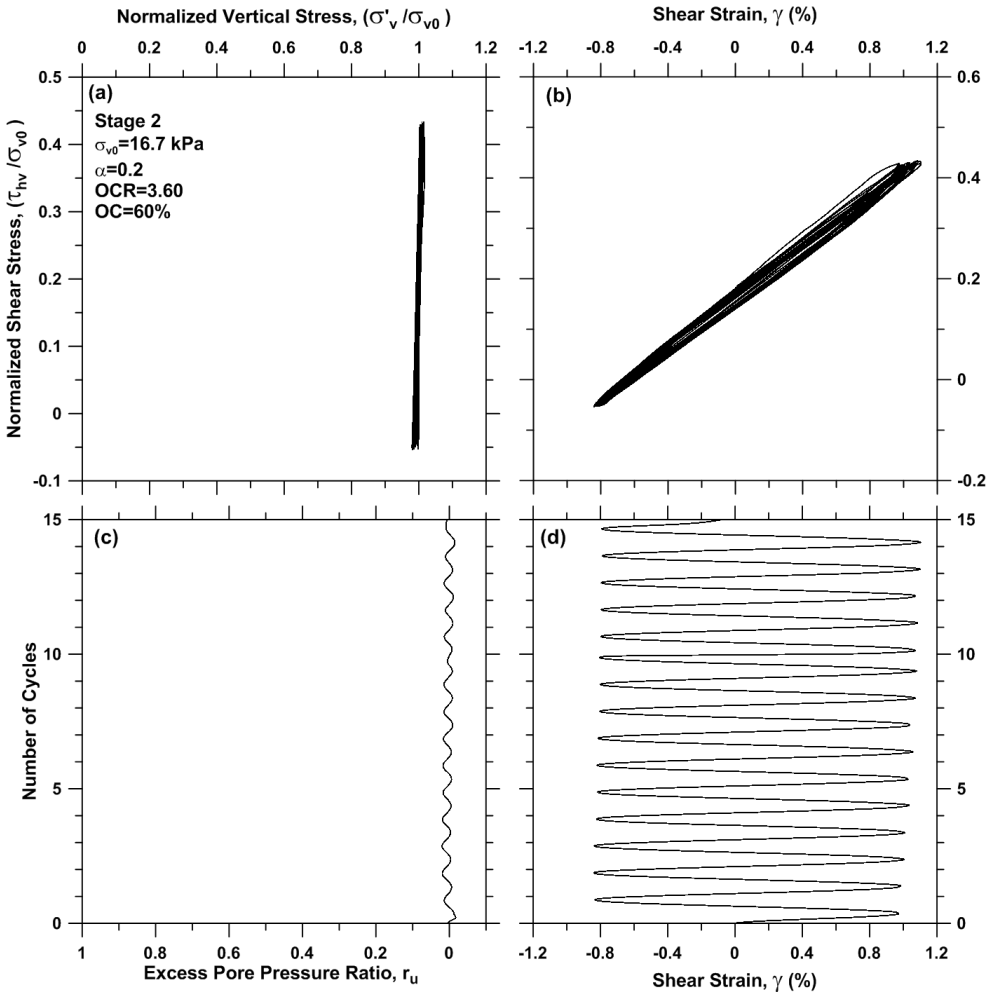

Figure A.55 Cyclic stress-controlled DSS test results on specimen BH9S1_7.0, stage 2

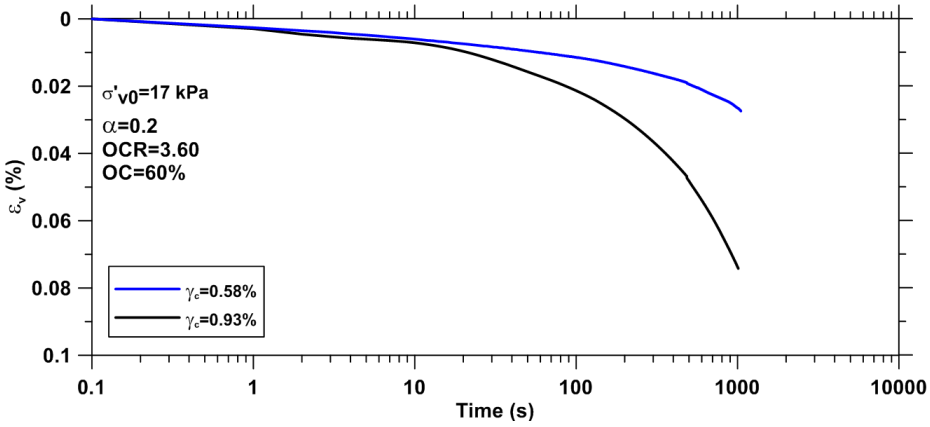

Figure A.56 Post-cyclic volume change following stress-controlled DSS tests on specimen BH9S1_7.0

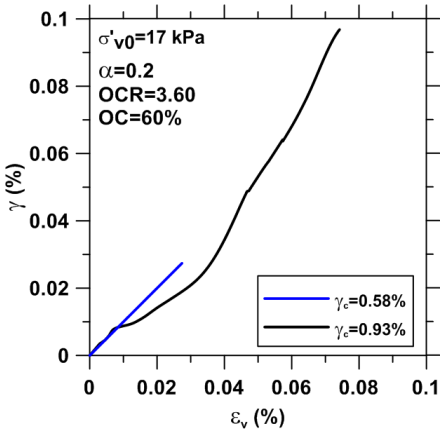

Figure A.57 Post-cyclic shear strain versus post-cyclic volume change for specimen BH9S1_7.0

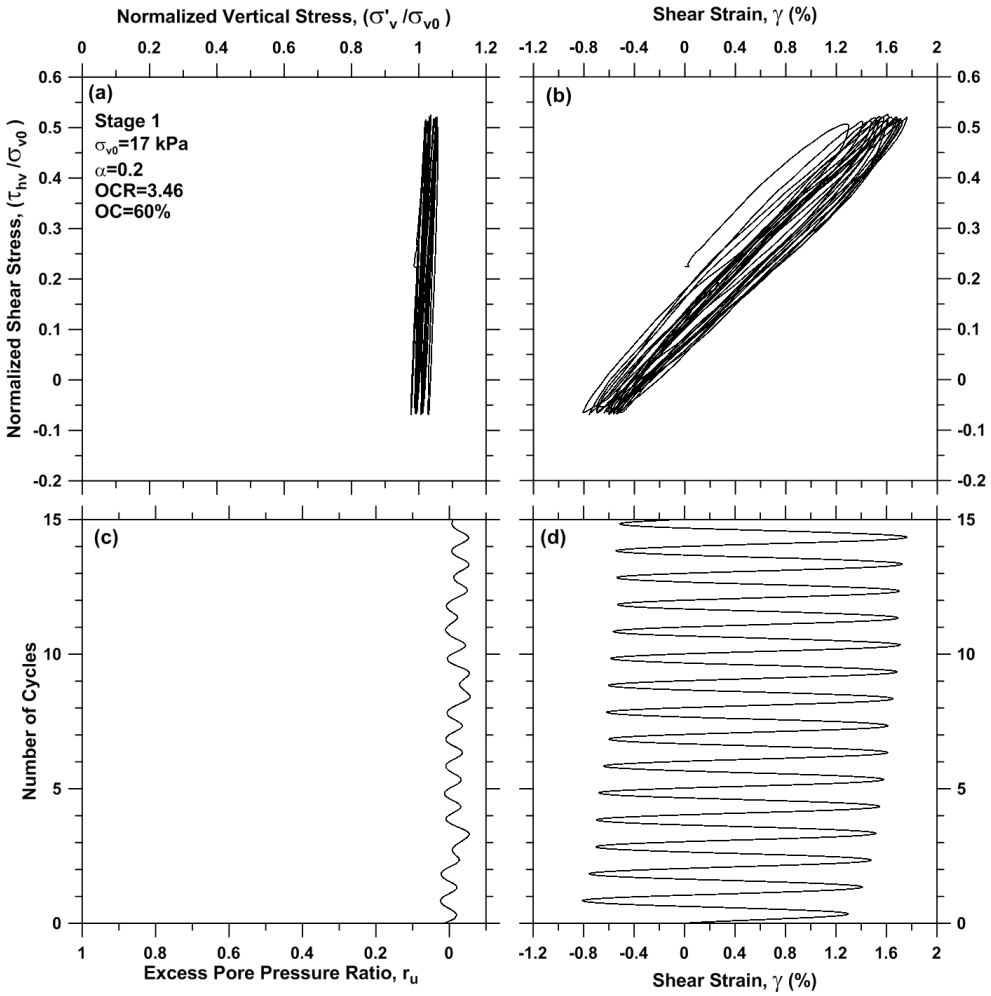

Figure A.58 Cyclic stress-controlled DSS test results on specimen BH9S2_7.1, stage 1

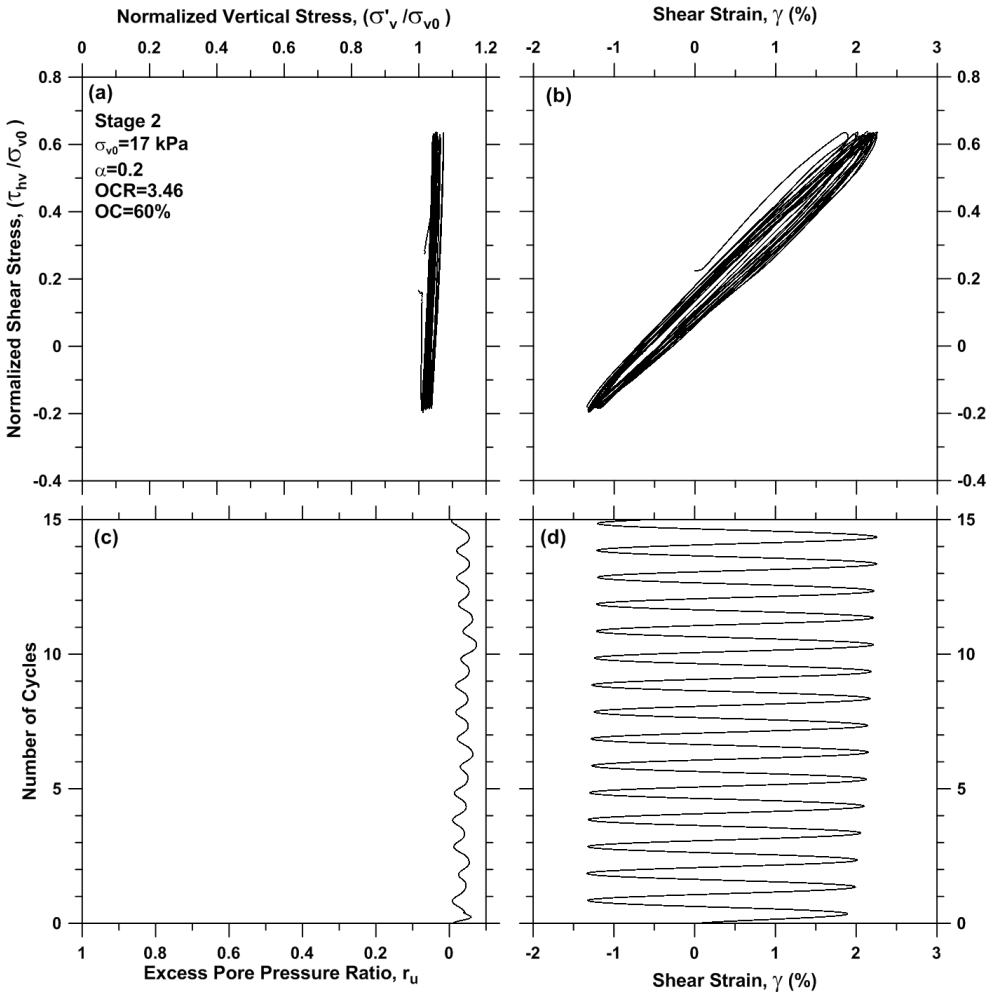

Figure A.59 Cyclic stress-controlled DSS test results on specimen BH9S2_7.1, stage 2

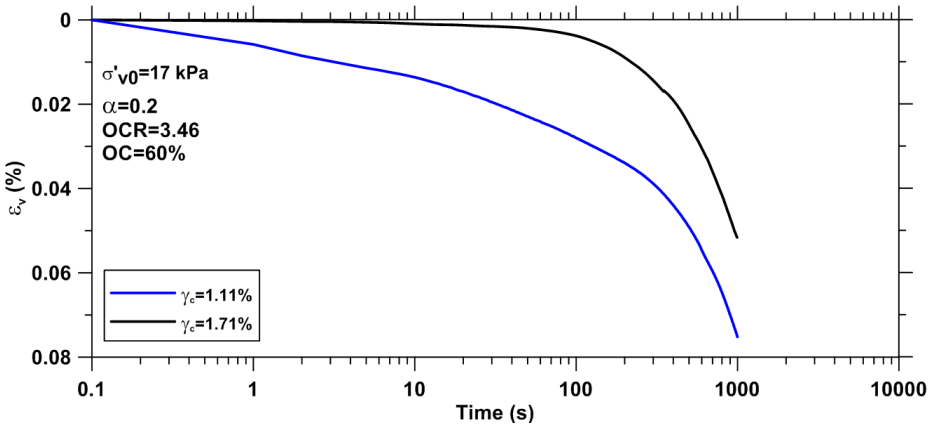

Figure A.60 Post-cyclic volume change following stress-controlled DSS tests on specimen BH9S2_7.1

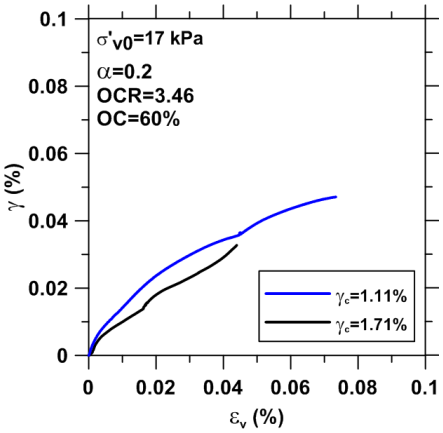

Figure A.61 Post-cyclic shear strain versus post-cyclic volume change for specimen BH9S2_7.1

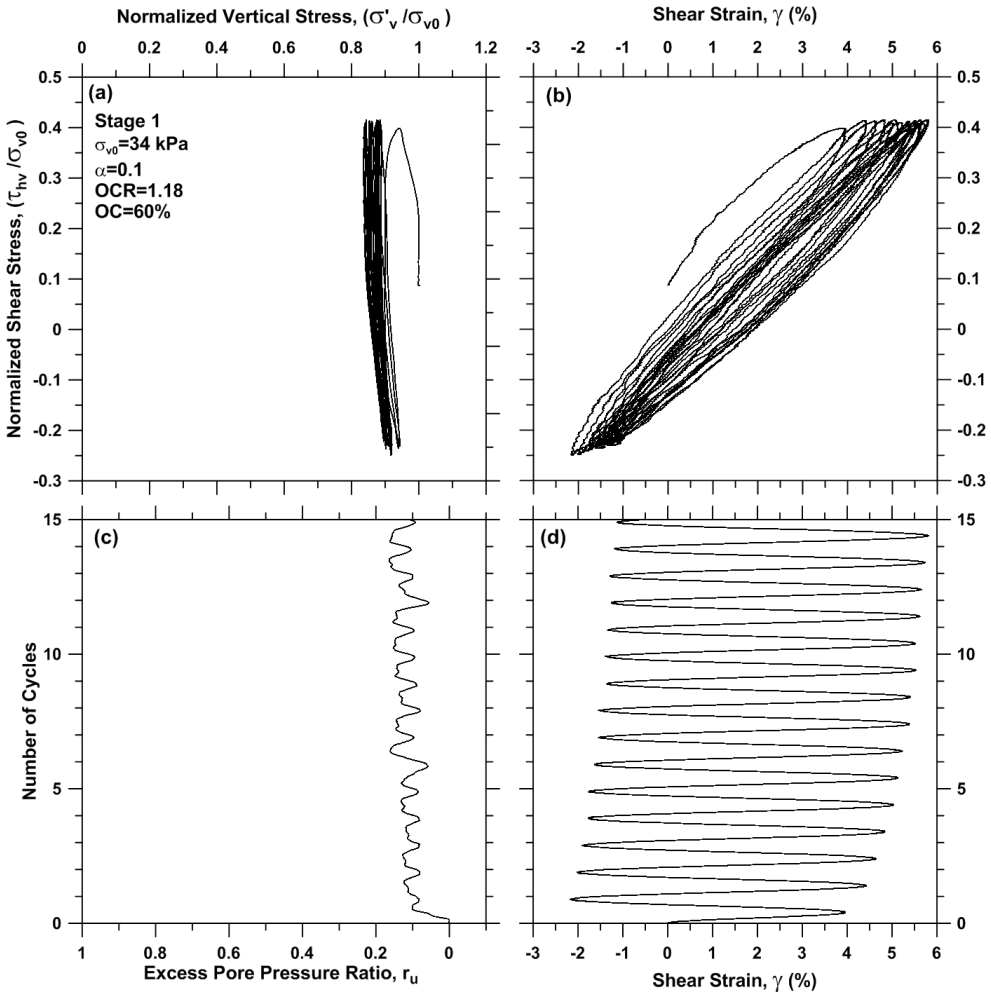

Figure A.62 Cyclic stress-controlled DSS test results on specimen BH9S4_7.3, stage 1

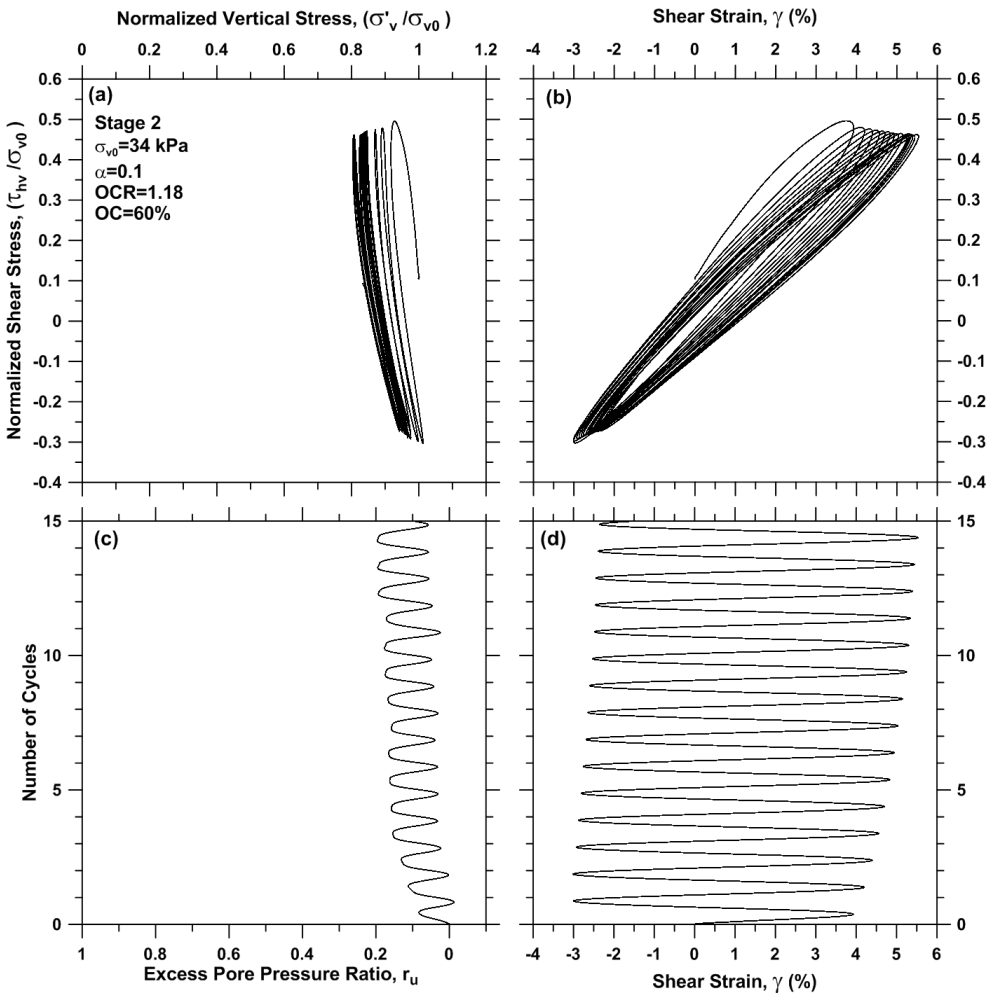

Figure A.63 Cyclic stress-controlled DSS test results on specimen BH9S4_7.3, stage 2

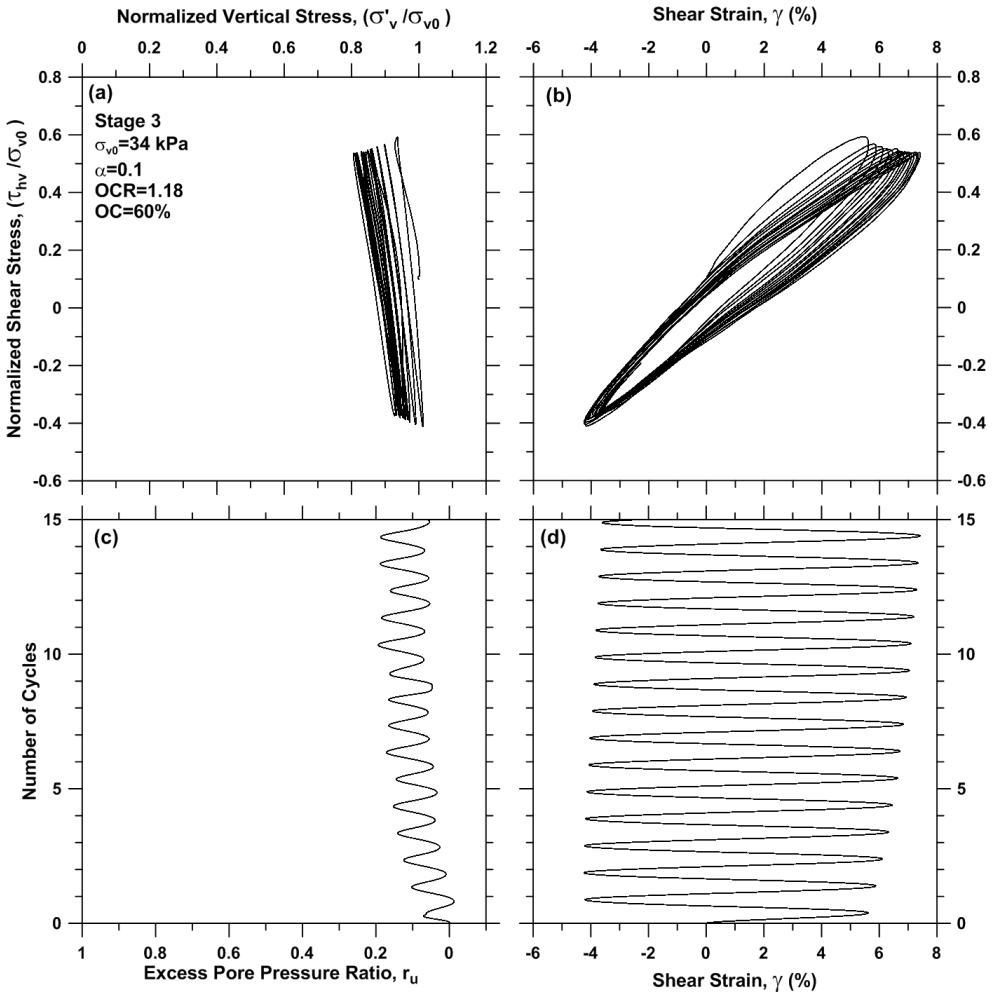

Figure A.64 Cyclic stress-controlled DSS test results on specimen BH9S4_7.3, stage 3

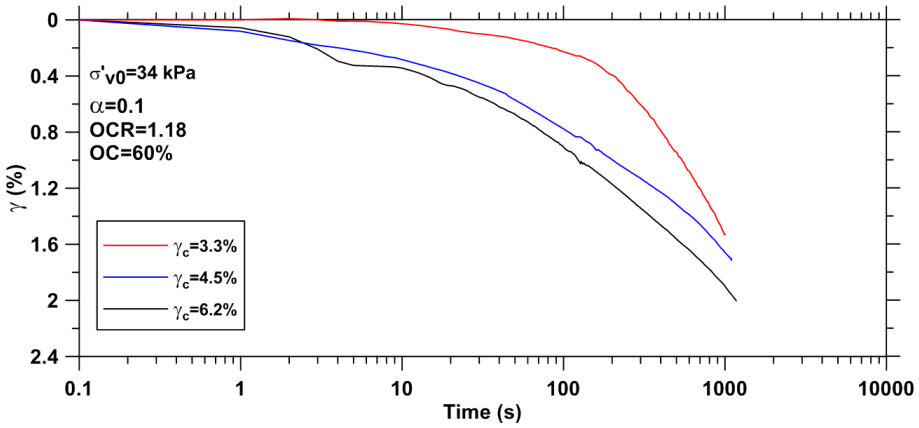

Figure A.65 Post-cyclic volume change following stress-controlled DSS tests on specimen BH9S4_7.3

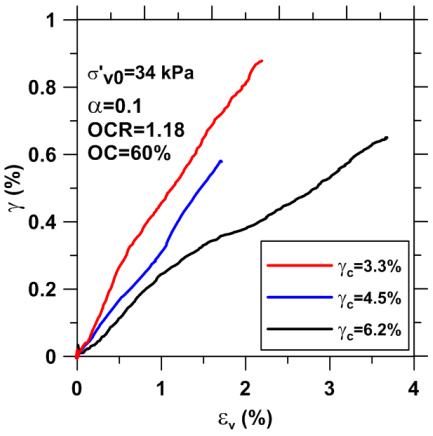

Figure A.66 Post-cyclic shear strain versus post-cyclic volume change for specimen BH9S4_7.3

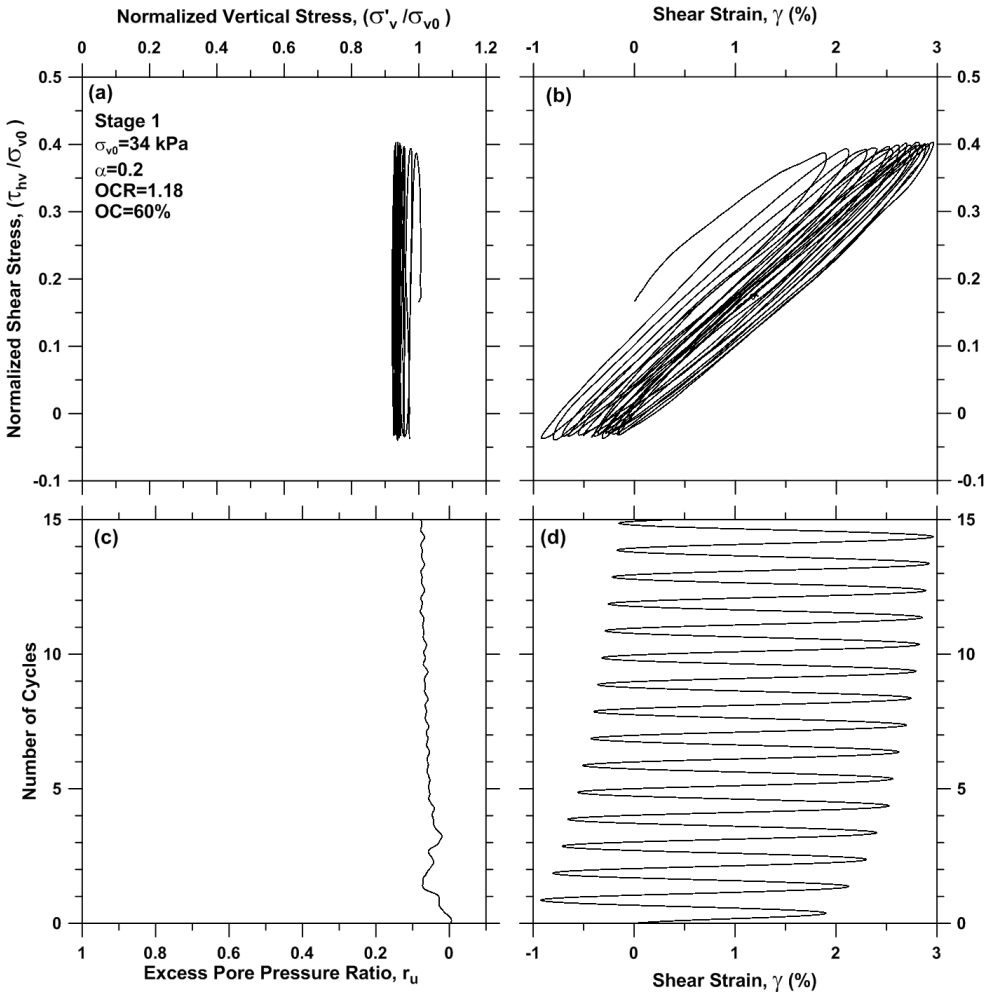

Figure A.67 Cyclic stress-controlled DSS test results on specimen BH9S5_7.4, stage 1

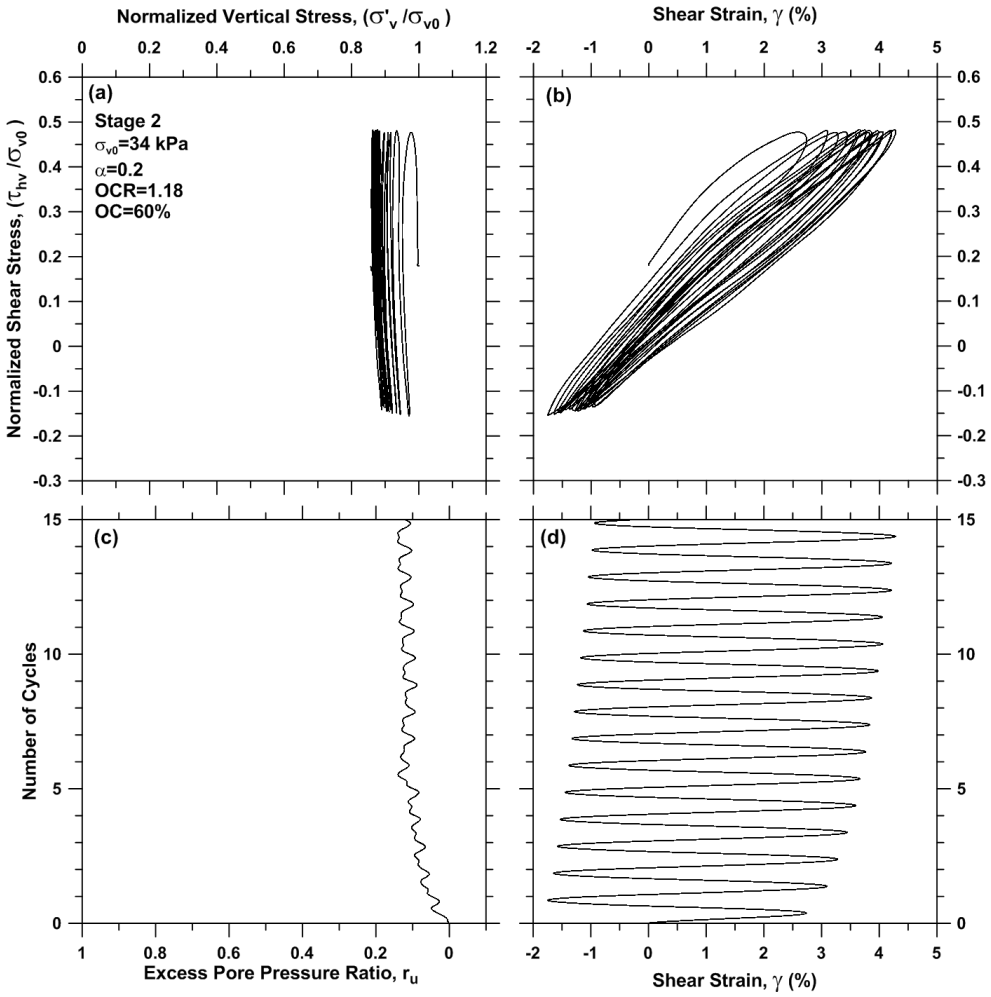

Figure A.68 Cyclic stress-controlled DSS test results on specimen BH9S5_7.4, stage 2

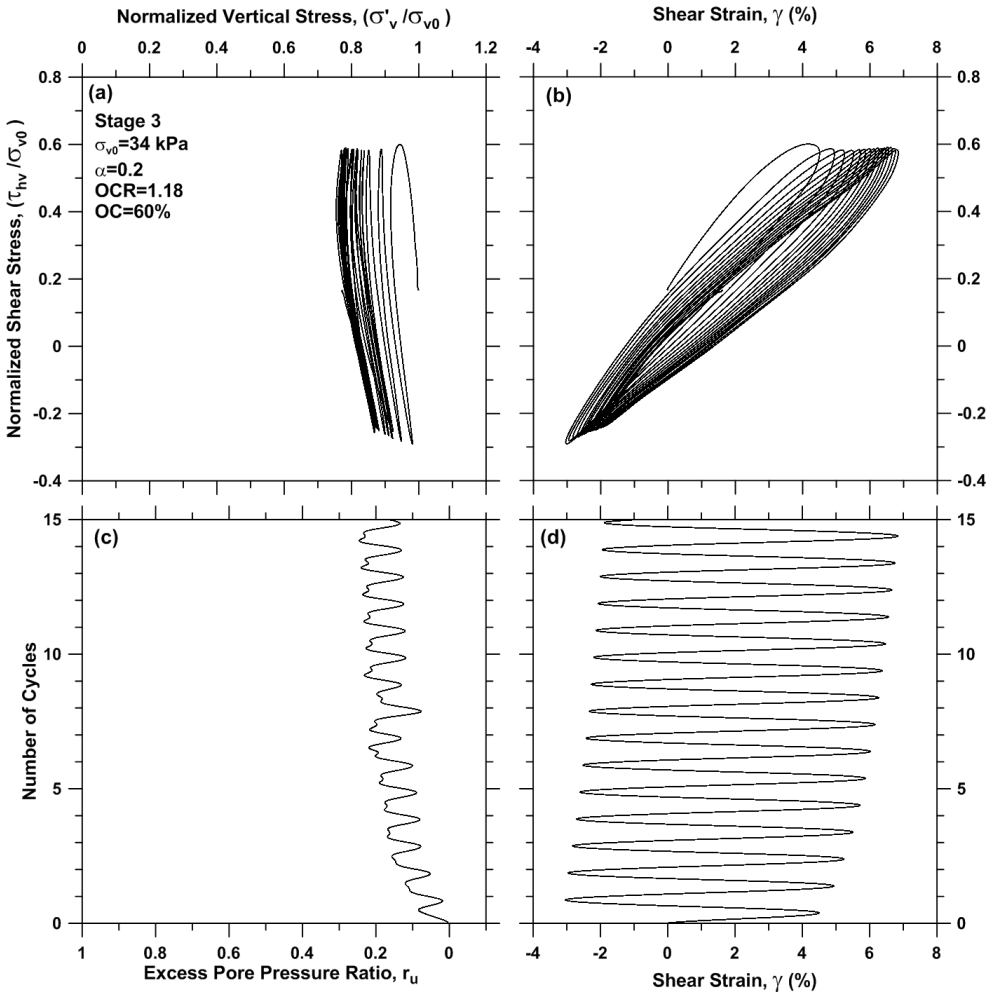

Figure A.69 Cyclic stress-controlled DSS test results on specimen BH9S5_7.4, stage 3

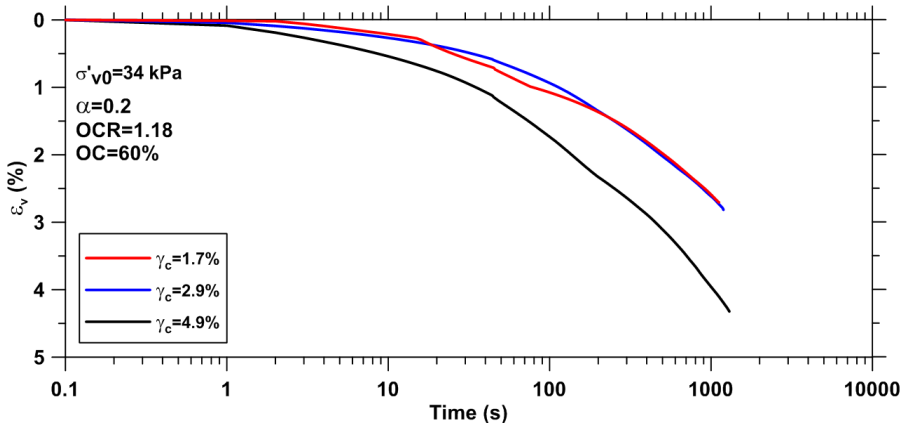

Figure A.70 Post-cyclic volume change following stress-controlled DSS tests on specimen BH9S5_7.4

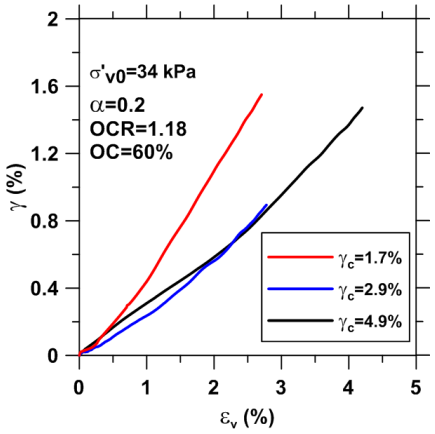

Figure A.71 Post-cyclic shear strain versus post-cyclic volume change for specimen BH9S5_7.4

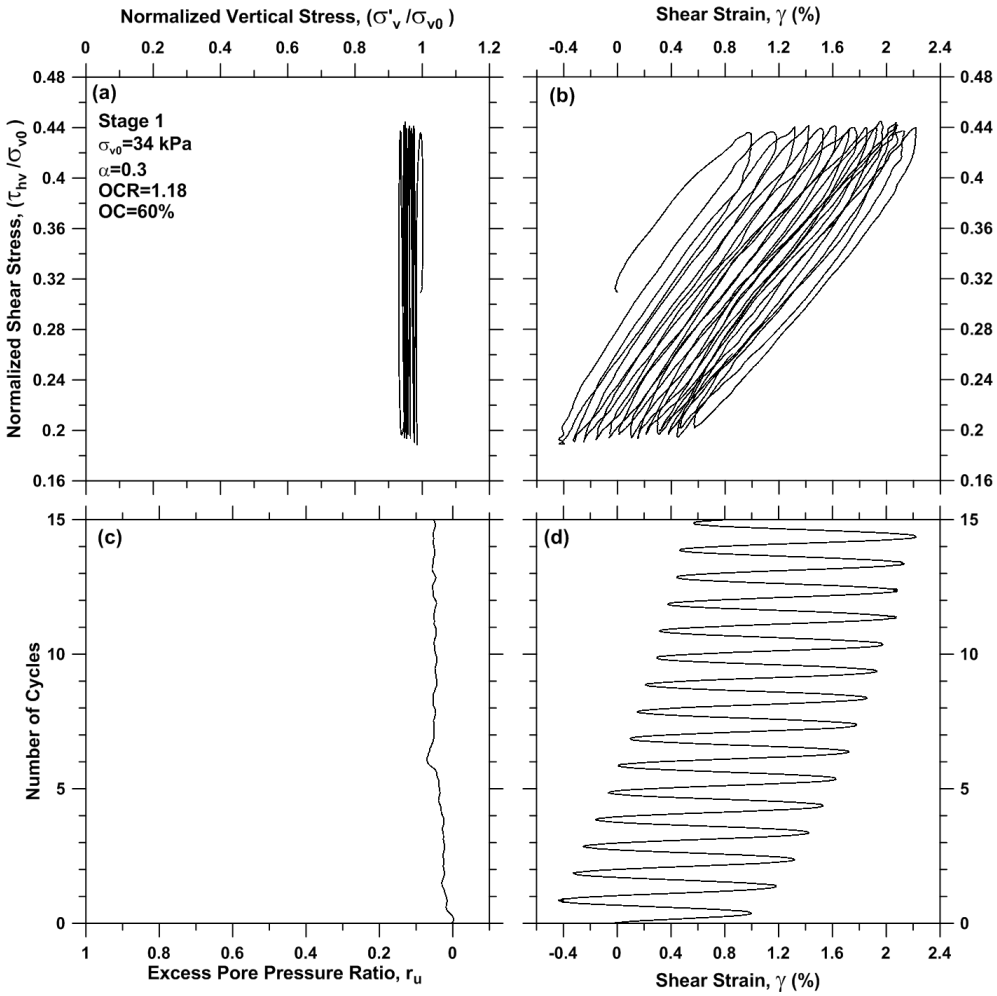

Figure A.72 Cyclic stress-controlled DSS test results on specimen BH9S6_7.5, stage 1

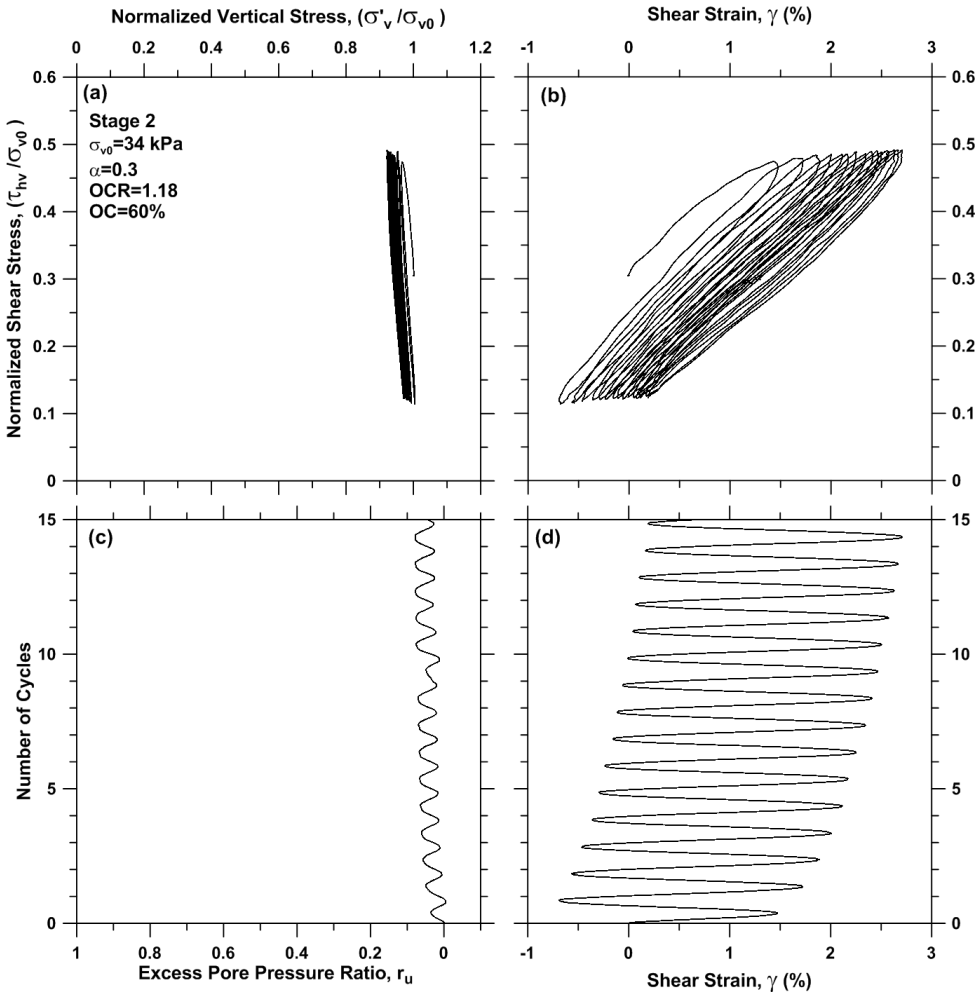

Figure A.73 Cyclic stress-controlled DSS test results on specimen BH9S6_7.5, stage 2

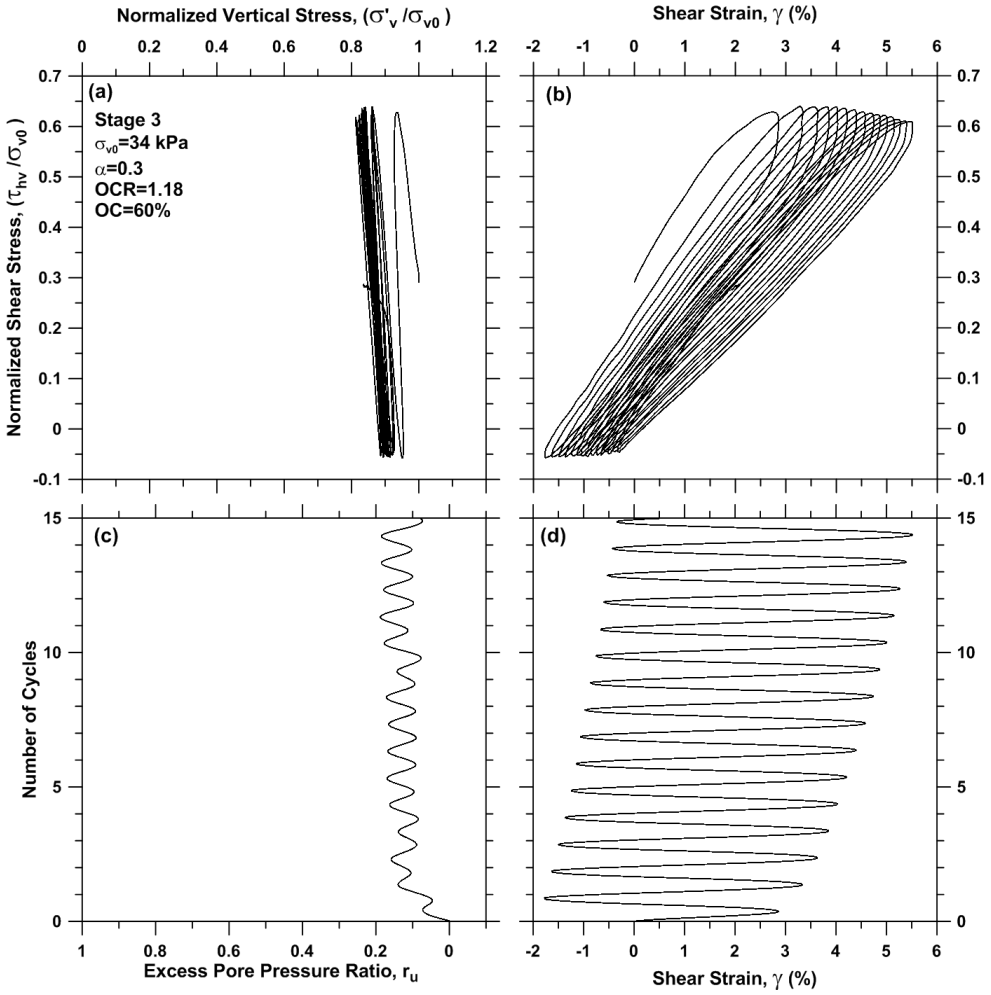

Figure A.74 Cyclic stress-controlled DSS test results on specimen BH9S6_7.5, stage 3

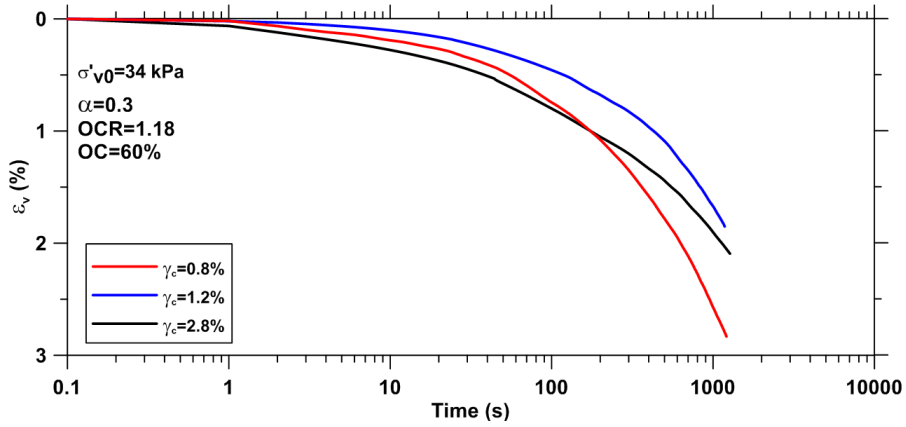

Figure A.75 Post-cyclic volume change following stress-controlled DSS tests on specimen BH9S6_7.5

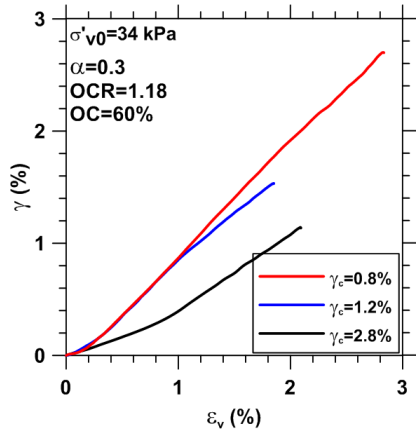

Figure A.76 Post-cyclic shear strain versus post-cyclic volume change for specimen BH9S6_7.5

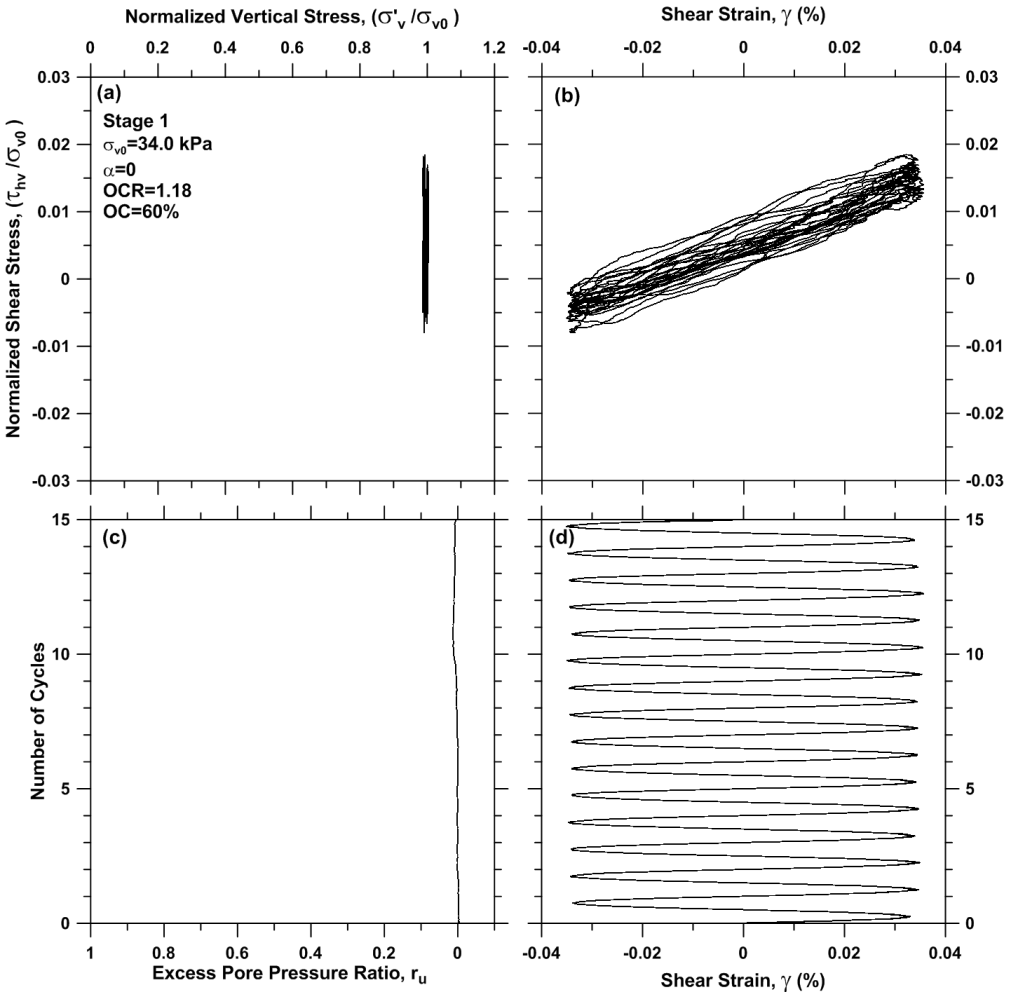

Figure A.77 Cyclic strain-controlled DSS test results on specimen BH9S8_7.8, stage 1

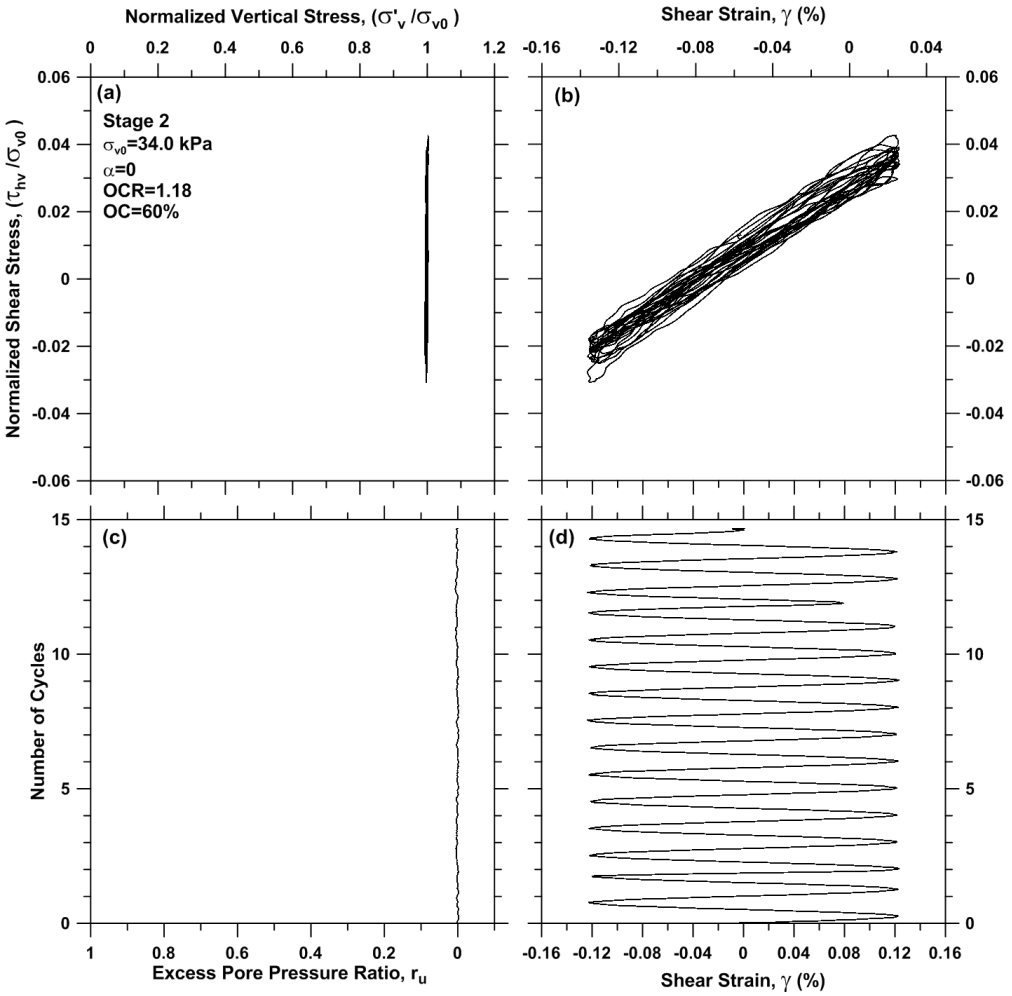

Figure A.77 Cyclic strain-controlled DSS test results on specimen BH9S8_7.8, stage 2

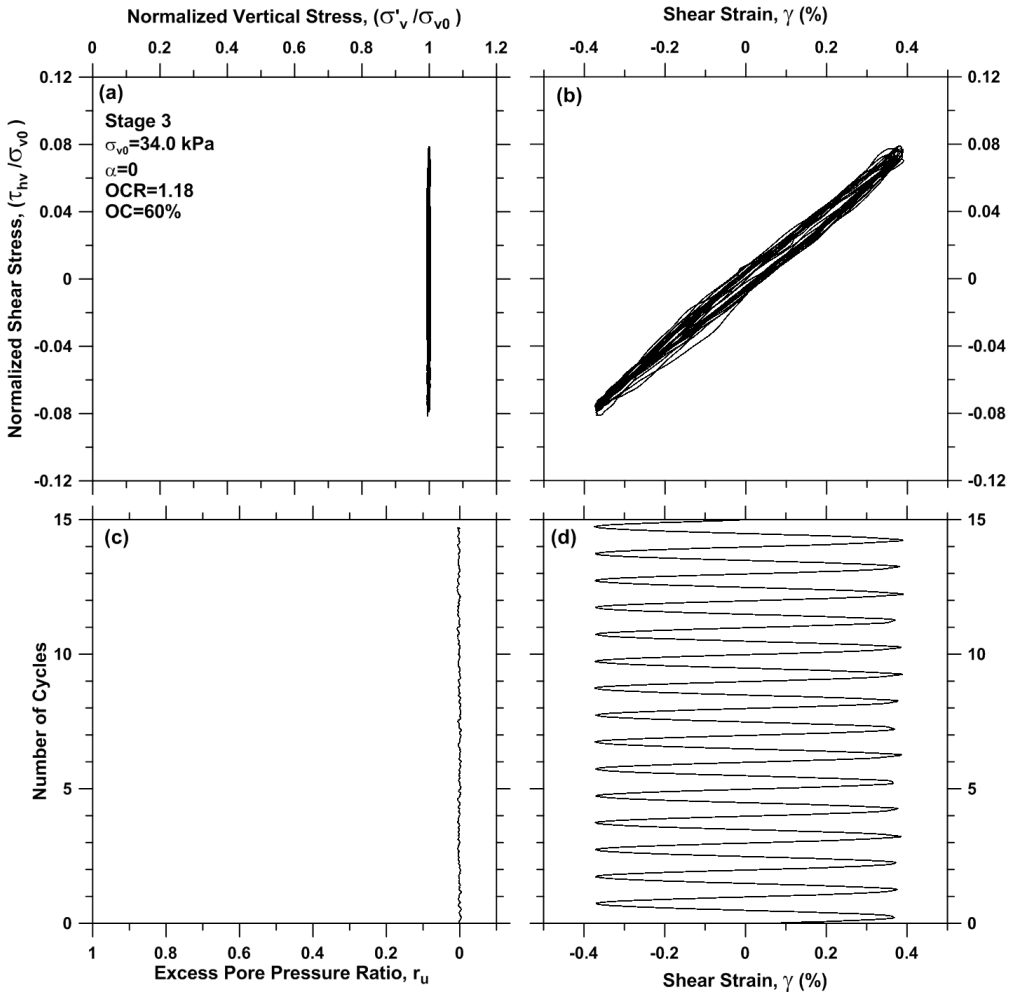

Figure A.78 Cyclic strain-controlled DSS test results on specimen BH9S8_7.8, stage 3

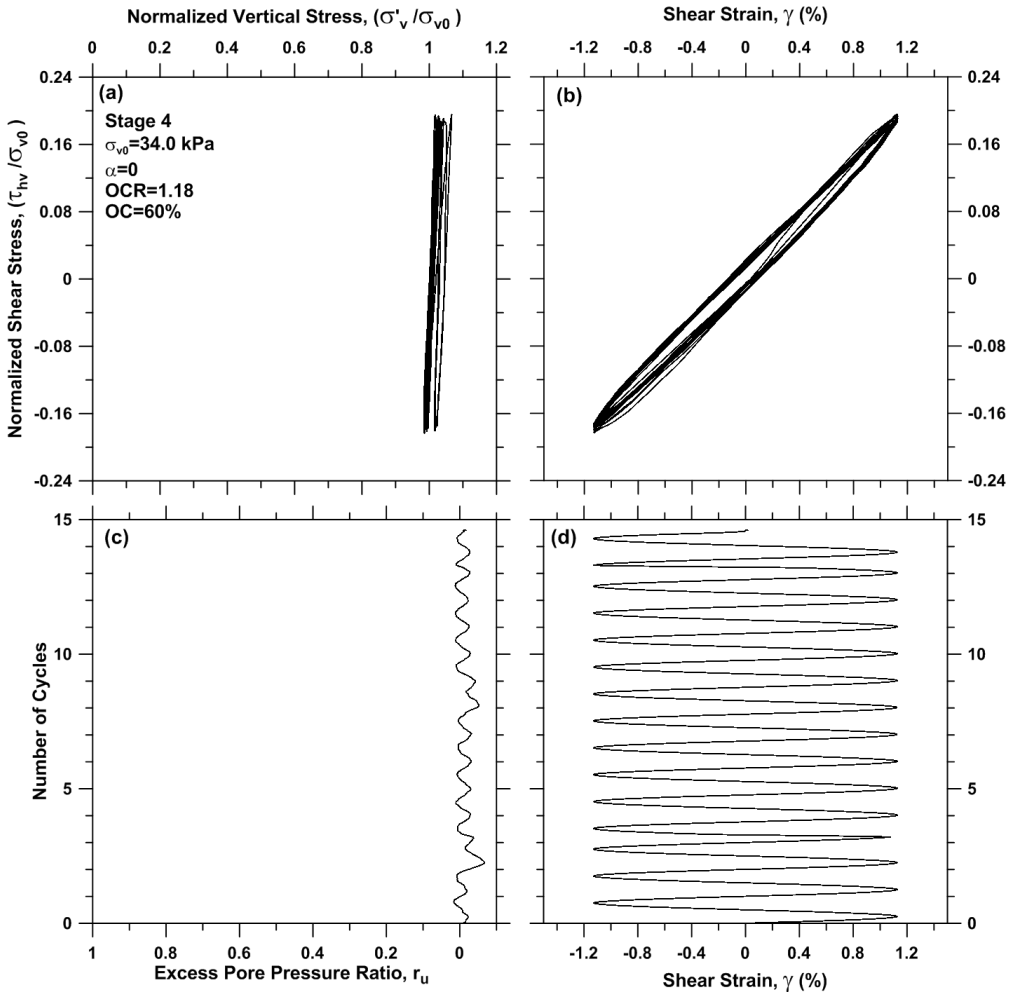

Figure A.79 Cyclic strain-controlled DSS test results on specimen BH9S8_7.8, stage 4

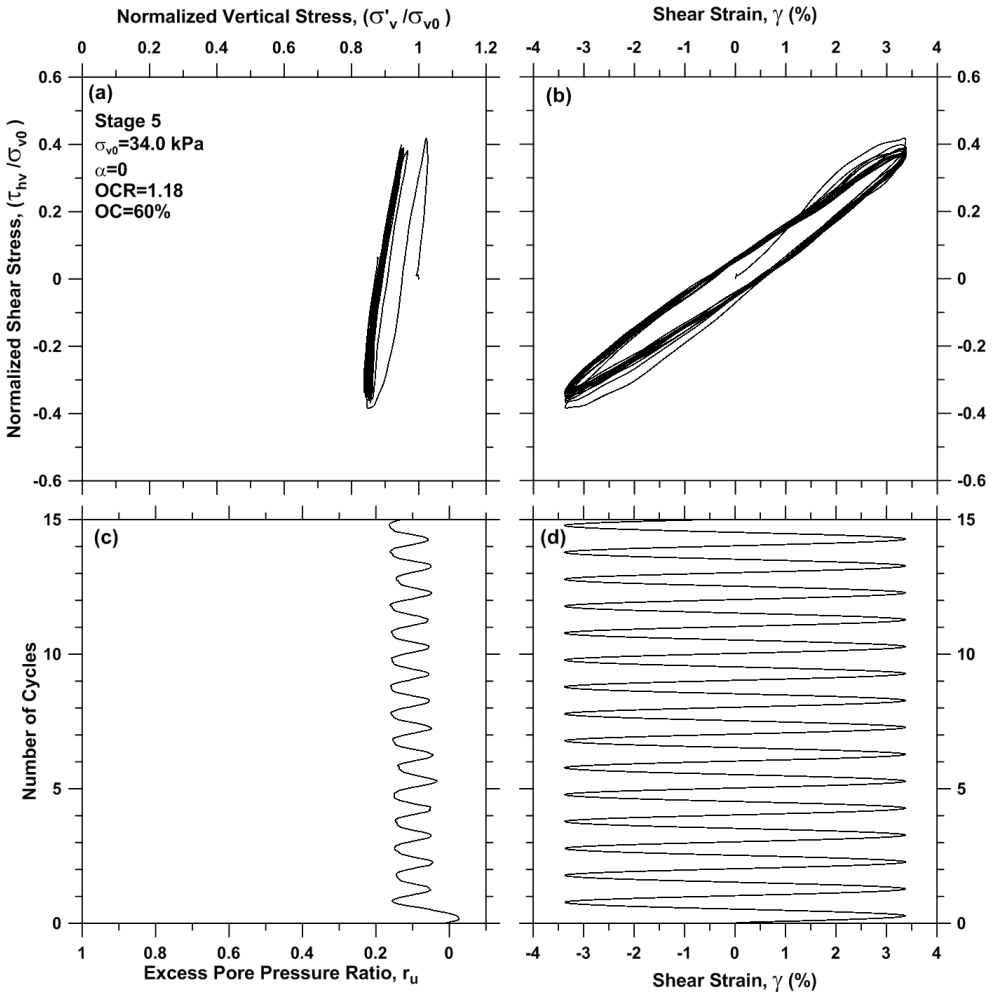

Figure A.80 Cyclic strain-controlled DSS test results on specimen BH9S8_7.8, stage 5

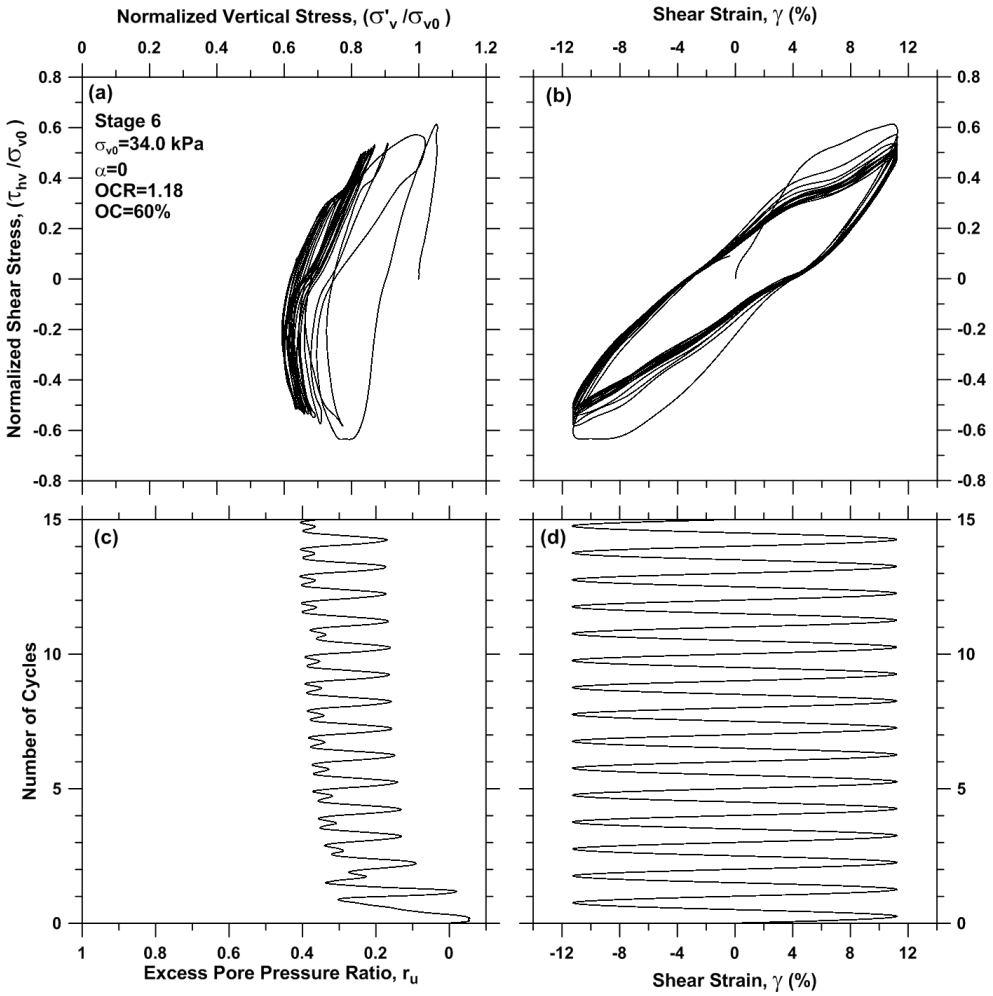

Figure A.81 Cyclic strain-controlled DSS test results on specimen BH9S8_7.8, stage 6

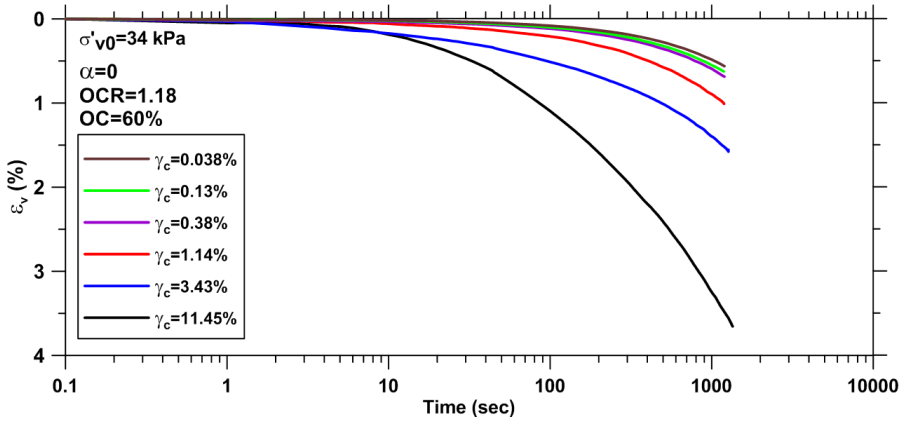

Figure A.82 Post-cyclic volume change following strain-controlled DSS tests on specimen BH9S8_7.8

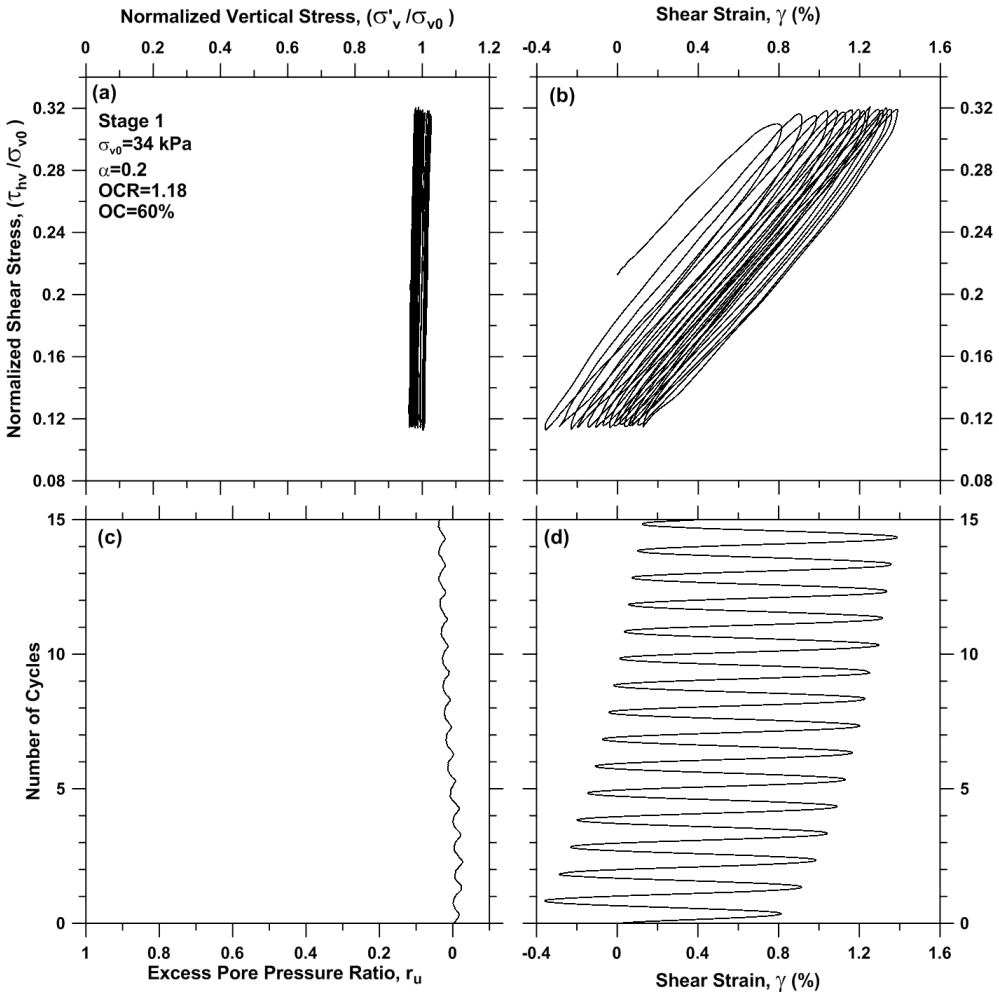

Figure A.83 Cyclic stress-controlled DSS test results on specimen BH9S9_8.0, stage 1

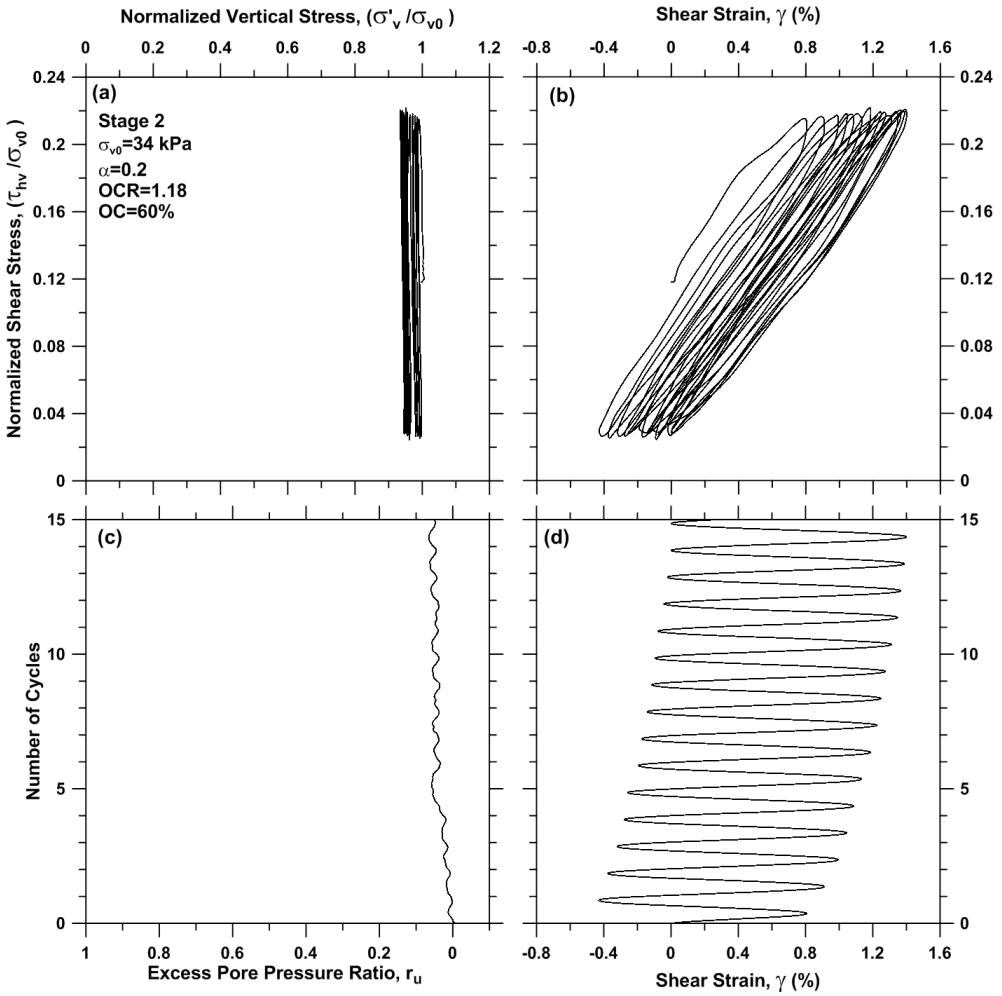

Figure A.84 Cyclic stress-controlled DSS test results on specimen BH9S9_8.0, stage 2

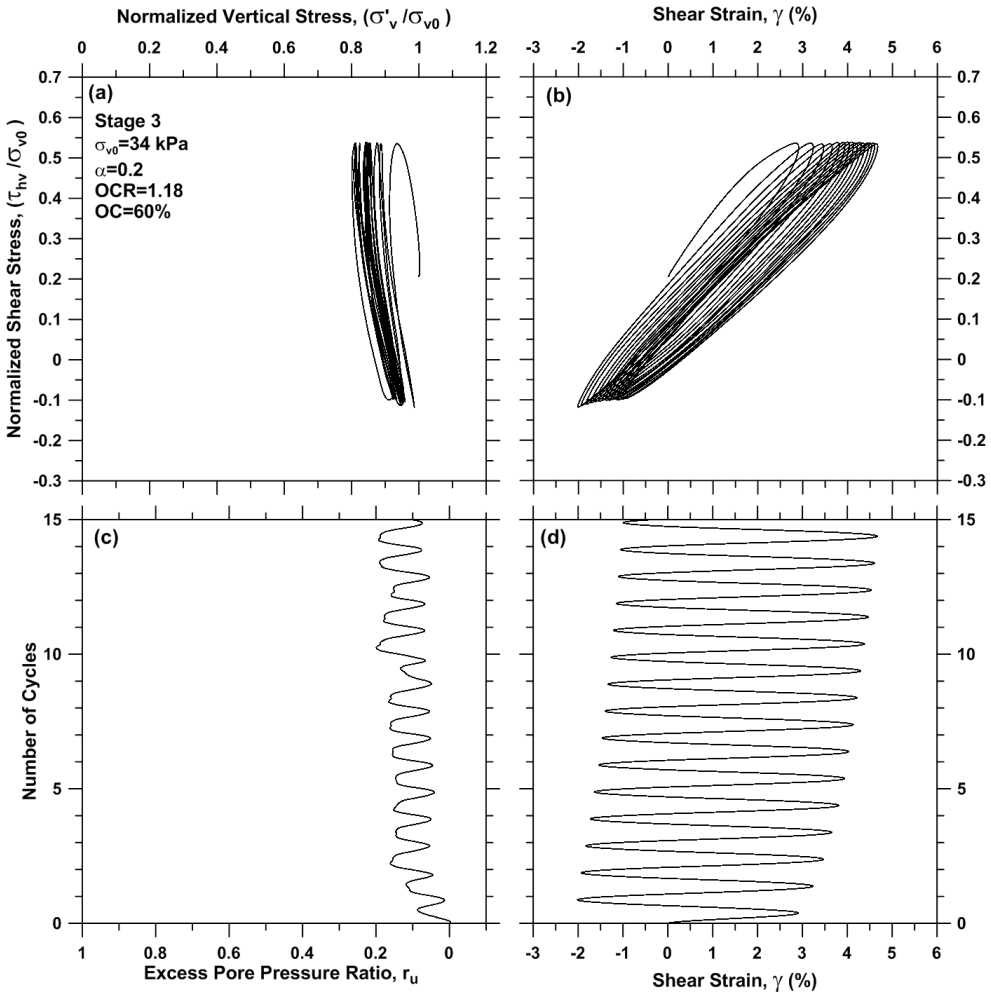

Figure A.85 Cyclic stress-controlled DSS test results on specimen BH9S9_8.0, stage 3

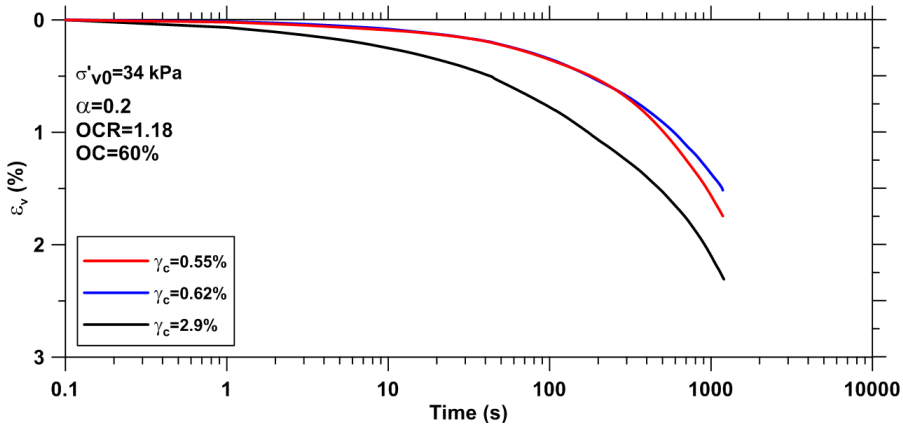

Figure A.86 Post-cyclic volume change following stress-controlled DSS tests on specimen BH9S9_8.0

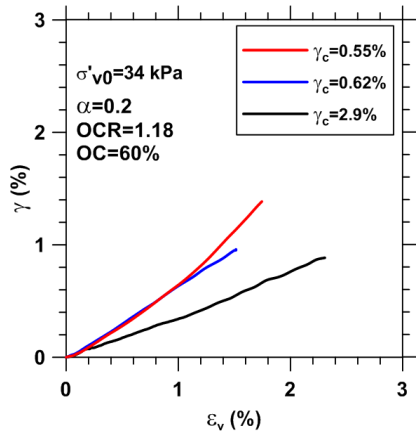

Figure A.87 Post-cyclic shear strain versus post-cyclic volume change for specimen BH9S9_8.0

REFERENCES

Adams, J. I., 1961, "Laboratory Compression Test on Peat," *Proc., 7th Muskeg Research Conf.,* NRC, Ottawa, ACSSM Technical Memorandum, Vol. 71, pp. 36–54.

Ancheta, T.D., and Stewart, J.P., 2015, "Conditional Simulation of Spatially Variable Motions on 2D Grids," *12th International Conference on Applications of Statistics and Probability in Civil Engineering*, Vancouver, Canada

ASTM D6528-07: Standard Test Method for Consolidated Undrained Direct Simple Shear Testing of Cohesive Soils, Annual Book of ASTM Standards, ASTM International West Conshohocken, PA, 2010, www.astm.org.

Bell, F.G., 2000, *Engineering Properties of Soils and Rocks*, Malden, MA, Blackwell Sci., pp. 202-221.

Bjerrum, L.,1967, "Engineering Geology of Norwegian Normally Consolidated Marine Clays as Related to Settlement of Buildings," *Geotechnique*, Vol. 17, No. 2, pp. 81–118.

Bjerrum, L., and Landva, A., 1966, "Direct Simple Shear Tests on a Norwegian Quick Clay," *Geotechnique*, Vol. 16, No. 1, pp. 1–20.

Bommer, J. J., Stafford, P. J., and Alarcón, J.E., 2009, "Empirical Equations for the Prediction of the Significant, Bracketed, and Uniform Duration of Earthquake Ground Motion," *Bulletin of the Seismological Society of America*, Vol. 99, No. 6, pp. 3217–3233

Boulanger, R. W., 2003. "Relating K_a to Relative State Parameter Index." *Journal of Geotechnical and Geoenvironmental Engineering*, ASCE, Vol. 129, No. 8, pp. 770-773.

Boulanger, R. W., Arulnathan, R., Harder, L. F., Jr., Torres, R. A., and Driller, M. W., 1998, "Dynamic properties of Sherman Island Peat," *J. Geotech. Geoenviron. Eng.*, ASCE, Vol. 124, No.1, pp. 12-20.

Boulanger, R. W., and Idriss, I. M., 2006. "Liquefaction Susceptibility Criteria for Silts and Clays," *Journal of Geotechnical and Geoenvironmental Engineering*, ASCE, Vol. 132, No.11, pp. 1413-1426.

Boulanger, R. W., and Idriss, I. M., 2007, "Evaluation of Cyclic Softening in Silts and Clays," *Journal of Geotechnical and Geoenvironmental Engineering,* ASCE, Vol.133, No.6, pp. 641-652.

Boulanger, R.W., and Truman, S.P., 1996, "Void Redistribution in Sand under Post-Earthquake Loading," *Canadian Geotechnical J.*, Vol. 33, No. 5, pp. 829-834.

Brawner, C. O., 1958, "The Muskeg Problem in British Columbia Highway Construction," *Proc., 4th Muskeg Research Conf.,* NRC, ACSSM Technical Memorandum 54, National Research Council of Canada, Canada, pp. 45–53.

Bro, A.D., Stewart, J.P., and Pradel, D.E., 2013, "Estimating Undrained Strength of Clays from Direct Shear Testing at Fast Displacement Rates," *Geocongress 2013 -- Stability and Performance of Slopes and Embankments III,* San Diego, CA, ASCE Geotechnical Special Publication No. 231, CL Meehan, DE Pradel, MA Pando, and JF Labuz (eds.), Paper No. 5.

Casagrande, A., and Fadum, R.E., 1940, "Notes on Soil Testing for Engineering Purposes," *Harvard Soil Mechanics, Series No. 8*, Cambridge, Mass.

Castro, G., and Christian, J. T., 1976, "Shear Strength of Soils and Cyclic Loading," *Journal of Geotechnical Engineering Division*, Vol. 102, No. 9, pp. 887-894.

Chu, D.B., Stewart, J.P., Boulanger, R.W., and Lin, P.S., 2008. "Cyclic Softening of Low-Plasticity Clay and Its Effect on Seismic Foundation Performance," *Journal of Geotechnical and Geoenvironmental Engineering*, ASCE, Vol. 134, No.11, pp. 1595-1608.

Craig, R.F., 1992, *Soil Mechanics*, 5th Edition. London: Chapman & Hall.

CDWR, 1992, "Seismic Stability Evaluation of the Sacramento-San Joaquin Delta Levees," Phase I Report: Preliminary Evaluations and Review of Previous Studies, Division of Engineering, California Department of Water Resources (CDWR).

Dahl, K. R., DeJong, J. T., Boulanger, R. W., Pyke, R., and Wahl, D., 2014. "Characterization of an Alluvial Silt and Clay Deposit for Monotonic, Cyclic and Post-Cyclic Behavior," *Canadian Geotechnical Journal*, Vol. 51, No. 4, pp. 432-440.

Davis, J. H., 1997, "The Peat Deposits of Florida, Their Occurrence, Development and Uses," *Geological Bulletin No. 3*, Florida Geological Survey, Tallahassee, FL.

Degroot, D.J., Germaine, J.T., and Gedney, R., 1991, "An Electropneumatic Control System for Direct Simple Shear Testing," *Geotechnical Testing J.*, Vol. 14, No. 4, pp. 339-348.

Delta Risk Management Strategy, 2009, "Executive Summary Phase 1," *California Department of Water* Resource,s http://www.ca.gov/floodmgmt/sab/drmsp.

Drexler, J. Z., de Fontaine, C. S., and Knifong, D. L., 2007, "Age Determination of the Remaining Peat in the Sacramento-San Joaquin Delta, California, USA. U.S.," *Geological Survey Open File*, Report 2007-1303.

Duku, P.M., Stewart, J.P., Whang, D.H., and Venugopal, R., 2007, "Digitally Controlled Simple Shear Apparatus for Dynamic Soil Testing," *Geotechnical Testing J.*, Vol. 30, No. 5, pp. 1-10.

Duku, P.M., Stewart, J.P., Whang, D.H., and Yee, E., 2008, "Volumetric Strains of Clean Sands Subject to Cyclic Loads," *J. Geotech. & Geoenv. Engrg.*, ASCE, Vol. 134 No. 6, pp. 1073-1085.

Dyvik, R., Berre, T., Lacasse, S., and Raadim, B., 1987, "Comparison of Truly Undrained and Constant Volume Direct Simple Shear Tests," *Geotechnique*, Vol. 37, No. 1, pp. 3-10.

Edil, T.B. and Dhowian, A.W., 1981, "At-Rest Lateral Pressure of Peat Soils, "*Journal of the Geotechnical Engineering Division*, ACSE, Vol. 107, No.2, pp. 201-217.

Fox, P.J., and Edil, T.B., 1992, "C_α/C_c Concept Applied to Compression of Peat," *Journal of Geotechnical Engineering*, Vol. 118, No.8, pp. 1256-1263.

Fox, P.J., and Edil, T.B., 1994, "Closure to C_α/C_c Concept Applied to Compression of Peat," *Journal of Geotechnical Engineering*, Vol. 120, No. 4, pp. 767-770.

GeoVision, 2000, "Department of Water Resources Boreholes DHP-4D and DHP-5J3 Suspension P&S Velocities", prepared for California Water Department Resources.

Hanrahan, E. T., 1954, "An Investigation of Physical Properties of Peat," *Geotechnique,* Vol. 4, No. 3, pp. 108–121.

Hanzawa, H., Nutt, N., Lunne, T., Tang, Y.X., and Long, M., 2007, "A Comparative Study between the NGI Direct Simple Shear Apparatus and the Mikasa Direct Shear Apparatus," *Soils and Foundations*, Vol. 47, No. 1, pp. 47-58.

Hardy, R. M., 1968, "Design, Construction and Performance of Dykes Founded on Peat," *Proc., 3rd Int. Peat Congress*, Québec, Canada, pp. 39–44.

Hardy, R. M., and Thomson, S., 1956, "Measurements of Shearing Strength of Muskeg," *Proc., Eastern Muskeg Research Conf.,* NRC, Ottawa, ACSSM Technical Memorandum, Vol. 42, pp. 16–24.

Hobbs, N. B., 1986, "Mire Morphology and the Properties and Behaviour of Some British and Foreign Peats," *Quarterly Journal of Engineering Geology*, Vol. 19, pp. 7–80.

Hobbs, N.B., 1987. "A Note on the Classification of Peat," *Geotechnique*, Vol. 37, No.3, pp. 405-407.

Hsu, C. C., and Vucetic, M., 2006, "Threshold Shear Strain for Cyclic Pore-Water Pressure in Cohesive Soils," *J. Geotech. Geoenviron. Eng.*,Vol.132, No.10, pp.1325-1335.

Idriss, I.M., Dobry, R., and Singh, R.M., 1978. "Nonlinear Behaviour of Soft Clays during Cyclic Loading, " *Journal of Geotechnical Engineering,* ASCE, Vol. 104, GT12, pp.1427-47.

Idriss, I.M., and Boulanger, R.W., 2008, *Soil Liquefaction during Earthquakes*, Monograph MNO-12, Earthquake Engineering Research Institute, Oakland, CA, 261 pp.

Isenhower, W. M., and Stokoe, K. H., 1981, ''Strain-Rate Dependent Shear Modulus of San Francisco Bay Mud,'' *Proc., Int. Conf. on Recent Advances in Geotechnical Earthquake Engineering and Soil Dynamics*, Civil Engineering Dept., Univ. of Missouri–Rolla, Rolla, Mo., pp. 597–602.

Ishihara, K., 1993, "Liquefaction and Flow Failures during Earthquakes," *Geotehnique*, Vol. 43, No.3, pp. 351-451.

Ishihara, K., and Yamazaki, F., 1980, "Cyclic Simple Shear Tests on Saturated Sand in Multi-Directional Loading," *Soils and Foundations*, Vol. 20, No.1, pp. 45-59.

Ishihara, K. and Yoshimine, M., 1992, "Evaluation of Settlements in Sand Deposits Following Liquefaction during Earthquakes," *Soils and Foundations*, Vol. 32, No.1, pp. 173-188.

Iwasaki, T., Tatsuoka, F., and Takagi, Y., 1978, ''Shear Moduli of Sands under Cyclic Torsional Shear Loading,'' *Soils and Foundations*, Vol. 18, No.1, pp. 39–56.

Kammerer, A., Pestana, J., and Seed, R.B., 2002, "Undrained Response of 0/30 Sand under Multidirectional Cyclic Simple Shear Loading Conditions," *Geotechnical Engineering Research Report No. UCB/GT/02-01*, University of California, Berkeley, Department of Civil & Environmental Engineering.

Kazemian, S., Huat, B.B.K., Prasad, A., and Barghchi, M., 2011, "A State of Art Review of Peat: Geotechnical Engineering Perspective," *International Journal of Physical Sciences*, Vol.6, No.8, pp. 1974-1981.

Kishida, T., Boulanger, R.W., Abrahamson, N.A., Wehling, T.A., and Driller, M.W., 2009a. "Regression Models for Dynamic Properties of Highly Organic Soils," *J. Geotech. Geoenviron. Eng.*,Vol.133, No.7, pp.851-866.

Kishida, T., Boulanger, R.W., Abrahamson, N.A., Driller, M.W., and Wehling, T.A., 2009b, "Site Effects for the Sacramento-San Joaquin Delta," *Earthquake Spectra*, Vol. 25, No. 2, pp. 301-322.

Kramer, S. L., 1996, ''Dynamic Response of Peats,'' *Final Research Rep. No. WA-RD 412.1*, Washington State Transportation Center, Univ. of Washington, Seattle.

Kramer, S. L., 2000, ''Dynamic Response of Mercer Slough Peat.'' *J. Geotech. Geoenviron. Eng.,* Vol.126, No.6, pp. 504–510.

Kutter, B.L., and Sathialingam, N., 1992, “Elastic Viscoplastic Modelling of the Rate-Dpendent Behaviour of Clays,” *Geotechnique* Vol. 42, No.3, pp. 427-441.

Ladd, C.C., and DeGroot, D.J., 2003, "Recommended Practice for Soft Ground Site Characterization," The Arthur Casagrande Lecture, *Proceedings of the 12th Panamerican Conference on Soil Mechanics and Geotechnical Engineering*, Boston, MA, Vol. 1, pp. 3-57.

Ladd, C.C., and Foot, R., 1974, “New Design Procedure for Stability of Soft Clays,” *Journal of Geotechnical Engineering Division,* ASCE, Vol. 100, No.7, pp. 767-787.

Ladd, C.C., 1991, “Stability Evaluation during Staged Construction,” 22nd Karl Terzahgi Lecture, *Journal of Geotechnical Engineering*, Vol.11, No. 4, pp. 540-615.

Landva, A. O., and La Rochelle, P., 1983, “Compressibility and Shear Characteristics of Radforth Peats,” *Testing of Peat and Organic Soils*, STP 820, ASTM, West Conshohocken, Pa., pp. 157–191.

Landva, A. O., and Pheeney, P. E., 1980, “Peat Fabric and Structure.” *Can. Geotech. J.*, Vol. 17, No.3, pp. 416–435.

Lanzo, G., Vucetic, M., and Doroudian, M., 1997, ‘‘Reduction of Shear Modulus at Small Strains in Simple Shear,’’ *J. Geotech. Geoenviron. Eng*., Vol. 123, No.11, pp. 1035–1042.

Lea, N., and Brawner, C.O., 1963, “Highway Design and Construction over Peat Deposits in the Lower British Colombia,” *Highw. Res. Rec.*, Vol. 7, pp. 1–32.

Liu, A.H., Stewart, J.P., Abrahamson, N.A., and Moriwaki Y., 2001, “Equivalent Number of Uniform Stress Cycles for Soil Liquefaction Analysis,” *J. Geotech. & Geoenv. Engrg.*, Vol. 127, No. 12, pp. 1017-1026.

Lowe, J., and Johnson, T.C., 1960, "Use of Back Pressure to Increase Degree of Saturation of Triaxial Test Specimens," *Proc. Research Conference on Shear Strength of Cohesive Soils*, Boulder, Colorado, ASCE, pp. 819-836.

Lund, J., Hanak, E., Fleenor, W., Howitt, R., Mount, J., and Moyle, P., 2007, "Envisioning Futures for the Sacramento-San Joaquin Delta," Public Policy Institute of California, San Francisco, CA.

Matasovic, N., and Vucetic, M., 1993, "Cyclic Characterization of Liquefiable Sands," *ASCE Journal of Geotechnical and Geoenvironmental Engineering*, Vol. 119. No.11, pp. 1805-1822.

Mesri, G., and Ajlouni, M., 2007, "Engineering Properties of Fibrous Peats," *J. Geotech. Geoenv. Eng*., Vol.133, No.7, pp. 851-866.

Mesri, G., Stark, T.D., Ajlouni, M.A., and Chen, C.S., 1997, "Secondary Compression of Peat with or without Surcharging," *J. Geotech. Geoeviron. Eng*., Vol.123, No. 5, pp. 411-421.

MacFarlane, I. C., 1969, "Engineering Characteristics of Peat." *Muskeg Engineering Handbook*, I. C. McFarlane, ed., Univ. of Toronto Press, Canada, pp. 78–126.

Mount, J. F., and Twiss, R., 2005, "Subsidence, Sea Level Rise, Seismicity in the Sacramento–San Joaquin Delta," *San Francisco Estuary and Watershed Science*, Vol. 3, Article 5, available at http://repositories.cdlib.org/jmie/sfews/vol3/iss1/art5.

Pearson, K., 1900, "On the Criterion that a Given System of Deviations from the Probable in the Case of a Correlated System of Variables is such that It can be Reasonably Supposed to have Arisen from Random Sampling," *Philosophical Magazine*, Vol. 50, pp. 157–175.

Porcino, D., Caridi, G., Malara, M., and Morabito, E., 2006, "An Automated Control System for Undrained Monotonic and Cyclic Simple Shear Tests," *GeoCongress 2006 – Geotechnical Engineering in the Information Technology Age*, DeGroot, D.J., DeJong, J.T., Frost, J.D., and Baise L.G. (eds.), Atlanta, GA, Feb. 26 – March 1, 6 pages (electronic file).

Reinert, E.T., 2014, "Dynamic Shake Testing of a Model Levee on Peaty Organic Soil in the Sacramento-San Joaquin Delta," *Ph.D. Dissertation*, University of California Los Angeles.

Reinert, E.T., Brandenberg, S.J., Stewart, J.P., and Moss, R.E.S., 2012, "Dynamic Field Test of a Model Levee Founded on Peaty Organic Soil Using an Eccentric Mass Shaker," *15th World Conference on Earthquake Engineering*, Lisbon, Portugal.

Rutherford, C.J., 2012, "Development of a Multi-Directional Direct Simple Shear Testing Device for Characterization of the Cyclic Shear Response of Marine Clays," *Ph.D. Dissertation*, Texas A&M University.

Seed, H.B., 1979, "Soil Liquefaction and Cyclic Mobility Evaluation for Level Ground during Earthquakes," *J. Geotech. Engrg. Div.*, Vol. 105, No. 2, pp. 201–255.

Seed, H. B., and Idriss, I. M., 1970, ''Analyses of Ground Motions at Union Bay, Seattle, during Earthquakes and Distant Nuclear Blasts,'' *Bull. Seismol. Soc. Am.*, Vol. 60, No. 1, pp. 125–136.

Seed, H. B., and Idriss, I. M., 1982, "Ground Motions and Soil Liquefaction During Earthquakes," *Earthquake Engineering Research Institute*, Oakland, CA, 134 pp.

Seed, H.B., Idriss, I.M., Makdisi, F. and Banerjee, N., 1975. "Representation of Irregular Stress Time Histories by Equivalent Uniform Stress Series in Liquefaction Analyses," *Rpt. No. UCB/EERC 75-29*, Earthquake Engrg. Res. Ctr., Univ. of California, Berkeley.

Shafiee, A., Brandenberg, S.J., and Stewart, J.P., 2013, "Laboratory Investigation of the Pre- and Post-Cyclic Volume Change Properties of Sherman Island Peat,", *Proc*. *GeoCongress 2013*, San Diego.

Shamoto, Y., Zhang, J.M., and Tokimatsu, K., 1998, "New Charts for Predicting Large Residual Post-Liquefaction Ground Deformation," *Soil Dynamics and Earthquake Engineering*, Vol. 17, pp. 427-438.

Shen, C.K., Sadigh, K., and Hermann, L.R., 1978, "An Analysis of NGI Simple Shear Apparatus for Cyclic Load Testing," *Dynamic Geotechnical Testing*, ASTM STP 654, ASTM International, West Conshohocken, PA, pp. 148-162.

Stewart, J.P., Brandenberg S.J., Shafiee, A. 2013, *Laboratory Evaluation of Seismic Failure Mechanisms of Levees on Peat*, UCLA-SGEL 2013/04, Civil & Environmental Engineering Department, UCLA.

Stokoe, K. H., II, Bay, J. A., Rosenbald, B. L., Hwang, S. K., and Twede, M. R.,1996, ''In Situ Seismic and Dynamic Laboratory Measurements of Geotechnical Materials at Queensboro Bridge and Roosevelt Island,'' *Geotechnical Engineering Rep. No. GR94-5*, Civil Engineering Dept., Univ. of Texas at Austin.

Stokoe, K. H., II, Darendeli, M.B., Ardus, R.D., and Brown, L.T., 1999. Dynamic Soil Properties: Laboratory, Field and Correlation Studies, Theme Lecture, Session 1: Dynamic

Characterization of Soils, *Second International Conference on Earthquake Geotechnical Engineering*, Vol. 3, Lisbon, Portugal.

Tatsuoka, F., Iwasaki, T., and Takagi, Y., 1978, ‘‘Hysteretic Damping of Sands under Cyclic Loading and Its Relation to Shear Modulus,’’ *Soils and Foundations*, Vol. 18, No. 2, pp. 25–40.

Tatsuoka, F., and Silver, M.L., 1981, “Undrained Stress-Strain Behavior of Sand under Irregular Loading,” *Soils and Foundations*, Vol. 21, No. 1, pp. 51–66.

Taylor, D.W. ,1948, *Fundamentals of Soil Mechanics*, John Wiley and Sons, Inc. New York.

Terzaghi, K., Peck, R. B., and Mesri, G., 1996, *Soil Mechanics in Engineering Practice*. Wiley, New York, 549.

Thiers G.R., and Seed H.B., 1969, “Strength and Stress-Strain Characteristics of Clays Subjected to Seismic Loading Conditions,”, *Proc. ASTM STP* 450, pp. 3-56.

Thompson, J., 1957, “Settlement Geography of the Sacramento–San Joaquin Delta, California,” Dissertation, Stanford University.

Tokimatsu, K., and Seed, H.B., 1987, “Evaluation of Settlements in Sands due to Earthquake Shaking,” *Journal of Geotechnical Engineering*, ASCE, Vol. 113, No. 8, pp. 861-878.

Torres, R.A., Abrahamson, N.A., Brovold, F.N., Cosio, G., Driller, M.W., Harder, L.F., Marachi, N.D., Neudeck, C.H., O’Leary, L.M., Ramsbotham, M., and Seed, R.B., 2000, “Seismic Vulnerability of the Sacramento – San Joaquin Delta Levees,” Levees and Channels Technical Team, Seismic Vulnerability Sub-Team, CALFED Bay-Delta Program, 30 pp. plus appendices.

Tressider, J. O., 1958, "A Review of Existing Method of Road Construction over Peat," *Tech. Paper No. 40*, DSIR, RRL, London.

Vaid, Y.P., and Finn, W.D.L., 1979, "Static Shear and Liquefaction Potential," *J. Geotech. Eng.*, ASCE, Vol. 105, No. 10, pp. 1233-1246.

Vucetic, M., and Dobry, R., 1991, ''Effect of Soil Plasticity on Cyclic Response,'' *J. Geotech. Eng.*, Vol. 117, No. 1, pp. 89–107.

Vucetic, M., Lanzo, G., and Doroudian, M., 1998, ''Damping at Small Strains in Cyclic Simple Shear Test,'' *J. Geotech. Geoenviron. Eng.*, Vol. 124, No. 7, pp. 585–594.

Vucetic, M., and Mortezaie, A., 2015, "Cyclic Secant Shear Modulus versus Pore Water Pressure in Sands at Small Cyclic Strains," Vol. 70, pp. 60-72.

Weber, W. G., 1969, "Performance of Embankments Constructed over Peat." *J. Soil Mech. and Found. Div.*, Vol. 95, No. 1, pp. 53–76.

Wehling, T. M., Boulanger, R. W., Arulnathan, R., Harder, L. F., Jr., and Driller, M. W., 2003, "Nonlinear Dynamic Properties of a Fibrous Organic Soil," *Journal of Geotechnical and Geoenvironmental Engineering*, ASCE, Vol. 129, No. 10, pp. 929-939.

Wijewickreme, D., 2010, "Cyclic Shear Response of Low Plastic Fraser River Silt," *Proc. 9th U.S. and 10th Canadian Conf. on Earthquake Engineering*, Toronto, Ontario, Canada, Paper No. 1431.

Wu, J., 2002, "Liquefaction Triggering and Post-Liquefaction Deformation of Monterey 0/30 Sand under Uni-Directional Cyclic Simple Shear Loading," *Ph.D. Dissertation* , University of California, Berkeley.

Wu, J., and Seed, R.B., 2004, "Estimation of Liquefaction Induced Ground Settlement (Case Studies)," *Proc. 5th Int. Conf. Case Histories in Geotechnical Engineering*, New York, NY.

Yamaguchi, H., Ohira, Y., Kogure, K., and Mori, S., 1985a, "Undrained Shear Characteristics of Normally Consolidated Peat under Triaxial Compression and Extension Conditions," *Japanese Society of Soil Mech., and Found. Eng.*, Vol. 25, No. 3, pp. 1–18.

Yamaguchi, H., Ohira, Y., Kogure, K., and Mori, S., 1985b, "Deformation and Strength Properties of Peat," *Proc., 11th Int. Conf. on Soil Mechanics and Foundation Engineering*, Vol. 4, pp. 2461–2464.

Yasuhara, K., 1994, "Postcyclic Undrained Strength for Cohesive Soils," *J. Geotech. Engrg.,* Vol. 120, No. 11, pp. 1961-1979.

Yasuhara, K., Murakami, S., Toyota, N. and Hyde, A.F.L., 2001, "Settlements in Fine-Grained Soils under Cyclic Loading," *Soils and Foundations*, Vol. 41, No. 6, pp. 25-36.

Yee, E., Duku, P.M., and Stewart, J.P., 2013, "Cyclic Volumetric Strain Behavior of Sands with Fines of Low Plasticity," *J. Geotech. Geoenviron. Eng.,* Vol. 140, No. 4, 04013042.

Yee, E., Stewart, J.P., and Schoenberg, R.P., 2011, "Characterization and Utilization of Noisy Displacement Signals from Simple Shear Device using Spectral, Linear, and Kernel Regression," *Soil Dynamics and Earthquake Engineering*, Vol. 31, No. 1, pp. 25-32.

Yee, E., Stewart, J. P., and Tokimatsu, K., 2013, "Elastic and Large-Strain Nonlinear Seismic Site Response from Analysis of Vertical Array Recordings," *J. Geotech. Geoenviron. Eng.,* Vol. 139, No. 10, pp. 1789-1801.

Youd, T., Idriss, I., Andrus, R., Arango, I., Castro, G., Christian, J., , Dobry, R., Finn, W., Harder, L., Jr., Hynes, M., Ishihara, K., Koester, J., Liao, S., Marcuson, W., Martin, G., Mitchell, J., Moriwaki, Y., Power, M., Robertson, P., Seed, R., and Stokoe, K., 2001), "Liquefaction Resistance of Soils: Summary Report from the 1996 NCEER and 1998 NCEER/NSF Workshops on Evaluation of Liquefaction Resistance of Soils." *J. Geotech. Geoenviron. Eng.*, ASCE, Vol. 127, No. 10, pp. 817–833.